

UNCLASSIFIED

AD NUMBER	
AD368639	
CLASSIFICATION CHANGES	
TO:	UNCLASSIFIED
FROM:	CONFIDENTIAL
LIMITATION CHANGES	
TO: Approved for public release; distribution is unlimited.	
FROM: Distribution authorized to U.S. Gov't. agencies and their contractors; Administrative/Operational Use; DEC 1965. Other requests shall be referred to Air Force Rocket Propulsion Laboratory, Research and Technology Division, Edwards AFB, CA.	
AUTHORITY	
31 dec 1972, per document marking AFRPL ltr 7 May 1973	

THIS PAGE IS UNCLASSIFIED

S U B J E C T T O

THE GENERAL DECLASSIFICATION SCHEDULED IN ACCORDANCE WITH

INFORMATION SECURITY PROGRAM REGULATION DATED - JUNE 1972

**DOD 5200.1-R & EXECUTIVE ORDER 11652
(EXECUTIVE ORDER 10501 AMENDED)**

BY

**Defense Documentation Center
Defense Supply Agency
Cameron Station
Alexandria, Virginia 22314**

DECEMBER 1972

SECURITY

MARKING

The classified or limited status of this report applies to each page, unless otherwise marked.

Separate page printouts MUST be marked accordingly.

THIS DOCUMENT CONTAINS INFORMATION AFFECTING THE NATIONAL DEFENSE OF THE UNITED STATES WITHIN THE MEANING OF THE ESPIONAGE LAWS, TITLE 18, U.S.C., SECTIONS 793 AND 794. THE TRANSMISSION OR THE REVELATION OF ITS CONTENTS IN ANY MANNER TO AN UNAUTHORIZED PERSON IS PROHIBITED BY LAW.

NOTICE: When government or other drawings, specifications or other data are used for any purpose other than in connection with a definitely related government procurement operation, the U. S. Government thereby incurs no responsibility, nor any obligation whatsoever; and the fact that the Government may have formulated, furnished, or in any way supplied the said drawings, specifications, or other data is not to be regarded by implication or otherwise as in any manner licensing the holder or any other person or corporation, or conveying any rights or permission to manufacture, use or sell any patented invention that may in any way be related thereto.

CONFIDENTIAL

Report AFRPL-TR-65-191

HIGH CHAMBER PRESSURE ROCKETRY PROGRAM (U)

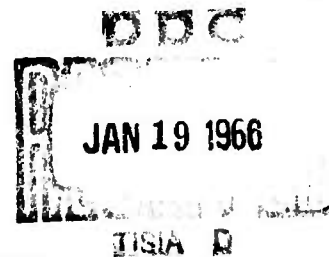
Final Report

Contract AF 04(611)-8191

Book Two
of Two

Prepared for

ROCKET PROPULSION LABORATORY
Research and Technology Division
Air Force Systems Command
United States Air Force
Edwards, California



AIR FORCE PROGRAM STRUCTURE NO. 750G
AFSC PROJECT NO. 3058
AFSC TASK NO. 305802

CONFIDENTIAL

0652

368639

CONFIDENTIAL

December 1965

Report AFRPL-TR-65-191

AGC Report 8191-F

HIGH CHAMBER PRESSURE ROCKETRY PROGRAM (u)

Final Report

Contract AF 04(611)-8191

Book Two
of Two

Prepared for

ROCKET PROPULSION LABORATORY
Research and Technology Division
Air Force Systems Command
United States Air Force
Edwards, California

AIR FORCE PROGRAM STRUCTURE NO. 750G
AFSC PROJECT NO. 3058
AFSC TASK NO. 305802

GROUP 4

DOWNGRADED AT 3 YEAR INTERVALS; DECLASSIFIED AFTER 12 YEARS.

" THIS DOCUMENT CONTAINS INFORMATION AFFECTING THE NATIONAL DEFENSE OF THE UNITED STATES
WITHIN THE MEANING OF THE ESPIONAGE LAWS, TITLE 18, U.S.C., SECTIONS 793 AND 794. ITS TRANSMISSION
OR THE REVELATION OF ITS CONTENTS IN ANY MANNER TO AN UNAUTHORIZED PERSON IS PROHIBITED BY LAW. "

6381T

AEROJET-GENERAL CORPORATION
A SUBSIDIARY OF THE GENERAL TIRE & RUBBER COMPANY

CONFIDENTIAL

Book Two

FIGURE LIST

	<u>Figure</u>
Real Gas Effects on the Performance Efficiency-- MR = 2.1	VIII-A-1
Real Gas Effects on the Performance Efficiency-- MR = 2.3	VIII-A-2
Real Gas Effects on the Performance Efficiency-- MR = 2.6	VIII-A-3
Uncooled TCA Test Data	VIII-A-4
Uncooled TCA Tests Performance Efficiencies	VIII-A-5
Cooled TCA Test Data	VIII-B-1
Cooled TCA Tests I_g Efficiency	VIII-B-2
Parameters Computed with Film-Cooling Model	VIII-C-1
Comparison of Film-Cooling Model with Experimental Data, HiPc Tests	VIII-C-2
Comparison of Film-Cooling Model with Experimental Data, ICP Tests	VIII-C-3
Performance Comparison for Film Cooling in the HiPc and ICP Tests	VIII-C-4
Correlation of ICP Film-Cooling Test Data, Test -024	VIII-D-1
Correlation of ICP Film-Cooling Test Data, Test -025	VIII-D-2
Correlation of ICP Film-Cooling Test Data, Test -027	VIII-D-3
Comparison of Experimental and Theoretical Wall Temperatures for Test -YAM-027	VIII-D-4
Comparison of Experimental and Theoretical Wall Temperatures for Test -YAM-036	VIII-D-5
Film Coolant Required to Cool Chamber and Throat	VIII-E-1
Assumed Chamber Geometry	VIII-E-2
Film Coolant Required to Cool Throat	VIII-E-3
Film Coolant Required to Cool Chamber	VIII-E-4
Combustion Stability Test Data	IX-A-1
Installation of High-Pressure Transducers Mounted on Injector Frequency Monitoring System	IX-B-1
Installation of Kistler Water-Cooled Probe Adapter in Ablative Chamber Liner	IX-B-2
Ampex Playback-- Concentric Ring (Mod III)	IX-C-1
Ampex Playback-- Concentric Ring (Mod VIII)	IX-C-2
Ampex Playback-- Concentric Ring (Mod VIIIA) plus Cooled Throat Segment	IX-C-3

Book Two

FIGURE LIST (cont.)

	<u>Figure</u>
Ampex Playback-- Concentric Ring (Mod VIIIB) plus Cooled Throat and Exit Cone	IX-C-4
Ampex Playback-- Concentric Ring (Mod VIIIB) plus Drilled L* Segment	IX-C-5
Ampex Playback-- Transpiration Cooled Injector	IX-D-1
Optimum Nozzle Area Ratio vs Thrust Chamber Pressure, DeLaval Nozzle	X-A-1
Optimum Nozzle Area Ratio vs Thrust Chamber Pressure, Forced-Deflection Nozzle	X-A-2
Optimum Nozzle Area Ratio vs Thrust Chamber Pressure, Upper-Stage Vehicle-- $V_1 = 10,000$ ft/sec	X-A-3
Optimum Nozzle Area Ratio vs Thrust Chamber Pressure, Upper-Stage Vehicle-- $V_1 = 15,000$ ft/sec	X-A-4
Optimum Nozzle Area Ratio vs Thrust Chamber Pressure Upper-Stage Vehicle-- $V_1 = 20,000$ ft/sec	X-A-5
Relative Payload vs Thrust Chamber Pressure, Single Stage to 300 N.M. Orbit	X-A-6
Relative Payload vs Thrust Chamber Pressure, First-Stage Vehicle-- $V_1 = 20,000$ ft/sec	X-A-7
Relative Payload vs Thrust Chamber Pressure, First-Stage Vehicle-- $V_1 = 10,000$ ft/sec	X-A-8
Relative Payload vs Thrust Chamber Pressure, Upper-Stage Vehicle-- $V_1 = 20,000$ ft/sec	X-A-9
Relative Payload vs Thrust Chamber Pressure, Upper-Stage Vehicle-- $V_1 = 15,000$ ft/sec	X-A-10
Relative Payload vs Thrust Chamber Pressure, Upper-Stage Vehicle-- $V_1 = 10,000$ ft/sec	X-A-11
Payload to Takeoff Weight Ratio vs Thrust Chamber Mixture Ratio	X-A-12
Vehicle Cost Per Pound of Payload vs Thrust Chamber Mixture Ratio	X-A-13
Effect of Film Cooling on Delivered Payload, Staged Combustion Cycle	X-A-14
Effect of Film Cooling on Delivered Payload, Gas Generator Cycle	X-A-15
Turbopump Weights	X-B-1
Engine Less TPA weights	X-B-2
DeLaval Nozzle Weight Variations	X-B-3
Forced-Deflection Nozzle Weight Variation	X-B-4

Book Two

FIGURE LIST (cont.)

	<u>Figure</u>
Symbols for Cycle Analysis	X-C-1
Gas Generator Cycle Schematic Diagram	X-C-2
I_{sp} Degradation, Gas Generator Cycle	X-C-3
Specific Impulse vs Chamber Pressure	X-C-4
ΔI_{sp} Due to Pump Work	X-C-5
Specific Impulse vs Chamber Pressure, Gas Generator Cycle	X-C-6
Staged Combustion Cycle Schematic	X-C-7
Pump Discharge Pressure vs Chamber Pressure, Gas Generator Cycle	X-C-8
Chamber Pressure vs Pump Discharge Pressure, Staged-Combustion Cycle	X-C-9
Engine Mixture Ratio vs Thrust Chamber Mixture Ratio	X-C-10
Engine Development Cost	X-D-1
Propellant Costs for Engine Development	X-D-2
Facility Costs	X-D-3
GSE Costs	X-D-4
Engine Production Tooling Costs	X-D-5
Stage Development Cost	X-D-6
Engine Production Cost	X-D-7
Engine Acceptance Testing Cost	X-D-8
Stage Production Cost	X-D-9
Stage Transportation Cost	X-D-10
Stage Launch Operation Cost	X-D-11
Propellant Cost	X-D-12
Film-Cooling Model, No Mixing	X-E-1
Film-Cooling Models, Partial and Complete Mixing	X-E-2
Specific Impulse Loss Due to Film Cooling, No Mixing	X-E-3
Specific Impulse Loss Due to Film Cooling, Partial Mixing	X-E-4
Film-Cooling Models, Complete Mixing	X-E-5
Specific Impulse Loss Due to Film Cooling, Complete	X-E-6
Specific Impulse Loss Due to Film Cooling with Burnoff	X-E-7

Book Two

FIGURE LIST (cont.)

	<u>Figure</u>
Relative Payload vs Chamber Pressure, $N_2O_4/N_2H_4 + Al$	X-F-1
Relative Payload vs Chamber Pressure, $N_2O_4/N_2H_4 + AlH_3$	X-F-2
Relative Payload vs Chamber Pressure, $N_2O_4/N_2H_4 + Be$	X-F-3
Relative Payload vs Chamber Pressure, $N_2O_4/N_2H_4 + BeH_2$	X-F-4
Relative Payload vs Chamber Pressure, $H_2O_2/N_2H_4 + Al$	X-F-5
Relative Payload vs Chamber Pressure, $H_2O_2/N_2H_4 + AlH_3$	X-F-6
Relative Payload vs Chamber Pressure, $H_2O_2/N_2H_4 + Be$	X-F-7
Relative Payload vs Chamber Pressure, $H_2O_2/N_2H_4 + BeH_2$	X-F-8
Relative Payload vs Chamber Pressure, N_2O_4/A_{50}	X-F-9
Forced-Deflection Engine Installation, 20-Module Design	XI-B-1
DeLaval Engine Installation, 20-Module Design	XI-B-2
Vacuum Performance Summary	XI-C-1
Forced-Deflection Engine Altitude Compensation, 1000-psi Chamber Pressure	XI-C-2
Forced-Deflection Engine Altitude Compensation, 2800-psi Chamber Pressure	XI-C-3
Forced-Deflection Engine Altitude Compensation, 5000-psi Chamber Pressure	XI-C-4
Total Velocity Increments, DeLaval Nozzles	XI-D-1
Total Velocity Increments, Forced-Deflection Nozzles	XI-D-2
Forced-Deflection Skirt Weight	XI-E-1
Engine Weight Summary	XI-E-2
Rack and Rail Gimbal	XI-E-3
Airframe Weight Summary	XI-E-4
Area Ratio Optimization, Single-Stage DeLaval Nozzle	XI-F-1
Area Ratio Optimization, Forced-Deflection Nozzle	XI-F-2
Area Ratio Optimization, Booster DeLaval Nozzle	XI-F-3
Area Ratio Optimization, Forced-Deflection Nozzle	XI-F-4
Area Ratio Optimization, Upper-Stage DeLaval Nozzle	XI-F-5
Optimum Area Ratio vs Chamber Pressure, Staged Cycle	XI-F-6
Chamber Pressure Optimization, Single Stage	XI-F-7
Chamber Pressure Optimization, Booster	XI-F-8
Chamber Pressure Optimization, Upper Stage	XI-F-9

Book Two

FIGURE LIST (cont.)

	<u>Figure</u>
Tube Design Regimes	XI-G-1
Tube Weight vs Diameter Design Curves	XI-G-2
Tube Weight vs Diameter	XI-G-3
DeLaval Nozzle Weight	XI-G-4
DeLaval Nozzle-Stiffener Weight	XI-G-5
Test Engine Schematic Diagram	XII-A-1
Pumping System Installation, Test Stand H-3	XII-A-2
Gas Generator and Y-Manifold Installed on Test Stand H-3	XII-A-3
Fuel Turbopump Installation, Test Stand H-3	XII-A-4
Uncooled Thrust Chamber Assembly Installed on Test Stand H-3	XII-A-5
Cooled Throat and Exit Cone Installed on Test Stand H-3	XII-A-6
Original Gas Generator Valve Sequence	XII-A-7
Final Gas Generator Valve Sequence	XII-A-8
Typical Uncooled TCA Start Transient	XII-B-1
Typical Uncooled TCA Shutdown Transient	XII-B-2
Original Turbopump Assembly Design	XII-C-1
Pumping System Data, Test 1.2-02-YAP-001	XII-C-2
Pumping System Data, Test 1.2-02-YAP-002	XII-C-3
Pumping System Data, Test 1.2-02-YAP-003	XII-C-4
Pumping System Data, Test 1.2-02-YAP-004	XII-C-5
Pumping System Data, Test 1.2-02-YAP-005	XII-C-6
Final Turbopump Assembly Design	XII-C-7

CONFIDENTIAL

Book Two

VIII. THRUST CHAMBER PERFORMANCE

The results of the analysis of the 50K hot-firing performance data obtained on this program are discussed in this section. The objectives of this analysis are to (1) determine the injector performance obtained, (2) determine the effect on performance of adding supplemental film cooling, (3) establish the minimum film cooling required to adequately cool a high-pressure rocket engine and, (4) establish how this minimum film cooling is affected by the thrust chamber pressure.

Uncooled and cooled chamber performance is discussed in Section VIII,A and B, respectively. Included are methods used to reduce the data, corrections factors applied and discussion of results. Results of this analysis showed that the highest injector performance recorded was 97% of theoretical c^* and was achieved with the transpiration cooled, swirl tube injector. This was the only test on this injector which yielded valid steady-state data. The majority of testing was accomplished using the concentric-ring injector. Performance measured on this injector was between 92 and 96% of theoretical c^* and was dependent on mixture ratio. Results of film-cooled testing showed performance losses were approximately proportional to 0.75 times the ratio of film-coolant flow rate to injector flow rate for film coolant injected in the thrust chamber. Greater losses resulted when the film coolant was injected downstream of the throat.

An analytical model, which shows the effect of film cooling on performance, is presented and compared with film cooled test data in Section VIII,C. It is shown that this model can generally be used to predict performance losses resulting from film cooling. The film cooling data obtained is compared with that predicted by a mathematical model in Section VIII,D. A modified Hatch and Pappel relationship is used in this analysis. Although the temperature data showed a rather wide scatter, fair agreement with the model is shown. This temperature data scatter resulted from nonuniform distribution of film cooling in the chamber. Consequently, relatively large quantities of film cooling were required and theoretical minimum film cooling could not be demonstrated.

CONFIDENTIAL

Book Two

VIII, Thrust Chamber Performance (cont.)

The film cooling model was then incorporated into an analysis to show the effect of chamber pressure on the minimum quantity of film cooling required. Results of this analysis showed that below 1170-psia chamber pressure, no film cooling is required. Above this pressure, minimum required film cooling increases nearly linearly to approximately 4.0% of the injector flow rate at 3000 psia chamber pressure and 6.5% of the injector flow rate at 5000 psia in a 100K thrust chamber.

A. UNCOOLED CHAMBER PERFORMANCE

1. Methods of Analysis

The purpose of the uncooled chamber tests was to develop a satisfactory injector prior to conducting the cooled nozzle tests. Once an acceptable injector concept was selected, the uncooled performance as a function of mixture ratio was experimentally determined. Data for basic injector performance as a function of mixture ratio are necessary (1) to define the driving force temperature of the main-stream gases with film cooling and (2) to establish a basis to which the film cooling effects on nozzle performance can be compared.

These tests were conducted with an ablative chamber and nozzle which are both described in detail in Section XI. The problem with determining performance for this type of nozzle is that the throat area varies with time throughout the test duration. In these tests the throat area was assumed to vary linearly with time from start to shutdown and an average throat area selected at the mean time over which valid data were obtained.

Performance parameters of importance in these tests are specific impulse and characteristic velocity. The thrust coefficients for the nozzles tested are not indicative of good performance because of the large losses from flow divergence. These nozzles are truncated sections of a large area ratio ($\epsilon = 182:1$) "Rao" optimum nozzle and the exit wall angles are quite large at the lower area ratios. Hence the flow exits with a large radial component resulting in a significant reduction in axial thrust efficiency.

CONFIDENTIAL

Book Two

VIII, A, Uncooled Chamber Performance (cont.)

Specific impulse is calculated in the standard manner by dividing the measured thrust by the weight flow. Impulse efficiency is then obtained by dividing by the theoretical specific impulse as obtained from the Chemical Composition Program for the corresponding test conditions. However, vacuum specific impulse and impulse efficiency is essentially independent of chamber pressure, while sea level values are not. Hence, to eliminate the effect of chamber pressure level on the performance comparison, all data are converted to vacuum conditions. This conversion consists of adding the ambient pressure times the nozzle exit area to the sea-level thrust. The theoretical specific impulse for determining the impulse efficiency is that corresponding to the area ratio of the nozzle tested.

Characteristic velocity for the uncooled tests is calculated by two methods. First by the standard technique using the following expression:

$$c^* = \frac{g_c P_{sn} A_t}{\dot{w}}$$

This employs a measured value of chamber pressure to calculate an effective stagnation pressure for the nozzle plus the measured weight flow and the mean throat area to calculate characteristic velocity. Here the effective stagnation pressure depends on the location of the pressure tap in the chamber and the contraction ratio of the chamber. A second method for computing characteristic velocity is to use the following:

$$c^* = \frac{g_c F}{C_F W}$$

In this expression the thrust coefficient in the denominator is determined by subtracting certain theoretically computed losses from the shifting equilibrium thrust coefficients. Computed losses in nozzle thrust include (1) divergence, (2) shear drag along the nozzle wall, and (3) real gas effects due to incomplete combustion in the chamber. Each of these losses and their respective methods of calculation are discussed in the following paragraphs.

CONFIDENTIAL

Book Two

VIII, A, Uncooled Chamber Performance (cont.)

Flow Divergence

This loss results from the flow leaving the nozzle with a radial component which is not useful for producing axial thrust. Its effect is computed by solving for the flow field within the nozzle using the method of characteristics for supersonic flow. Because the nozzle tested in this program was a truncated segment of a much larger nozzle, divergence losses were quite high. In fact, the initial expansion region out to 21:1 area ratio consist of a conical section of 35° half-angle. A tabulation of the loss factors for the different nozzle geometrys encountered in this test program is shown below:

Expansion Ratio, ϵ	$C_{f_{vac}}$ (3-dim)	$C_{f_{vac}}$ (1-dim)	Divergence Loss $\eta_g - \%$
4.5	1.470	1.637	10.2
8.3	1.558	1.733	10.1
21.0	1.669	1.841	9.4
70.0	1.799	1.939	7.2
183.0	1.943	1.943	2.6

Since the maximum area ratio tested during the uncooled test series was approximately 21:1, the flow divergence losses were quite high, on the order of 10%. This is by far the biggest loss associated with the thrust efficiency of the nozzle and also the most precisely predicted by analytical methods.

Shear Drag

Viscous effects between the nozzle wall and the gaseous boundary layer result in a shear force on the nozzle wall which degrades nozzle thrust. An empirical approach based on the extended Frankl-Voishel analysis was used to

CONFIDENTIAL

Book Two

VIII, A, Uncooled Chamber Performance (cont.)

obtain friction coefficients for the configurations tested. The results showed that drag losses increased with area ratio as follows:

Expansion Ratio, ϵ	Drag Loss, $\eta_D - \%$
4.5	.21
8.3	.33
21.0	.46
70.0	.69
183.0	.95

Thus, this loss accounted for less than 0.5% reduction in thrust efficiency in the uncooled nozzle configurations.

Real Gas Effects

The first two losses factor can be considered as essentially independent of the injector combustion efficiency. Where incomplete combustion exists, the effect is to reduce both c^* and nozzle thrust efficiency. The effect of combustion efficiency on the nozzle thrust coefficient may be seen by examining the thermochemistry of the combustion products. With complete combustion there is a considerable amount of dissociated species in the chamber which combine and add heat to the gas stream during expansion. Heat release from the recombination process increases the effective nozzle performance as compared to a nonequilibrium or frozen flow process. Incomplete combustion in the chamber results in less dissociated species and hence less heat released within the nozzle. The effect is a reduced nozzle thrust efficiency when compared to the shifting equilibrium performance for complete combustion.

CONFIDENTIAL

Book Two

VIII, A, Uncooled Chamber Performance (cont.)

2. Test Data Analysis

Figures VIII-A-1, 2 and 3 show the degradation in nozzle efficiency with combustion efficiency for N_2O_4 /A-50 propellants at mixture ratios of 2.1:1, 2.3:1, and 2.6:1, respectively. These data were obtained by running the chemical composition program at a series of reduced chamber enthalpies. The results show that nozzle thrust-losses increase with decreased combustion efficiency and increased nozzle area ratio. Because this loss results from an interaction between combustion efficiency and thrust efficiency, the absolute value for each case must be determined by a trial and error iteration for a known specific impulse efficiency.

The use of the two methods for computing characteristic velocity described in Section VIII,A,1, above, permits an independent check on the consistency of the test data. Both methods should show relatively close agreement ($\pm 1\%$) in these uncooled tests and discrepancies greater than 1% are indicative of errors in the test data or the interpolated throat area. In the conventional method for determining c^* , an error in defining the throat area is directly proportional to the resulting error in the c^* calculated. However, with the second method just described (using thrust and C_F), the throat area is only used to define expansion ratio for the theoretical thrust coefficient and any error in the throat area interpolation is reduced by a factor of about six to eight in the resulting c^* calculation.

Figure VIII-A-4 contains a tabulation of all the valid uncooled chamber test results obtained in this program with the Rigimesh-face concentric-ring and transpiration-cooled injectors. The first eight tests in this tabulation were conducted with concentric-ring injector; combustion efficiency was about 92 to 96% with this configuration. The three tests in which the Drilled L^* segment was evaluated are included in this tabulation. Although these tests were part of the cooled chamber program, the performance obtained is representative of uncooled chamber performance, since the L^* segment was regeneratively cooled with no film cooling except the small amount normally supplied by the injector in the uncooled tests. The last test shown in the figure was with the swirl tube, transpiration-cooled injector; this test demonstrated the highest c^* efficiency obtained in the program.

CONFIDENTIAL

Book Two

VIII, A, Uncooled Chamber Performance (cont.)

Specific impulse and c^* efficiencies as a function of mixture ratio for these tests are shown on Figure VIII-A-5. The largest deviations from the mean lines drawn through the test data were on Tests -030 and -034. These were low area-ratio nozzles ($\epsilon = 4.5:1$), where the specific impulse variation with area ratio is quite steep. These small errors in defining the mean throat area for the data period can have a significant effect on the determination of specific impulse efficiency. At higher area ratios, this effect diminishes considerably.

The mean line through the test data shows both the specific impulse and c^* efficiencies increasing with injector mixture ratio. While the selection of this line is somewhat arbitrary, an attempt was made to follow the general trend of the data. Use will be made of the mean c^* trend in a later section for defining a film cooling model to describe the cooled nozzle test results.

CONFIDENTIAL

Book Two

VIII, Thrust Chamber Performance (cont.)

B. COOLED CHAMBER PERFORMANCE

The objective of the cooled chamber tests was to determine the effect of film cooling on TCA performance. One of the problems with finding performance results with film cooling is the difficulty in defining an effective stagnation pressure for the chamber. There is strong evidence supporting the stand that the measured chamber pressure cannot be converted directly to stagnation pressure for a film-cooled chamber. Some of the reasons for this are that (1) heat loss to the film cooling tends to reduce stagnation pressure of the mainstream gases as they approach the nozzle throat, and (2) it is likely that the total pressures of the film coolant and mainstream gases differ significantly, thereby making it difficult to determine a mean effective pressure for the combined streams.

Because of the difficulties in evaluating stagnation pressure with film cooling, characteristic velocity as calculated from measured chamber pressure has little or no meaning and can often result in a misinterpretation of the test data. The only meaningful performance parameter then is specific impulse, which can, of course, be determined from thrust and weight flow alone. Also, it is beneficial to determine specific impulse efficiency under vacuum conditions to negate the dependence on effective stagnation pressure.

A tabulation of the valid cooled chamber performance obtained in this program is given in Figure VIII-B-1. Included in this tabulation are reported values for both characteristic velocity (c^*) and c^* efficiency based on measured chamber pressures in each test. While these values are thought to be inaccurate, as explained previously, they are presented for comparison with film cooling model results in the next section. Characteristic velocity as calculated herein includes the total weight flow at the nozzle throat, whereas specific impulse includes the entire TCA weight flow. These flow rates differ by the amount of film cooling introduced downstream of the nozzle throat.

CONFIDENTIAL

Book Two

VIII, B, Cooled Chamber Performance (cont.)

The efficiencies in Figure VIII-B-1 are based on theoretical values of specific impulse and characteristic velocity at the injector mixture ratio conditions. Injector mixture ratio is used as a basis rather than overall mixture ratio in order to point out the real effects of film cooling on TCA performance. Use of overall mixture ratio as a basis for defining theoretical performance will, for the most part, result in higher reported efficiencies, but this is not a true indication of the performance gains that could be attained if film cooling is reduced or eliminated altogether.

The first five tests, shown on Figure VIII-B-1, were conducted using a low area ratio nozzle ($\epsilon = 8.3$). Performance efficiency results for these tests are significantly lower than for the remainder of the tests. There appears to be no logical reason for the low performance in these tests: one explanation could be instrumentation or data reduction errors in connection with the measured film cooling flow rates; however, it is unlikely that such errors would be repeated throughout the entire test series. Another possible explanation could be that some portion of the film coolant escapes from the nozzle prior to complete evaporation. The cooling added downstream of the throat is below critical pressure upon injection and also has little time to heat sufficiently to vaporize entirely. The effect of this would be to lower nozzle performance in an unpredictable manner since it is impossible to resolve how much coolant fails to vaporize in the nozzle.

Discrepancies in the low area-ratio test data are readily apparent when the results of Tests -012 and -018 are compared. Both tests had the same percent film cooling but yielded a 4% difference in measured performance. Some of the inconsistencies in the test results can be more easily seen on a plot of specific impulse efficiency as shown in Figure VIII-B-2. Data points for the 8.3 area ratio tests are shown as circles on this plot. Since injector mixture ratio was almost identical in these tests, performance was expected to decrease

CONFIDENTIAL

Book Two

VIII, B, Cooled Chamber Performance (cont.)

uniformly with increased percent film cooling. However, as shown on Figure VIII-B-2, the performance results seem to vary randomly, and therefore, no general conclusions can be drawn from these five tests.

The remainder of the cooled tests employed a nozzle extension with an area ratio of 21, except Test -029 which had an extension of area ratio 70. Performance results for these tests are also shown on Figure VIII-B-2. All data at the higher area ratios seems to be relatively consistent except for Test -033. The nozzle throat section in this test sustained some minor erosion; however, an attempt was made to use only the test data prior to the time when erosion occurred. The results indicate that either erosion had started within the test period or the engine performance had not steadied sufficiently during the data period.

Test -024 had the lowest performance of the higher area-ratio nozzles; however it also operated at a very low injector mixture ratio. This data is realistic since basic injector performance also decreases at lower mixture ratios. Test -036 yielded the highest impulse efficiency of the cooled nozzle tests. This chamber used only 11% film cooling, with no film cooling downstream of the nozzle throat. It showed a 4.5% increase in performance over that of Test -021 for a 6% reduction in coolant flows between the two tests.

One of the objectives of the film cooling performance investigation was to examine the effect of a high area-ratio nozzle on performance recovery through coolant afterburning in the nozzle exit section. If a significant amount of the film cooling were to burn in the nozzle, its effect on performance would be reflected in a higher nozzle thrust efficiencies for a large area ratio nozzle relative to a lower area ratio. Only one test (Test -029) was conducted with the high area-ratio nozzle extension ($\epsilon = 70$). The resulting specific impulse efficiency in this test was definitely higher (about 3%) than the 21:1 area ratio nozzles at approximately the same percent film cooling (Figure VIII-B-2). However, part of this variation is due to the different flow divergence loss characteristics

CONFIDENTIAL

Book Two

VIII, B, Cooled Chamber Performance (cont.)

between the two configurations. The 21:1 area ratio nozzle had a divergence loss of 9.4% compared with 7.2% in the 70:1 area ratio nozzle. This 2.2% difference in flow divergence losses should be evidenced by a higher efficiency in the larger area-ratio nozzle. The variation between the experimental difference (about 3%) and the flow divergence correction (about 2.2%) for these two nozzles is probably within the accuracy of the measuring technique, so that no conclusions can be drawn as to the film cooling performance recovery in high area-ratio nozzles. Another reason for reaching this conclusion is that in the high area-ratio nozzle test (Test -029), the injector mixture ratio was 2.73 and, thus, quite oxidizer-rich. It would be almost impossible for the oxidizer film cooling to contact any unburned fuel under these conditions, so that afterburning of the film coolant is questionable for this test.

A further appraisal of the cooled nozzle test results is presented in the next section which discusses the film cooling model for predicting performance.

CONFIDENTIAL

Book Two

VIII, Thrust Chamber Performance (cont.)

C. FILM COOLING PERFORMANCE CORRELATION

A study was conducted to establish the effect of film cooling on rocket engine performance. As part of the study, a mathematical model which describes the effect of film cooling on nozzle performance was developed. The application of this model to the test data of the High Chamber Pressure Rocketry Program (HiP_c), as well as to some of the data from the Integrated Components Program (ICP), Contract AF 04(611)-8548, is discussed in Section VIII,C,1. The mathematical expressions of the model are presented in Section VIII,C,2.

1. Application of Performance Correlation Model

The performance correlation model was applied to experimental data from the HiP_c Program to demonstrate (1) the precision to which performance can be predicted, and (2) certain limitations associated with the initial assumptions. An almost identical film cooling model has also been applied to experimental data from ICP. The only difference between the two models is in the calculation of film coolant total temperature at the nozzle throat. This difference was necessary to account for the fact that the ICP and HiP_c chambers used different film coolant injection techniques. In the ICP chamber, coolant was injected parallel to the nozzle wall at one location (the entrance to the convergence section) and in an axial direction. Multiple injection stations were used in the HiP_c chamber with coolant injection tangential to the wall in a swirled motion with essentially no axial component. Differences between the heat transfer characteristics associated with these two cooling techniques are discussed in Section VIII,D.

The mathematical model divides the performance losses into two categories: (1) those losses which are independent of c^* efficiency, and (2) interacting losses which affect both c^* and nozzle thrust efficiency.

CONFIDENTIAL

Book Two

VIII, C, Film Cooling Performance Correlation (cont.)

Interacting losses include both film cooling and incomplete combustion as they effect performance, while nozzle friction and flow divergence affect only the nozzle thrust efficiency. With both factors defined, the overall specific impulse efficiency for a given nozzle can be determined as follows:

$$\eta_{I_s} = \eta_T \times \eta_c$$

where η_T is the nozzle thrust efficiency, and includes the effects of nozzle friction, flow divergence, film cooling, and incomplete combustion on the actual thrust coefficient.

η_c is the characteristic velocity efficiency which includes incomplete combustion at the injector, heat lost to the film coolant, plus the film coolant mass discharge at the nozzle throat conditions.

The parameters defined in the analysis are shown in Figure VIII-C-1. Both streams are expanded separately in static pressure equilibrium, assuming no mixing or chemical reaction. Heat transfer from the mainstream to the film coolant is considered in the performance model upstream of the throat, but neglected for the downstream region.

An assumption is made that both the film coolant and mainstream flows are at sonic speed conditions in the nozzle throat. This permits calculation of the effective flow area for each gas stream and a mean effective characteristic velocity. The model also computes an effective stagnation pressure for the combined flows as well as different stagnation pressures for both the film coolant and mainstream. Effective stagnation pressures computed by the model differ considerably from measured chamber pressure with film cooling. However this should be anticipated since measured chamber pressures with film cooling often result in misinterpreted experimental characteristic velocity values.

CONFIDENTIAL

Book Two

VIII, C, Film Cooling Performance Correlation (cont.)

Additional details of the mathematical model are given in Section VIII, C-2. The model was applied to five sets of performance data corresponding to Tests -014, -023, -027, -029, and -036. A comparison between the experimental performance for these tests and that predicted by the coolant model is given in Figure VIII-C-2. The parameter of interest in this comparison is the specific impulse since little correlation is anticipated for c^* or chamber pressure because of the effects of film cooling on stagnation pressure. Examining the difference between predicted and experimental specific impulse values on this tabulation shows a maximum difference of 3.2% obtained in Test -014. However, as discussed in Section VIII,B, the low area-ratio nozzles ($\epsilon = 8.3$) had much lower performance than anticipated. Neglecting this test, the model predicted specific impulse satisfactorily in the remaining tests used in the comparison. Differences between predicted and experimental performance ranged from 0.1% in Test -036 to 1.8% in Test -027. Since the test that showed the best agreement between predicted and experimental performance used no film cooling downstream of the nozzle throat, there could be some questions raised concerning the method for handling the downstream film coolant in the mathematical model. However, Test -029 had film coolant downstream of the throat included in the performance prediction with only a 0.4% difference from that obtained experimentally.

Figure VIII-C-2 also includes the experimental and predicted characteristic velocities for these tests. Little can be generalized from a c^* comparison since the predicted values are higher in two tests and lower in three tests over that obtained experimentally.

The effect of film cooling and incomplete combustion on the nozzle thrust efficiency is also shown in this tabulation. Nozzle losses ranged from 1.8% for Test -036 to 5.8% in Test -014. The relatively low value for Test -036 as compared with the other four test results from no film cooling addition downstream of the throat section. Another parameter for comparison is the effective characteristic velocity efficiency (η_c) as a function of percent

CONFIDENTIAL

Book Two

VIII, C, Film Cooling Performance Correlation (cont.)

film cooling. This parameter varied from 0.828 to 0.894 for 23 to 11% film cooling, respectively. The general trend is toward increased c^* efficiency with decreased film cooling. These effects illustrate, in general, the degradation in performance associated with film cooling and point out the relatively severe penalty paid for adding film cooling to the downstream section of the nozzle.

Three film cooling tests were conducted as part of the Integrated Components Program (Contract AF 04(611)-8548). Performance results and a comparison with the film cooling model are shown for these tests in Figure VIII-C-3. Predicted performance agreed quite favorably (0.2%) with that obtained experimentally in Test 1.2-05-WAM-024. The other Tests (Tests -025 and -027) showed relatively poor correlation. However the experimental data for these three tests appear to be inconsistent. Test -025 had 14.8% film cooling and delivered 4 sec less specific impulse than Test -024 with 17.5% film cooling. In Test -027 the film cooling is almost half of that used in Test -024 and the performance increase was only 3.5 sec. Because of the inconsistencies in the ICP test data, it is impossible to state categorically that the film cooling model correlates with the experimental data.

Additional comparisons can also be made from the data on Figure VIII-C-3. For instance, the predicted c^* with film cooling was always lower than that obtained experimentally, with the difference increasing at the higher film cooling flows. The characteristic velocity efficiency showed the same general trend as the HiP_c data as a decreased efficiency with increased film cooling.

Some general conclusions can be made from a comparison of the ICP and HiP_c data. First, the c^* efficiencies for the film cooling model are higher for the ICP chamber for identical film cooling flow rates. This is shown in Figure VIII-C-4, where c^* efficiency is plotted as a function of percent

CONFIDENTIAL

Book Two

VIII, C, Film Cooling Performance Correlation (cont.)

film cooling for both the ICP and HiP_c tests. The percent film cooling used here refers to conditions at the nozzle throat, and the c^* efficiency is that calculated by the film cooling model. A comparison can be made on this basis since the uncooled injector performance in both test series was almost identical. The differences shown amount to about 1.5% at higher coolant flows and steadily decrease as coolant flow is reduced. In addition, during the HiP_c tests where coolant was injected downstream of the throat, the increased nozzle loss attributable to the coolant is about 3 to 4%. Hence the multiple injection scheme used in the HiP_c chamber results in some performance disadvantages over more conventional methods of film cooling. However, this technique may be more efficient from a heat transfer standpoint, therefore requiring less cooling and tending to make the performance comparable.

2. Film-Cooling Model

a. Assumptions

- (1) One-dimensional gas flow with heat exchange between streams up to the nozzle throat.
- (2) Static pressure equilibrium between streams.
- (3) No mixing or combustion of the film coolant.

b. Calculations

- (1) The first step is to compute the temperature of the film coolant at the nozzle throat plane. This can be found by using the relationships established in Section VIII,D for computing the film-cooling effectiveness for heat transfer. Coolant temperature calculated by the resulting equations is

CONFIDENTIAL

Book Two.

VIII, C, Film Cooling Performance Correlation (cont.)

the adiabatic wall or recovery temperature. In this case, it is also assumed to be the coolant stagnation temperature (which would be exact if the Prandtl number equalled one) to simplify the computation.

(2) The heat absorbed by the film coolant can then be found as follows:

$$\Delta Q_{fc} = \dot{w}_{fc} \bar{c}_{pc} (T_{c_{throat}} - T_{c_{in}})$$

Heat absorbed by the coolant reduces the mainstream total enthalpy by the following:

$$\Delta H_m = \Delta Q_{fc} / \dot{w}_m$$

Mainstream total enthalpy reduction effects both the characteristic velocity and the nozzle thrust coefficient for a real gas.

(3) Incomplete combustion by an injector also results in a reduced chamber enthalpy. The magnitude of this effect must be determined by testing the engine without film cooling by using an ablative nozzle. Preferably, the uncooled tests should be conducted over a range of injector mixture ratios so that the effect of basic injector performance can be included in optimizing film-cooled performance. For instance, if the basic injector performance is relatively constant with mixture ratio, then the injector should be operated close to stoichiometric for maximum performance with film cooling (for a storable propellant system). If injector performance decreases as mixture ratio increases, the optimum performance with film cooling is obtained by running the injector below stoichiometric conditions.

The uncooled injector performance is employed in the film cooling model on the basis of $MR_{inj} = 2.1:1$, $N_2O_4/A-50$ propellants, and $P_c = 2770$ psia. Figure VIII-A-1 shows the effect of reduced chamber enthalpy

CONFIDENTIAL

Book Two

VIII, C, Film Cooling Performance Correlation (cont.)

on the various performance efficiencies. For a c^* efficiency corresponding to the uncooled injector performance, the reduced chamber enthalpy for incomplete combustion of the propellants is given on the abscissa of Figure VIII-A-1.

The total reduction in mainstream enthalpy to the nozzle throat is then a sum of that absorbed by the film coolant plus the basic injector value as determined by the c^* efficiency without film coolant. From the total reduced enthalpy, a c^* efficiency for the mainstream gas is found by again referring to Figure VIII-A-1. This is then used to determine the effective c^* of the mainstream gases as follows:

$$c_{\text{main}}^* = \eta_c \times c_{\text{ideal}}^*$$

where

η_c is derived from Figure VIII-A-1, and c_{ideal}^* is the value ascribed by the computer program to 100% combustion of the injector propellants.

(4) The next step is to calculate an effective c^* for the film-coolant stream. Here an assumption is made that the film coolant is at Mach 1 at the nozzle throat. The previous assumption that both streams are in static pressure equilibrium also applies. Knowing the total temperature, molecular weight, and ratio of specific heats for the film coolant, the velocity at Mach 1 is

$$v_{f_c} = \sqrt{\frac{2 g_c \gamma R T_{c \text{ throat}}}{(\gamma + 1)}}$$

which is then used to determine the film cooling characteristic velocity in the following equation

$$c_{f_c}^* = \frac{v_{f_c}}{\gamma} \left(\frac{\gamma + 1}{2} \right)^{\frac{\gamma}{\gamma - 1}}$$

CONFIDENTIAL

Book Two

VIII, C, Film Cooling Performance Correlation (cont.)

$$(5) \text{ An effective } c_{\text{eff}}^* = \frac{w_m c_m^* + w_{fc} c_{fc}^*}{\dot{w}_{\text{total}}}$$

which can also be used to find the effective stagnation pressure from

$$P_{o_{\text{eff}}} = \frac{c_{\text{eff}}^* \dot{w}_{\text{total}}}{g_c A_t}$$

The computed stagnation pressure usually differs from the measured chamber pressure. This is to be expected since both the film coolant and mainstream will probably possess different total pressure and entropy changes (due to heat loss, friction, mixing, etc.) and act in such a way as to lower the effective stagnation pressure at the nozzle throat.

(6) Before the nozzle performance is computed, it is necessary to calculate the stagnation pressures of both streams. This is a trial-and-error solution, with the following steps required:

(a) Assume a stagnation pressure for the mainstream.

(b) Calculate the flow area of the mainstream gases:

$$A_m^* = \frac{c_m^* \dot{w}_m}{g_c P_{o_m}}$$

(c) A flow area for the film coolant is found by difference from the total throat area.

$$A_{fc}^* = A_t - A_m^*$$

CONFIDENTIAL

Book Two

VIII, C, Film Cooling Performance Correlation (cont.)

(d) Then a stagnation pressure for the coolant is computed from:

$$P_{o_{fc}} = \frac{c_{fc}^* \dot{w}_{fc}}{g_c A_{fc}^*}$$

(e) Static pressure at the throat is computed from the critical pressure ratio of the mainstream and the assumed stagnation pressure (step (a)).

(f) A static pressure is also calculated for the film coolant at throat conditions from:

$$P_{fc} = P_{o_{fc}} \left(\frac{\gamma + 1}{2} \right)^{-\frac{\gamma}{\gamma - 1}}$$

and when the static pressures in both streams are equal, the assumed stagnation pressure for the mainstream is correct.

(7) This step can be eliminated when no film cooling is added downstream of throat. Adding film coolant requires a new heat and momentum balance.

(a) Heat Balance

$$\dot{w}_{\text{Total}} T_{o2} = \dot{w}_{fc} T_{o1} + \Delta \dot{w}_{fc} T_{inj}$$

(b) Momentum Balance (constant pressure injection)

$$\dot{w}_{\text{Total}} V_T = \dot{w}_{fc} V_1 + \dot{w}_{fc} V_{inj}$$

CONFIDENTIAL

Book Two

VIII, C, Film Cooling Performance Correlation (cont.)

(c) Static temperature, Mach number, and a stagnation pressure are then computed for the combined film coolant streams.

If the film coolant is added too far downstream, the injection conditions should be recomputed at each point. To simplify the calculations employed here, it is assumed that all film coolant downstream of the throat is added to the flow at the throat conditions.

(8) Next, assume an exit static pressure for the nozzle and expand both streams to this pressure.

(a) Mainstream

For the mainstream pressure ratio specified, the exit density and velocity are found from a plot of the chemical composition values as a function of reduced chamber enthalpy. These are used to find the mainstream exit area as follows:

$$A_{e_m} = \frac{\dot{w}_m}{\rho_{e_m} V_{e_m}}$$

(b) Film Coolant

The pressure ratio of the film coolant is used to calculate the exit Mach number for this stream by solving:

$$\frac{P_{o_{fc}}}{P_e} = \left(1 + \frac{\gamma-1}{2} M_e^2\right)^{\gamma/(\gamma-1)}$$

CONFIDENTIAL

Book Two

VIII, C, Film Cooling Performance Correlation (cont.)

This can then be used to calculate the exit density and velocity of the coolant as well as the coolant exit area:

$$A = \frac{\dot{w}_{fc}}{\rho_{e_{fc}} V_{e_{fc}}}$$

Summing the exit area of both streams, a comparison is then made with the total exit area of the nozzle. Significant errors in the total area comparison make it necessary to assume a new exit static pressure and start this step over.

(9) Thrust and specific impulse for vacuum conditions are then computed as follows:

(a) Thrust

$$F_{vac} = \frac{\dot{w}_m V_{e_m}}{gc} + \frac{\dot{w}_{fc} V_{e_{fc}}}{gc} + P_e A_e$$

(b) Specific Impulse

$$I_{s_{vac}} = \frac{F_{vac}}{\dot{w}_{total}}$$

This can then be used to calculate the specific impulse efficiency of the nozzle with film cooling:

$$\eta_{I_s} = \frac{I_{s_{vac}} \text{ (calculated)}}{I_{s_{vac}} \text{ (theoretical) at inj MR}}$$

and similarly the characteristic velocity efficiency:

$$\eta_c = \frac{c^*_{eff} \text{ (calculated)}}{c^* \text{ (theoretical) at inj MR}}$$

CONFIDENTIAL

Book Two

VIII, C, Film Cooling Performance Correlation (cont.)

Then combining the above two efficiencies, it is possible to calculate the nozzle thrust efficiency:

$$\eta_T = \eta_c / \eta_{I_s}$$

This value of the nozzle thrust efficiency includes only the losses associated with incomplete combustion at the injector and the film coolant addition. Other losses, such as flow divergence associated with the nozzle geometry and shear drag along the nozzle wall must be added to arrive at an overall nozzle thrust efficiency. Each of these losses is assumed to be additive since they are calculated separately, neglecting any interactions that might occur. Once an overall thrust efficiency is determined, an overall specific impulse efficiency can be found by:

$$\eta_{\frac{I_s}{I_s}} = \eta_c \eta_T$$

and the predicted specific impulse with film cooling determined by:

$$I_{s_{vac}}(\text{predicted}) = \eta_{\frac{I_s}{I_s}} \times I_{s_{vac}}(\text{theoretical at inj MR})$$

CONFIDENTIAL

Book Two

VIII, Thrust Chamber Performance

D. EFFECTIVENESS OF FILM COOLING

The film cooled convergent and throat segment was designed to study the effect of film cooling on TCA performance. Thermocouples were placed within the nozzle walls between film coolant injection station to measure the wall temperature and thus permit adjustment of the coolant flows in each channel as required by the temperature limits of the metal wall. This temperature data was analyzed to determine the effectiveness of this method of film cooling for protecting the nozzle wall.

Oxidizer film cooling was used in these tests. The coolant injection design incorporates 18 separate coolant passages spaced approximately 0.75 in. apart axially along the nozzle wall. Coolant is injected peripherally through several holes spaced evenly around the nozzle wall in an attempt to obtain uniform coolant distribution. Because this is a new concept in film cooling, there is no previous analysis to draw upon which adequately describes the heat transfer phenomena. The temperature data for several of these tests was plotted and is presented in Section VII.

A modified Hatch and Papell equation was used to analyze this data. This equation was derived using data from the ICP Contract, AF 04(611)-8548, and was further modified to account for the unique film coolant injection method used in the Hi Pc program. Therefore, the deviation of this equation from the basic Hatch and Papell relationship using ICP data as well as Hi Pc data is presented.

Film cooled chamber testing on ICP was conducted using an N_2O_4 film cooled ablative nozzle. Film cooling was injected in an axial direction through a series of ports located just upstream of the nozzle convergence section. In these tests, thermocouples were placed within the nozzle wall

CONFIDENTIAL

Book Two

VIII, D, Effectiveness of Film Cooling (cont.)

flush with the hot surface. These thermocouples registered the adiabatic wall temperature with film cooling. Test data from ICP was then correlated to a modified Hatch and Papell equation.

1. ICP Film Cooling Analysis

The basic Hatch and Papell (Ref 1) correlation was empirically derived from experimental tests using a flat plate with coolant injected from a slot, tangential to the mainstream flow. In their tests the mainstream flow was uniform over the entire test section. Their final correlating equation is as follows:

$$\frac{T_{ad} - T_w}{T_{ad} - T_{c_{init.}}} = \eta = e^{-\left[\frac{hLx}{W_{fc} C_{pc}} - 0.04\right]} \left(\frac{SV_g}{x_c}\right)^{0.125} f\left(\frac{V_g}{V_c}\right)$$

In the original derivations all the variables in the above expression are constant as a function of length (x) and temperature being defined at slot inlet conditions. The first term of the exponential comes from a heat balance across the boundary between the coolant and mainstream. In a rocket nozzle the heat transfer coefficient (h) and film cooled width (L) are a function of distance from the injection slot (x). Therefore this variation should be included in the above expression when applied to rocket nozzles. This can be done by expressing these terms as a function of length prior to integrating the heat balance equation or by employing mean values over the cooled length. Also, with supercritical N_2O_4 coolant the specific heat varies significantly with temperature; this should also be considered. If the latter effect is neglected, then the advantages of the endothermic decomposition of film coolant are not shown by the calculations.

CONFIDENTIAL

Book Two

VIII, D, Effectiveness of Film Cooling (cont.)

Lucas and Golladay (Ref 2) showed they could correlate data from a low-pressure rocket motor with JP-4/oxygen propellants and a nonreactive coolant (nitrogen) by including just the variation in heat-transfer coefficient with cooled length. They also found that the constant 0.04 in the first term of the exponential was much smaller than originally obtained by Hatch and Papell. This constant comes from an approximation of the distance required downstream from the injection slot before any heat can pass through the coolant film and raise the wall temperature. In Ref 2 they indicated that radiant heat-transfer would influence the value of this constant and that 0.04 should be used with convective heat-transfer alone. Data from the ICP tests seems to correlate quite well by simply neglecting this constant altogether, which is the same as saying that the adiabatic wall temperature begins to rise immediately downstream of the injection slot. At the high pressures and temperatures obtained in these tests this is a logical assumption.

As a result of the preceding discussion the following deviation is offered as a better means for describing film cooling in a rocket nozzle with a reactive coolant. This model is based on a heat balance over an increment of cooled area in the nozzle.

CONFIDENTIAL

Book Two

VIII, D, Effectiveness of Film Cooling (cont.)

The heat balance for an adiabatic wall is as follows:

$$h_g A (T_{ad} - T_c) = W_{fc} C_{pc} dT$$

where: $A = \pi D_c dx$

and the heat transfer coefficient can be expressed:

$$h_g = \frac{DB(W_m^{0.8})}{D_c^{1.8}}$$

where: DB is the Dittus-Boelter coefficient which includes all constants and transport properties associated with the dimensionless Nusselt relationship.

Thus the heat balance can be expressed as follows:

$$\frac{\pi(W_m^{0.8})}{W_{fc}} \int_0^x \frac{DB dx}{D_c^{0.8}} = \int_{T_{c_{init}}}^{T_w} C_{pc} \frac{dT}{(T_{ad} - T)}$$

Integrating for mean values of the coolant specific heat and the DB coefficient yields:

$$\frac{T_{ad} - T_w}{T_{ad} - T_{c_{init}}} = e^{-\left[\frac{\pi \overline{DB} W_m^{0.8}}{W_{fc} \overline{C}_{pc}} \int_0^x \frac{dx}{D_c^{0.8}} \right]}$$

For a conical chamber and nozzle the chamber diameter can readily be expressed as a function of length and the integral in the exponential evaluated.

CONFIDENTIAL

Book Two

VIII, D, Effectiveness of Film Cooling (cont.)

The remaining terms in the exponential expression developed by Hatch and Papell were derived empirically by a best-fit to their experimental data. The first of these terms is the dimensionless parameter SV_g/α . This parameter correlated all their data at a velocity ratio (V_g/V_c) of one.^c This can be interpreted as a form of the Peclet number which is a ratio of the inertial force to the heat-diffusion flux for the coolant. The parameter, S, in this expression is the effective slot width of the coolant. Papell (Ref 3) showed that S could be defined for a series of circular injection ports as the total coolant flow area divided by the width of the cooled section. As applied to the ICP tests, this becomes:

$$S = \frac{\sum A_p}{\pi D_{c_{inj}}}$$

where: A_p is the area of each injection port, D_c is the chamber diameter at the coolant injection station.

The second empirical relationship developed by Hatch and Papell was used to correlate their data for a wide range of velocity ratio conditions. The necessity of this correction is attributable to the increased mixing that takes place when the velocities are unequal. This relation is as follows:

CONFIDENTIAL

Block Two

VIII, D, Effectiveness of Film Cooling (cont.)

$$f\left(\frac{V_g}{V_c}\right) = 1 + 0.4 \tan^{-1} \left(\frac{V_g}{V_c} - 1 \right) \quad \text{for } \frac{V_g}{V_c} \geq 1.0$$

or

$$f\left(\frac{V_g}{V_c}\right) = \left(\frac{V_c}{V_g}\right)^{1.5 \left(\frac{V_c}{V_g} - 1 \right)} \quad \text{for } \frac{V_g}{V_c} < 1.0$$

The correlating parameters of Hatch and Papell are evaluated at injection slot conditions, and as such do not vary with film cooled length. It remains to be seen whether this will hold true for a rocket nozzle.

Use of the revised heat balance expression and the correlating parameters yields the following equation for the film cooling effectiveness, η :

$$\frac{T_{ad} - T_w}{T_{ad} - T_c} = \eta = e^{-\left[\frac{\pi \overline{DB} W_m^{0.8}}{W_{fc} \overline{C}_{pc}} \int_0^x \frac{dx}{D_c^{0.8}} \right] \left(\frac{SV_g}{\alpha_c} \right)^{0.125} f\left(\frac{V_g}{V_c}\right)}$$

The ICP thermocouple data from tests -024, -025, and -027 are compared to the above correlating expression as shown on Figures VIII-D-1, -2, and -3. These plots show the film cooling effectiveness (η) as a function of the parameters involved on semilog coordinates where the straight line represents the above expression. The data agrees quite closely with that predicted through the convergent section and up to the nozzle throat. Beyond the nozzle throat there is very little agreement between the experimental and predicted cooling effectiveness with the experimental being considerable higher. Lucas and Golladay observed this same effect when attempting a similar correlation of film cooling results. They felt that this might be due to the film coolant mixing with the mainstream and forming a buffer layer. Then the driving force to the film coolant should be the lower bulk temperature of the buffer layer, and this is used in defining the effectiveness.

CONFIDENTIAL

Book Two

VIII, D, Effectiveness of Film Cooling (cont.)

Regardless of what causes this effect it is believed that what is seen here exists and that some attempt should be made to include this in the overall correlation of the data. One simple approach would be to assume that the film-cooling effectiveness is constant at the throat value for all locations downstream of the nozzle throat. This is shown as a dashed line on Figures VIII-D-1, -2, and -3. When compared to the experimental data plotted in this region, it still yields a conservative estimate of the adiabatic wall temperature to overcool the nozzle exit section.

The preceding discussion establishes the premise that a modified form of the Hatch and Papell equation can be used to describe N_2O_4 film cooling in a high-pressure rocket engine. The next section will describe what changes are necessary to apply the modified expression to the type of film cooling employed in the HiPc tests.

2. HiPc Film Cooling Analysis

The basic form of the modified Hatch and Papell relation derived from the ICP experience also applies to the HiPc data with specific variations in the latter two empirical terms to account for different injection conditions. This relation as it applies to the HiPc film cooling conditions is as follows:

$$\eta = e^{-\frac{\pi D E W_m^{0.8}}{W_{fc} C_{pc}} \int_{x_n}^{x_{n+1}} \frac{dx}{D_c^{0.8}} \left(\frac{SV_g}{a_c} \right)^{0.125} f\left(\frac{V_g}{V_c}\right)}$$

With the type of coolant injection used in the HiPc tests the coolant velocity in the axial directions is essentially zero. This effects the last term of the above expression which is in its expanded form:

$$f\left(\frac{V_g}{V_c}\right) = 1 + 0.4 \tan^{-1} \left(\frac{V_g}{V_c} - 1 \right)$$

CONFIDENTIAL

Book Two

VIII, D, Effectiveness of Film Cooling (cont.)

As coolant velocity decreases toward zero, the arc tangent term approaches $\pi/2$ (the angle whose tangent is infinite); thus in the limit the entire expression becomes 1.628. The other limit of this expression is reached when the coolant axial velocity is equal to the mainstream gas velocity where this term is unity. The lower limit of this term results in the highest film cooling effectiveness or, conversely, the injection mechanism used in the HiPc tests has the lowest film cooling efficiency because of mixing problems. The reason is that equal velocities between film coolant and mainstream gas minimizes mixing between the two streams, while a large velocity gradient promotes mixing.

The other term that requires special consideration with the HiPc injection conditions is the effective slot width (S) times the mainstream gas velocity (V_g) at injection inlet. These have to be computed independently at each station and a summation made with all previous values to find the overall effective value.

Use of the modified Hatch and Papell expression as just described necessitates a new heat balance be performed at each injection station. In this way a mean coolant initial temperature is calculated by summing the heat content from all previous stations with that of the station being calculated. Detailed calculations were made for two of the HiPc test cases corresponding to Tests -027 and -036, and the results are shown on Figures VIII-D-4 and -5. Calculated wall temperatures appears as saw-toothed lines on these plots. The upper lines assume complete mixing of coolant with previous film coolant at the injection station. This line represents a maximum temperature expected as calculated by the film cooling relation. The lower line assumes mixing takes place linearly between stations with the wall temperature equal to the coolant inlet temperature at the injection point. This represents a lower limit of predicted wall temperatures.

Measured wall temperatures during these tests are also shown on Figures VIII-D-4 and -5 for these steady-state values. In most cases these temperatures were approximated since firing durations were too short to fully attain

CONFIDENTIAL

Book Two

VIII, D, Effectiveness of Film Cooling (cont.)

steady-state conditions. Thermocouples were located midway between each injection station as shown in the plotted data. Most of the experimental temperature data falls within the limits predicted by the film cooling relation. The film cooling calculations assume a uniform distribution of coolant around the periphery of the nozzle wall. Some measured temperatures are significantly higher or lower than the mean predicted values. This undoubtedly is a result of poor film cooling distribution. If injector streaking had been a problem in these tests, a regular temperature pattern would have resulted for all thermocouples along same radially line. For instance, thermocouple No. 7 on Figure VIII-D-4 registered quite a high temperature; however, both No. 2 and No. 12 registered normal temperatures. Actually, the concentric-ring injector used in these tests was not expected to cause streaking if properly aligned, and based on the wall temperature patterns in the nozzle, no streaking occurred.

An ablative nozzle extension with eight thermocouples imbedded in the wall was employed in Test -036. These thermocouples were used to measure the adiabatic wall temperatures in the nozzle exit section with film cooling. Steady-state temperature data is included on Figure VIII-D-5. These temperatures are much lower than those predicted by the modified Hatch and Papell relation similar to the ICP test experience described earlier. While a constant effectiveness at the throat would not fit this data as it does the ICP test results, an empirical correlation could be made to the HiPc results.

The overall comparison between the experimental film cooling data and the modified Hatch and Papell relation indicates relatively good agreement such that the method described should be sufficiently accurate to use for design purposes. Also, by more careful design with respect to coolant flows and injection port location, some additional reduction in film cooling requirements appears possible based on the empirical method outlined. The most significant problem area is the difficulty in obtaining uniform film cooling distribution. This could probably be corrected with some more basic testing of the distribution channels in a cold air fixture where just the flow details are investigated.

CONFIDENTIAL

Book Two

REFERENCES (Section VIII, D)

1. Hatch, J. E. and Papell S.S., "Use of a Theoretical Flow Model to Correlate Data for Film Cooling or Heating an Adiabatic Wall by Tangential Injection of Gases of Different Fluid Properties," NASA TN D-130, 1959.
2. Lucas, J. G. and Golladay R.L, "An Experimented Investigation of Gaseous-Film Cooling of a Rocket Motor," NASA TN D-1988, 1963.
3. Papell, S.S., "Effect on Gaseous Film Cooling of Coolant Injection Through Angled Slots and Normal Holes," NASA TN D-299, 1960.

CONFIDENTIAL

Book Two

NOMENCLATURE (Section VIII, D)

DB	Dittus-Boetter coefficient
D_c	Chamber diameter
C_p	Specific heat
h	Mainstream heat transfer coefficient
L	Coolant width or chamber circumference at injection location
S	Coolant slot height
T_{ad}	Mainstream adiabatic wall (recovery) temperature
T_c	Coolant temperature
T_w	Wall temperature
V_c	Coolant temperature
V_g	Mainstream gas velocity
\dot{W}_{fc}	Film coolant flow rate
\dot{W}_M	Mainstream flow rate
X	Axial distance from coolant slot exit
α_c	Coolant thermal diffusivity
η	Cooling effectiveness

CONFIDENTIAL

Book Two.

VIII, Thrust Chamber Performance (cont.)

E. EFFECT OF CHAMBER PRESSURE ON REQUIRED FILM COOLING

1. Introduction

The objective of this study was to establish the quantity of film coolant required to cool a high-performance thrust chamber as a function of chamber pressure. The ultimate use of this study is to establish thrust chamber specific impulse as a function of chamber pressure for use in determining the optimum chamber pressure for a rocket engine in the Final System Studies (see Section X). The resultant curve showing film cooling flow rate as a function of chamber pressure is presented in Figure VIII-E-1.

2. Approach

The amount of film cooling required to adequately cool a thrust chamber depends upon what other type of cooling, such as regenerative cooling, may be used. In addition, allowable chamber wall temperature, thrust, L^* , basic geometry, and the manner in which the film coolant is injected, all effect the amount of film cooling that is required. Therefore, it was necessary to establish certain constraints in these areas so that a unique solution would result. These constraints were established on the basis of best knowledge and latest technology available from this and other programs such as ICP or that show the reasonable promise of being available for use in a high-pressure rocket engine. These are discussed below.

a. Thrust

A thrust level of 100,000-lb per thrust chamber was selected for the Advanced Storable Engine, currently beginning development under Contract AF 04(611)-10830. Therefore the 100K-lb thrust level was used in this study.

CONFIDENTIAL

Book Two

VIII, E, Effect of Chamber Pressure on Required Film Cooling (cont.)

b. Chamber Construction

The thrust chamber is regeneratively cooled, supplemented by film cooling. Tube walls are of Inconel 718 and are approximately 0.020-in. thick. A thermal barrier composed of 85% W, 12% ZrO_2 , 3% Si is used to increase the allowable gas-side wall temperature to 3900°R. Maximum allowable outside wall temperature for the Inconel 718 tubes is 2100°R.

c. Film Coolant Injection Considerations

There are numerous methods of injecting film coolant in a chamber. In the HiPc program, multiple-slot injection was used. In ICP, injection at a plane at the beginning of the convergent nozzle was used. Both methods offer practical means of introducing the film coolant. However in a regeneratively cooled chamber, the multiple-slot injection is difficult to apply. Therefore film cooling injected at two locations in the chamber was selected: one at the injector face and the other at the beginning of the convergent portion of the nozzle. N_2O_4 was the film coolant used.

d. Chamber Geometry

For this study, the configuration shown in Figure VIII-E-2 was used. A contraction ratio of four was selected because this results in reasonably shaped combustion chambers within conventional ranges of characteristic length (L^*) from 30 to 50 in. A convergent half-angle (θ) of 15° was selected. Using this half-angle and a contraction ratio of four results in an L^* of approximately 20 in. in the convergent section at chamber pressures of interest. An L^* of 25 in. was assumed for the cylindrical section, which gave an overall L^* of 45 in.

CONFIDENTIAL

Book Two

VIII, E, Effect of Chamber Pressure on Required Film Cooling (cont.)

e. Regenerative Cooling Heat Flux

The amount of heat that can be absorbed by the regenerative coolant is limited by the available pressure drop for the coolant jacket and the design of thrust chamber. Although the precise determination of this heat flux limit requires extensive analysis, experience shows the limit of a chamber of the type described. If the coolant jacket pressure drop is to be maintained below 1000 psi (a reasonable upper limit value for a high-pressure engine), then the maximum allowable heat flux is approximately $17 \text{ Btu/in.}^2 \text{ sec}$ at the throat and is approximately $15 \text{ Btu/in.}^2 \text{ sec}$ in the chamber. These values were used in this study. Heat flux in excess of this amount must be absorbed by the film coolant.

f. Film Cooling Model

The film cooling model used was the modified Hatch and Papell relationship described in Section VIII,D.

g. Analysis

The analysis is presented in four parts. First a general expression which describes the amount of film cooling required as a function of dependent variables is derived. Second, each dependent variable is analyzed and reduced to its dependency on pressure alone for the conditions in the convergent portion of the chamber. Third, a similar analysis is conducted for the cylindrical portion of the chamber. Fourth, the terms derived in the second and third steps are incorporated in the general film-cooling expression, and equations are derived that describe the amount of film cooling required to cool the cylindrical and convergent portions of the chamber.

CONFIDENTIAL

Book Two

VIII, E, Effect of Chamber Pressure on Required Film Cooling (cont.)

(1) Derivation of Film Cooling Equation

A heat balance between the film coolant and the wall is

$$Q_W = h_{fc} f_a (T_C - T_W) \quad (\text{Eq 1})$$

From the definition of Dittus Boelter coefficient,

$$h = \frac{DB \dot{w}_m^{0.8}}{D_c^{1.8}} \quad \text{in a rocket thrust chamber} \quad (\text{Eq 2})$$

$$Q_W = \frac{DB_{fc} \dot{w}_m^{0.8}}{D_c^{1.8}} f_a (T_C - T_W) \quad (\text{Eq 3})$$

The coolant temperature can be established from the modified Hatch and Papell equation described in Section VIII,D.

$$T_C = T_{ad} - (T_{ad} - T_{cin}) e^{-\left[\frac{\pi DB \dot{w}_m^{0.8}}{\dot{w}_{FC} C_{PC}} \int_0^x \frac{dx}{D_c^{0.8}} \right] \left(\frac{SV_g}{a_c} \right)^{0.125} f \left(\frac{v_g}{v_c} \right)} \quad (\text{Eq 4})$$

where: T_{cin} is film coolant inlet temperature.

CONFIDENTIAL

Book Two

VIII, E, Effect of Chamber Pressure on Required Film Cooling (cont.)

Substituting Eq 3 into 4 yields

$$Q_W = \frac{\overline{DB}_{fc} \dot{W}_n^{0.8}}{D_c^{1.8}} f_a \left[T_{ad} - T_W - (T_{ad} - T_{cin}) e^{-\left[\frac{\pi \overline{DB} \dot{W}_m^{0.8}}{W_{FC} C_{PL} O} \int \frac{dx}{D_c^{0.8}} \right] \left(\frac{5V_g}{\alpha_c} \right)^{0.125} f \left(\frac{V_g}{V_c} \right)} \right] \quad (\text{Eq 5})$$

Solving this equation for W_{FC}

$$W_{FC} = \frac{\left[\frac{\pi \overline{DB} \dot{W}_m^{0.8}}{C_{PL} O} \int \frac{dx}{D_c^{0.8}} \right] \left(\frac{5V_g}{\alpha_c} \right)^{0.125} f \left(\frac{V_g}{V_c} \right)}{\ln \frac{\overline{DB}_{fc} \frac{\dot{W}_T}{D_c^{1.8}} f_a (T_{ad} - T_{in})}{\overline{DB}_{fc} \frac{\dot{W}_T}{D_c^{1.8}} f_a (T_{ad} - T_W) - Q_W}} \quad (\text{Eq 6})$$

This general equation can be used to calculate the required film cooling if gas properties, coolant properties, chamber pressure, film coolant injection design, chamber design, and temperature conditions are known. Consequently the solution of this equation in terms of pressure requires that conditions regarding all other independent variables be established. This restricts the application of any solution of this equation in terms of pressure alone to the design constraints already discussed and elaborated on below. The solution presented is applicable to the engine assumed for the Final System Studies only. However, by defining the independent variable in terms of pressure for any chamber type, similar equations can be derived from Eq 6 for other design concepts, propellants, coolants, and thrust levels.

CONFIDENTIAL

Book Two

VIII, E, Effect of Chamber Pressure on Required Film Cooling (cont.)

(2) Solution of General Equation for Convergent Region

Each term of this equation will now be solved as a function of P_c as follows:

(a) Q_w -- The practical limit of heat flux is given.

$$Q_w = 17 \text{ Btu/in.}^2 \cdot \text{sec.}$$

(b) \dot{w}_m -- The thrust chamber flow rate is used here. The analysis will be performed for a constant sea-level thrust of 100,000 lb. Therefore $\dot{w}_T = 350 \text{ lb/sec}$ ($I_s = 286 \text{ sec}$).

(c) $\frac{\dot{w}_m^{1.8}}{D_c}$ can be related to pressure as follows:

D_c is evaluated at the plane where the temperature is to be established; in this case it is at the throat. Therefore, $D_c = D_t$, D_t and \dot{w}_m are related through the c^* equation,

$$c^* = \frac{P_c A_t g}{\dot{w}_m} = \frac{\pi D_t^2 P_c g}{4 \dot{w}_m} \quad (\text{Eq 7})$$

also

$$c^* = \frac{Fg}{C_F \dot{w}_n}$$

which solves for \dot{w}_n as follows

$$\dot{w}_n = \frac{Fg}{C_F c^*} \quad (\text{Eq 8})$$

CONFIDENTIAL

Book Two

VIII, E, Effect of Chamber Pressure on Required Film Cooling (cont.)

Substituting Eq 8 into 7 and solving for D_t yields

$$D_t = \sqrt{\frac{4F}{\pi P_c C_F}} \quad (\text{Eq 9})$$

Equations 8 and 9 are used to solve for $\frac{\dot{w}_n^{.8}}{D_t^{1.8}}$,

$$\frac{\dot{w}_n^{.8}}{D_t^{1.8}} = 12.8 \frac{P_c^{0.9} C_F^{0.1}}{c^{*.8} F^{0.1}} \quad (\text{Eq 10})$$

For 97% combustion efficiency

$$c^* = 0.97 \times 5700 = 5540 \text{ ft/sec.}$$

For reasonable nozzle designs, C_F varies from 1.63 at 1000 psia P_c to 1.795 at 5000 psia, $C_F^{.1}$ varies from 1.05 at 1000 psia P_c to 1.06 at 5000 psia.

Therefore 1.055 is used for $C_F^{.1}$

$$\frac{\dot{w}_n^{.8}}{D_c^{1.8}} = 4.27 \times 10^{-3} P_c^{0.9} \quad (\text{Eq 11})$$

(d) T_{ad} is 6231°R for N_2O_4 AeroZINE 50 propellant.

(e) T_W is 3900°R for the thermal barrier assumed.

CONFIDENTIAL

Book Two

VIII, E, Effect of Chamber Pressure on Required Film Cooling (cont.)

(f) T_{cin} is $600^{\circ}R$ (coolant inlet temperature).

(g) DB is 2×10^{-3} for the mainstream gas.

(h) DB_{FC} is 1.25×10^{-3} was calculated from the gas properties.

(i) C_{PL} was established as a function of pressure at $2800^{\circ}R$ to be approximately 0.330 in the pressure range of interest. There is no significant effect of pressure on this value.

(j) $\int_0^x \frac{dx}{L_c^{0.8}}$ was established from the chamber geometry

shown in Figure VIII-E-2.

$$\sin \theta = \frac{D_{cc} - D_c}{2x}$$

Therefore

$$D_c = D_{cc} - 2x \sin \theta$$

Substituting and integrating,

$$\begin{aligned} \int_0^x \frac{dx}{D_c^{0.8}} &= \int_0^{\frac{L_{CN}}{\cos \theta}} \frac{dx}{(D_{cc} - 2x \sin \theta)^{0.8}} \\ &= \frac{(D_{cc} - 2x \sin \theta)^{0.2}}{-0.4 \sin \theta} \bigg|_{x=0}^{x=\frac{L_{CN}}{\cos \theta}} + \frac{D_{cc}^{0.2}}{0.4 \sin \theta} \end{aligned} \quad (\text{Eq 12})$$

CONFIDENTIAL

Book Two

VIII, E, Effect of Chamber Pressure on Required Film Cooling (cont.)

L_{CN} is related to D_{cc} through the following equation (refer to Figure VIII-E-2).

$$L_{CN} = \frac{D_{cc} - D_t}{2 \tan \theta}$$

and for a contraction ratio of β

$$L_{CN} = D_{cc} \frac{1 - \frac{1}{\beta}}{2 \tan \theta}$$

Substituting this equation into Eq 12,

$$\int_0^x \frac{dx}{D_{CN}^{0.8}} = \frac{1 - \frac{1}{\beta}}{0.4 \sin \theta} D_{cc}^{0.2} \quad (\text{Eq 13})$$

Values of β and θ of 4 and 15° , respectively, were selected as representative of common thrust chamber design practice

$$\int_0^x \frac{dx}{D_{CN}^{0.8}} = 1.26 D_c^{0.2} \quad (\text{Eq 14})$$

Eq 14 can be written in terms of D_t

$$\int_0^x \frac{dx}{D_{CN}^{0.8}} = 1.45 D_t^{0.2} \quad (\text{Eq 15})$$

CONFIDENTIAL

Book Two

VIII, E, Effect of Chamber Pressure on Required Film Cooling (cont.)

D_t can be expressed as a function of P_c through the c^* equation

$$D_t = \sqrt{\frac{4}{\pi} \frac{c^* \dot{w}}{P_c g}} = \frac{277}{P_c^{0.5}} \quad (\text{Eq 16})$$

for the conditions in these chambers.

Substituting this into Eq 15 yields,

$$\int_0^x \frac{dx}{D_{CN}^{0.8}} = \frac{4.47}{P_c^{0.1}} \quad (\text{Eq 17})$$

$$(k) \left(\frac{SV_g}{a_c} \right)^{0.125} f \left(\frac{V_g}{V_c} \right) \text{ is insensitive to changes}$$

in pressure. Therefore this was evaluated at 2800 psi and used as a constant.

$$\left(\frac{SV_g}{a_c} \right)^{0.125} f \left(\frac{V_g}{V_c} \right) = 5.27$$

(3) Solution of General Equation for Cylindrical Region

$$(a) Q_w = 15 \text{ is given (paragraph VIII.E 2.e)}$$

$$(b) \dot{w}_n = 350 \text{ (same as throat)}$$

$$(c) \frac{\dot{w}_n^{0.8}}{D_c^{1.8}} \text{ The same general equation applies as}$$

was used in the throat region, except that now D_c is the chamber diameter instead of the throat diameter, therefore,

CONFIDENTIAL

Book Two

VIII, E, Effect of Chamber Pressure on Required Film Cooling (cont.)

$$\frac{\dot{w}_n^{.8}}{D_c^{1.8}} = 4.27 \times 10^{-3} x \frac{1}{(\sqrt{\beta})^{1.8}} x P_c^{.9}$$

$$\beta = 4$$

$$\frac{\dot{w}_n^{.8}}{D_c^{1.8}} = 1.22 \times 10^{-3} P_c^{.9} \quad (\text{Eq 18})$$

$$(d) \quad T_{ad} = 6231^\circ R$$

$$(e) \quad T_w = 3900^\circ R$$

$$(f) \quad T_{cin} = 600^\circ R$$

(g) DB -- Heat transfer coefficients were increased to 50% higher than those resulting from a simple Bartz equation in the cylindrical portion of the combustion chamber to account for turbulence in the combustion zone. This is reflected in this analysis by increasing the DB number by 1.5 for both the main gas stream and the film coolant. Therefore, $DB = 3 \times 10^{-3}$.

$$(h) \quad DB_{fc} = 1.88 \times 10^{-3}$$

$$(i) \quad C_{PL} = .330$$

$$(j) \quad \int_0^x \frac{dx}{D_c^{.8}} \quad \text{In the cylindrical portion of the}$$

chamber, D_c is not a function of x . Therefore

CONFIDENTIAL

Book Two

VIII, E, Effect of Chamber Pressure on Required Film Cooling (cont.)

$$\int_0^x \frac{dx}{D_c \cdot .8} = \frac{x}{D_c \cdot .8} \quad (\text{Eq 19})$$

where x is the length of the cylindrical portion of the chamber. This is established from the L* of 20.

$$L^* = \frac{V_c}{A_t} = L_c \beta$$
$$L_c = \frac{L^*}{\beta} = x = 6.25 \text{ in. } (\beta = 4) \quad (\text{Eq 20})$$

From Eq 16

$$D_t = \frac{277}{P_c \cdot .5} \quad (\text{Eq 16})$$

$$D_{cc} = \sqrt{\beta} \frac{277}{P_c \cdot .5} = \frac{554}{P_c \cdot .5} \quad (\text{Eq 21})$$

Combining Eq 20 and 21 into Eq 19 gives

$$\int_0^x \frac{dx}{D_i \cdot .8} = .0397 P_c \cdot .4 \quad (\text{Eq 22})$$

$$(k) \left(\frac{SV_g}{a_c} \right)^{1.25} f \left(\frac{V_g}{V_c} \right) = 5.27 \text{ (same as for}$$

convergent region.)

CONFIDENTIAL

Book Two

VIII, E, Effect of Chamber Pressure on Required Film Cooling (cont.)

(4) Solution of General Equation

Eq 6 represents the amount of film cooling required to maintain a given wall temperature in a regeneratively cooled chamber. Careful examination reveals that when

$$DB_{fc} \frac{\dot{w}_n^{.8}}{D_c^{1.8} f_a} (T_{ad} - T_w) < Q_w \quad (Eq 23)$$

no film cooling is required. Since these terms can be expressed as a function of pressure, there is a chamber pressure below which film cooling is not necessary. This pressure can be calculated by substitution of the appropriate terms from sections (2) and (3) above for the convergent and cylindrical portion of the chamber, respectively.

For the convergent region, this expression reduces to

$$18.7 \times 10^{-3} P_c^{.9} < 17$$

$$P_c < 1930 \text{ psia}$$

and below 1930 psia, no film cooling is required. However, if no film cooling is applied, then DB should replace DB_{fc} in Eq 23 to establish whether the regenerative tubes can carry away the heat from the main stream boundary layer. The DB number then is increased from .00125 to .002, and substitution in Eq 23 yields

$$30.1 \times 10^{-3} P_c^{.9} < 17$$

$$P_c < 1170 \text{ psia}$$

CONFIDENTIAL

Book Two

VIII, E, Effect of Chamber Pressure on Required Film Cooling (cont.)

Similarly, in the cylindrical portion of the chamber, use of $DB_{fc} = 1.88 \times 10^{-3}$ in Eq 23 yields

$$8.05 \times 10^{-3} P_c^{.9} < 15$$

$$P_c < 4300 \text{ psia}$$

Use of $DB = 3 \times 10^{-3}$ in Eq 23 yields

$$12.9 \times 10^{-3} P_c^{.9} < 15$$

$$P_c < 2550$$

for no film cooling required.

There is, then, a range in pressures over which a rigorous analytical solution of Eq 6 will not be practical. To gain better understanding of the differences involved, Eq 6 was solved using both DB numbers for both the convergent and cylindrical portion of the chamber. These equations are presented below.

(a) Convergent Region, $DB = 1.25 \times 10^{-3}$, (film coolant properties)

$$\dot{w}_{FC} = \frac{49 P_c^{-.1}}{\ln \frac{45.2 \times 10^{-3} P_c^{.9}}{18.7 \times 10^{-3} P_c^{.9} - 17}} \quad (\text{Eq 24})$$

(b) Convergent Region, $DB = 2 \times 10^{-3}$, (main stream properties)

CONFIDENTIAL

Book Two

VIII, E, Effect of Chamber Pressure on Required Film Cooling (cont.)

$$\dot{w}_{FC} = \frac{49 P_c^{-.1}}{72.4 \times 10^{-3} P_c^{.9}} \quad (\text{Eq 25})$$

$$\ln \frac{1}{30.1 \times 10^{-3} P_c^{.9} - 17}$$

(c) Cylindrical Region, $DB = 1.88 \times 10^{-3}$, (film coolant properties)

$$\dot{w}_{FC} = \frac{.653 P_c^{.4}}{19.4 \times 10^{-3} P_c^{.9}} \quad (\text{Eq 26})$$

$$\ln \frac{1}{8.05 \times 10^{-3} P_c^{.9} - 15}$$

(d) Cylindrical Region, $DB = 3 \times 10^{-3}$, (main stream properties)

$$\dot{w}_{FC} = \frac{.653 P_c^{.4}}{31 \times 10^{-3} P_c^{.9}} \quad (\text{Eq 27})$$

$$\ln \frac{1}{12.9 \times 10^{-3} P_c^{.9} - 15}$$

Eq 24 through 27 are plotted as dotted lines on Figures VIII-E-3 and -4 to show a comparison between film coolants calculated using heat-transfer coefficients for the main stream and film coolant. Examination of these curves reveals that the film coolant required rises sharply initially and then more gradually as chamber pressure is increased. This indicates that a certain amount of film cooling is required to just wet the wall and establish a fluid boundary consisting chiefly of film coolant. Thus, the flection of the curve indicates a change in film properties. At film coolant flow rates above this flection, the boundary layer consists of film coolant, and film coolant properties apply. Therefore

CONFIDENTIAL

Book Two

VIII, E, Effect of Chamber Pressure on Required Film Cooling (cont.)

Eq 2¹ and 26 apply in this region. At film-coolant flow rates below the flection, chamber gases are mixed in and cooled down by the film coolant, and the boundary layer properties approach those of the main stream as the film coolant approaches zero. In this region, the film cooling required lies somewhere between the two curves. Film cooling required in this region was estimated by connecting a straight-line tangent to the curve based on film coolant heat-transfer coefficient and by intersecting the point at which no film cooling is needed using the main-stream heat-transfer coefficient. The resultant curves are shown plotted as solid lines on Figures VIII-E-3 and -4. The total film cooling required in the chamber was then determined by adding the flows required on Figures VIII-E-3 and -4 and are shown plotted on Figure VIII-E-1. Figure VIII-E-1 was used in the final systems studies.

CONFIDENTIAL

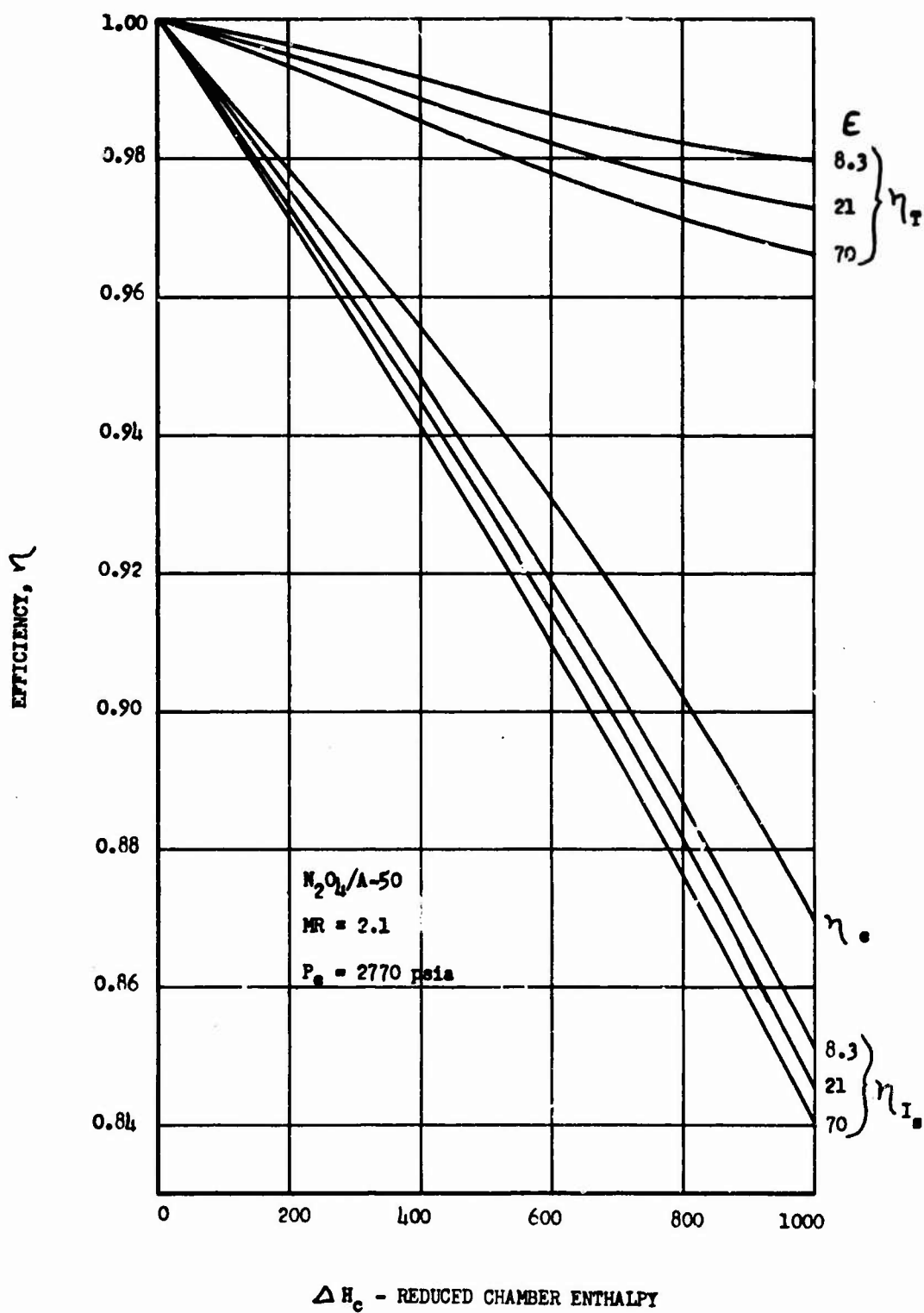
Book Two

VIII, E, Effect of Chamber Pressure on Required Film Cooling (cont.)

NOTATION

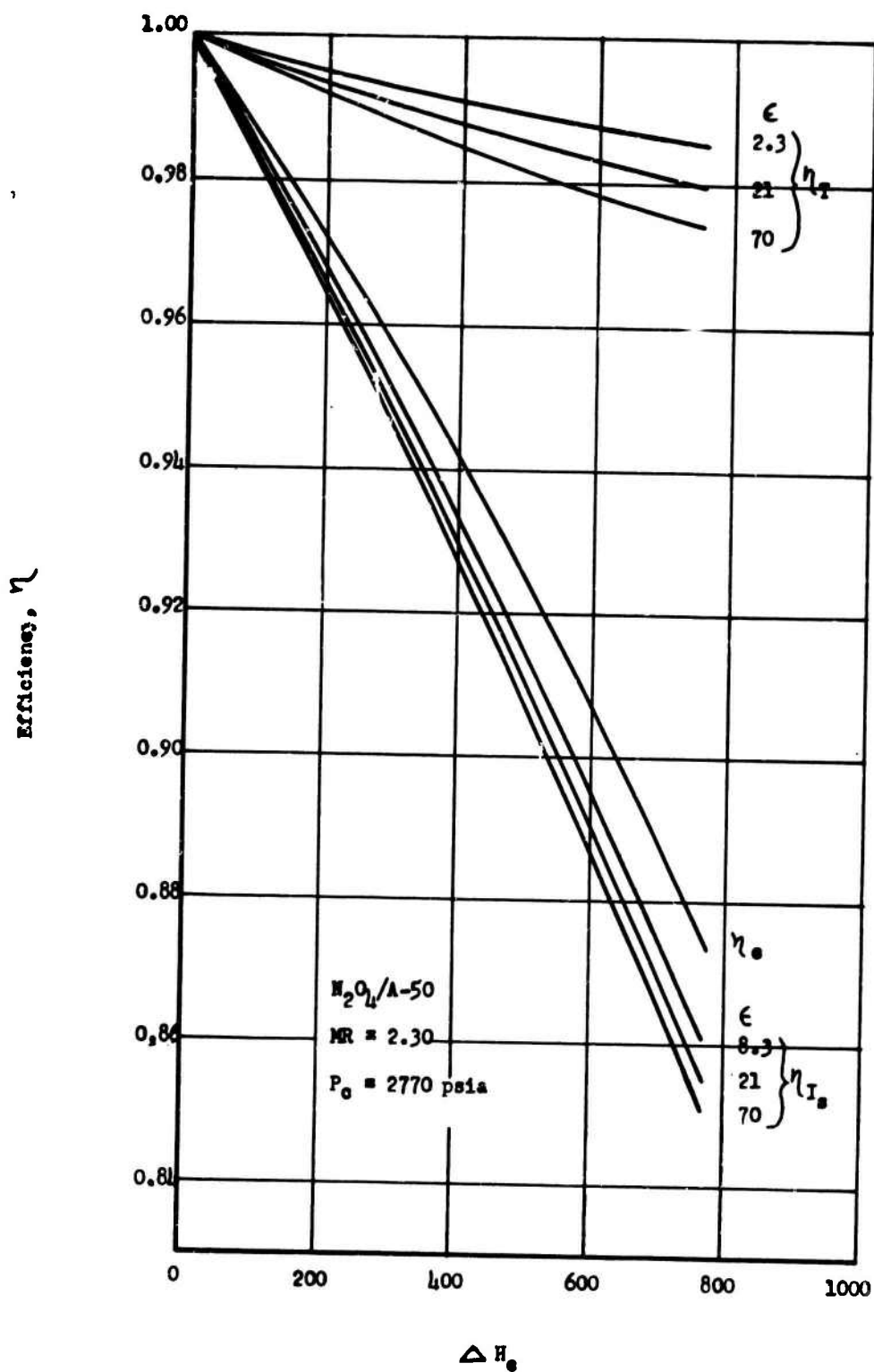
Q_w	=	Heat flux to the wall, Btu/in. ² -sec
h	=	Heat-transfer coefficient, Btu/in. ² -sec
h_{fc}	=	Heat-transfer coefficient of film coolant
h_g	=	Heat-transfer coefficient of main stream gas
T_c	=	Coolant temperature at the station of interest, °R
T_w	=	Wall temperature, °R
T_{ad}	=	Adiabatic wall temperature, °R
DB	=	Dittus Boelter coefficient
DB_{fc}	=	Dittus Boelter coefficient for the film coolant
DB_m	=	Dittus Boelter coefficient for the main flow
\dot{w}_m	=	Main stream gas flow rate, lb/sec
D_c	=	Chamber diameter at any station
f_a	=	Correction factor to account for two-dimensional heat transfer in tube walls ≈ 1.5
T_{cin}	=	Film coolant inlet temperature, °R
c^*	=	Characteristic velocity of the main stream, ft/sec
A_t	=	Thrust chamber throat area, in. ²
P_c	=	Thrust chamber pressure, psia
g	=	Gravity constant = 32.2 ft/sec
F	=	Thrust, lb
C_F	=	Thrust coefficient
D_{cc}	=	Diameter at cylindrical section of the combustion chamber, in.
L_{CN}	=	Convergent nozzle length, in.
β	=	Chamber contraction ratio
D_t	=	Throat diameter, in.

Book Two



Real Gas Effects on the Performance Efficiency--MR = 2.1

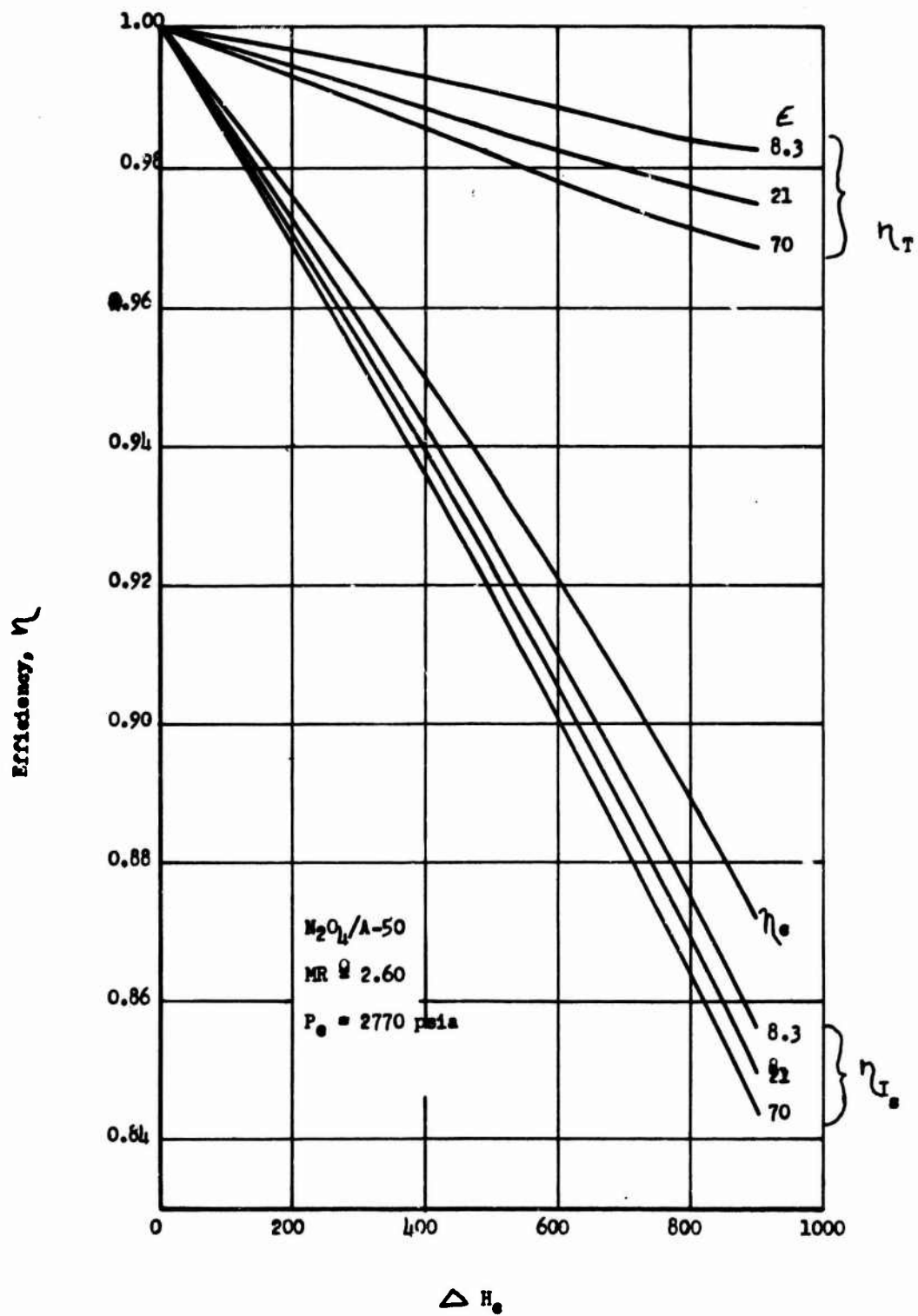
Figure VIII-A-1



Real Gas Effects on the Performance Efficiency--MR = 2.3

Figure VIII-A-2

Book Two



Real Gas Effects on the Performance Efficiency--MR = 2.6

Figure VIII-A-3

CONFIDENTIAL

Book Two

Test No.	-006	-007	-008	-009	-010	-030	-031	-034	-038	
Injector Type	Mod V	Mod VI	ModVII	ModVII	Mod VIII	←————→			Mod VIII	Trans. Cooled Injector
Chamber L*	100	←————→							100	
Chamber Pressure	2833	2997	2931	2782	2869	2573	2456	2475	3051	
Thrust, Sea Level	49,102	53,515	46,610	45,975	39,678	36,792	38,421	43,479	46,316	
Thrust, Vacuum	52,242	56,655	49,705	49,070	40,339	37,455	39,084	46,561	49,391	
Throat Area	11.48	12.0	10.32	10.91	9.90	10.39	11.08	12.25	10.06	
Exit Area	211.0	211.0	211.0	211.0	45.1	45.1	45.1	209.6	209.6	
Area Ratio	18.6	17.8	20.5	19.4	4.55	4.3	4.1	17.1	20.8	
Injector Weight Flow	196.1	215.4	182.9	180.2	171.4	162.8	164.8	178.5	173.2	
Injector Mixture Ratio	1.82	2.07	2.35	2.52	2.55	2.43	2.23	2.1	2.15	
1. Experimental Performance										
a. Vacuum I _s	266.3	275.8	272.0	272.3	235.4	230.5	237.5	260.8	285.3	
b. C*(1) = $\frac{g_c P_c A_t}{\dot{W}}$	5345	5445	5285	5300	5180	5280	5310	5465	5710	
c. C*(2) = f(F, \dot{W})	5390	5470	5310	5335	5115	5060	5240	5210	5530	
2. Theoretical Performance										
a. Vacuum I _s	326.5	327.5	325	319.3	282.4	283.0	286.2	326.6	330.7	
b. C*	5800	5752	5625	5547	5528	5588	5682	5738	5717	
3. Calculated Efficiencies										
a. η_{I_s}	0.815	0.842	0.837	0.853	0.834	0.815	0.830	0.799	0.863	
b. $\eta_{c(1)}$	0.922	0.947	0.940	0.955	0.937	0.945	0.934	0.953	0.999	
c. $\eta_{c(2)}$	0.930	0.952	0.946	0.961	0.926	0.906	0.922	0.909	0.967	

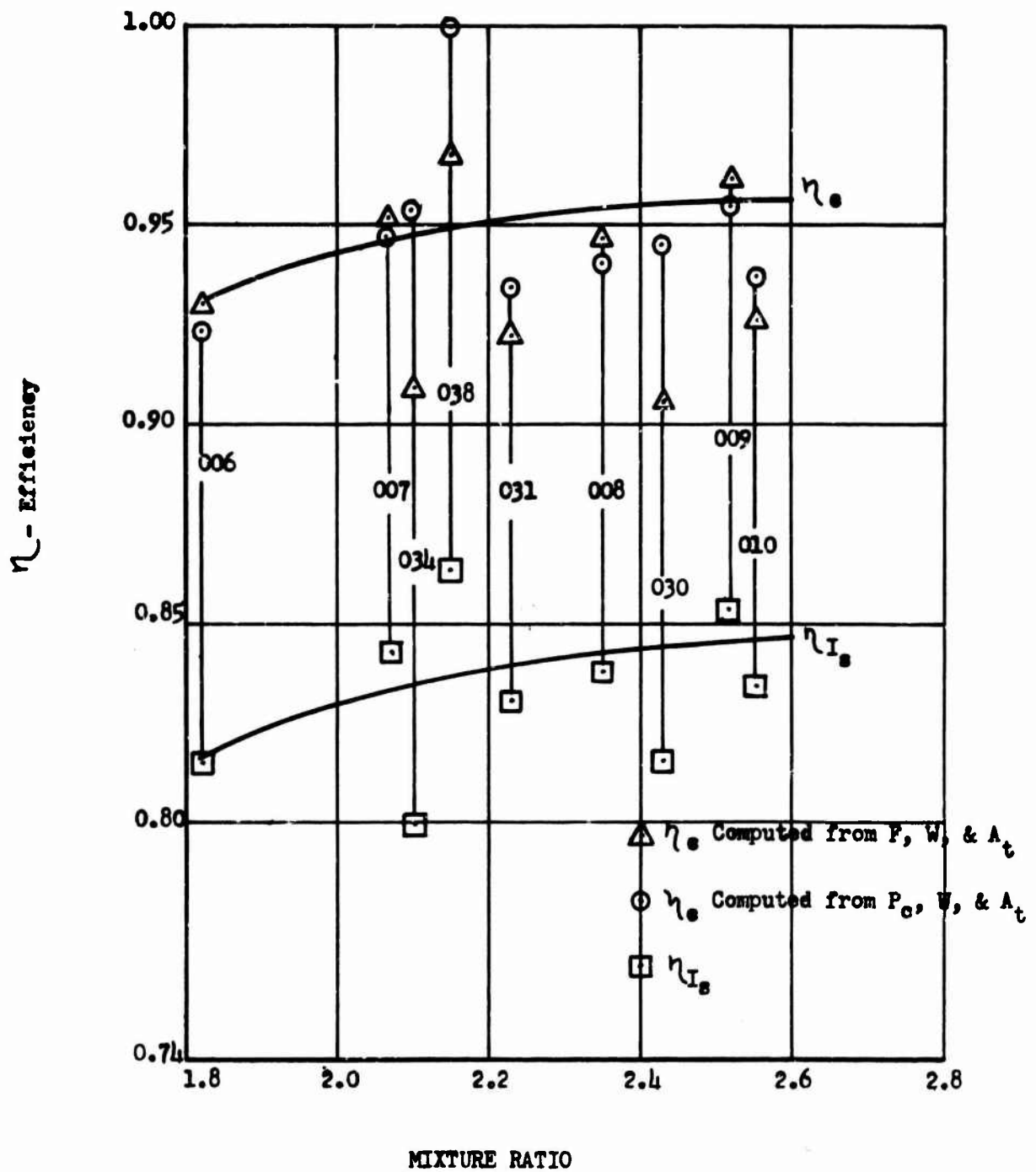
Uncooled TCA Test Data (u)

Figure VIII-A-4

CONFIDENTIAL

CONFIDENTIAL

Book Two



Uncooled TCA Tests Performance Efficiencies (u)

Figure VIII-A-5

CONFIDENTIAL

CONFIDENTIAL

Book Two

Test No.	-012	-014	-015	-017	-018	-021	-023	-024	-025	-027	-029	-033	-036
Injector Type	Mod VIII												Mod VIII
Chamber L*	100												100
Chamber Pressure	2955	2990	3052	3007	2946	3054	2686	2304	2749	2609	2532	2615	2651
Thrust, Sea Level	42,547	42,384	43,164	43,265	42,505	45,629	40,119	33,795	40,983	38,413	33,234	38,752	39,683
Thrust, Vacuum	43,640	43,577	44,357	44,458	43,698	48,669	43,159	36,835	44,023	41,453	43,354	41,845	42,579
Throat Area	9.80	9.80	9.80	9.80	9.80	9.88	9.88	9.88	9.88	9.88	9.88	9.88	9.56
Exit Area	81.1	81.1	81.1	81.1	81.1	207.0	207.0	207.0	207.0	207.0	691.0	210.4	197.0
Area Ratio	8.28	8.28	8.28	8.28	8.28	21.1	21.1	21.1	21.1	21.1	70.0	21.3	20.6
Injector Weight Flow	163.8	167.9	175.6	165.0	174.7	173.5	142.1	145.9	146.7	145.2	140.5	156.5	148.3
Throat Weight Flow	203.5	208.8	210.7	210.3	213.3	202.9	175.3	174.3	178.8	172.1	169.4	186.0	166.7
TCA Weight Flow	210.4	221.1	217.5	222.9	224.1	209.2	184.5	180.5	180.5	185.7	178.5	189.6	166.7
Injector Mixture Ratio	2.24	2.29	2.28	2.25	2.18	2.43	2.15	1.59	2.22	2.32	2.73	2.64	2.42
Throat Mixture Ratio	3.02	3.09	2.91	3.15	2.88	3.01	2.88	2.09	2.92	3.02	3.51	3.33	2.85
TCA Mixture Ratio	3.16	3.33	3.06	3.38	3.07	3.13	3.08	2.22	3.08	3.16	3.62	3.41	2.85
Film Cooling Weight Flow	46.6	53.2	41.9	57.9	49.4	35.7	42.4	34.6	39.0	36.0	34.3	33.1	18.4
Percent Film Cooling	22.1	24.1	19.3	26.0	22.1	17.1	23.0	19.2	21.0	20.2	19.6	17.5	11.0
1. Experimental Performance													
a. Vacuum I_s	207.4	197.6	203.9	199.5	195.0	233.0	234.3	204.0	237.0	232.6	247.8	220.4	255.3
b. C^* , Chamber	4585	4465	4565	4515	4360	4770	4875	4210	4895	4810	4760	4475	4890
2. Theoretical Performance													
a. $I_s(vac)$ at MR_{inj}	308.2	307.1	307.5	308.0	309.4	323.4	331.0	322.7	330.0	327.1	330.1	316.4	323.3
b. C^* at MR_{inj}	5676	5652	5660	5672	5703	5588	5719	5787	5685	5639	5450	5475	5595
3. Calculated Efficiencies													
a. η_s at MR_{inj}	0.673	0.643	0.663	0.648	0.630	0.721	0.707	0.633	0.718	0.712	0.751	0.697	0.766
b. η_c at MR_{inj}	0.808	0.791	0.807	0.797	0.764	0.856	0.852	0.728	0.862	0.852	0.873	0.817	0.874

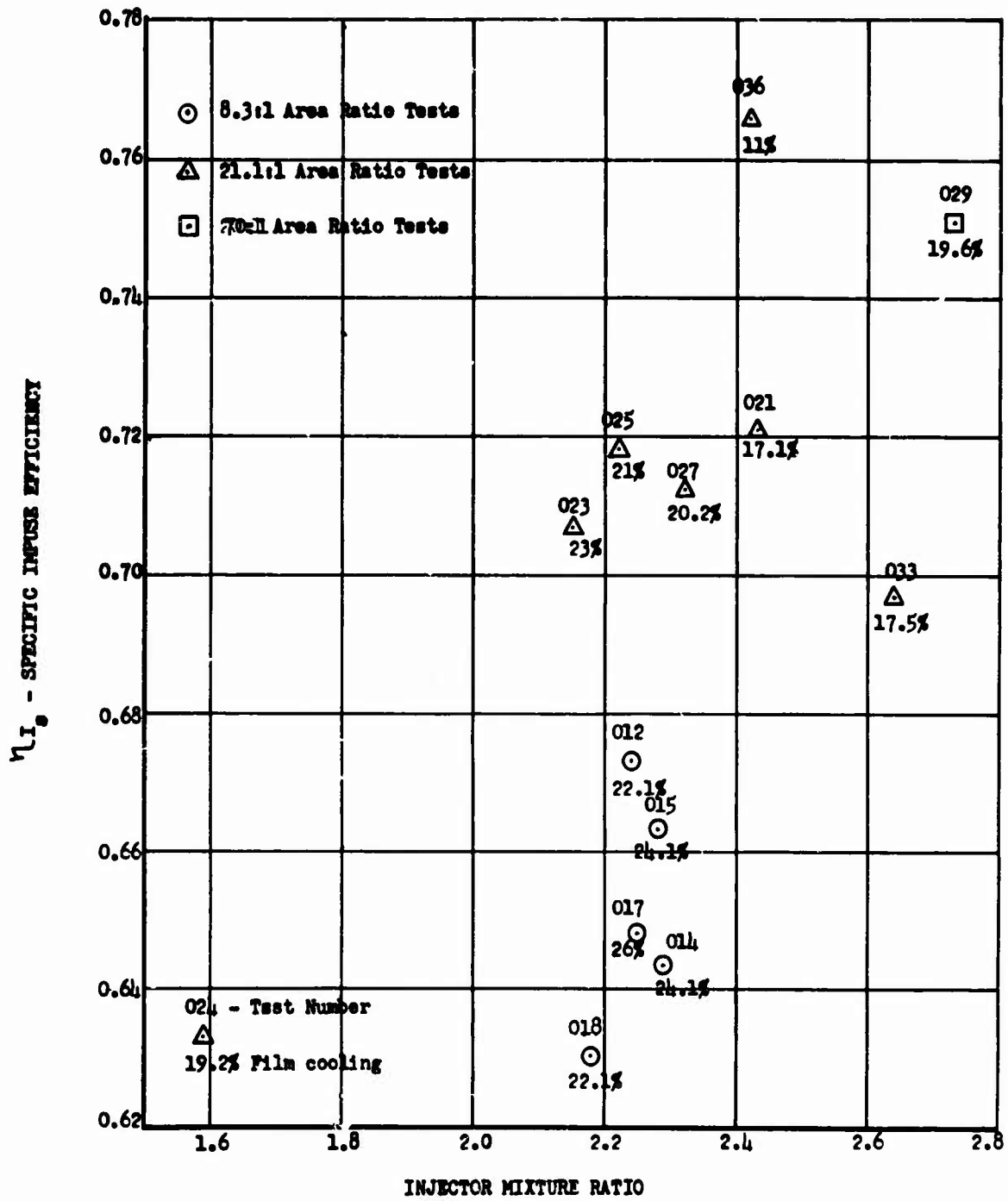
Cooled TCA Test Data (u)

Figure VIII-B-1

CONFIDENTIAL

CONFIDENTIAL

Book Two



Cooled TCA Tests I_s Efficiency (η)

Figure VIII-B-2

CONFIDENTIAL

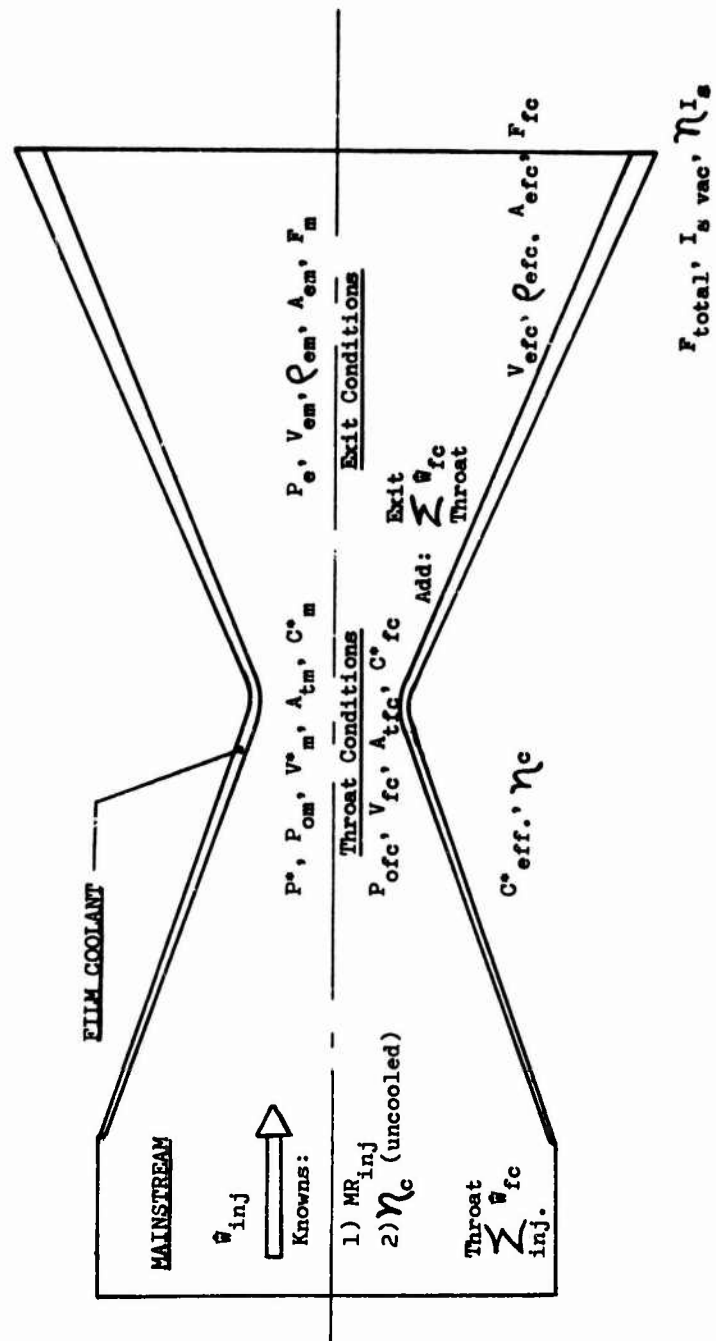


Figure VIII-C-1

Parameters Computed with Film-Cooling Model

CONFIDENTIAL

Book Two

Test No.	-014	-023	-027	-029	-036
ϵ	8.3:1	21:1	21:1	70:1	20.6:1
MR_{inj}	2.29	2.15	2.32	2.73	2.42
$I_{s,theo}$	307.1	331.0	327.1	330.9	323.1
C^*_{theo}	5650	5717	5639	5450	5593
W_{fc}/W_{total}	24.1%	23%	20.2%	19.6%	11.0%
A. Nozzle Efficiency					
Geometric Loss	10.04	9.33	9.33	7.13	9.33
Drag Loss	0.33	0.47	0.47	0.69	0.47
F.C. + Comb Loss	<u>5.80</u>	<u>5.60</u>	<u>4.40</u>	<u>4.40</u>	<u>1.8</u>
Total Losses	16.17	15.40	14.20	12.22	11.60
η_T	0.838	0.846	0.858	0.878	0.884
B. Characteristic Velocity Efficiency					
η_c (comb + f.c.)	0.831	0.828	0.845	0.849	0.894
C. Specific Impulse Efficiency					
$\eta_{I_s} = \eta_T \times \eta_c$	0.696	0.70	0.725	0.746	0.79
D. Performance					
$I_{s,pred.} (vacuum)$	213.7	232	236.8	246.8	255.0
$I_{s,exp.} (vacuum)$	197.3	234.3	232.6	247.8	255.3
% Difference	3.2	1.0	1.8	0.4	0.1
C^*_{pred}	4690	4740	4765	4620	5000
C^*_{exp}	4465	4875	4810	4760	4890
$P_{sn,pred}$	3105 psia	2620 psia	2590 psia	2470 psia	2705 psia
$P_{sn,exp}$	2990 psia	2686 psia	2609 psia	2532 psia	2651 psia

Comparison of Film-Cooling Model with Experimental Data--HiPc Tests (u)

Figure VIII-C-2

CONFIDENTIAL

CONFIDENTIAL

Book Two

Test No.	-024	-025	-027
ϵ	16.8:1	16.8	16.8
MR_{inj}	2.08	2.06	2.21
$I_{s,theo}$	326.3	326.2	325.6
C^*_{theo}	5748	5756	5689
W_{fc}/W_{total}	17.5%	14.8%	9.4%
A. Nozzle Efficiency			
Geometric Loss	1.7	1.7	1.7
Drag Loss	0.9	0.9	0.9
F.C. + Comb Loss	<u>2.0</u>	<u>1.9</u>	<u>2.2</u>
Total Losses	4.6	4.5	4.8
η_T	0.954	0.955	0.952
B. Characteristic Velocity Efficiency			
η_c (comb + f.c.)	0.860	0.877	0.912
C. Specific Impulse Efficiency			
$\eta_{Is} = \eta_T \times \eta_c$	0.821	0.837	0.869
D. Performance			
$I_{s,pred}(vacuum)$	268.0	272.8	282.5
$I_{s,exp}(vacuum)$	267.3	263.3	270.8
% Difference	0.2	3.6	4.3
C^*_{pred}	4940	5040	5190
C^*_{exp}	5145	5150	5225
$P_{sn,pred}$	2330	2450	2510
$P_{sn,exp}$	2420	2500	2530

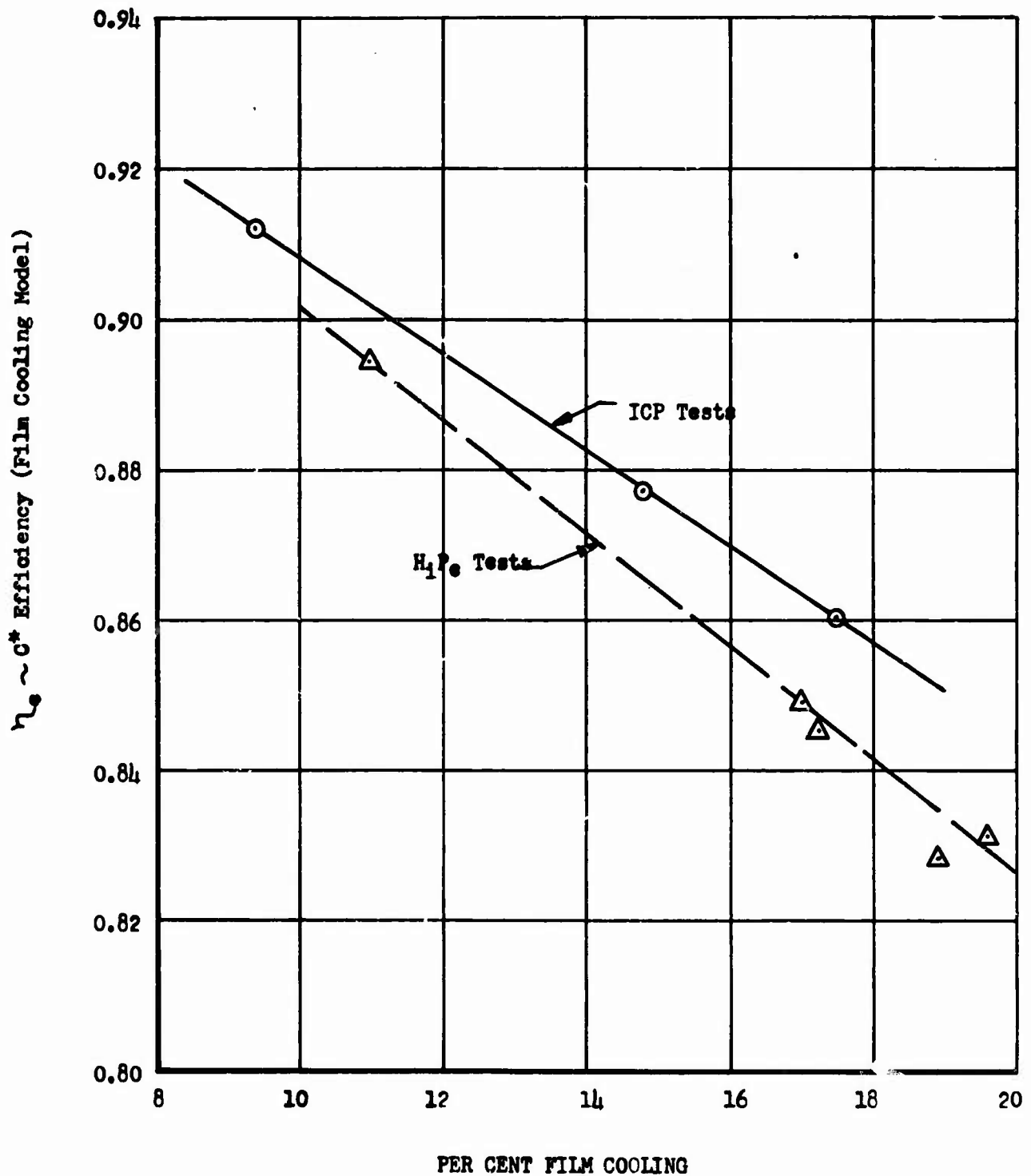
Comparison of Film-Cooling Model with Experimental Data--ICP Tests (u)

Figure VIII-C-3

CONFIDENTIAL

CONFIDENTIAL

Book Two

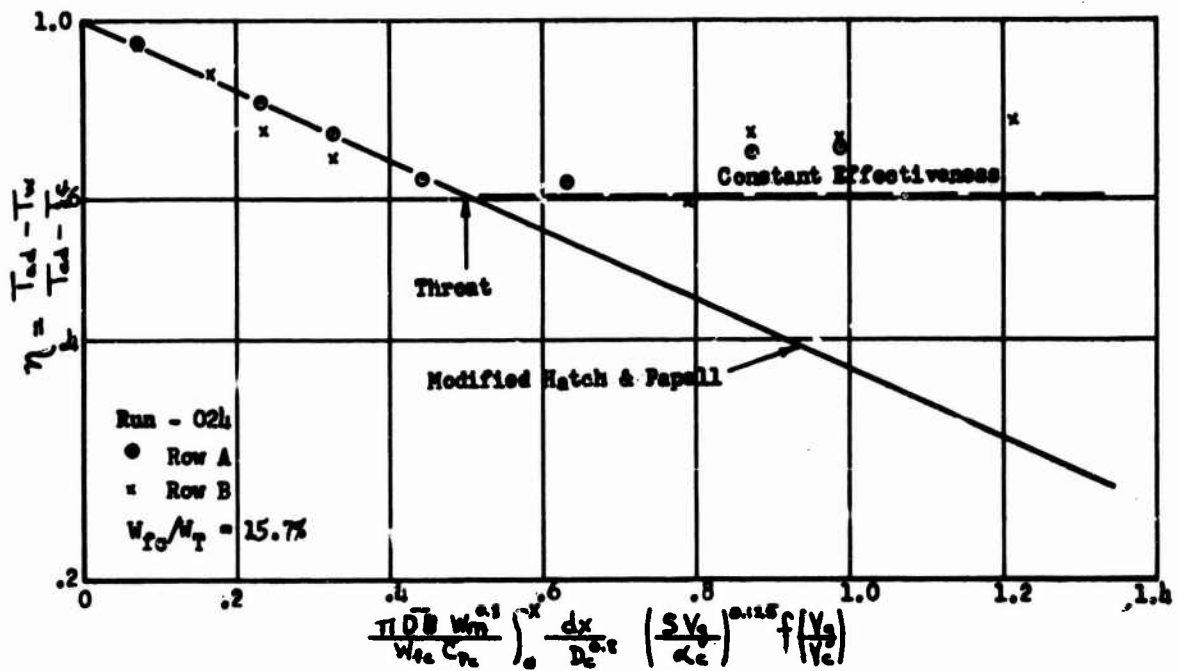


Performance Comparison for Film Cooling in the HiPc and ICP Tests (u)

Figure VIII-C-4

CONFIDENTIAL

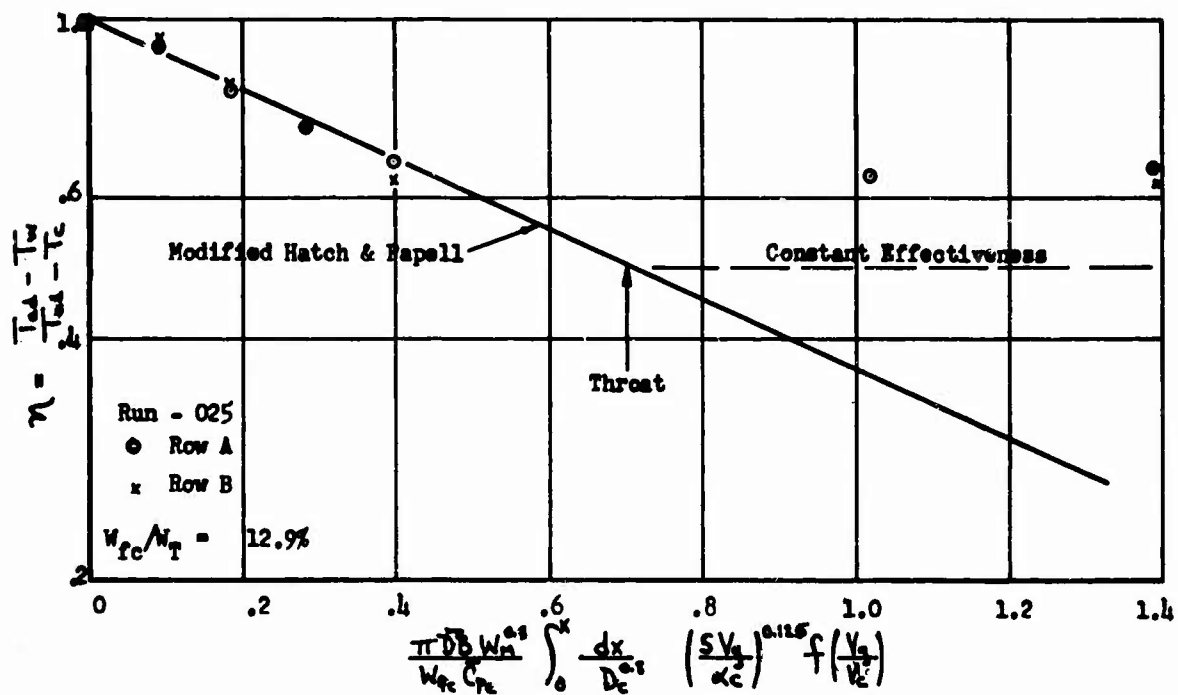
Book Two



Correlation of ICP Film-Cooling Test Data, Test -024

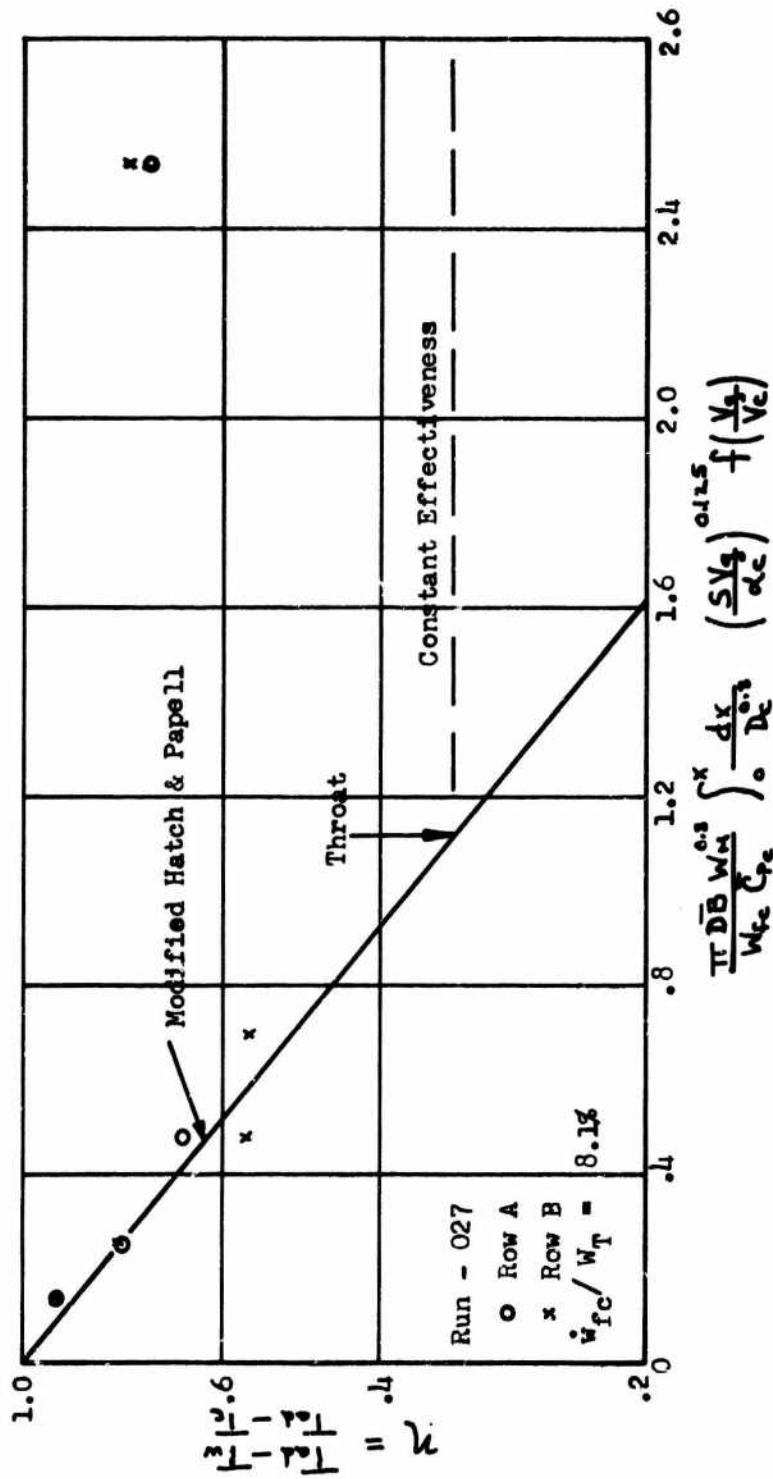
Figure VIII-D-1

Book Two



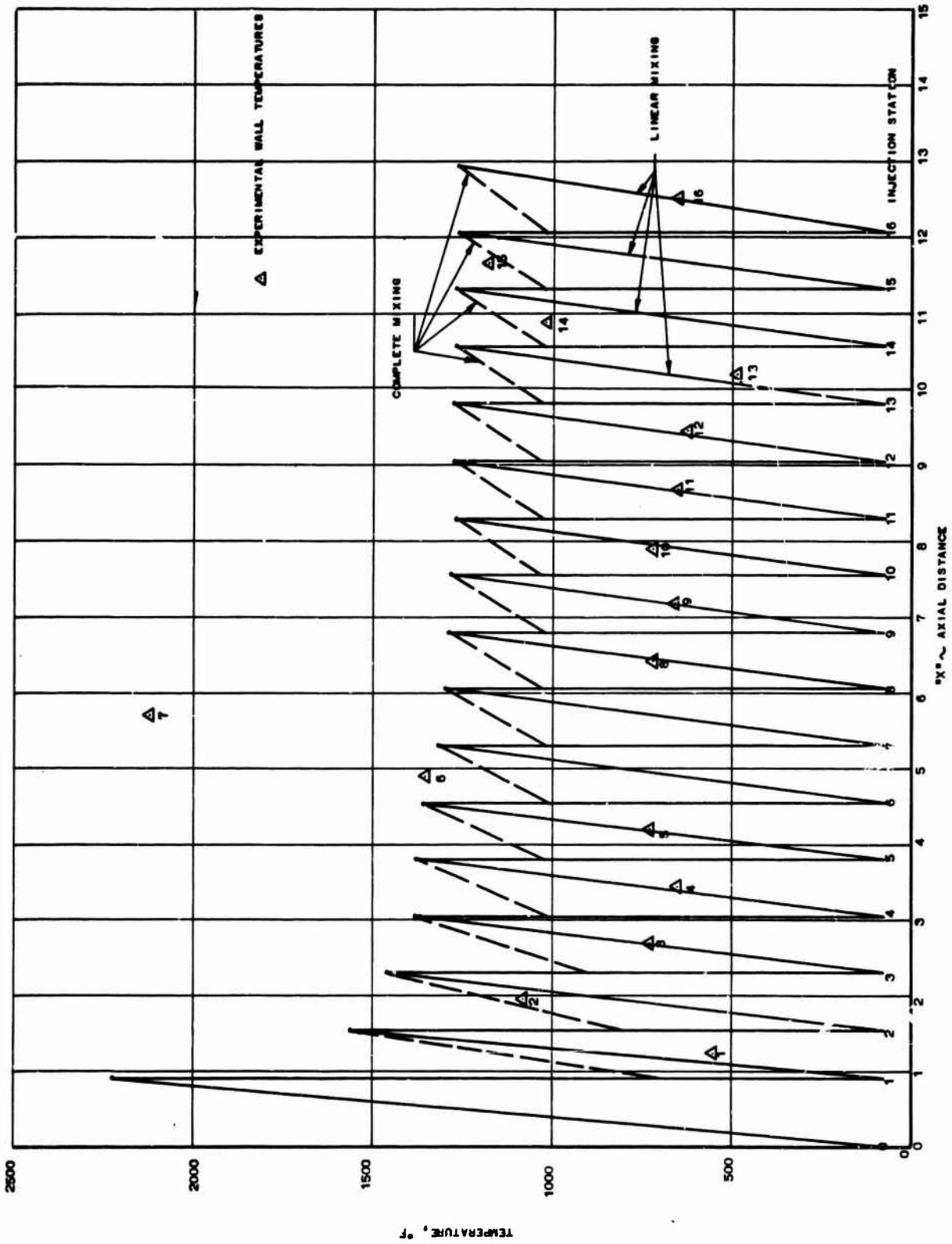
Correlation of ICP Film-Cooling Test Data, Test -025

Figure VIII-D-2



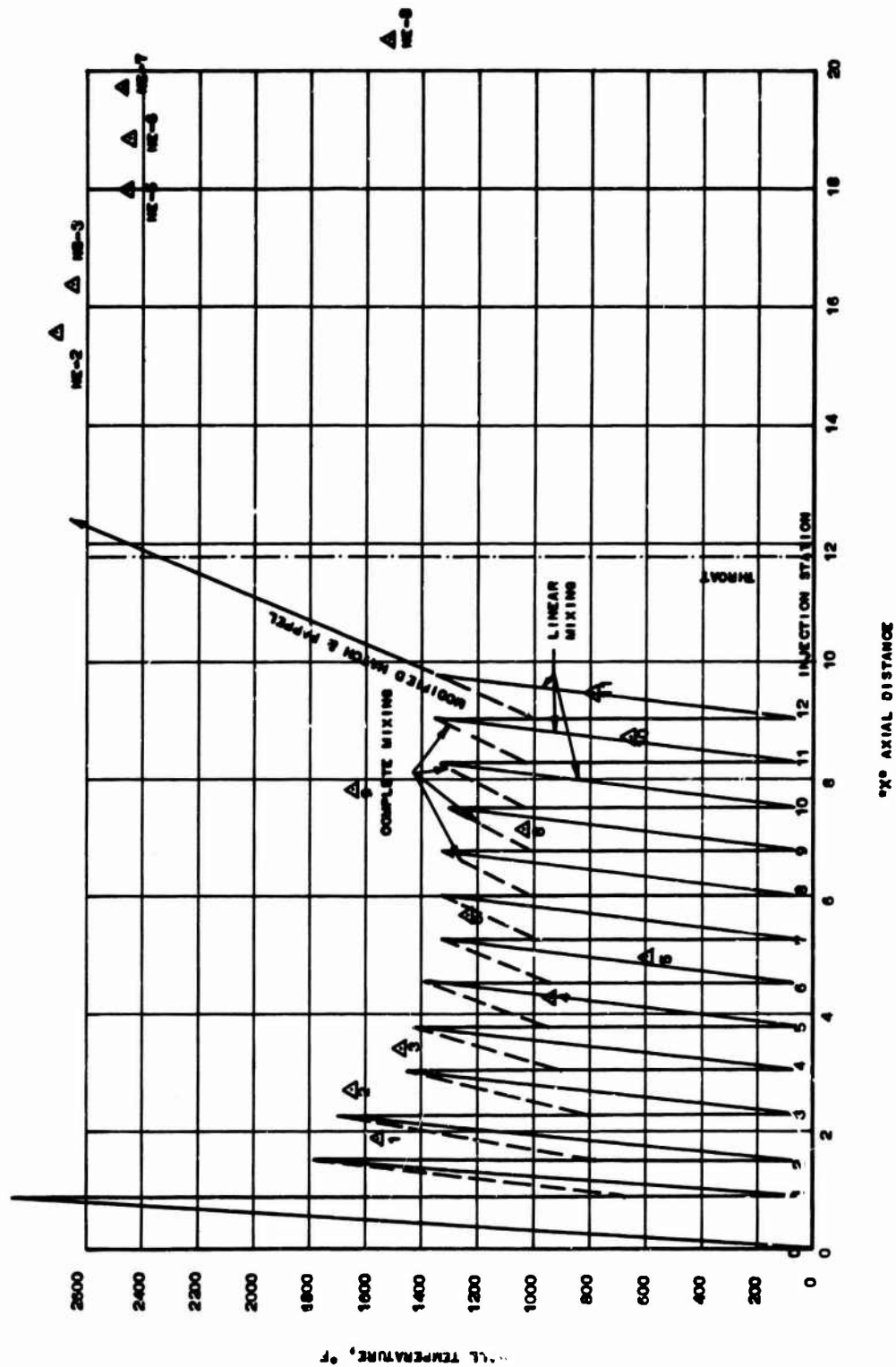
Correlation of LCP Film-Cooling Test Data, Test -027

Figure VIII-D-3



Comparison of Experimental and Theoretical Wall Temperatures
for Test -YAM-027

Figure VIII-D-4



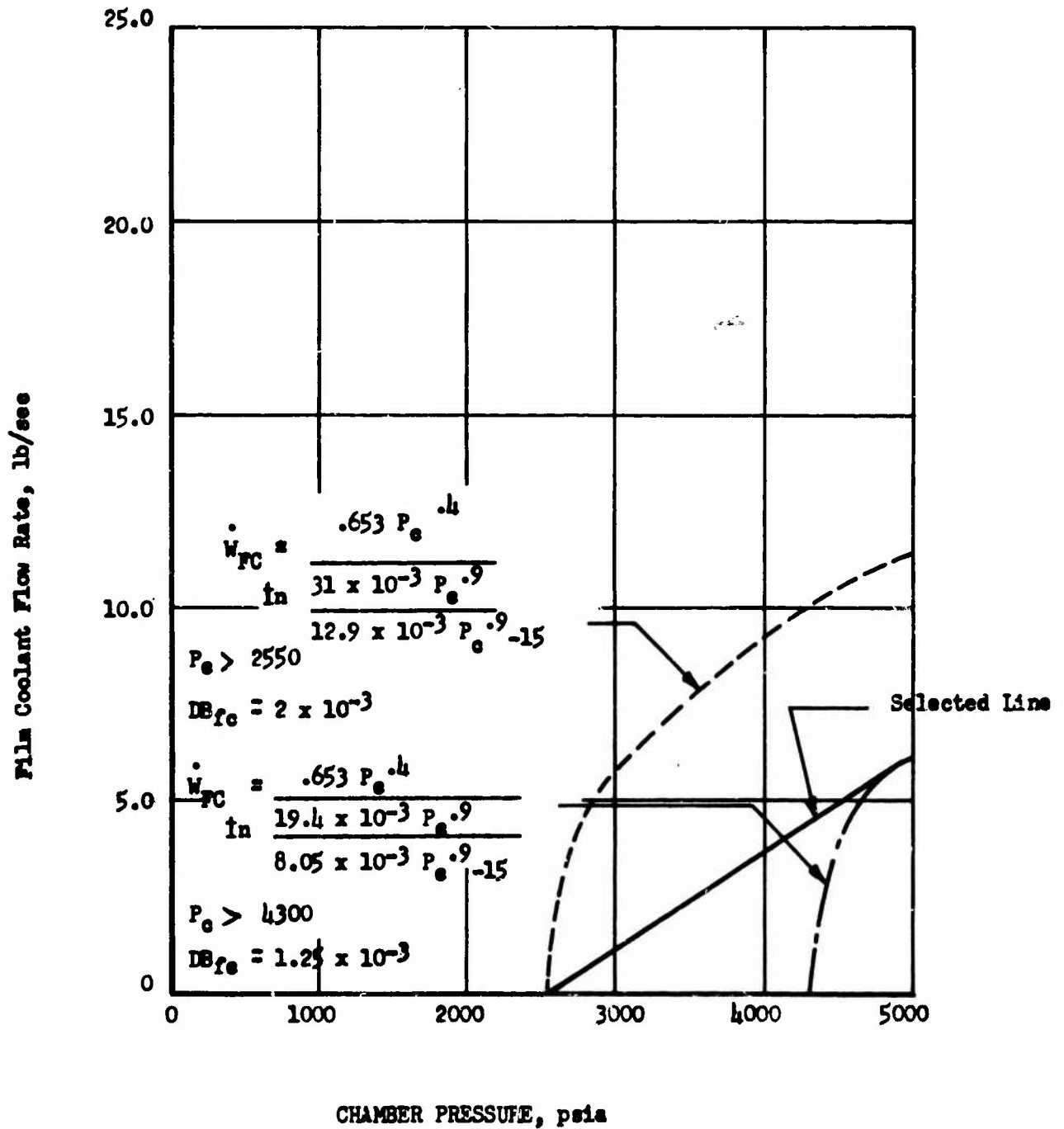
Comparison of Experimental and Theoretical Wall Temperatures
for Test -YAM-036

Figure VIII-D-5

CONFIDENTIAL

NOTE:

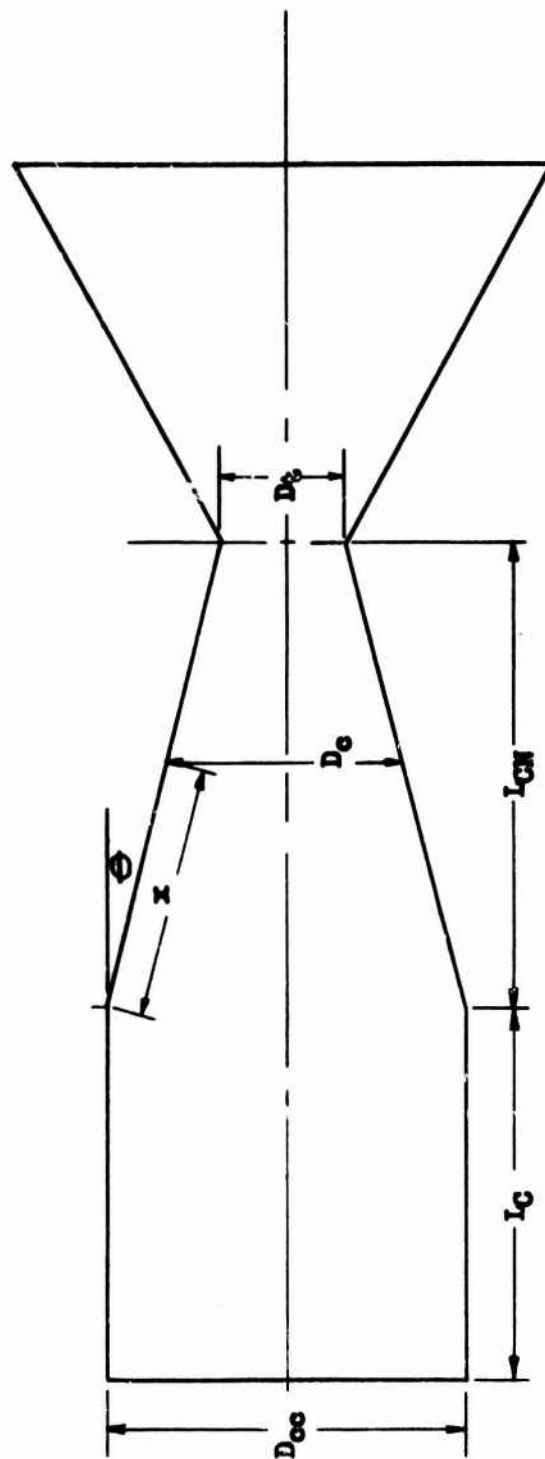
$P = 100,000 \text{ lb}$
 $N_2O_4/A-50$
 $N_2O_4 \text{ Film Coolant}$
 $T_{wg} = 3900^\circ F$
 $Q_{max} = 15 \text{ btu/in}^2 \text{ sec}$



Film Coolant Required to Cool Chamber and Throat (u)

Figure VIII-E-1

CONFIDENTIAL



Assumed Chamber Geometry

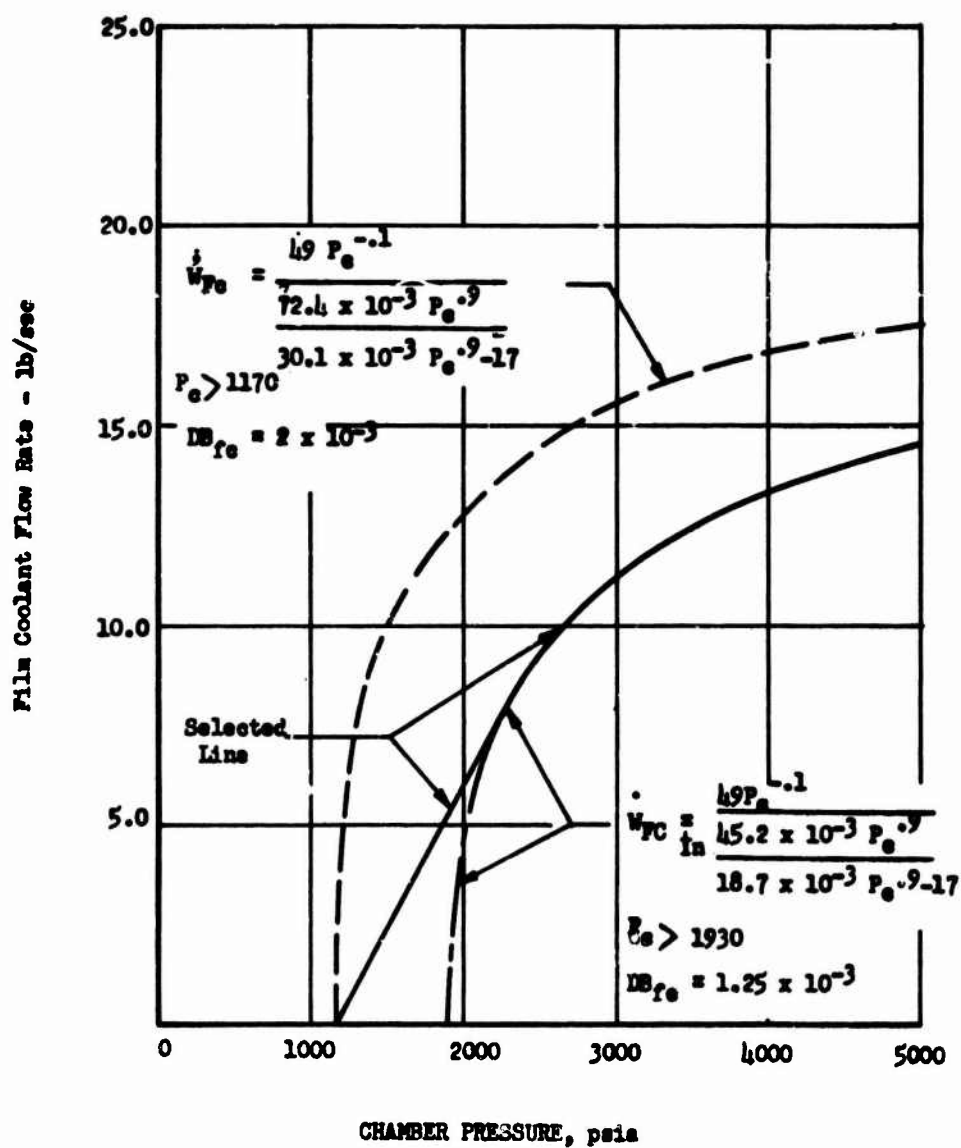
Figure VIII-E.2

CONFIDENTIAL

Book Two

NOTE:

$F = 100,000 \text{ lbs}$
 $N_2O_4/A-50$
 $N_2O_4 \text{ Coolant}$
 $T_{\text{avg}} = 3900^\circ\text{F}$
 $Q_{\text{max}} = 17 \text{ btu/in}^2 \text{ sec}$



Film Coolant Required to Cool Throat (u)

Figure VIII-E-3

CONFIDENTIAL

CONFIDENTIAL

Book Two

NOTE:

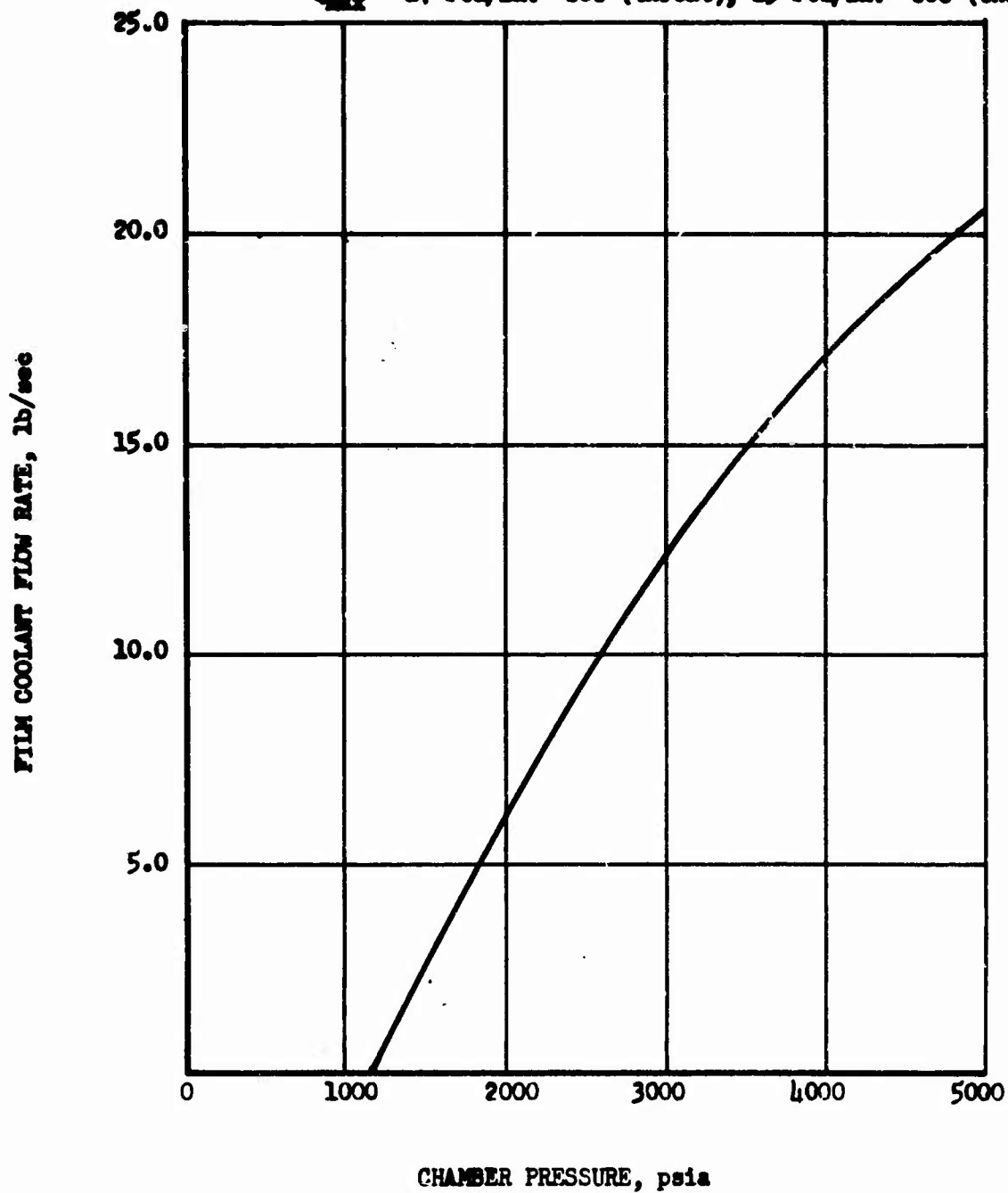
$P = 100,000$

$N_2O_4/A-50$

N_2O_4 Film Coolant

$T_{wg} = 3900^\circ F$

$Q_{max} = 17 \text{ btu/in.}^2 \text{ sec (throat), } 15 \text{ btu/in.}^2 \text{ sec (chamber)}$



Film Coolant Required to Cool Chamber (u)

Figure VIII-E-4

CONFIDENTIAL

CONFIDENTIAL

Book Two

IX. COMBUSTION STABILITY

A. INTRODUCTION AND CONCLUSIONS

A detailed investigation of combustion stability was not within the scope of the High Chamber Pressure Rocketry Program. However, high-frequency instrumentation was used in a number of the tests to determine the combustion characteristics of the injectors evaluated in the program and to determine if the combustion characteristics were affected when the injectors were used in conjunction with the film-cooled hardware. Investigations were conducted for both low-frequency system pressure oscillations, as well as for high-frequency combustion stability characteristics.

The frequencies and amplitudes for the tests which were investigated for stability characteristics are tabulated in Figure IX-A-1. The instrumentation used to obtain these data is discussed in Section IX,B, below. A discussion of the results, including the stability characteristics of the concentric ring injector, transpiration-cooled injector, and vortex injector, are given in Sections IX,C, IX,D and IX,E, below.

The following conclusions can be made from the combustion stability analysis:

1. The combination of the concentric ring injector and the uncooled 100-in. L* chamber produced pressure oscillations corresponding to the second longitudinal mode. No other regular frequency patterns were evident.
2. Film cooling from the concentric ring injector as well as from the chamber walls had only a negligible effect on the amplitude of pressure oscillations and none whatever on their frequencies.
3. The transpiration cooled injector is very stable in combination with the 100-in. uncooled chamber. Pressure oscillations were less than 2% of static chamber pressure.

CONFIDENTIAL

Book Two

IX, A, Introduction and Conclusions (cont.)

4. Based on very limited data, the vortex injector appears to be stable. Because of the small amount of data obtained with this injector, definite conclusions cannot be drawn.

B. STABILITY MEASUREMENTS

Kistler quartz pressure transducers were used to measure dynamic pressure oscillations within the engine system. They were mounted on the injector feed manifolds (Figure IX-B-1). On several tests, these transducers were mounted in the thrust chamber wall to monitor chamber pressure. In this case the Kistler transducer was used with a water cooled adapter (Figure IX-B-2). The chamber wall installations were subsequently discontinued because the pressure tap promoted erosion in that area.

The Kistler transducer is rated at 5000 psi static pressure and has a response time of 3 microsec. This dynamic instrument has its ac signal conditioned by passing it through a 150-cps filter and charge amplifier. The amplified signal is fed to an Ampex 14-channel FM tape recorder. The recording tape speed is 60 in./sec. At this speed, the tape can resolve up to 100,000 cps. The Ampex tape is played back at 3.75 in./sec (a 16:1 reduction in speed and frequency). A specially instrumented Consolidated Electrodynamics oscillograph is used to create a visible record from the Ampex tape.

Taber transducers were positioned adjacent to their respective Kistler transducers and the ac component from the Tabers was also recorded on tape. The oscillatory traces from the Taber instruments were recorded simultaneously with the Kistler traces to provide frequency back-up information. The apparent amplitude of Taber signals is a function of transducer tubing length and can only be considered in a relative sense from test to test.

CONFIDENTIAL

Book Two

IX, B, Stability Measurements (cont.)

Because of the limited scope of the combustion stability effort on this program, only limited stability analyses were performed. The oscillatory pressure traces on the oscillograph records were interpreted to determine modes of system resonance. The high-frequency oscillations observed were then compared to the theoretical values calculated for the chamber geometry. The observed low-frequency oscillations were compared to calculated theoretical feed line resonances.

In order to completely define the combustion stability characteristics of a system (not attempted on this program), it is necessary to include at least three flush mounted transducers within the chamber to provide meaningful data. This data must then be used in conjunction with a detailed high frequency analysis to determine the interaction index and associated combustion time-lag criteria.

C. CONCENTRIC RING INJECTOR

1. Uncooled Tests

The original, uncooled chamber employing the concentric ring injector (Mod I, II, III) experienced two different regimes of oscillations. During the start transient, the feed system and chamber perturbations occurred at frequencies of 200 to 250 cps and peak-to-peak amplitudes of 500 to 1500 psi. At approximately two-thirds of steady-state chamber pressure, the low-frequency oscillations ended abruptly and were superseded by pressure perturbations at frequencies of 1200 and 2400 cps in the combustion chamber and in both oxidizer and fuel injector manifolds. These corresponded to the first and second longitudinal acoustic modes. The amplitude of these oscillations varied from 500 psi peak-to-peak in the combustion chamber to 1000 psi peak-to-peak in the fuel line. Representative samples of these pressure traces are shown in Figure IX-C-1.

Dynamic analyses of the oxidizer and fuel feed lines indicated peak resonances of 230 to 250 cps in the oxidizer line and 290 to 330 cps in the fuel line.

CONFIDENTIAL

Book Two

IX, C, Concentric Ring Injector (cont.)

The low-frequency, high-amplitude oscillations were therefore attributed to feed system resonance, and the high-frequency oscillations were attributed to the injector. The 2-cycle filter, originally used to limit Kistler data, was changed to a 150-cycle filter to prevent amplifier overloading and corresponding loss of signal during the start transient.

The addition of a porous material (Rigimesh) to the injector face in the oxidizer circuit of the concentric-ring injector design Mod IV did not affect the basic concentric-ring stability; the raised fuel ring of the Mod IV concentric-ring injector design did affect it. The basic frequency of pressure oscillations in the chamber and both feed lines changed to 2100 cps and the amplitudes decreased to 100 to 225 psi and 300 to 700 psi for the combustion chamber and the feed lines, respectively.

The rigid structure of Mod IV injector design resulted in no basic change to the stability performance obtained with Mod V injector, but the major modifications involved in Mod VII injector again changed the principal resonant frequencies present in both feed lines and chamber pressure. The oxidizer manifold pressure was oscillating at a frequency of 7500 cps at an amplitude of 600 psi and the fuel manifold pressure was oscillating at 4100 cps at an amplitude of 900 psi. Chamber pressure, however, varied only 200 psi peak-to-peak.

The final basic injector design (Mod VIII) did not exhibit any changes in the frequencies of feed-system oscillations; however, the oxidizer manifold perturbations dropped to between 350 and 500 psi, and the fuel perturbations dropped to between 350 and 500 psi. Figures IX-C-2 through IX-C-5 illustrate typical pressure traces of the basic Mod VIII type injector design. The "beat" frequency as observed in Figure IX-C-5 can result from a spinning tangential mode as well as from a difference frequency between two chamber frequencies. It was not possible to determine the significance of the observed beat frequency in Figure IX-C-5 because of insufficient chamber transducer coverage.

CONFIDENTIAL

Book Two

IX, C, Concentric Ring Injector (cont.)

In all concentric-ring injector tests in which combustion stability data was obtained, no test data indicated a divergence of pressure amplitudes through the steady-state period of operation. All tests exhibited an interim period of low-frequency, high-amplitude pressure oscillations during the early transient portion of the test, and were attributed to feed system resonances.

2. Cooled Tests

The advent of cooled testing brought forth a new manifolding arrangement indicated in Figure VII-D-14. This new manifolding altered the length and volume of the injector feed lines, and the flex lines altered the rigidity of the system. The net effect of these manifold changes was to reduce the amplitude of low-frequency oscillations on startup and establish random frequencies during the same period.

At steady-state operating conditions, neither the additional length of lines, the change in rigidity of the lines, nor the introduction of film coolant appeared to affect the resonant frequencies present in the feed lines and chamber. However, the amplitude of the oscillations in the feed lines decreased from a maximum of 500 psi to a maximum of 400 psi. Chamber pressure oscillations decreased from between 350 and 500 psi to between 100 and 200 psi. Figures IX-C-3 and IX-C-4 illustrate pressure traces in typical cooled-chamber tests.

It was concluded that (1) serious pressure oscillations were encountered in the second longitudinal acoustic mode only, (2) no other modes of severe pressure oscillations existed because of the absence of the appropriate harmonic frequencies, and (3) the presence of chamber film cooling had only negligible effect on the amplitude of pressure oscillations, and none whatever on their frequencies.

CONFIDENTIAL

Book Two

IX, Combustion Stability (cont.)

D. TRANSPIRATION COOLED INJECTOR

This injector was tested during the final two tests of the High Chamber Pressure Program. The high-frequency records for this injector exhibit background noise only, and the tests are classed as absolutely stable. Figure IX-D-1 represents pressure traces taken from one of these tests. Kistler data indicate that the amplitude of feed-line oscillations is less than 2% of static chamber pressure. Taber data also indicate a very low level of pressure oscillations. No particular repeating frequencies were evident in examination of the Kistler data.

E. VORTEX INJECTOR

The original vortex injector attained steady-state on the first uncooled test. No high-frequency instrumentation was used on this test, but the results of an analysis of the Taber transducer data are presented in the following paragraphs.

Pc-1, located at the center of the injector face, experienced oscillations of 400 cps at an amplitude of ± 80 psi; a 1500 cps oscillation of low amplitude was superimposed on the 400 cycle carrier frequency.

Pc-2, at the outer edge of the injector, recorded very regular oscillations of 110 to 144 cps at amplitudes of ± 200 psi. A low-amplitude 1100-cps oscillation is superimposed on the 110 to 114 cycle carrier.

PcP, at the beginning of the chamber convergent section, recorded 500 cps at ± 60 psi with no superimposed higher frequencies.

None of these amplitudes continued to grow with time and the injector was considered stable. Chamber detonations associated with injector erosion were followed by instantaneous recovery to the stable combustion pattern.

CONFIDENTIAL

Book Two

IX, E, Vortex Injector (cont.)

Kistler transducers were installed in the chamber during the test in which the Mod I design was evaluated. The test hardware never reached steady-state operation because of injector failure, but transient high-frequency data indicated the existence of severe pressure oscillations between the first longitudinal acoustic mode and the first tangential mode. When an observed chamber frequency is found to be numerically between two different modes such as the theoretical longitudinal and theoretical tangential mode, it is necessary to have sufficient transducers installed in the chamber to identify the actual mode. Three transducers are necessary to properly identify a tangential mode; the high-frequency chamber installation in this program was limited to one flush-mounted transducer, therefore precluding complete definition of the acoustical modes. No detailed quantitative analysis is presented for this Mod I vortex design because of the transient nature of the data and the injector erosion which occurred during the test firing.

No detailed stability analysis was conducted for the Mod II vortex injector because of the extensive injector erosion which occurred on its only test firing and the subsequent elimination of the vortex injector concept in the program.

CONFIDENTIAL

Book Two

TEST NUMBER AND REMARKS	TIME, SEC. FROM T-0	$P_{01}^P - M(T)$	$P_{01}^{-1} - M(T)$	$P_{01}^{-1} - F(K)$	$P_{01} - M(T)$	$P_{01} - F(K)$	$P_{01} - M(T)$	$P_{01} - F(K)$
		(TAPER) FREQ., OPS	AMP (PP), OPS	FREQ., OPS	AMP (PP), OPS	AMP (PP), OPS	(TAPER) FREQ., OPS	(RITLER) FREQ., OPS
1.2-05-100-004 CONCENTRIC INLET, VERT. VILL. & SHUTTER LO	STEADY STATE	1100 WAF	INVALID			400 WAF	200	1100 WAF
1.3-05-100-001 VERTICAL INJECTOR	STEADY STATE	5/0	60 400/1000 80/20					

INSTRUMENTATION SYMBOLS

$P_{01} - M(T)$ = CLOSE COUPLED TAPER TRANSDUCER & ORIFICE INJECTOR MANIFOLD

$P_{02} - M(T)$ = CLOSE COUPLED TAPER TRANSDUCER & FUEL INJECTOR MANIFOLD

$P_{03} - M(T)$ = CLOSE COUPLED TAPER TRANSDUCER & CHAMBER 2-14, FROM INJECTOR FACE

$P_{04} - M(T)$ = CLOSE COUPLED TAPER TRANSDUCER & CHAMBER 2-14, FROM CONVERGENT SECTION

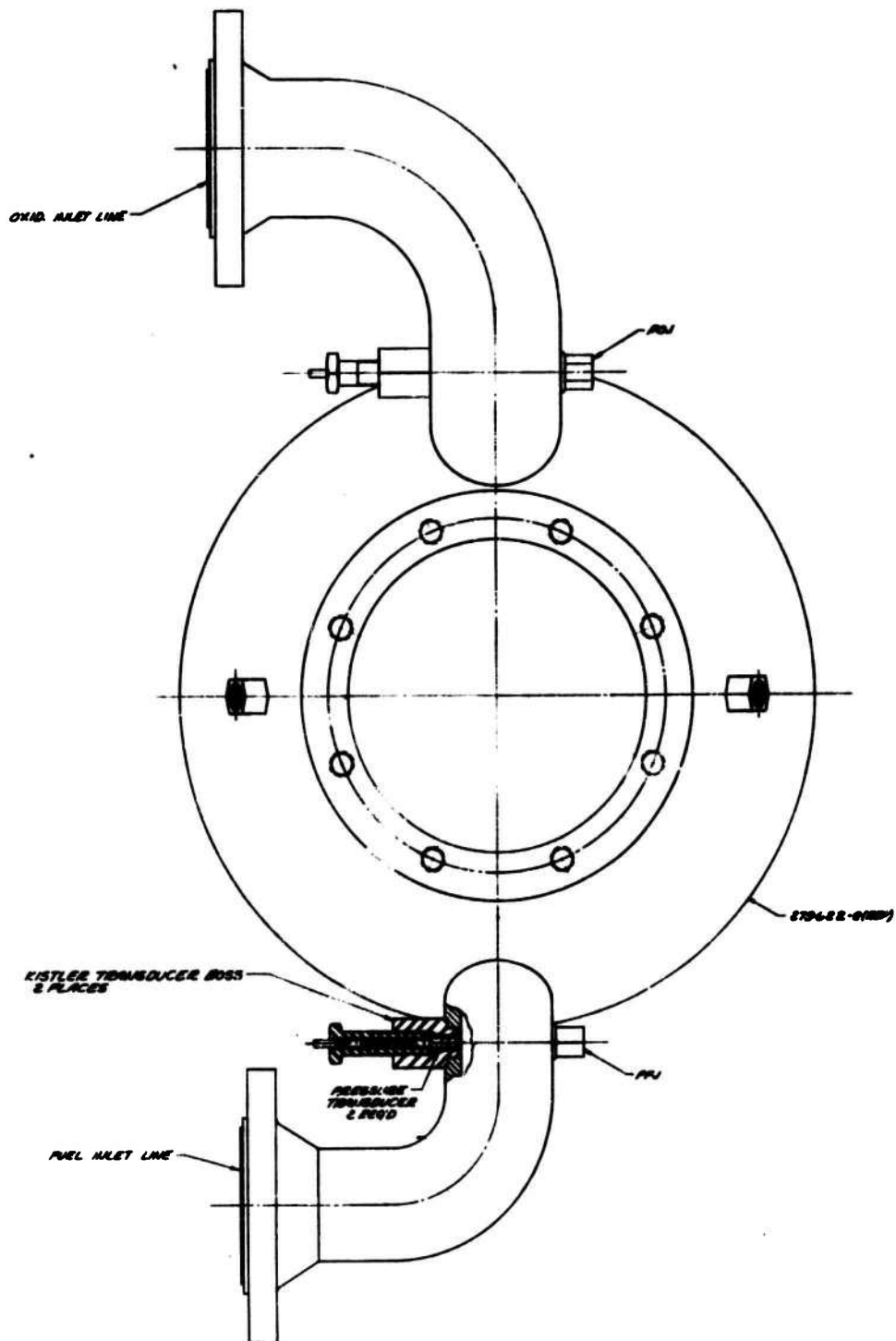
$F(K)$ = FLUX MOUNTED RITLER TRANSDUCER

Combustion Stability Test Data (u)

Figure IX-A-1, Sheet 2 of 2

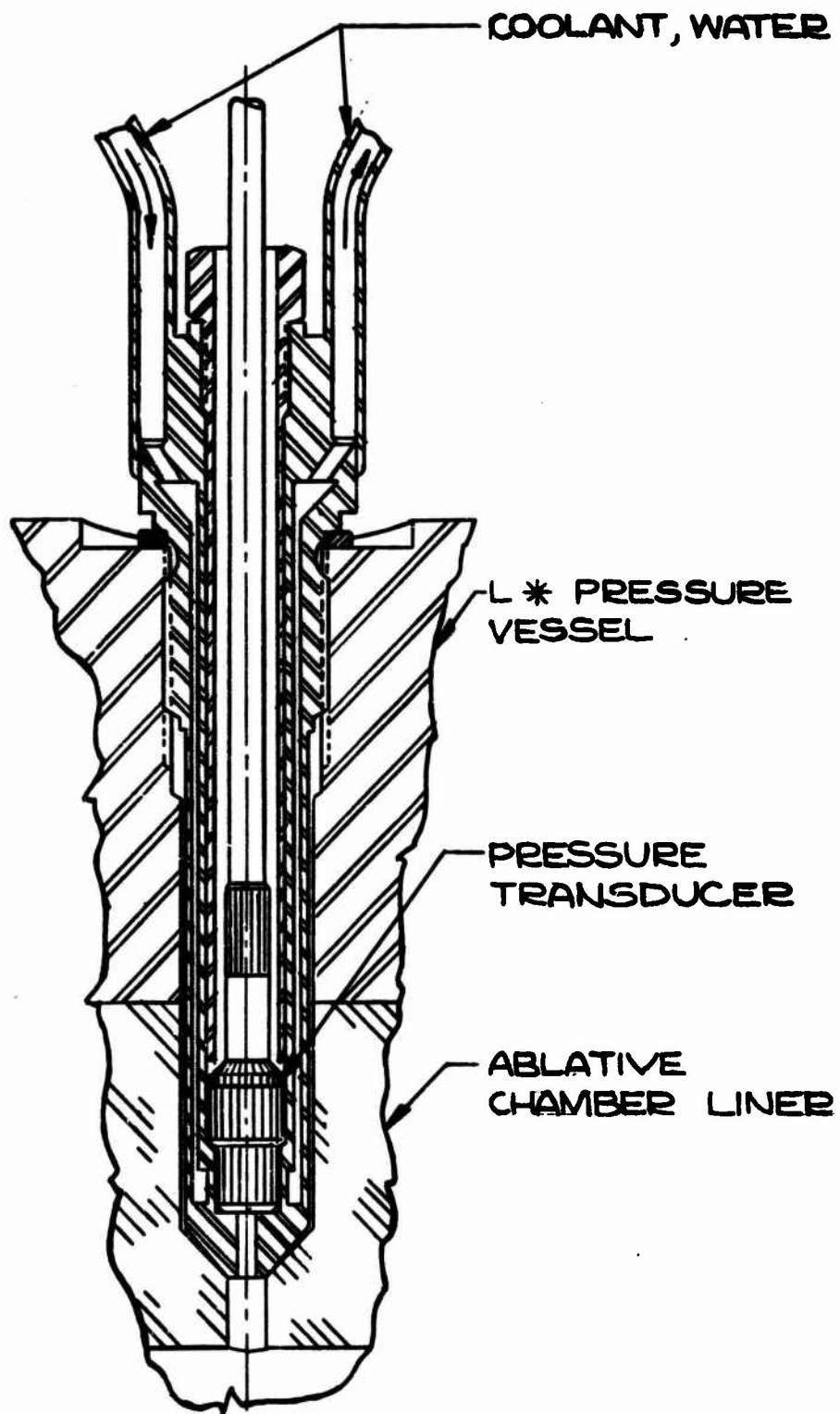
CONFIDENTIAL

Book Two



Installation of High-Pressure Transducers Mounted on Injector
Frequency Monitoring System

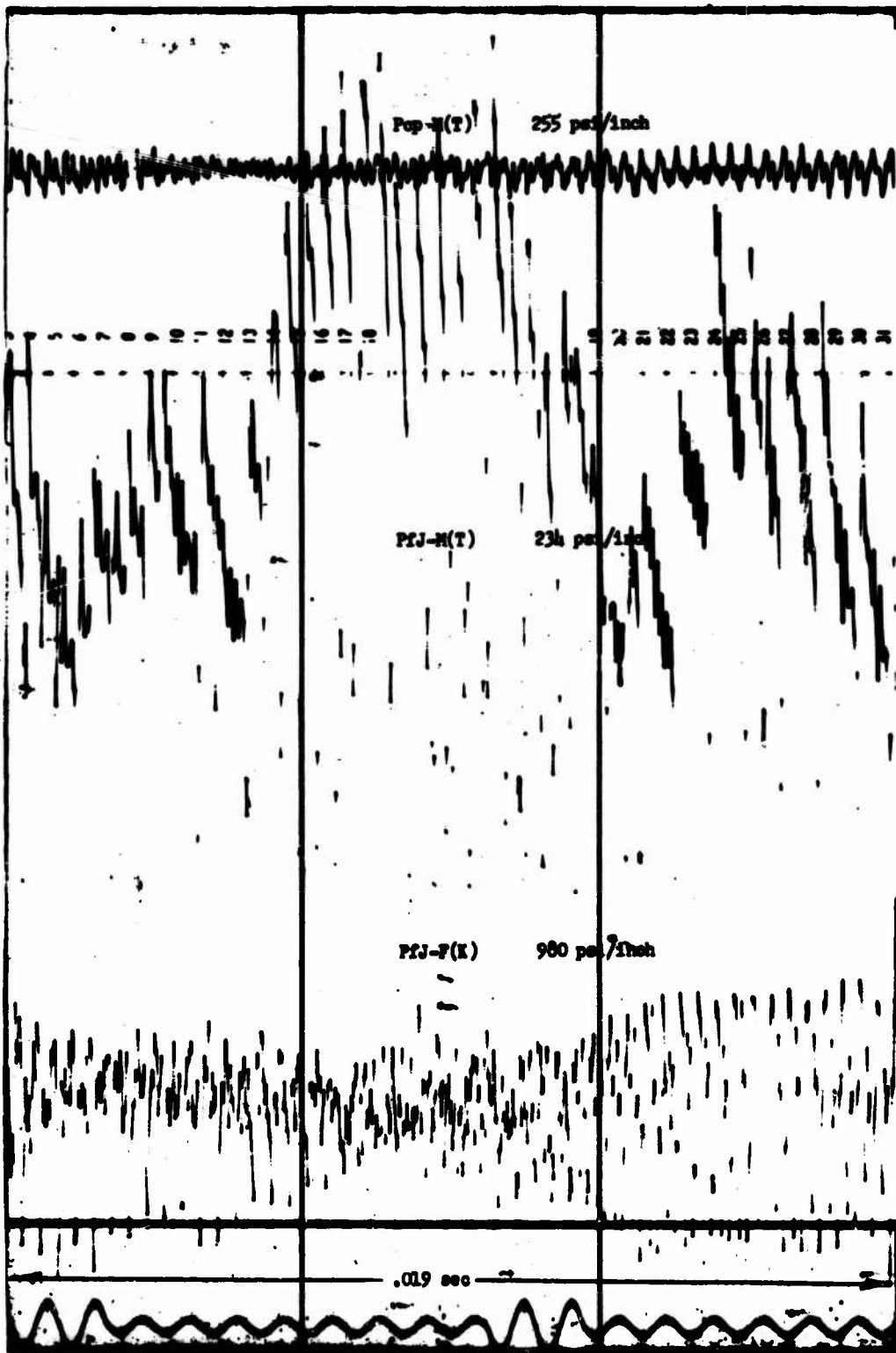
Figure IX-B-1



Installation of Kistler Water-Cooled Probe Adapter in Ablative Chamber Liner

Figure IX-B-2

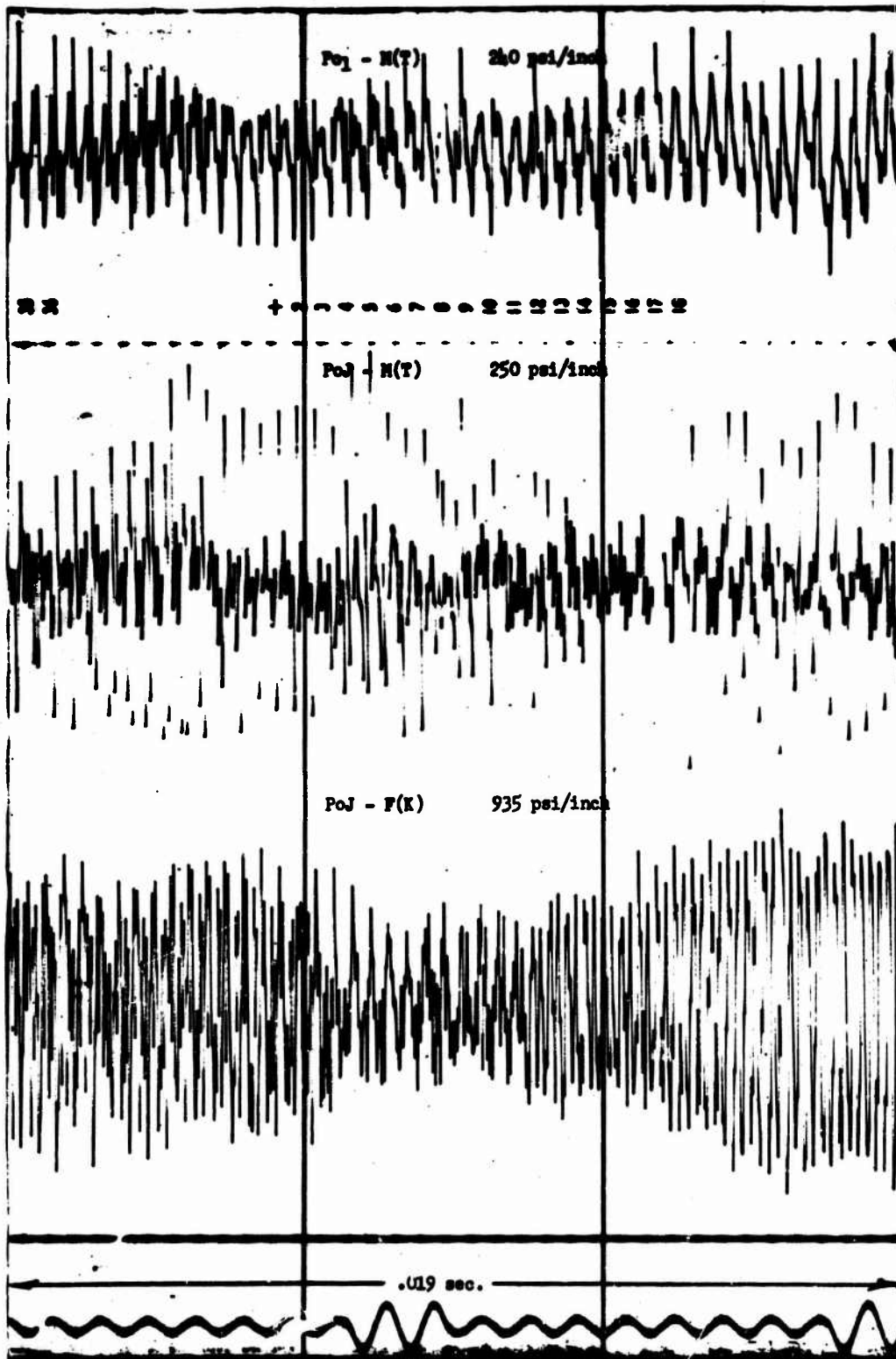
Book Two



Ampex-Playback--Concentric Ring (Mod III)

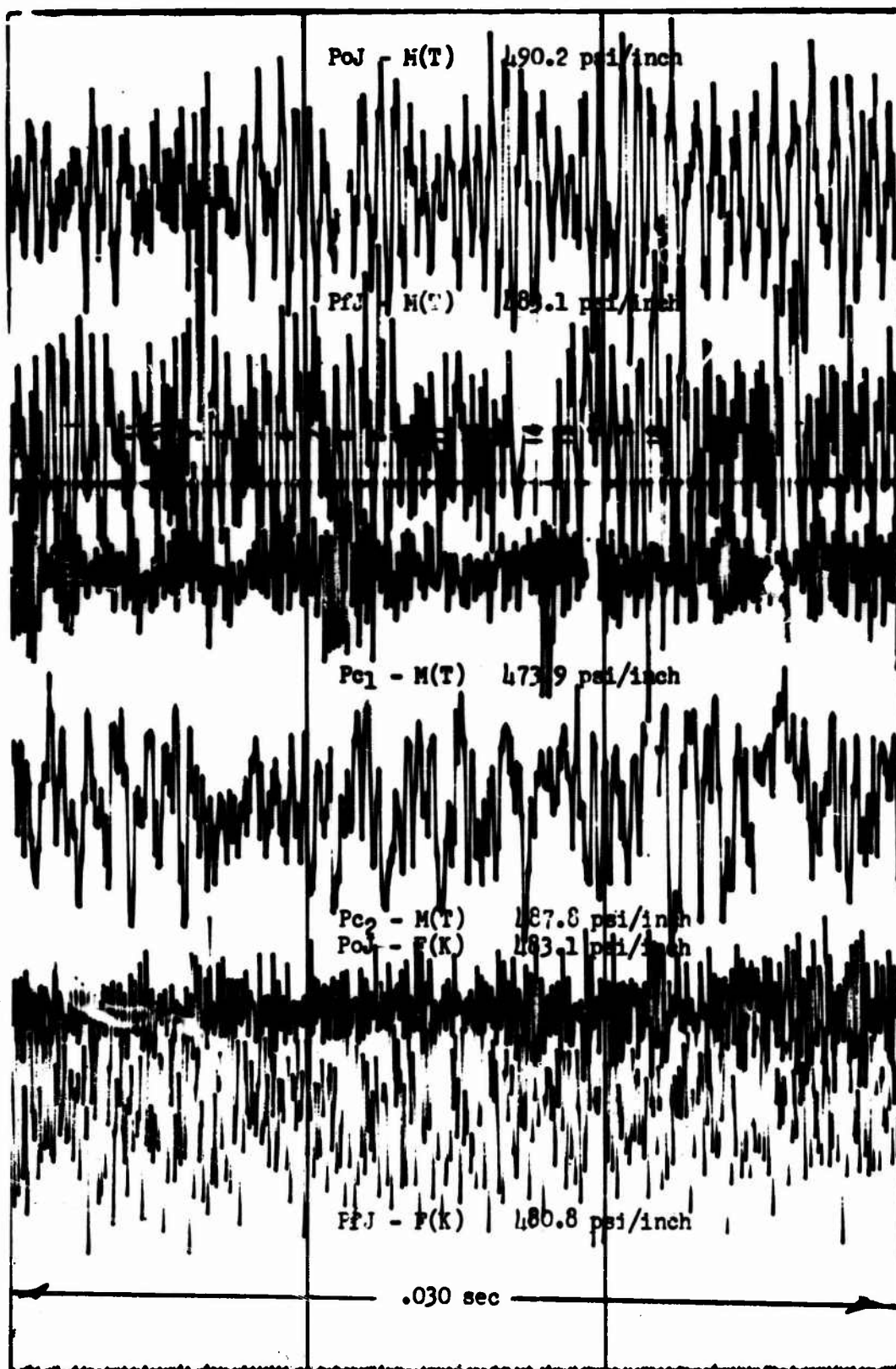
Figure IX-C-1, Sheet 1 of 2

Book Two



Ampex Playback--Concentric Ring (Mod III)

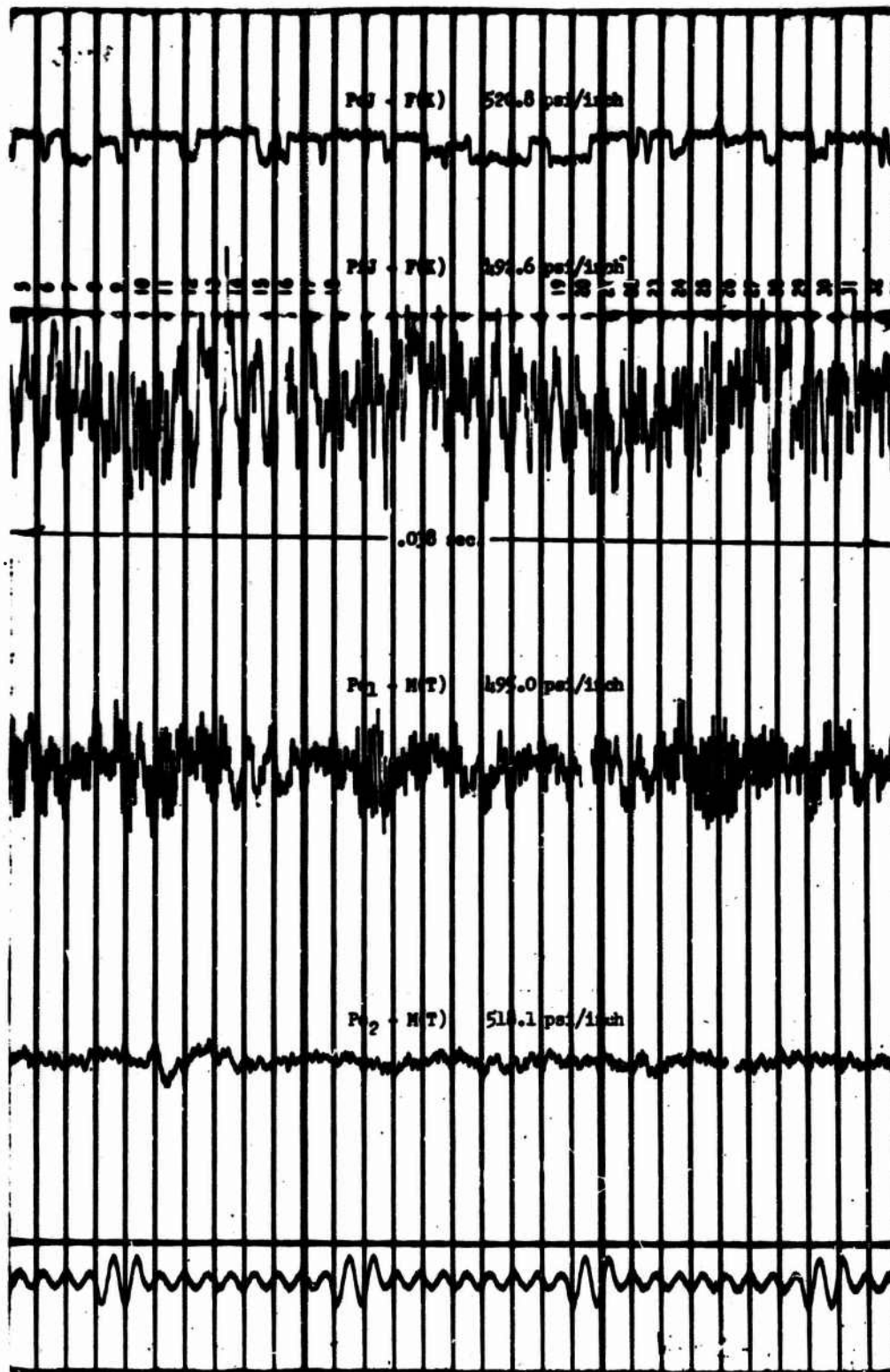
Book Two



Ampex Playback--Concentric Ring (Mod VIII)

Figure IX-C-2

Book Two



Ampex Playback--Concentric Ring (Mod VIIIA) plus Cooled Throat Segment

Figure IX-C-3

Book Two

$$+ 2 \pi \cdot \text{POI}(\mathbf{x}) = 625.8 \text{ psi/inch}^2 = 1.1 \text{ in}$$

PoJ-M(T) 819.7 psi/inch

PfJ-F(K) 657.9 psi/inch

PRJ-M(T) 813.0 psi/inch

Pc₁-F(K) 625.0 psi/inch

$P_{c_1} - M(T)$ 704.2 psi/inch

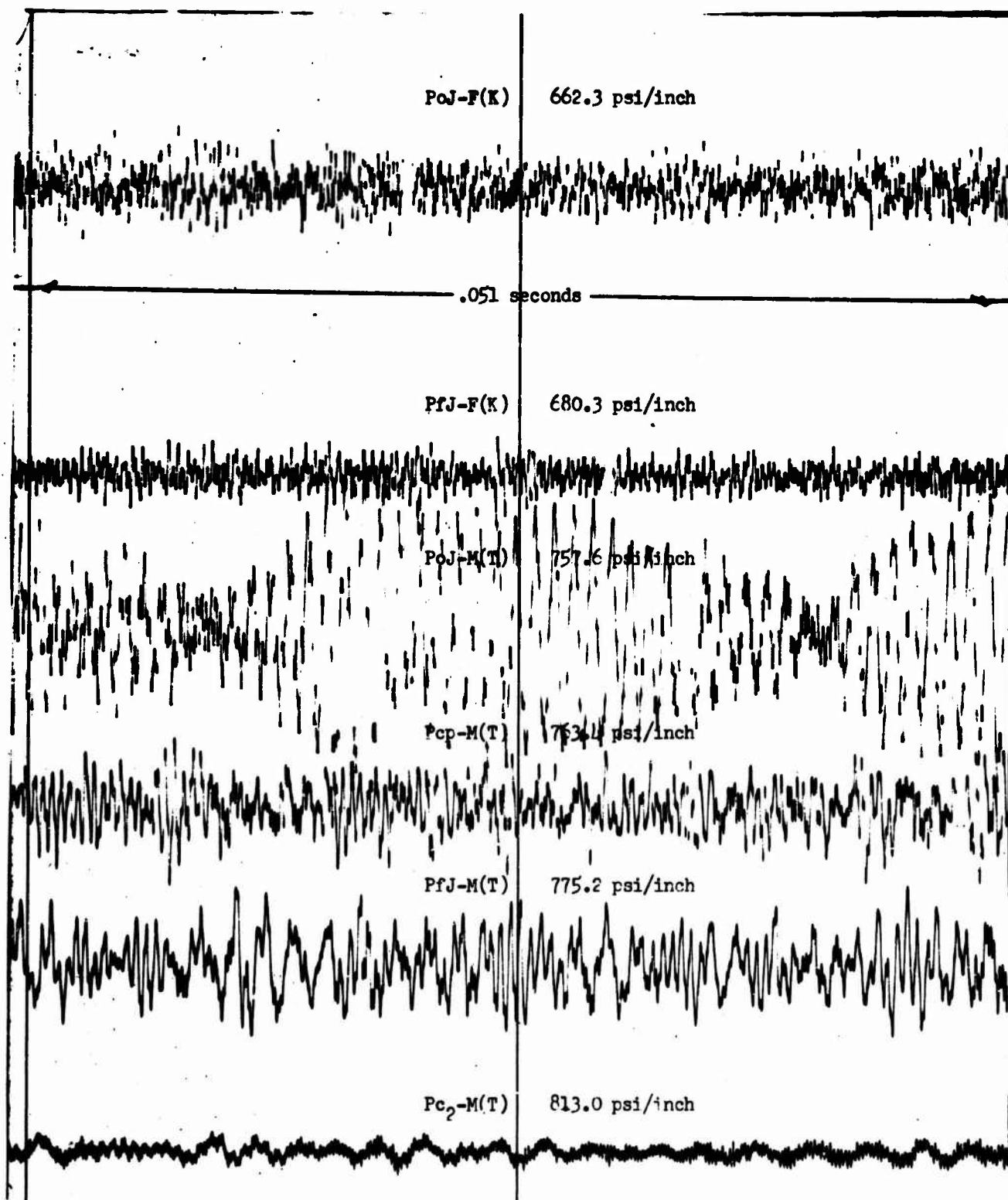
Pc₂-M(T) 699.3 psi/inch

.030 seconds

Ampex Playback--Concentric Ring (Mod VIIIB) plus Cooled Throat and Exit Cone

Figure IX-C-4

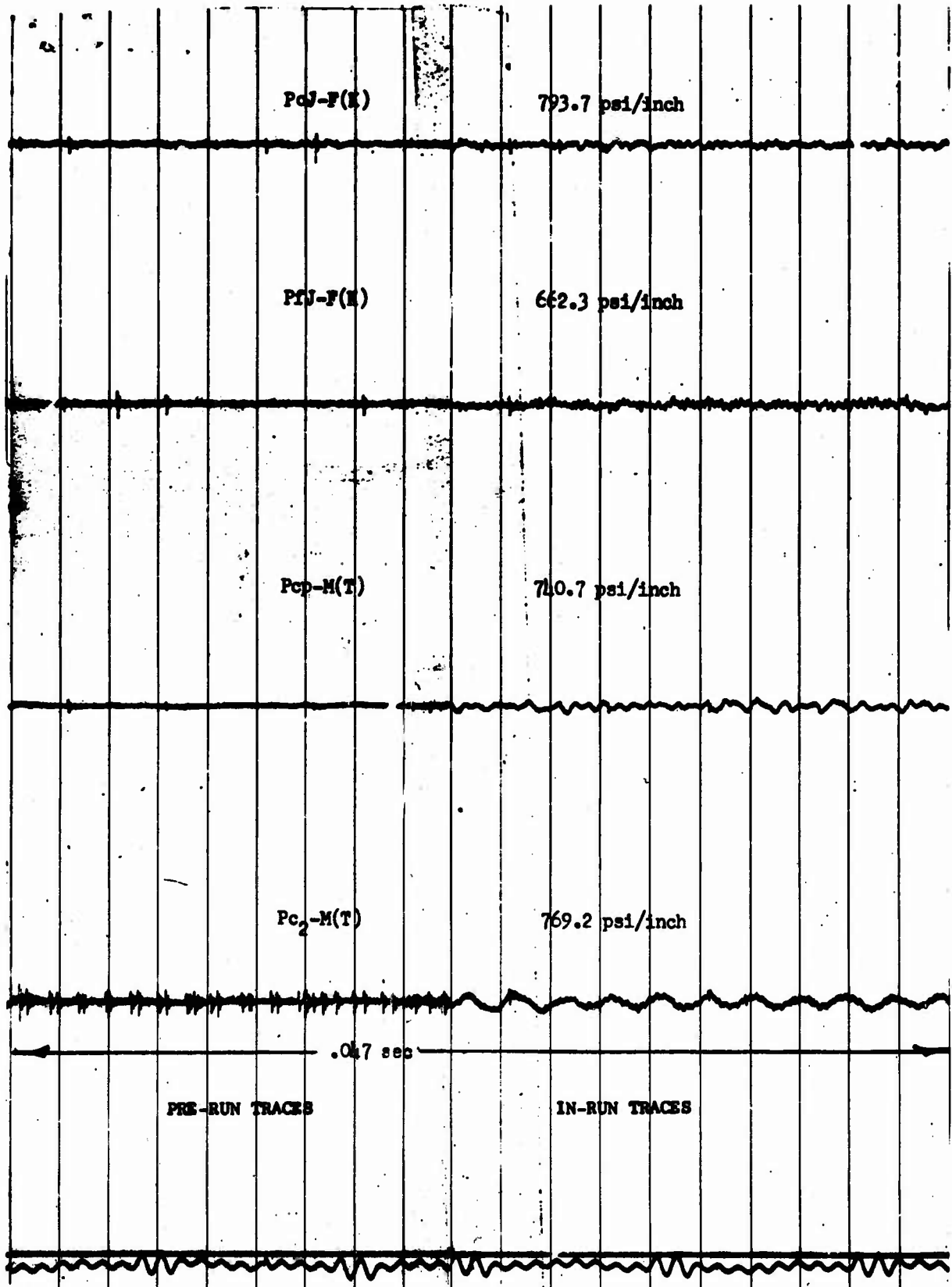
Book Two



Ampex Playback--Concentric Ring (Mod VIIIB) plus Drilled L* Segment

Figure IX-C-5

Book Two



Ampex Playback--Transpiration Cooled Injector

Figure IX-D-1

CONFIDENTIAL

Book Two

X. PRELIMINARY SYSTEM STUDIES

A. PARAMETER STUDY

1. Introduction

The objectives of the preliminary system study is to determine the practical upper limit of chamber pressure and to select the best nozzle area ratio and propellant mixture ratio. The selection of these engine parameters is based upon vehicle performance, cost, and weight. The basic study was conducted for N_2O_4 /AeroZINE 50 propellants. A later study was conducted for some of the metalized storable propellants. Results of this analysis are presented in Section X, F.

A variety of vehicles was analyzed to determine best chamber pressure, area ratio, and mixture ratio. These vehicles incorporate the following variables:

Nozzle Type

DeLaval

Forced deflection (first stages only)

Engine Cycle

Gas generator

Staged combustion

Type of Mission

First stages (ideal velocity increment,
 $V_i = 10,000$ and $20,000$ ft/sec)

Single stage to 300 NM orbit, polar launch

CONFIDENTIAL

Book Two

X, A, Parameter Study (cont.)

To fulfill the objectives of the study, a number of subtasks were necessary. These tasks are described in the following paragraphs:

a. Propulsion System Weight

Propulsion system weights were obtained from analytically derived weight expressions for turbopumps and thrust chambers, combined with existing data from previously designed engine systems (see Section X,B).

b. Performance and Cycle Analysis

Engine performance evaluation includes the determination of engine specific impulse as a function of thrust-chamber pressure, and engine mixture ratio as a function of thrust-chamber mixture ratio. This was completed for both the gas generator and staged-combustion cycles, and is presented in Section X,C.

c. Cost Model

The cost model that was used to study the cost effects of parameter variation is presented in Section X,D.

d. Film-Cooling Effect on Performance

The specific-impulse degradation from film cooling was determined for various percentages of fuel film coolant and injection locations. This analysis is presented in Section X,E. The analysis was completed for three conditions of mixing of the film coolant with the main stream: no mixing, partial mixing, and complete mixing.

CONFIDENTIAL

Book Two

X, A, Parameter Study (cont.)

2. Conclusions

Basic conclusions reached from the preliminary system studies are as follows.

- a. Chamber pressures in the range of 2500 to 3000 psi show a clear gain in performance for the staged-combustion cycle.
- b. The best chamber pressure for a gas-generator cycle engine is approximately 500 to 1000 psi lower than for a staged-combustion cycle engine (N_2O_4 /AeroZINE 50).
- c. Cost effects of increasing chamber pressure were found to be negligible.
- d. The staged-combustion cycle yields significantly higher performance than the gas-generator cycle.
- e. The mixture ratio corresponding to maximum specific impulse will result in maximum vehicle payload.
- f. Optimum nozzle area ratio is independent of the cycle type selected.
- g. The ideally compensating nozzle yields significantly higher performance than the DeLaval nozzle.
- h. Burning of the film coolant does not show performance gain.
- i. Significant payload gains result from the use of high chamber pressures with the advanced propellants studied. In general, the analyses showed

CONFIDENTIAL

Book Two

X, A, Parameter Study (cont.)

that with the staged-combustion cycle, the maximum pressure obtainable is best. With the gas-generator cycle, clear gains up to a chamber pressure of 3000 psi were shown.

3. Analysis and Results

a. Area-Ratio Selection

Stage payload was used as the basis for selecting optimum area ratios; the following effects were included:

- (1) Thrust-chamber specific-impulse variations with chamber pressure and area ratio (see Section X,C). Perfect compensation (nozzle exit pressure equals ambient pressure at all levels of altitude) was assumed.
- (2) Variation of turbopump weight with propellant flow rates and pressure (see Section X,B).
- (3) Change in nozzle skirt weight with area ratio (see Section X,B).
- (4) Change of ideal velocity increment with area ratio (booster and first stage only).
- (5) Thrust-chamber mixture ratio of 2.0.
- (6) 98% combustion efficiency and 97% nozzle efficiency.
- (7) Interstage structure weight was included in upper stages.

CONFIDENTIAL

Book Two

X, A, Parameter Study (cont.)

(8) Constant sea-level thrust of 2,000,000 lb for all booster and single-stage engines and vacuum thrust of 200,000 and 2,000,000 lb for all upper-stage engines.

(9) Constant thrust-to-liftoff-weight ratio of 1.25 for boosters and single-stage vehicles.

(10) Thrust-to-liftoff-weight ratio for upper stages was optimized for each upper-stage velocity increment, and varies with stage velocity increment as follows:

$$V_1 = 10,000 \text{ ft/sec} \quad F/M_{LO} = 1.14$$

$$V_1 = 15,000 \text{ ft/sec} \quad F/M_{LO} = 1.40$$

$$V_1 = 20,000 \text{ ft/sec} \quad F/M_{LO} = 1.72$$

(11) 1% ullage and 1% outage for all stages.

Payloads are all calculated with the following expression

$$M_{PL} = M_{TO} - K_T F_V - \left[1 + K_{out} + (1 + K_{out} + K_{ull}) \frac{K_{AF}}{\rho_B} \right] \left(1 - e^{-\frac{V_1}{g I_{sv}}} \right) M_{LO}$$

where:

- M_{PL} - Payload, lb
- M_{LO} - Liftoff weight, lb
- K_T - Thrust dependent factor (see Section X,D)
- F_V - Vacuum thrust, lb
- K_{out} - Outage factor
- K_{ull} - Ullage factor
- K_{af} - Airframe factor, cu ft/lb (see Section X,4)
- ρ_B - Propellant bulk density, lb/cu ft
- V_1 - Ideal velocity increment, ft/sec
- I_{sv} - Vacuum specific impulse, sec

CONFIDENTIAL

Book Two

X, A, Parameter Study (cont.)

The staged-combustion cycle was used for determining stage payloads. Early effort in this study showed that optimum area ratio was independent of type of engine cycle.

Nozzle surface friction and heat-transfer losses were disregarded in this study. Therefore the best area ratio will be slightly smaller than that indicated by the peak payload points. Area ratios at 1% off peak payload points were selected as optimum; this selection has the effect of decreasing the nozzle length and surface area to account for the effects of heat transfer and friction.

The results of the booster and single-stage studies are presented in Figures X-A-1 through 5.

The optimum area ratio for upper-stage vehicles includes the effects of interstage structure weight and configuration. The following paragraphs describe the method used to account for these effects.

At an instant prior to light-off of the upper stage, the total load on the interstage structure is equal to the light-off weight of the upper stage times the burnout acceleration of the booster. The weight of the interstage structure for a conical or cylindrical configuration is proportional to the load on the structure and to the length of the structure. The thrust of the upper-stage engine is proportional to the throat area and to the chamber pressure. The engine diameter and length are proportional to the square root of the thrust per engine and inversely proportional to the square root of the chamber pressure.

$$W_{iss} \propto P L \quad (\text{Eq 1})$$

$$P = \frac{W_{LO}}{g} a \quad (\text{Eq 2})$$

CONFIDENTIAL

Book Two

X, A, Parameter Study (cont.)

$$F_1 = C_F P_c A_t \quad (\text{Eq 3})$$

$$= C_F P_c \frac{A_e}{\epsilon}$$

$$= C_F P_c \frac{\pi D_e^2}{4 \epsilon}$$

$$D_e = \sqrt{\frac{4 F_1 \epsilon}{\pi C_F P_c}}$$

$$L_e = k \sqrt{\frac{F_1 \epsilon}{P_c}} \quad (\text{Eq 4})$$

where:

- W_{iss} - Weight of interstage structure, lb
- P - Load on structure, lb
- L - Length of structure, ft
- W_{LO} - Light-off weight of upper stage, lb
- a/g - Burnout g's of lower stage
- F_1 - Vacuum thrust per engine, upper stage, lb
- C_F - Vacuum thrust coefficient
- P_c - Chamber pressure, psia
- A_t - Throat area, sq in.
- A_e - Exit area, sq in.
- ϵ - Nozzle area ratio, A_e/A_t
- D_e - Exit diameter, in.
- L_e - Engine length, ft

Also, because the length of the interstage structure will be dependent upon the length of the engine, the result can be written by substituting Equations 2 and 4 into Equation 1 and rearranging,

$$\frac{W_{iss}}{W_{LO}} = K \frac{F_1}{P_c} \quad (\text{Eq 5})$$

where K includes $\left(\frac{a}{g}\right)_{Bo}$ of the booster.

CONFIDENTIAL

Book Two

X, A, Parameter Study (cont.)

The factor K was determined for several existing vehicle designs including Titan and Saturn. The value used in this analysis is 56.2×10^{-6} . Although increasing upper-stage velocity increment indicates that the lower stage burns out at a lower thrust-to-weight ratio, the above load factor was held constant for simplicity.

The optimized thrust-to-light-off-weight ratio (F/W_{LO}) varies with stage velocity increment. The weight of the interstage structure varies directly with stage light-off weight. Therefore, when the interstage structure is considered, optimum area ratio varies with both thrust level and velocity increment.

The analysis was conducted for velocity increments of 10,000, 15,000, and 20,000 ft/sec, and for thrust levels of 200,000 and 2,000,000 lb. Results are shown in Figures X-A-3 through -5. It can be seen that optimum area ratio increases with increased velocity increment but decreases with increased thrust level. It is also significant to note that the interstage structure has an increasingly greater effect upon optimum area ratio with increasing thrust level.

b. Selection of Best Thrust-Chamber Pressure

The selection of the best thrust-chamber pressure is based upon maximum vehicle payload capability because the effect of chamber pressure upon cost was shown to be insignificant (see Section X,D). Using the previously optimized area ratios and a thrust-chamber mixture ratio of 2.0, vehicle payloads were calculated and plotted over a range of thrust-chamber pressures. Results are shown in Figures X-A-6 through -11.

Chamber pressures selected are presented in the following table:

CONFIDENTIAL

Book Two

X, A, Parameter Study (cont.)

FIRST- AND SINGLE-STAGE VEHICLES

<u>Nozzle</u>	<u>Cycle</u>	<u>Mission</u>		<u>Single-Stage 300-NM Orbit</u>
		<u>10,000 ft/sec</u>	<u>20,000 ft/sec</u>	
DL	GG	4500 psia	4400 psia	3500 psia
DL	S-C	3600*	3600*	3300
F-D	GG	3200	3000	3000
F-D	S-C	3600*	3500	3300

UPPER-STAGE VEHICLES

<u>Nozzle</u>	<u>Cycle</u>	<u>10,000 ft/sec</u>	<u>15,000 ft/sec</u>	<u>20,000 ft/sec</u>
DL	S-C	3600* psia	3600* psia	3600* psia
DL	GG	2800	2800	2800

The figures with asterisks represent values limited by the maximum chamber pressure attainable with the staged-combustion cycle at a turbine inlet temperature of 1200°F. This limit of chamber pressure can be increased by increasing the turbine inlet temperature.

c. Selection of Best Thrust-Chamber Mixture Ratio

After establishing the best area ratio and thrust-chamber pressure for each mission at a thrust-chamber mixture ratio of 2.0, this mixture ratio was then varied from 1.6 to 2.4 and single-stage payloads were calculated for each point. The results shown in Figure X-A-12 show that, except for very small variations in maximum payload (less than 1%), the optimum thrust-chamber mixture ratio does not depend upon engine configuration or cycle but corresponds to the maximum specific-impulse mixture ratio of approximately 2.1. Because payload variations with mixture ratio will decrease as total mission velocity decreases,

CONFIDENTIAL

Book Two

X, A, Parameter Study (cont.)

it was not necessary to perform a mixture-ratio optimization study for lower-velocity missions. It can be concluded that maximum specific-impulse mixture ratio is optimum from a payload standpoint for all missions.

d. Cost Effects

The influence of cost on the selection of parameters is discussed in this section. The cost model presented in Section X,D was used for these analyses.

The major elements are classified as development, production, and facility costs; these are discussed in the following paragraphs. It will be shown that the optimum parameters selected on the basis of payload are also very nearly optimum from the standpoint of cost per pound of payload.

(1) Development Costs

The major development costs can be placed under one of the three following categories: (1) engineering, fabrication, and testing, (2) facilities, or (3) propellants.

A careful analysis was made to determine what effect increased pressure would have upon these costs. After the present high-pressure experimental programs are completed, there should be no increase in development difficulty with increases in pressure. The only cost difference, then, is in the high-pressure testing facilities. The facilities affected are the run tanks for thrust-chamber development. Conventional pressure thrust chambers are fed from pressurized tanks, whereas it has been found to be more economical to use low-pressure tanks and test-stand pumps for high-pressure testing. A comparison has been made at 100,000-lb thrust in connection with Contract AF 04(611)-8017. Run tank costs for various pressures are summarized as follows:

CONFIDENTIAL

Book Two

X, A, Parameter Study (cont.)

<u>Pressure, psi</u>	<u>Relative Cost</u>
5000	1.0
1800	0.5
200	0.4

An 1800-psi run tank would be used for conventional engine thrust-chamber testing. The 200-psi tanks would be combined with turbopumps for high-pressure testing. The turbopump would cost approximately \$500,000 to develop and \$100,000 per unit thereafter. In addition, there may be some turbopump maintenance during the program. Turbopumps of this type should have very long life expectancy. Therefore, 100 thrust-chamber tests per turbopump set should be easily attainable. For a program of 1000 thrust-chamber assembly tests, 10 sets of turbopumps would be adequate. The total costs for run tanks would be \$1,200,000 (three test stands) for conventional-pressure tests and \$1,900,000 for high-pressure tests. This difference is negligible when compared with the overall development program costs of \$100,000,000.

(2) Production Costs

These costs will be treated with reference to figures evolved for NASA Contract NAS 5-1025, "Design Study of a Large Unconventional Liquid Propellant Rocket Engine and Vehicle." In this study, both low-pressure conventional engines and high-pressure advanced engines were designed and costs were determined at the 2,000,000-lb-thrust level using LO_2/LH_2 as a propellant.

There are several major components of the engine that are affected by increases in thrust-chamber pressure: (1) thrust-chamber assembly (including the injector), (2) turbopump assembly, (3) gas generator, and (4) valves and lines.

Increases in thrust-chamber pressure result in decreases in the physical size of the chamber and, hence, decreases in the cost. The injector

CONFIDENTIAL

Book Two

X, A, Parameter Study (cont.)

must become simpler because higher thrust per element is needed to achieve higher injection density. This simplicity will result in lower production costs. The effects of the various thrust-chamber cooling methods comprise the experimental objective of this contract and consequently will not be considered in this discussion.

The pressure effect on the turbopump assembly dictates the necessity for inducers; the physical size of the main stage decreases with increasing pressure, and the main-stage pressure balance becomes more critical. The effects in the main-stage portion tend to cancel out; therefore, the net cost difference is attributable entirely to the inducers.

In the gas generator, increases in pressure bring about increases in flow. This increase in flow is offset by the accompanying increase in density, with the result that the volume flow remains approximately constant. Under these conditions, the size and cost remain unaffected by changes in pressure.

There are only slight pressure effects in the valves and lines. The valves may require somewhat closer tolerances in the seats, and the lines would require thicker walls. Cost influences are negligible for these components.

The main production cost differences lie in the turbopumps and the injectors.

Cost figures derived during the performance of Contract NAS 5-1025 place the turbopump cost for a 2,000,000-lb-thrust 1000-psia chamber pressure engine at \$150,000. A high-pressure gas-generator-driven turbopump would be similar to the low-pressure turbopump except that two inducers would be added. This would result in six major rotating components in the high-pressure turbopump (two inducers, two main-stage pumps, and two turbines) as compared with four major components at 1000-psia chamber pressure (two main-stage pumps and two turbines).

CONFIDENTIAL

Book Two

X, A, Parameter Study (cont.)

Assuming that the cost of each major rotating component is about the same, the high-pressure turbopump for a gas-generator cycle engine will cost half as much more than for a conventional pressure engine. This results in a turbopump cost increase of \$75,000 for high-pressure operation. By comparison, the turbopump cost for the same basic system but with the advanced engine which incorporates chamber pressure of 2500 psia was also costed in Contract NAS 5-1025 and is \$165,000. The advanced engine turbopump is simpler, however, because it has only two turbine wheels, and both main-stage pumps are on a common shaft. Tending to increase the system cost are the oxidizer inducer and the second hydrogen pump stage.

Injector costs were also estimated for the 2,000,000-lb-thrust LO_2/LH_2 conventional and advanced engines. The estimated injector cost for the conventional engine is \$110,000. The estimated cost for the eight injectors in the advanced (high-pressure) engine is \$17,600. This significantly lower cost results from the smaller size and fewer injection elements, both of which result from the higher pressure.

The net result of the above costs indicate that a high-pressure engine would cost approximately \$9,000 less than a conventional engine. The total engine cost is approximately \$600,000. Because the difference is only 1- $\frac{1}{2}$ %, it can be concluded that thrust-chamber pressure has only a negligible effect upon production costs.

(3) Facility Costs

Facility and propulsion cost variations with thrust-chamber pressure have been shown to be negligible (Section X,D). Therefore, the variation in vehicle cost with chamber pressure will also be negligible, and the optimum chamber pressure will correspond to the chamber pressure which yields maximum payload.

CONFIDENTIAL

Book Two

X, A, Parameter Study (cont.)

Selection of the best mixture ratio was also determined on the basis of cost per pound of payload. The only cost element that varies significantly with mixture ratio is the cost of propellant. Because the cost of AeroZINE 50 is greater than N_2O_4 , the propellant cost decreases with increases in mixture ratio. However, this cost change with mixture ratio represents only a small percentage of the total vehicle program cost. The results given in Figure X-A-13 show that on the basis of cost, the optimum mixture ratio is approximately 2.2. The results also indicate optimum mixture ratio is independent of nozzle type and engine cycle.

e. Effect of Film Cooling on Engine Parameters

An analysis was conducted to determine the effect of various percentages of film cooling on vehicle payload.

Specific-impulse degradation data were based on an average between no mixing and partial mixing losses and then adjusted for differences in area ratios and thrust-chamber pressures (see Section X,E). The area ratio at each pressure is the optimum selected for an engine without film cooling. The injector mixture ratio is 2.1--the optimum selected on the basis of the performance study. Four film coolant decomposition points were assumed with equal amounts of coolant decomposing at each point. The main stream pressures at these points were 100, 83.3, 10, and 2% of the thrust-chamber pressure, respectively. The coolant was assumed to decompose at the pressure of the main stream at each point. Results of this analysis are shown in Figures X-A-14 and -15. These results include cycle effects of additional fuel flow as well as specific-impulse effects and reflect the change in injector mixture ratio from the 2.0 used in the performance study.

In Figures X-A-14 and -15, the performance curves for the gas-generator cycle do not show the marked divergence at higher thrust-chamber pressures that is shown for the staged-combustion cycle. This lack of divergence results because the required pump discharge pressure does not vary with different percentages of film cooling for the gas-generator cycle as it does for the staged-combustion cycle.

CONFIDENTIAL

Book Two

X, Preliminary System Studies (cont.)

B. PROPULSION SYSTEM WEIGHT STUDY

1. Engine Weight

A method for determining engine weight was derived. Using this method, engine weight can be determined from nozzle throat area, nozzle area ratio, chamber pressure, nozzle type (DeLaval or forced deflection), mixture ratio, and oxidizer and fuel turbopump flow rates.

The engine was divided into two major components to perform the weight analysis: the turbopump assembly (TPA) and the engine less the TPA weights. The basic independent variables selected for the TPA weight are propellant flow rate and discharge pressure and propellant density. TPA weights are shown in Figure X-B-1. These weights are based upon parametric analyses combined with several existing and designed TPAs, also tabulated in Figure X-B-1.

Engine less TPA weights are presented in Figure X-B-2. Thrust-chamber throat area and pressure were chosen as the independent variables; the weight curves were developed for a constant nozzle exit area. Nozzle weight--area ratio variation was calculated and plotted for DeLaval and forced-deflection nozzles (Figures X-B-2, -3 and -4). The method and assumptions used to determine these weights are discussed below.

a. TPA Weight

Turbopump weight relationships were established using previously designed turbopump system data coupled with analytical expressions relating pump impeller mean diameter to pressure, flow, speed and fluid density. The results of this study are shown in Figure X-B-1. Pump flow rate and pressure were selected as the independent variables.

b. Engine Less the TPA Weight

Engine less TPA weights are based upon two assumptions. First, cooling tube wall thickness is constant. Secondly, weight differences of the gas

CONFIDENTIAL

Book Two

X, B, Propulsion System Weight Study (cont.)

generators, combustion chambers, injectors and manifolds are insignificant at the same flow rate with changes in chamber pressure, as pressure vessel criteria are approximated. Using these assumptions, the engine less TPA weights will be identical for different chamber pressures, provided that the nozzle exit area does not vary. The assumption of constant tube wall thickness is based upon previous heat-transfer studies that indicate that a minimum tube wall thickness is desirable regardless of chamber pressure. This can be accomplished if tube diameter is reduced as pressure is increased. If construction materials other than tubes are used, there may be significant weight differences with pressure. In this event the weight curves will be changed accordingly.

The nozzle exit area maintained in the weight study is that obtained with a nozzle area ratio of 30 and a chamber pressure of 1000 psia. For this exit area, the area ratio at chamber pressures of 2000, 3000, 4000, and 5000 psia are 60, 90, 120, and 150, respectively.

At these small nozzle exit areas the engine less TPA weight difference is negligible for DeLaval and forced-deflection nozzles.

The nozzle weights were based upon contours resulting in an average velocity vector angle at the nozzle exit of 10° . This represents a nozzle exit half-angle of approximately 8° .

To determine engine weights at area ratios other than those assumed in the engine less TPA weight study, a nozzle weight--area ratio relationship was established. Figures X-B-2, -3 and -4 present the change in nozzle weight divided by chamber pressure and throat area as a function of area ratio change, based upon a 1000-psia chamber pressure. Using the equation shown on the figures, the curve can be used for other chamber pressures.

CONFIDENTIAL

Book Two

X, B, Propulsion System Weight Study (cont.)

These nozzle weights are based upon contours that produce an average exit velocity vector angle of 8° . This selection was based upon previous studies which indicate the payload of 8° nozzles are 1 to $1\frac{1}{2}\%$ greater than for 10° nozzles. For this reason, 8° was the basis for nozzle weight in this study.

2. Airframe Weight

Stage airframe weight (stage inert weight excluding the engine) is calculated from inert weight parameters (K_T , K_{AF}), which were established in previous weight studies (Aerojet-General Contract NAS 5-1025). The inert weight parameters for N_2O_4 /AeroZINE 50 are:

	<u>Single Stages</u>	<u>First Stages</u>	<u>Upper Stages</u>
K_T	0.0070	0.00845	0.0072
K_{AF}	0.813	0.813	0.913

Using these weight parameters, stage airframe weight can be calculated by the following formula:

$$M_{(inert)} = (KT)(FV) + (KAF)(VPT)$$

where: KT - Thrust dependent inert weight factor (excluding the engine)

FV - Vacuum thrust, lb

KAF - Volume-dependent inert weight factor, lb/cu ft

VPT - Total propellant tank volume, cu ft

These inert weight parameters were used for the vehicle performance analysis.

CONFIDENTIAL

Book Two

X, Preliminary System Studies (cont.)

C. CYCLE ANALYSIS

The purpose of this analysis is to determine performance degradation pressure drops, and engine mixture ratios for gas-generator and staged-combustion cycle engine systems. Performance degradation is defined herein as the difference between thrust-chamber specific impulse and overall engine specific impulse. Engine system pressure drop determinations yield the relationship of pump discharge pressure to thrust-chamber pressure. This, in turn, is used to establish turbopump weights. Engine mixture ratio is the ratio of engine oxidizer flow to engine fuel flow, and differs from thrust-chamber mixture ratio for the gas-generator cycle because of the low-mixture-ratio gas generator.

A list of symbols for cycle analysis is shown in Figure X-C-1.

1. Performance Degradation

a. Gas-Generator Cycle

A schematic of gas-generator cycle engine is shown in Figure X-C-2. The oxidizer and fuel turbopump assembly are driven by a single bipropellant gas generator. The gas-generator propellants are tapped from the main pump discharge lines, injected into the generator, and burned. After passing through the turbine, the gases are expanded through a nozzle, providing additional thrust. Performance degradation of the gas-generator cycle is a result of the low specific impulse associated with these turbine exhaust products. Figure X-C-3 is a plot of performance degradation versus thrust-chamber specific impulse for a N_2O_4 /AeroZINE 50 gas-generator cycle engine. The following analysis shows the development of this curve:

CONFIDENTIAL

Book Two

X, C, Cycle Analysis (cont.)

I_s degradation (I_{s_D}) is given by

$$I_{s_D} = I_{s_{TC}} - I_{s_E} \quad (\text{Eq 1})$$

$$I_{s_E} = \frac{(\dot{w}_{o_{TC}} + \dot{w}_{f_{TC}}) I_{s_{TC}} + (\dot{w}_{o_{GG}} + \dot{w}_{f_{GG}}) I_{s_{TE}}}{(\dot{w}_{o_{TC}} + \dot{w}_{f_{TC}}) + (\dot{w}_{o_{GG}} + \dot{w}_{f_{GG}})}$$

These equations can be combined into the following form

$$I_{s_D} = \frac{I_{s_{TC}} - I_{s_{TE}}}{\frac{\dot{w}_{f_{TC}}}{\dot{w}_{f_{GG}}} \frac{(1 + MR_{TC})}{(1 + MR_{GG})} + 1} \quad (\text{Eq 2})$$

The three unknown in this expression are $I_{s_{TC}}$, $I_{s_{TE}}$ and $\frac{\dot{w}_{f_{TC}}}{\dot{w}_{f_{GG}}}$. These are determined as described in Paragraphs (1), (2), and (3) below.

(1) Determination of $\frac{\dot{w}_{f_{TC}}}{\dot{w}_{f_{GG}}}$

The relation of gas-generator flow to thrust-chamber flow is found by equating pump horsepower requirements to turbine power output. The pump horsepower requirements are

$$SHP_o = \frac{H_o (\dot{w}_{o_{TC}} + \dot{w}_{o_{GG}}) K_{ind}}{550 \eta_o} \quad (\text{Eq 3})$$

$$SHP_f = \frac{H_f (\dot{w}_{f_{TC}} + \dot{w}_{f_{GG}}) K_{ind}}{550 \eta_f} \quad (\text{Eq 4})$$

The K_{ind} is an assumed value which provides for the additional horsepower requirements of a hydraulic, turbine-driven inducer if used.

CONFIDENTIAL

Book Two

X, C, Cycle Analysis (cont.)

Turbine power output is expressed by

$$(\dot{w}_{o_{GG}} + \dot{w}_{f_{GG}}) (C_p \Delta T \frac{J}{550} \eta_T) \quad (\text{Eq 5})$$

Equating pump requirements to turbine output gives

$$\frac{H_o (\dot{w}_{o_{TC}} + \dot{w}_{o_{GG}}) K_{ind}}{550 \eta_o} + \frac{H_f (\dot{w}_{f_{TC}} + \dot{w}_{f_{GG}}) K_{ind}}{550 \eta_f} = (\dot{w}_{o_{GG}} + \dot{w}_{f_{GG}}) C_p \frac{\Delta T J}{550} \eta_T \quad (\text{Eq 6})$$

For a given pump discharge pressure, thrust-chamber pressure can be found from Figure X-B-7. The following terms are defined for ease of manipulation of Equation 4.

$$\frac{H_o K_{o_{ind}}}{550 \eta_o} = K_1$$

$$\frac{H_f K_{f_{ind}}}{550 \eta_f} = K_2$$

$$\frac{C_p \Delta T \eta_T}{550} = K_3$$

Substituting K_1 , K_2 , and K_3 into Equation 4 gives

$$K_1 (\dot{w}_{o_{TC}} + \dot{w}_{o_{GG}}) + K_2 (\dot{w}_{f_{TC}} + \dot{w}_{f_{GG}}) = K_3 (\dot{w}_{o_{GG}} + \dot{w}_{f_{GG}})$$

CONFIDENTIAL

Book Two

X, C, Cycle Analysis (cont.)

which can be written as follows

$$\frac{\dot{w}_{f_{TC}}}{\dot{w}_{f_{GG}}} = \frac{MR_{GG} (K_3 - K_1) + (K_3 - K_2)}{MR_{TC} (K_1) + K_2} \quad (\text{Eq 7})$$

(2) Determination of $I_{s_{TC}}$

Thrust-chamber specific-impulse values are obtained from computer calculations based upon shifting equilibrium flow of the combustion products (Figure X-C-4). The thrust-chamber specific impulse obtained from this curve represents a thermochemical energy level of the combustion products. This energy level does not include energy put into the propellants by the pumps. Consequently, the actual energy level (or specific impulse) of the combustion products is somewhat higher than that which the computer thermochemical data predicts. The correction is calculated as follows:

By applying a momentum equation, it can be shown that

$$I_s = \frac{\lambda v_e}{g} \quad (\text{Eq 8})$$

From an energy equation for flow through a nozzle

$$v_e = \sqrt{2g\Delta h} \quad (\text{Eq 9})$$

Substituting Equation 8 into 9 gives

$$I_s = \frac{\lambda}{g} (2g\Delta h)^{1/2} \quad (\text{Eq 10})$$

CONFIDENTIAL

Book Two

X, C, Cycle Analysis (cont.)

The change in specific impulse for a change in Δh can be found by taking the first derivative of Equation 10 with respect to Δh .

$$dI_s = \frac{\lambda}{\sqrt{2g}} \frac{d\Delta h}{(\Delta h)^{1/2}} \quad (\text{Eq 11})$$

Substituting Equation 11 into Equation 10 gives

$$dI_s = \frac{\lambda^2}{g} \frac{d(\Delta h)}{I_{s_{TMC}}} \quad (\text{Eq 12})$$

where $I_{s_{TMC}}$ is the specific impulse resulting from thermochemical energy along

$d(\Delta h)$ is the energy per pound of propellant added by the pumps through the shaft.

$$d(\Delta h) = \left[\frac{H_f}{\eta_f} + \frac{H_o}{\eta_o} MR_{TC} \right] \times \frac{1}{1 + MR_{TC}} \quad (\text{Eq 13})$$

Finally, substituting Equation 13 into Equation 12 gives

$$dI_s = \frac{\lambda^2 \left[\frac{H_f}{\eta_f} + \frac{H_o}{\eta_o} MR_{TC} \right]}{g I_{s_{TMC}} (1 + MR_{TC})} \quad (\text{Eq 14})$$

Therefore, the $I_{s_{TC}}$ that is used in Equation 2 is the thermochemical $I_{s_{TMC}}$ obtained from Figure X-C-4 plus the $d I_{s_{PW}}$ calculated using Equation 14. A plot of $d I_{s_{PW}}$ versus $I_{s_{TC}}$ for various thrust-chamber pressures is shown in Figure X-C-5.

CONFIDENTIAL

Book Two

X, C, Cycle Analysis (cont.)

(3) Determination of $I_{s_{TE}}$

From the definition of specific impulse it can be shown that

$$I_{s_{TE}} = \frac{C_F c^*}{g} \quad (\text{Eq 15})$$

where c^* (characteristic velocity) is calculated using turbine exit properties and C_F is established for whatever nozzle is used. In this analysis, optimum expansion at sea level and frozen equilibrium conditions were assumed.

(4) Procedure for Calculating Engine Specific Impulse

All required expressions for the calculation of engine specific-impulse degradation using Equation 2 have now been derived. The degradation results are shown in Figure X-C-3. Using Figures X-C-3, -4, and -5, optimum sea-level engine specific impulse for the gas-generator cycle can now be determined as follows:

- (a) At the given P_c obtain $I_{s_{TMC}}$ from Figure X-C-4.
- (b) With the $I_{s_{TMC}}$ obtained in Step 1, determine $d I_{s_{PW}}$ pump work using Figure X-C-5.
- (c) Add the $d I_{s_{PW}}$ to the $I_{s_{TMC}}$. Using this number and the given P_c , refer to Figure X-C-3 and read the I_{s_D} degradation.
- (d) The engine I_{s_E} is then $I_{s_E} = I_{s_{TMC}} + d I_{s_{PW}} - I_{s_D}$.

CONFIDENTIAL

Book Two

X, C, Cycle analysis (cont.)

A plot of engine I_{s_E} at optimum sea-level expansion versus chamber pressure for various thrust-chamber mixture ratios is shown in Figure X-C-6. This curve is developed by following the above procedure for several thrust-chamber mixture ratios and chamber pressures. A similar curve can be readily developed for vacuum specific impulse.

b. Staged-Combustion Cycle

The staged-combustion cycle (shown schematically in Figure X-C-7) consists of a gas-generator-driven turbine with the turbine exhaust injected into the thrust chamber. Because the turbine exhaust is expanded through the main thrust chamber, the staged-combustion cycle engine specific impulse is equal to the thrust-chamber specific impulse. Also, there is no effect of pump work upon specific impulse because whatever energy is input in the system by the pumps is thus removed by the turbine. Therefore staged-combustion cycle engine specific impulse is equal to thermochemical specific impulse as predicted by the computer (Figure X-C-4). It is recognized that there is an entropy increase in this system because of the irreversible processes resulting from pump and turbine inefficiencies and line losses. However, this is reflected in the pressure drop between the pump discharge and the main combustor resulting in a lower pressure ratio for a given engine exit area. Therefore, the entropy increase is automatically included when specific impulse is calculated for the actual nozzle area ratio.

2. Pressure Drops

a. Gas-Generator Cycle

Pump discharge pressure as a function of chamber pressure is shown in Figure X-C-8 for the gas-generator cycle. The tabulated pressure drops and their variation with chamber pressure are presented in Figure X-C-8. The curves shown in this figure are independent of thrust level.

CONFIDENTIAL

Book Two

X, C, Cycle Analysis (cont.)

The fuel pressure drop through the coolant jacket, approximately 200 psi, was based upon the Titan LR87-AJ-5 engine. To scale this pressure drop to other chamber pressures, it was estimated that half of the 200-psi drop results from coolant-tube "turn-arounds" and splits in the combustion chamber and throat section as well as the "straight-line" tube pressure drop in the skirt section. This pressure drop will remain approximately constant at all chamber pressures. The remaining 100-psi drop is caused by the coolant tubes in the throat and combustion chamber section. With increasing chamber pressure at constant thrust, combustion chamber size will decrease and heat-transfer coefficients will increase. Coolant velocity must therefore be increased. As a result, the pressure drop in these areas is increased with increases in chamber pressure. For scaling purposes, the pressure drop was assumed to be directly proportional to chamber pressure.

$$\Delta P \text{ Coolant Jacket} = 100 + 100 \frac{P_c}{P_{c\text{Titan}}}$$

b. Staged-Combustion Cycle

The main factor affecting a staged-combustion cycle pressure schedule is turbine pressure ratio. Increased thrust-chamber pressure can be provided only at the expense of the turbine pressure ratio. Figure X-C-9 shows the relationship of chamber pressure to pump discharge for a N_2O_4 /AeroZINE 50 staged-combustion engine. The maximum chamber pressure obtainable with this engine for the given gas-generator mixture ratio is approximately 3900 psia. This "peaking" of the chamber pressure results from the fact that a point has been reached where any incremental change in pump discharge is more than overcome by the attendant pressure ratio increase needed by the turbine to develop that additional pump discharge pressure. Higher chamber pressures can be reached only by increasing the turbine inlet temperature, i.e., changing the gas-generator mixture ratio, thus increasing the energy per pound of drive gas. Shown on Figure X-C-9 are the assumed pressure drops used in obtaining the curve. The derivation of the analytical expression used in determining the turbine pressure ratio follows.

CONFIDENTIAL

Book Two

X, C, Cycle Analysis (cont.)

The turbine pressure ratio is related to the temperature ratio by

$$P_1/P_2 = (T_1/T_2)^{K/K-1}$$

The temperature drop across the turbine is calculated from the required isentropic spouting velocity (C_o).

$$C_p (T_1 - T_2) = \frac{C_o^2}{2g \times 778}$$

The isentropic spouting velocity is also related to the energy required to deliver the necessary horsepower, as follows:

$$\dot{w}_{GG} \frac{C_o^2}{2g} = \frac{SHP_T \times 550}{\eta_T}$$

where \dot{w}_{GG} is the turbine flow rate and η_T is the turbine efficiency.

The total shaft horsepower is given by the sum of the pump horsepowers.

$$SHP_T = \frac{\dot{w}_{ox} H_{ox} K_{ind, ox}}{550 \eta_{pox}} + \frac{\dot{w}_f H_f K_{ind, f}}{550 \eta_{pf}}$$

K_{ind} accounts for the additional power requirements of the hydraulically driven inducer.

CONFIDENTIAL

Book Two

X, C, Cycle Analysis (cont.)

3. Engine Mixture Ratio

a. Gas-Generator Cycle

Engine mixture ratio is defined as engine oxidizer flow divided by engine fuel flow.

$$\begin{aligned}
 MR_E &= \frac{\dot{w}_{oTC} + \dot{w}_{oGG}}{\dot{w}_{fTC} + \dot{w}_{fGG}} \\
 &= \left[\frac{\frac{\dot{w}_{oTC}}{\dot{w}_{fTC}} + 1}{\frac{\dot{w}_{oGG}}{\dot{w}_{fGG}} + 1} \right] \frac{\dot{w}_{oGG}}{\dot{w}_{fGG}} \\
 &= \left[\frac{\frac{\dot{w}_{fTC}}{\dot{w}_{fGG}} \frac{MR_{TC}}{MR_{GG}} + 1}{\frac{\dot{w}_{fTC}}{\dot{w}_{fGG}} + 1} \right] MR_{GG}
 \end{aligned}$$

An expression for $\frac{\dot{w}_{fTC}}{\dot{w}_{fGG}}$ has already been derived. Using the above expression, the relationship of MR_E versus MR_{TC} for a N_2O_4 /AeroZINE 50 staged-combustion cycle has been established (Figure X-C-10).

b. Staged-Combustion Cycle

For the staged-combustion cycle, engine mixture ratio is equal to thrust-chamber mixture ratio.

CONFIDENTIAL

Book Two

X, Preliminary System Studies (cont.)

D. COST MODEL

1. Introduction

The cost model contains major areas of propulsion costs as a function of the most important parameters. Costs apply to stages using conventional and advanced engines. This cost model contains the elements delineated as follows.

a. Development

(1) Engine

Figure

(a) Engineering

(b) Fabrication

(c) Testing

(d) R&D Tooling

(e) Propellants

(f) Facilities (R&D and production)

(g) GSE

(h) Production tooling

X-D-1

X-D-2

X-D-3

X-D-4

X-D-5

CONFIDENTIAL

Book Two

X, D, Cost Model (cont.)

(2) Airframe

Figure

(a) Engineering and project control

(b) Tooling

(c) Hardware

(d) Stand operation

(e) Propellant

X-D-6

b. Production

(1) Engine

X-D-7

(a) Fabrication and assembly

(b) Acceptance testing

X-D-8

(2) Airframe

(a) Fabrication

(b) Assembly

(c) Checkout

(d) Testing

(e) Miscellaneous items

(f) Transportation

X-D-9

X-D-10

CONFIDENTIAL

Book Two

X, D, Cost Model (cont.)

(3) Launch Support	<u>Figure</u>
(a) Stage checkout	X-D-11
(b) Range time	
(4) Propellants	X-D-12

Sources and justification for each of these elements as well as rationalization of the parametric variations of these cost follow.

2. Development Costs

a. Engine Development

(1) Engineering, Fabrication, Testing, R&D Tooling

The costs in Figure X-D-1 include all engine contractor costs (and fee) through engine qualification for the areas listed. Costs are based upon detailed engine cost studies at 2,000,000- and 24,000,000-lb sea-level thrust levels. These costs were partially established under Contract NAS 5-1025 and under recent cost studies.

The cost difference between conventional and advanced engines is negligible at thrust levels of 1,000,000 lb and less. However, at higher thrust levels, the advanced engine (multiple thrust chambers, single pump) becomes less expensive. The reason for the cost difference is that the advanced engine thrust-chamber development is conducted at a lower thrust level because of its clustered configuration. The largest cost saving results from the injector fabrication. This component becomes very costly to fabricate and test for high thrust levels.

CONFIDENTIAL

Book Two

X, D, Cost Model (cont.)

Engine development cost increases by a rate which is considerably less than the rate of thrust increase. This is rationalized as follows:

If the same type of development program was maintained as the thrust level was increased, development hardware and testing costs would increase substantially, but engineering costs would remain constant. However, as hardware and testing costs increase, it becomes economical to increase engineering effort to reduce the number of tests and, therefore, the amount of development hardware required. For each thrust level, an optimum division of effort exists. This shift of effort for an optimum program results in the development cost increase with thrust level shown in Figure X-D-1.

(2) Propellant for Engine Development

Propellant requirements for engine development are shown in Figure X-D-2. These requirements are based upon typical engine test schedules. The reduction in propellant per pound of thrust reflects the assumption that, as engines become larger and hardware and testing become more expensive, greater emphasis is placed upon engineering analysis for the solution of problems.

(3) Facilities

At 2,000,000-lb thrust, minor modification of existing or planned facilities are adequate for vehicle development, production, and launch. As thrust is increased, available facilities diminish. Then, at approximately 6,000,000- to 8,000,000-lb thrust, completely new facilities are required. Figure X-D-3 presents costs based upon all new facilities. This new facility combines engine and airframe development, production, and launch capabilities as follows:

CONFIDENTIAL

Book Two

X, D, Cost Model (cont.)

- (a) Administration and general plant services
- (b) Four combination engine and stage test and launch stands (two additional test stands are required for conventional engines because of higher produced thrusts of the TCA tests)
- (c) One turbopump assembly two-position test stand
- (d) Three control rooms including instrumentation
- (e) Battleship-type run tanks
- (f) Propellant storage tank
- (g) Fabrication and assembly plant
- (h) Land acquisition and development

Each test stand will have a set of battleship-type run tanks. For these large thrust level vehicles it was assumed that the airframe will be developed concurrently with the engine. Prior to the engine tests, battleship-type tanks will have been fabricated and cold-flow tested.

During the engine testing program, several stage sub-systems will also be qualified (i.e., pressurization system, propellant utilization system, and roll-control system). Development of the flight-weight stage will begin after the bulk of the engine tests have been completed.

The test stands will have launch capability. This permits stage build-up and testing without requiring the moving of the stage.

(4) Ground Support Equipment

The ground support equipment development costs in Figure X-D-4 include all transportation trailers, installation fixtures, special tools, ground checkout consoles, ground power supply, and any other special equipment required for engine operations.

CONFIDENTIAL

Book Two

X, D, Cost Model (cont.)

The cost of fabricating a sufficient number of units to support the production engine program is also included. The major variable in ground support equipment costs are transportation containers, trailers, and installation fixtures. Other costs, such as special tools and checkout consoles, do not change as the thrust level increases.

(5) Engine Production Tooling

The cost of equipment to initiate engine production is included in Figure X-D-5. Some of the R&D tooling included in engine development cost may be applied to engine production. However, there are additional production machines and fixtures that must be added.

b. Airframe Development

Costs included in airframe development cover the engineering, project control, tooling, and hardware expended for qualification of airframe components, test area operation, and propellants. Manpower requirements, costs, and schedules were developed from conferences with The Martin Company. The costs shown in Figure X-D-6 include only one delivered stage. Other stages are charged under production costs. Costs are for a 92-month program. This represents 72 months after delivery of the first unit.

Development cost appears to have minor dependence upon thrust because major costs are incurred from project management, functions which do not vary with the size of the stage. Therefore, the stage development cost changes only slightly with thrust level.

CONFIDENTIAL

Book Two

X, D, Cost Model (cont.)

3. Production Costs

a. Engine Production

(1) Fabrication and Assembly

The costs shown in Figure X-D-7 include raw materials, fabrication (or outside purchase of components), inspection, and quality control of all components, engine assembly, support engineering, overhead (general and administrative), and contractor's fees.

Figure X-D-7 was prepared by plotting known cumulative average production costs of 100 units for the Titan engines and several recently proposed engines as functions of thrust level. Engine costs at other production quantities can be determined by using a learning curve of 85%. The costs for a 2,000,000-lb-thrust booster engine, as well as a 6,000,000-lb thrust engine, were also used.

Figure X-D-7 shows a substantial reduction in engine production cost-per-pound of thrust as thrust is increased. This results because there are a substantial number of fixed costs in production such as inspection, support engineering, and quality control.

The fabrication cost of the advanced engine is 8% less than that of the conventional engine at the 1,000,000-lb-thrust level. At 20,000,000-lb thrust, the advanced engine is 40% less expensive than the conventional engine. The cost difference is due largely to the relative simplicity of the advanced engine injectors and the elimination of secondary frames and ducts for turbopump mounting and turbine exhaust disposal. The advanced engine incorporates a simplified injector in each combustor. These are much simpler to manufacture than the conventional drilled-orifice injectors.

CONFIDENTIAL

Book Two

X, D, Cost Model (cont.)

The time to fabricate a conventional engine injector for high thrust levels would be extensive because of its large size, welding of "pie shaped" segments, machining of external surfaces, drilling of holes, and machining around strengthening ribs to lighten the injector. Also, because of its size, the mounting of the conventional injector in the fixtures will take longer and be more expensive.

Fabrication of the pumps and nozzle should be approximately the same for the two types of engines.

(2) Engine Acceptance Testing

Rocket engine acceptance testing requires: (1) installation of the rocket engine into the test stand, (2) inspection, (3) installation of instrumentation, (4) checkout, (5) hot firing for calibration, (6) installation of required orifices for engine balance trim, (7) hot firing for acceptance, (8) post-fire inspection, and (9) removal from the test stand.

The cost of acceptance testing of major components, such as the thrust chamber assembly and turbopump assembly, is also included. Engine installation inspection and installation of instrumentation comprise the major portion of the cost of operations that are dependent upon thrust level.

The cost of these operations is a relatively minor portion of overall cost; therefore, acceptance testing cost increases very slightly as thrust level is increased. For clustered engines that are tested separately, the cost of acceptance test per engine module can be determined directly from the curve. Clustered engines tested as a unit would offer a small savings (approximately 30%) over testing of the separate modules. The total costs are shown in Figure X-D-8.

CONFIDENTIAL

Book Two

X, D, Cost Model (cont.)

b. Airframe Production

(1) Stage Production Cost

The stage production costs shown in Figure X-D-9 include: (1) stage fabrication (including purchased raw materials and subsystems), (2) detailed fabrication, (3) assembly, (4) production checkout, (5) stage acceptance testing, (6) postfire checkout, (7) flight instrumentation, (8) quality control and inspection, (9) flight evaluation, and (10) documentation.

These costs were established by reference to the Saturn S-II proposal* and through conferences between production personnel for the Aerojet-General Corporation and The Martin Company. In addition, fabrication costs of the cumulative 100-unit average were estimated for the airframe of a 2,000,000-lb-thrust O_2/H_2 booster, a 6,000,000-lb-thrust O_2/H_2 booster, and a 2,000,000-lb-thrust $O_2/RP-1$ booster. By comparison with these design costs, the costs in Figure X-D-9 appear to be conservative. Program airframe production costs were calculated using a learning curve of 85%.

Of these costs, only stage fabrication (exclusive of production checkout) shows a significant amount of increase as size increases. This cost increase is approximately the same as that for propellant tank volume (to the two-thirds power). As a consequence, the cost per pound of stage production decreases substantially with increased stage size.

(2) Stage Transportation Cost

The stage transportation costs in Figure X-D-10 include all costs involved in transporting a completed stage from the Aerojet-General Liquid

* Aerojet-General Corporation Proposal AGC-61102, Saturn S-II Stage Prime Contractor, July 1961.

CONFIDENTIAL

Book Two

X, D, Cost Model (cont.)

Rocket Plant in Sacramento, California, to Cape Kennedy, Florida. This involves transportation to the Sacramento River by trailer truck, to San Francisco by barge, and to Cape Kennedy via the Panama Canal by ship. A more detailed description of this transportation is available in the Saturn S-II proposal.

c. Launch Operations

(1) Launch Support

The launch support costs shown in Figure X-D-11 include those stage contractor's personnel that are required at the launch site. Again, the basis for establishing this cost was the Saturn S-II proposal. Because size has very little effect upon personnel required for this function, the cost is nearly constant.

(2) Launch Operation

It was assumed that the launch operation would be performed by customer personnel at the launch facility. Because a staff is continuously assigned to this facility, regardless of the types of vehicles being launched, no cost was included, except for range time for the actual period of launching. Range time cost was estimated by ascertaining Titan costs, which are approximately \$60,000 per hour for eight hours. It was assumed that this time was for approximately 20 equivalent units and that cost is independent of vehicle size. Based upon a learning curve of 85%, the average cost for 100 units would be \$330,000.

d. Propellant Costs for Operational Vehicles

Propellant cost for engine calibration, acceptance, stage acceptance testing, and flight is included. Other assumptions are noted in Figure X-D-12.

CONFIDENTIAL

Book Two

X, Preliminary System Studies (cont.)

E. EFFECT OF FILM COOLING UPON PERFORMANCE

An analysis was conducted to determine the effect on performance of using part of the fuel supply as a film coolant in the thrust chamber.

Liquid propellant introduced for film cooling causes a performance degradation because optimum burning of this propellant cannot be achieved. However, some thrust is realized from the expanding coolant over the nozzle pressure ratio. Determination of this thrust, from which final performance degradation was calculated, is discussed below.

Three methods for determining the amount of this thrust contribution were analyzed:

(1) The gaseous coolant film expands isentropically as an ideal gas in a separate boundary layer next to the nozzle wall as if it were passed through a convergent-divergent nozzle (see Figure X-D-1).

(2) The gaseous coolant is assumed to expand with partial mixing along the flow path, through the nozzle, with the propellant combustion products (see Figure X-E-2).

(3) The gaseous coolant is assumed to expand with complete mixing with the propellant combustion products (shown also in Figure X-E-2).

Each of the above methods is discussed below.

Very little mixing occurs between the film coolant and main stream. Therefore the average between losses occurring as a result of no mixing and partial mixing is considered most valid.

CONFIDENTIAL

Book Two

X, E, Effect of Film Cooling Upon Performance (cont.)

Burning of the fuel film by injecting oxidizer downstream was also investigated to determine if any performance loss could be regained.

1. No Mixing with the Main Stream

Various amounts of fuel film coolant and different locations of injection were considered. The fuel (AeroZINE 50) was assumed to decompose at the point of injection.

Other assumptions are as follows:

a. AeroZINE 50 is the film coolant and is injected as gaseous decomposition products at a temperature of 1800°F and a pressure equal to that of the propellant combustion products at the injection point in the nozzle.

b. The gaseous coolant is a nonreactive, homogeneous mixture during its flow through the nozzle and acts like an ideal gas with a constant specific heat ratio of 1.25.

c. The gaseous coolant is injected at Mach 1 for points downstream of the thrust chamber throat.

d. The equivalent chamber pressure for the gaseous coolant injector is 300 psia for positions of injection upstream of the thrust chamber throat.

e. The properties of the propellant N_2O_4 /AeroZINE 50 are calculated for conditions of shifting equilibrium.

f. Nozzle and combustion efficiencies are each 0.97

The theoretical model assumes the coolant gas film as flow through a separate DeLaval nozzle. The total performance is calculated by adding

CONFIDENTIAL

Book Two

X, E, Effect of Film Cooling Upon Performance (cont.)

the thrust of the coolant gas flow to the thrust of the main stream combustion products at the same pressure. The position along the equivalent nozzle is then determined by adding the cross-sectional areas of the coolant gas flow nozzle to the main stream combustion products nozzle at this pressure, and locating this cross-sectional area on the equivalent nozzle.

Figure X-E-3 is a graph of the loss in specific impulse versus the percentage of the fuel used for film coolant for various locations of fuel injection. The data for Figure X-E-3 are determined at the same nozzle centerline distance and cross-sectional area. This corresponds to different area ratios (see Figure X-E-1) for each case of film coolant flow rate because the resulting nozzle throat area varies in direct proportion to the propellant flow rate from the combustion chamber.

The results of this analysis show both the performance degradation associated with various amounts of fuel used for film cooling and the effect of injection location upon the amounts required.

2. Partial Mixing with the Main Stream

The following assumptions are made to analyze partial mixing of the fuel coolant film with the combustion products in the rocket nozzle.

All of the coolant film and an equal amount of the combustion products mix completely and instantaneously at some prescribed plane section in the nozzle.

The properties of the mixture are determined by assuming the two constituents are ideal gases and mix at the pressure of the main combustion products stream.

CONFIDENTIAL

Book Two

X, E, Effect of Film Cooling Upon Performance (cont.)

The nozzle is stepped at the mixing section to allow for the expansion of the fuel as it changes to a decomposed gas and mixes with the combustion products stream.

The mixture expands isentropically to the exit plane.

The properties and performance data of the combustion products of N_2O_4 /AeroZINE 50 are based upon shifting equilibrium conditions.

The performance and properties of the mixture are calculated at the pressure of the main stream at the exit area in question.

The performances of the two streams at the exit plane are added together and compared with the performance of a nozzle with the same cross-sectional area but without film cooling.

The results of this analysis are shown in Figure X-E-4.

3. Complete Mixing with the Main Stream

The complete mixing analysis is made in two parts. In Part A, it is assumed that all of the fuel film decomposes and mixes instantly with the whole main gas stream at the same prescribed cross-sectional area. Other assumptions are as follows:

(1) The combustion products act as an ideal gas before mixing for frozen equilibrium flow.

(2) There is no abrupt change in cross-sectional area of the nozzle at the mixing station; therefore, the pressure in the expansion section will be higher than for the nozzle without film cooling because of the mixing process.

(3) The mixture expands isentropically as an ideal gas in frozen equilibrium to the exit plane.

CONFIDENTIAL

Book Two

X, E, Effect of Film Cooling Upon Performance (cont.)

(4) A conical nozzle is assumed (see Figure X-E-5) with the comparison in performance made at the same cross-sectional area for a conical nozzle without film cooling.

In Part B, it is assumed that small (differential) amounts of the fuel film evaporate, decompose, and mix completely with the combustion products at each point along the entire length of the expansion cone. A numerical integration procedure is used to calculate the performance of the propellants at the exit plane.

The results of the analysis for complete mixing (Parts A and B) are presented in Figure X-E-6.

4. Film Coolant Burnoff

The purpose of burning off the film coolant is to increase the exit velocity of the boundary layer. This can be achieved by increasing the temperature of the film by burning it with oxidizer. The resultant increase in boundary velocity is accomplished at the expense of the mainstream since the oxidizer flow rate required for injection is deducted from the mainstream flow.

The analysis was conducted for oxidizer injection at various pressures. The results of this analysis are presented in Figure X-E-7. This figure shows percent I_g loss as a function of percent of fuel used for film cooling with variations in oxidizer injection pressure.

An outline of the method of analysis, together with the pertinent assumptions, follows.

a. Assumptions

- (1) Frozen equilibrium flow in mainstream and boundary layer.
- (2) No mixing between the boundary layer and mainstream.

CONFIDENTIAL

Book Two

X, E, Effect of Film Cooling Upon Performance (cont.)

- (3) Chamber pressure of 3000 psia.
- (4) Mixture ratio of 2.2:1 in chamber combustion and boundary combustion.
- (5) AeroZINE 50 coolant injected and decomposed above the exit plane of chamber. Decomposition temperature 1800°F at Mach 1 conditions (2545°R stagnation temperature).
- (6) Gas expanded to an area ratio of 100:1
- (7) Initial fuel and mainstream velocities (in chamber) are neglected.
- (8) Oxidizer is injected at a velocity of 200 ft/sec and at an angle of 15° to the boundary layer.
- (9) Boundary layer combusts at the chamber combustion temperature corresponding to the injection pressure at 2.2 mixture ratio.
- (10) Isentropic flow exists for all streams.

b. Method

The main stream velocity is determined by the energy equation

$$\begin{aligned} V_E &= 2g J \Delta h \\ &= 2g J C_p T_c \left[1 - \left(\frac{P_e}{P_c} \right)^{\frac{K-1}{K}} \right] \end{aligned}$$

where

- V_E = exit velocity, ft/sec
- Δh = enthalpy change, Btu/lb
- C_p = specific heat at constant pressure, Btu/lb-°R

CONFIDENTIAL

Book Two

X, E, Effect of Film Cooling Upon Performance (cont.)

$$j = 778, \text{ ft-lb/Btu}$$

$$T_c = \text{combustion temperature, } ^\circ\text{R}$$

$$P_e = \text{exit pressure, psia}$$

$$P_c = \text{chamber pressure, psia}$$

$$K = \text{ratio of specific heats}$$

The area of the mainstream is determined by,

$$\dot{W} = A V$$

where:

$$\dot{W} = \text{mainstream flow rate, lb/sec}$$

$$\rho = \text{exit density, lb/ft}^3$$

$$A = \text{exit area, ft}^2$$

and the exit density is determined from isentropic expansion from chamber conditions,

$$\text{i.e., } \rho_e = \rho_c \left(\frac{P_e}{P_c} \right)^{1/K}$$

The velocity of the boundary layer is determined in steps,

$$V_{Pi} = \sqrt{2g j c_p T_D \left[1 - \left(\frac{P_i}{P_c} \right)^{\frac{K-1}{K}} \right]}$$

where the terms are as previously defined, but apply to the uncombusted fuel film coolant. The term P_i refers to the pressure of the injection and T_D is the decomposition temperature. The oxidizer is then injected and the velocity of the mixture is determined by the conservation of momentum

$$\dot{W}_m V_m = \dot{W}_F V_F + \dot{W}_O V_O \cos 15^\circ$$

where the subscripts are

$$m = \text{combusted mixture}$$

$$F = \text{fuel film coolant}$$

$$O = \text{oxidizer injectant}$$

CONFIDENTIAL

Book Two

X, E, Effect of Film Cooling Upon Performance (cont.)

The exit velocity of the combusted boundary layer is determined in the same manner as that of the mainstream.

$$V_{E_{BL}} = \sqrt{2 g J C_p T_{c_{p1}} \left[1 - \left(\frac{P_e}{P_1} \right)^{\frac{K-1}{K}} \right] + V_m^2}$$

Where $V_{E_{BL}}$ is the exit velocity of the boundary layer and $T_{c_{p1}}$ is defined in the ninth assumption. The area of the boundary layer is found from the following expression:

$$W_{BL} = \rho_{E_{BL}} A_{E_{BL}} V_{E_{BL}}$$

The density at the point of combustion is determined from the perfect gas law,

$$\rho = \frac{P}{RT}$$

This density is then expanded isentropically to the exit condition.

When the total area corresponds to an area ratio of 100:1 the percent loss of specific impulse can be determined as previously outlined.

F. PERFORMANCE OF METALIZED PROPELLANT SYSTEMS

Vehicle performance comparisons were prepared for several advanced propellant combinations in order to establish the best operating pressure for each. The advanced propellants analyzed were: $N_2O_4/N_2H_4 + Al$, $N_2O_4/N_2H_4 + AlH_3$, $N_2O_4/N_2H_4 + Be$, $N_2O_4/N_2H_4 + BeH_2$, $H_2O_2/N_2H_4 + Al$, $H_2O_2/N_2H_4 + AlH_3$, $H_2O_2/N_2H_4 + Be$ and $H_2O_2/N_2H_4 + BeH_2$.

Only single-stage-to-300-nm-orbit vehicles were analyzed because they provide the most significant payload differences for different engine configurations and more adequately define peak chamber pressures. It has already been shown that the qualitative comparison of the various configurations is independent of the vehicle mission. The engine configurations considered are listed below.

CONFIDENTIAL

Book Two

X, F, Performance of Metalized Propellant Systems (cont.)

DeLaval nozzle--gas generator cycle

DeLaval nozzle--staged-combustion cycle

Forced-deflection nozzle--gas generator cycle

Forced-deflection nozzle--staged-combustion cycle

Experience has shown relatively large changes in area ratio about the optimum value result in very small losses in payload capability. Therefore, the rigorous analysis necessary to determine the optimum area ratio for each metalized propellant combination is not required; the optimum area ratios determined for N_2O_4 /AeroZINE 50 propellants will be used to determine the payload capability of the propellants under consideration.

The thrust chamber mixture ratios used were those reported in the propellant investigation portion of this contract and selected on the basis of optimum expansion sea-level specific impulse. The percentage of additive added to the N_2H_4 fuel was determined in the same manner.

On the basis of these parameters, and using all methods, constants, and engine weight used for N_2O_4 /AeroZINE 50, the final performance curves, Figures X-F-1 through 8, were prepared. These curves present relative payloads as a function of chamber pressure. A relative payload of 1.0 corresponds to a conventional N_2O_4 /AeroZINE engine (DeLaval nozzle, gas-generator cycle, 1000-psia chamber pressure). The N_2O_4 /AeroZINE 50 system is shown in Figure X-F-9 for comparison.

For each propellant combination, a complete cycle analysis was necessary for both the staged-combustion and gas-generator cycles. For the N_2O_4 systems, a tripropellant cycle was adopted utilizing N_2O_4/N_2H_4 for the gas generator in order to eliminate the difficulty attendant with driving the turbine with hot metalized particles. Mixture ratios were selected to provide a turbine inlet temperature of 1200°F. In the H_2O_2 systems, a monopropellant cycle using H_2O_2 only in the gas generator was adopted. This enables use of the simpler two-pump system using a proven monopropellant in the gas generator. This results in a turbine inlet

CONFIDENTIAL

Book Two

X, F, Performance of Metalized Propellant Systems (cont.)

temperature of 1700°F and, therefore, a considerable gain in performance resulting from this high-energy gas. All other aspects of the cycle analysis paralleled those of the N_2O_4 /AeroZINE 50 systems.

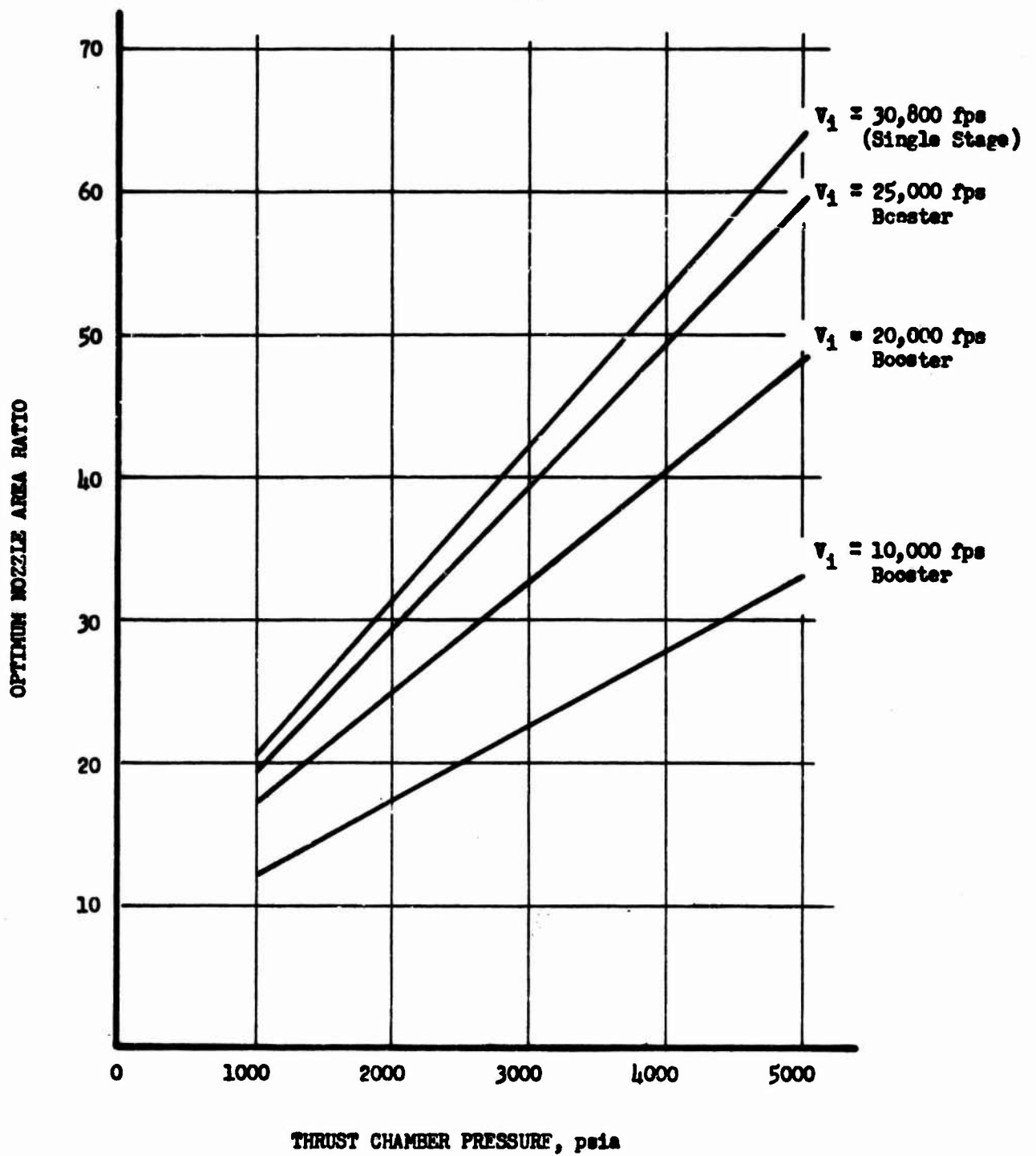
The results of the performance calculations are summarized below.

Propellant Combination	ENGINE CONFIGURATION			
	DeLaval, Gas Generator	Forced- Deflection, Gas Generator	DeLaval, Staged- Combustion	Forced-Deflection, Staged Combustion
N_2O_4 /AeroZINE 50	100%*	172%	189%	217%
$N_2O_4/N_2H_4 + Al$	306	346	352	405
$N_2O_4/N_2H_4 + AlH_3$	420	440	468	502
$N_2O_4/N_2H_4 + Be$	450	492	503	576
$N_2O_4/N_2H_4 + BeH_2$	560	633	618	710
$H_2O_2/N_2H_4 + Al$	358	397	435	478
$H_2O_2/N_2H_4 + AlH_3$	472	530	560	626
$H_2O_2/N_2H_4 + Be$	543	610	674	737
$H_2O_2/N_2H_4 + BeH_2$	695	795	865	975

*All performance figures are maximum relative payloads with the exception of the N_2O_4 /AeroZINE 50, DeLaval nozzle, gas-generator cycle engine, which is at 1000-psia chamber pressure (i.e., a conventional engine).

Book Two

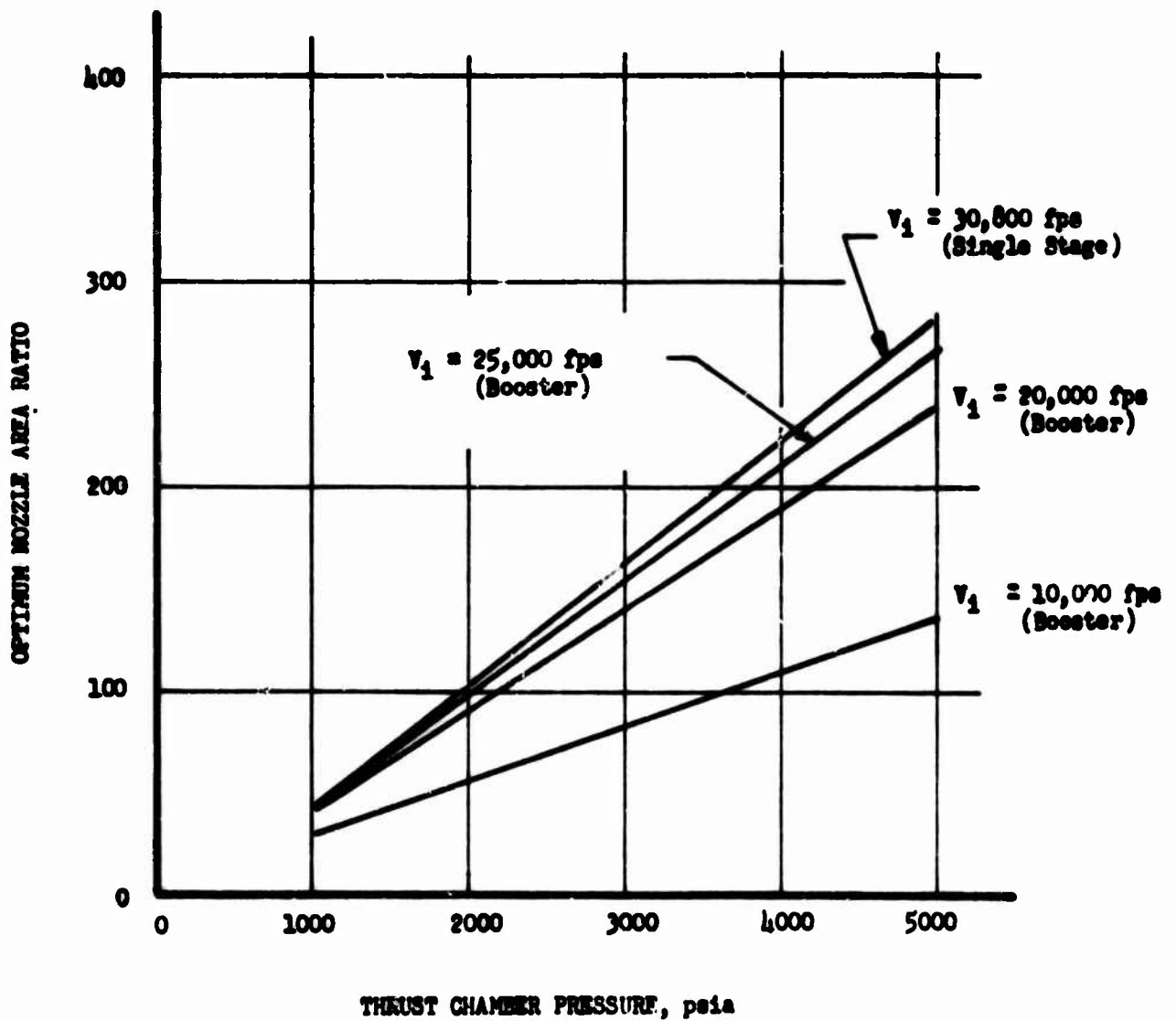
PROPELLANTS - $N_2O_4/A-50$



Optimum Nozzle Area Ratio vs Thrust Chamber Pressure, DeLaval Nozzle

Figure X-A-1

PROPELLANTS $H_2O_2/A-50$

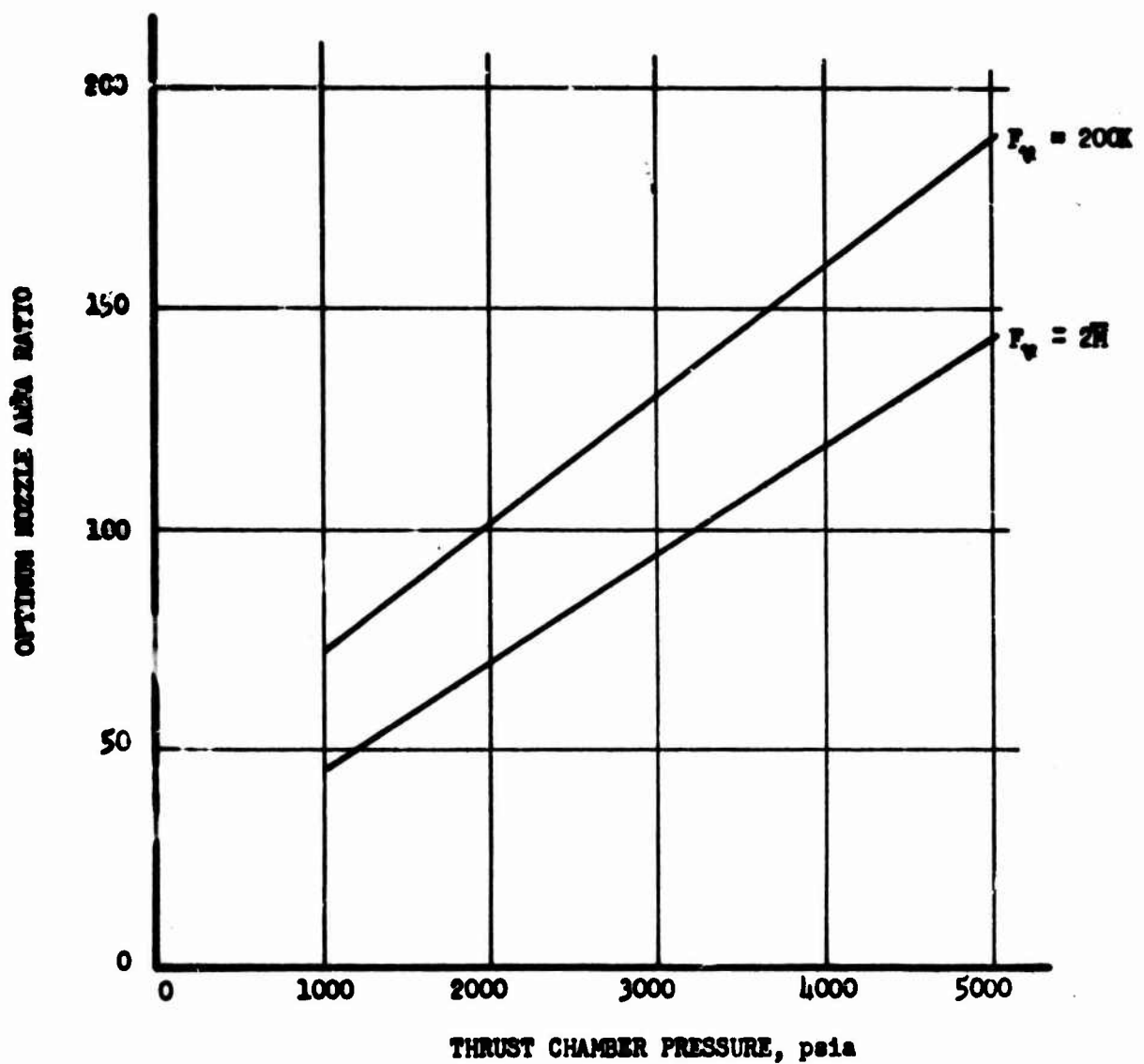


Optimum Nozzle Area Ratio vs Thrust Chamber Pressure, Forced-Deflection Nozzle

Figure X-A-2

Book Two

PROPELLANTS - $H_2O_2/A-50$

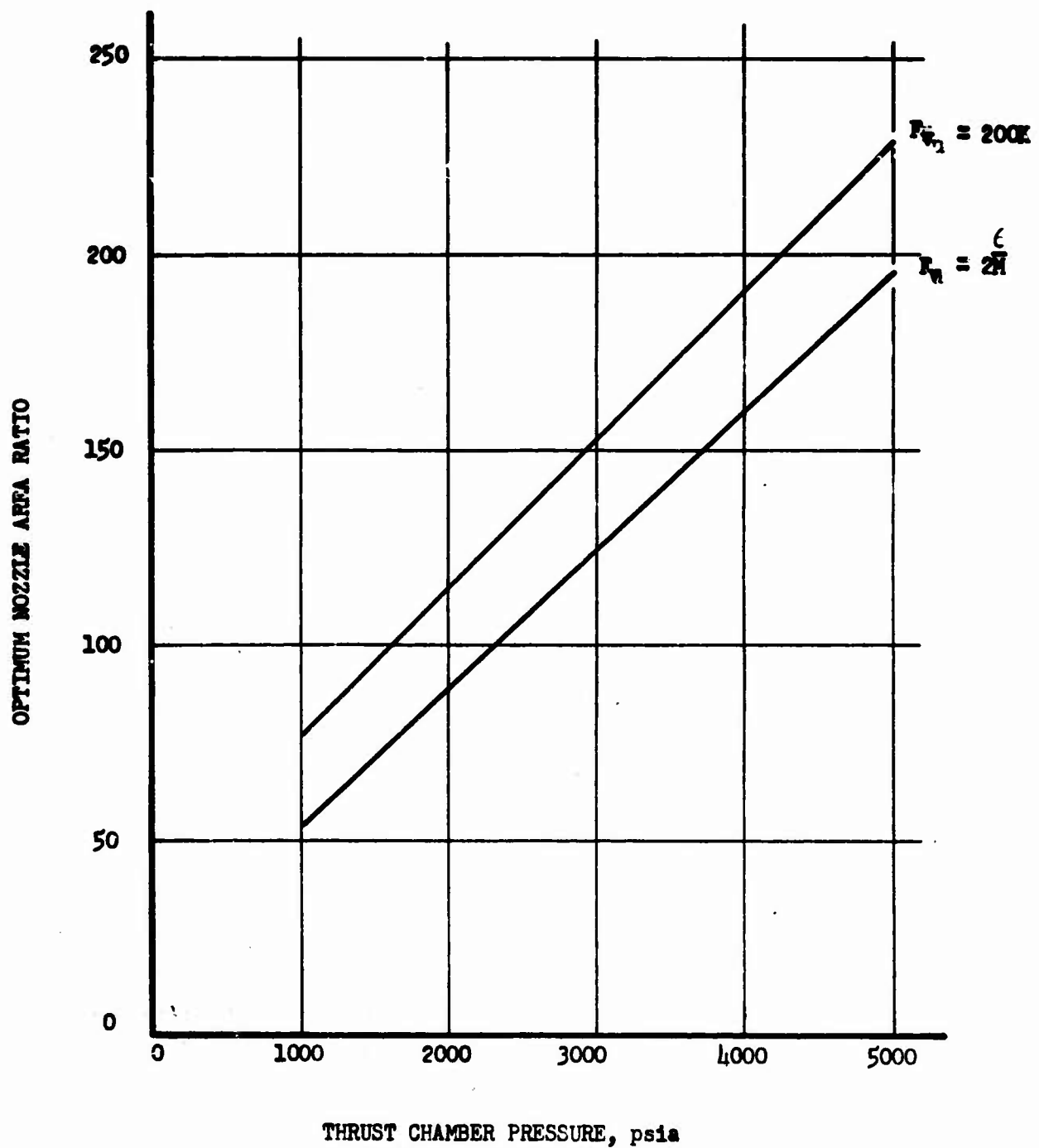


Optimum Nozzle Area Ratio vs Thrust Chamber Pressure, Upper-Stage
Vehicle-- $V_1 = 10,000$ ft/sec

Figure X-A-3

Book Two

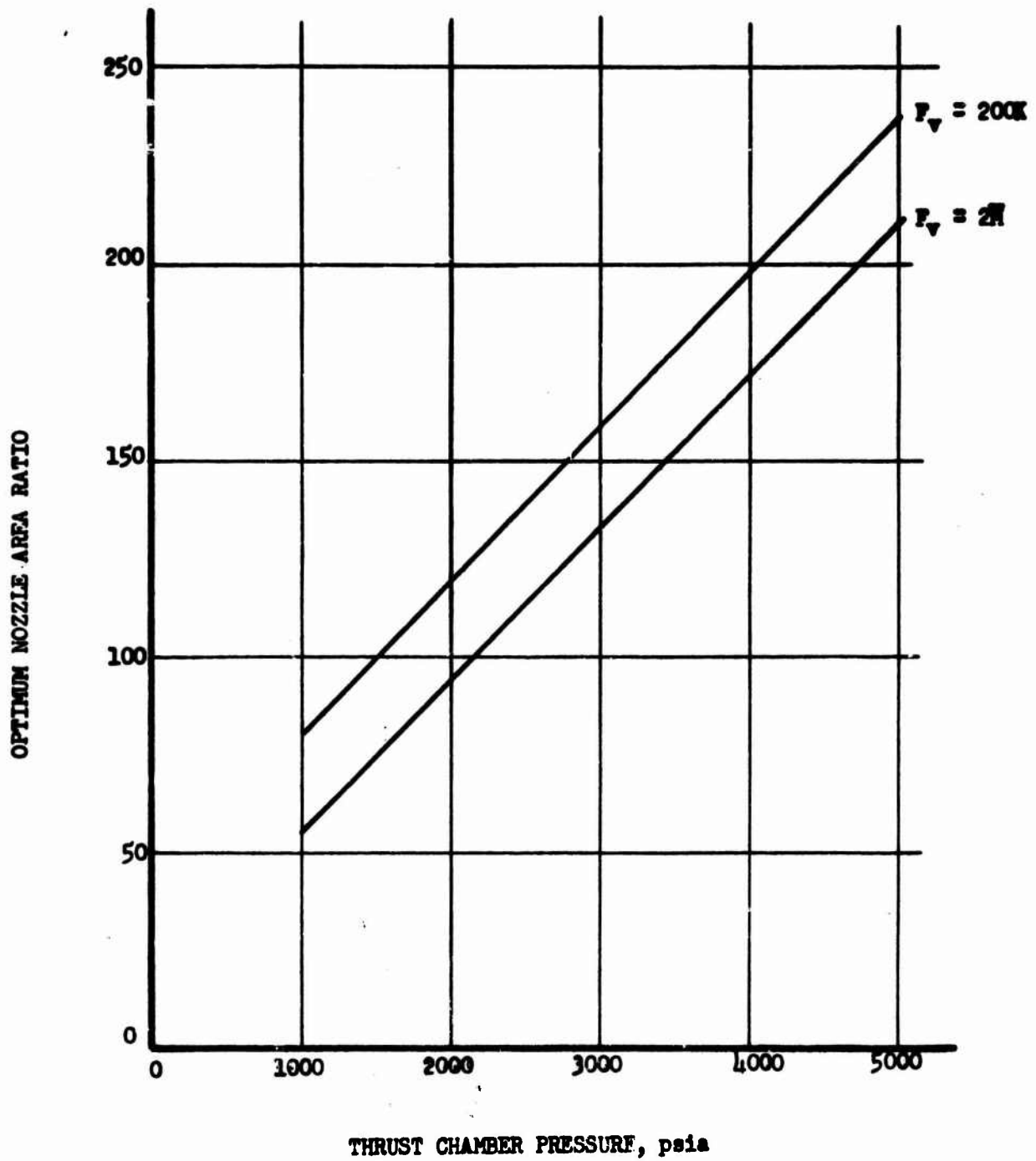
PROPELLANTS - $\text{H}_2\text{O}_2/\text{A-50}$



Optimum Nozzle Area Ratio vs Thrust Chamber Pressure, Upper-Stage
Vehicle-- $V_i = 15,000$ ft/sec

Figure X-A-4

Book Two
PROPELLANTS $\text{N}_2\text{O}_4/\text{A-50}$



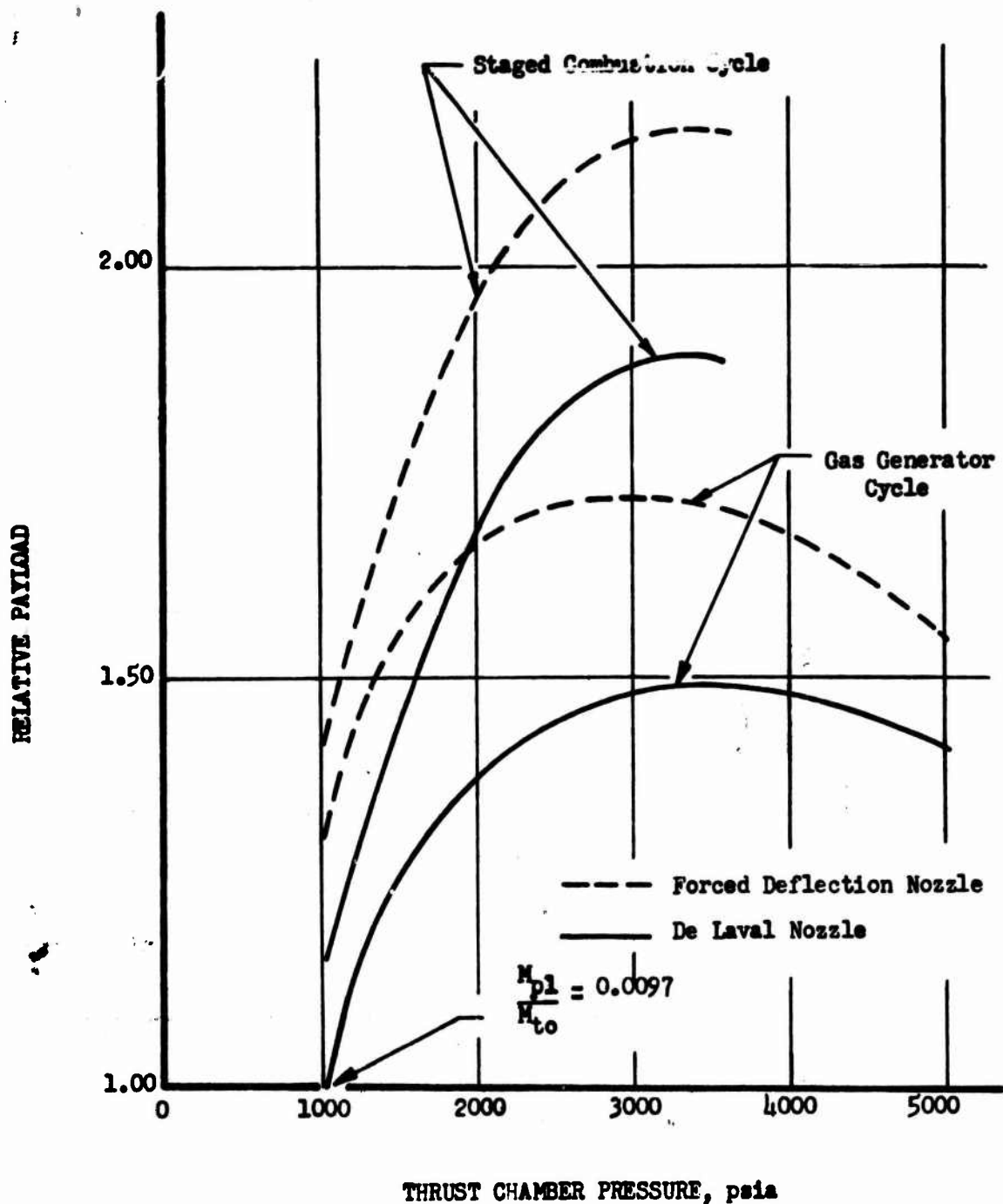
Optimum Nozzle Area Ratio vs Thrust Chamber Pressure, Upper-Stage
Vehicle-- $V_i = 20,000$ ft/sec

Figure X-A-5

CONFIDENTIAL

Book Two

PROPELLANTS - $N_2O_4/A-50$



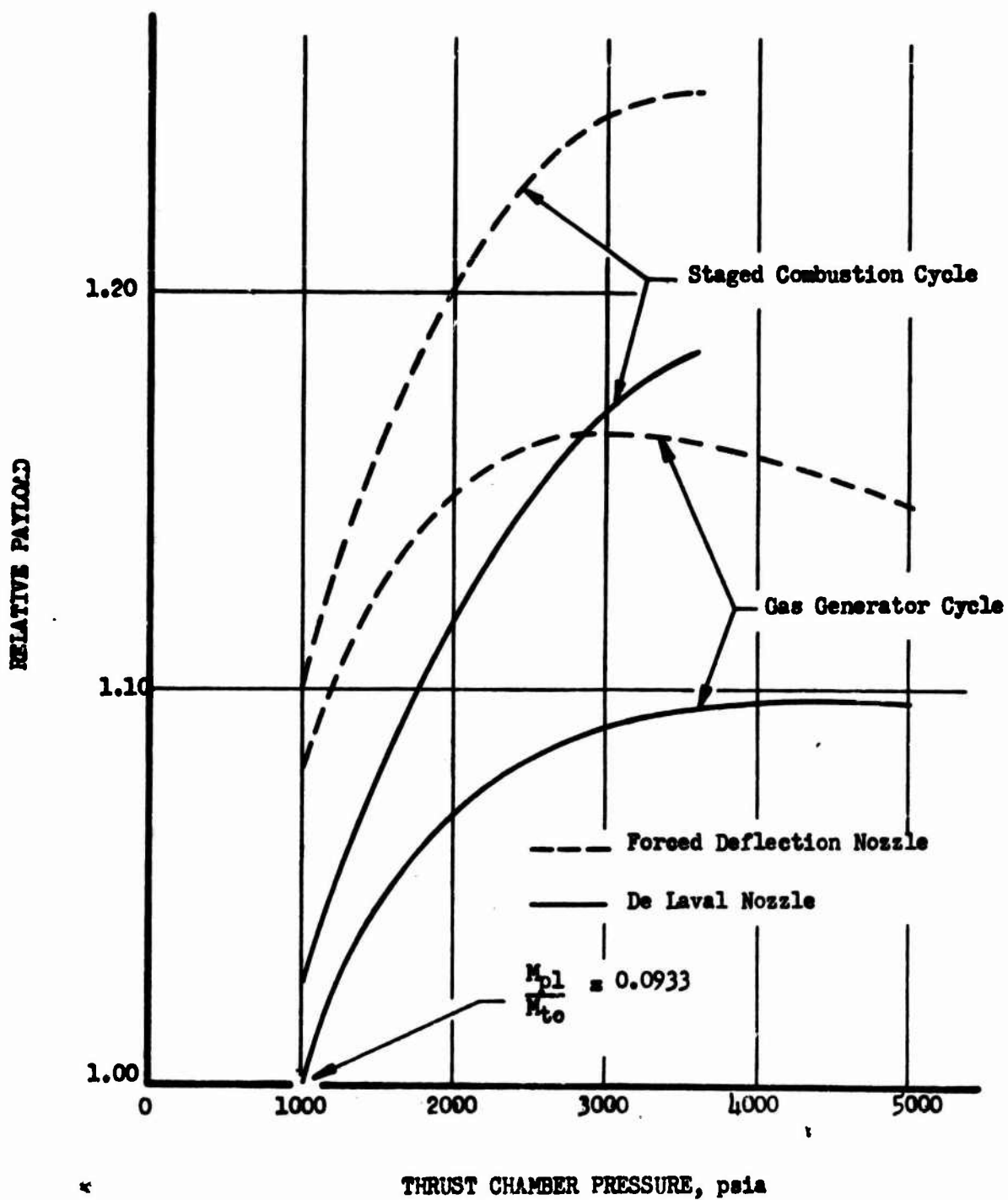
Relative Payload vs Thrust Chamber Pressure, Single Stage to 300 NM Orbit (u)

Figure X-A-6

CONFIDENTIAL

CONFIDENTIAL

Book Two
PROPELLANTS - $N_2O_4/A-50$



Relative Payload vs Thrust Chamber Pressure, First-Stage
Vehicle-- $V_i = 20,000$ ft/sec (u)

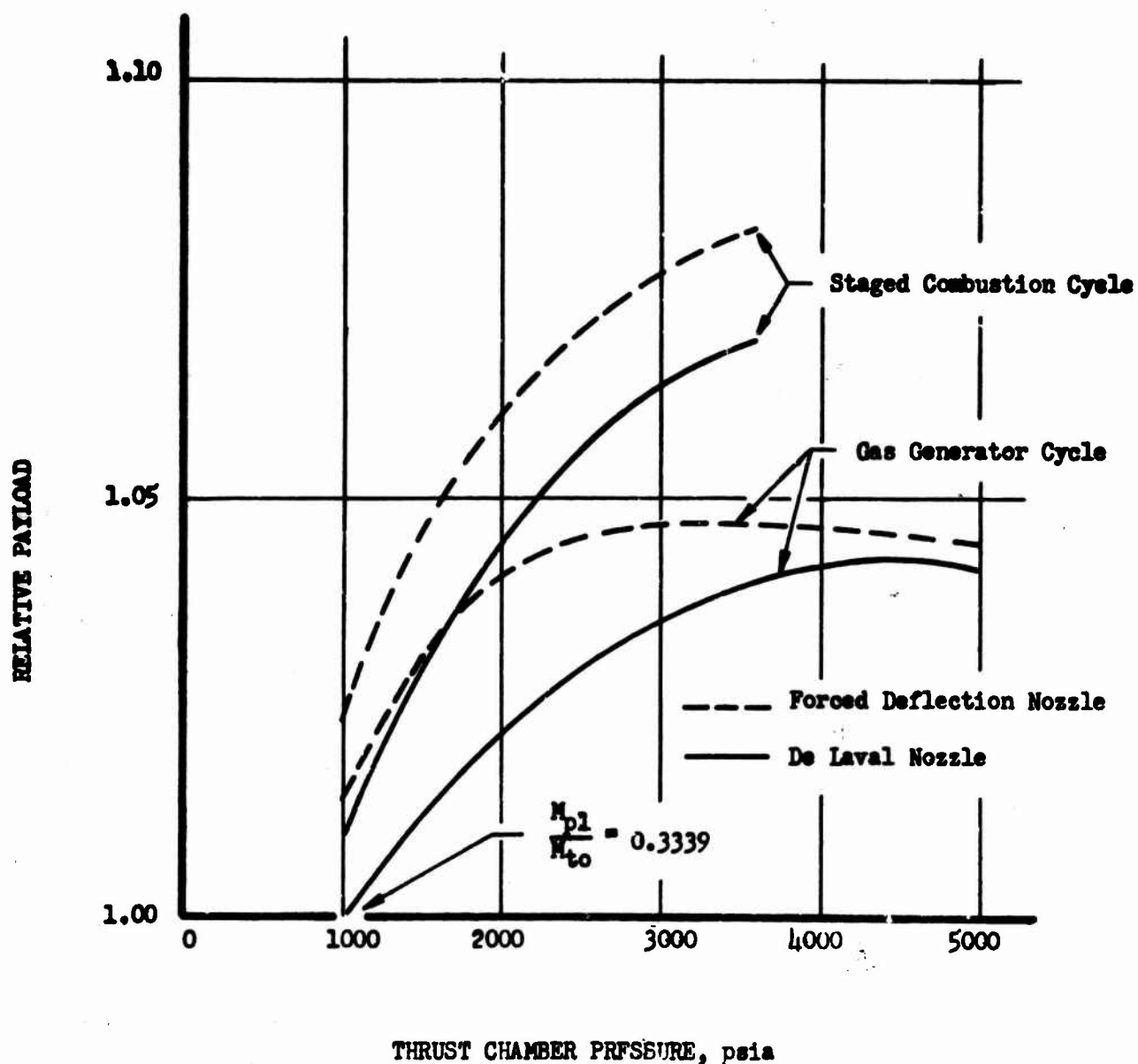
Figure X-A-7

CONFIDENTIAL

CONFIDENTIAL

Book Two

PROPELLANTS - $H_2O_2/A-50$



Relative Payload vs Thrust Chamber Pressure, First-Stage
Vehicle-- $V_i = 10,000$ ft/sec (u)

Figure X-A-8

CONFIDENTIAL

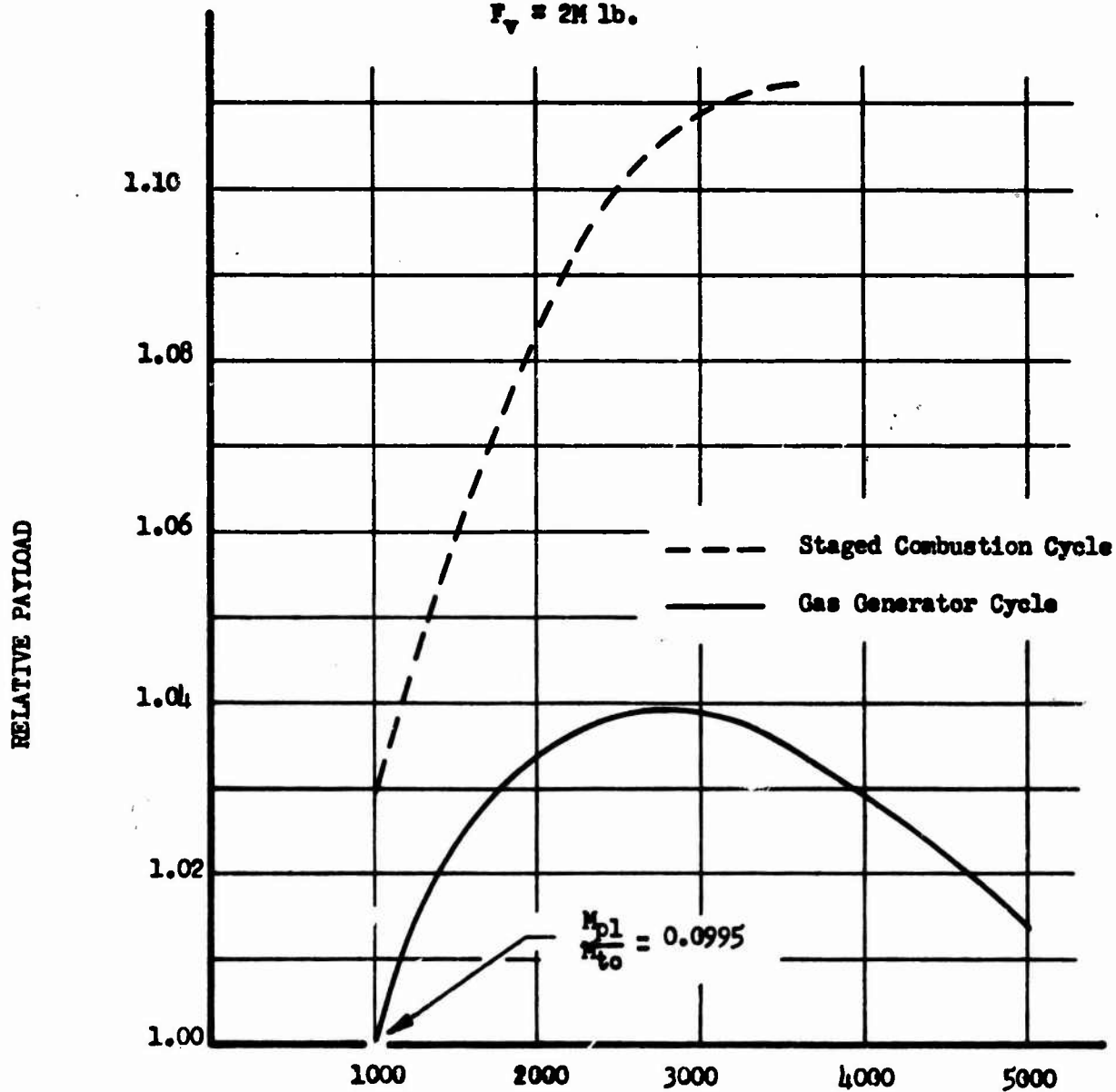
CONFIDENTIAL

Book Two

NOTE:

PROPELLANTS - $\text{N}_2\text{O}_4/\text{A-50}$

$F_v = 2\text{M lb.}$



Relative Payload vs Thrust Chamber Pressure, Upper-Stage
Vehicle-- $V_i = 20,000$ ft/sec (u)

Figure X-A-9

CONFIDENTIAL

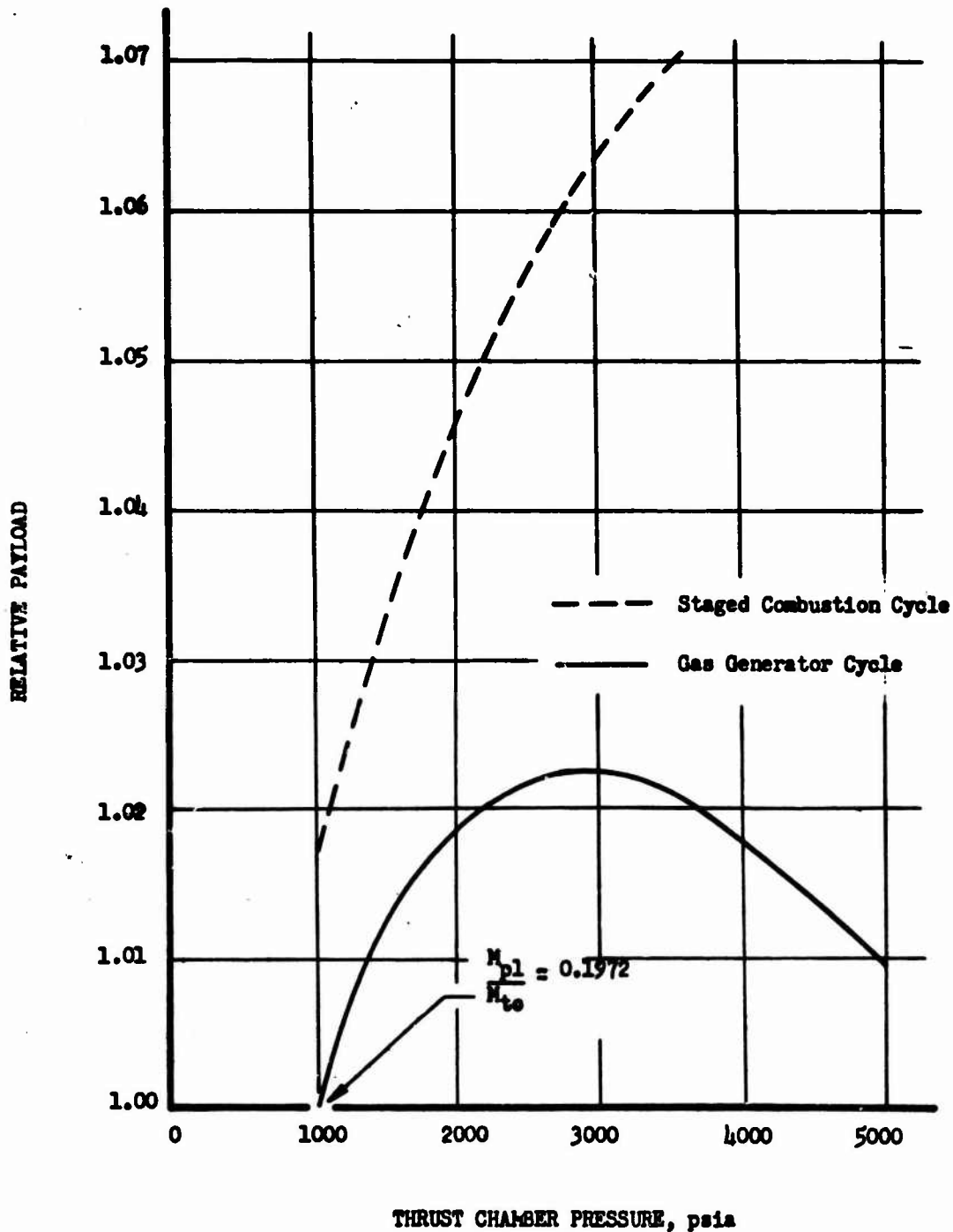
CONFIDENTIAL

Book Two

NOTE:

PROPELLANTS - $H_2O_2/A-50$

$P_v = 24.3 \text{ lbs}$



Relative Payload vs Thrust Chamber Pressure, Upper-Stage
Vehicle-- $V_i = 15,000 \text{ ft/sec (u)}$

Figure X-A-10

CONFIDENTIAL

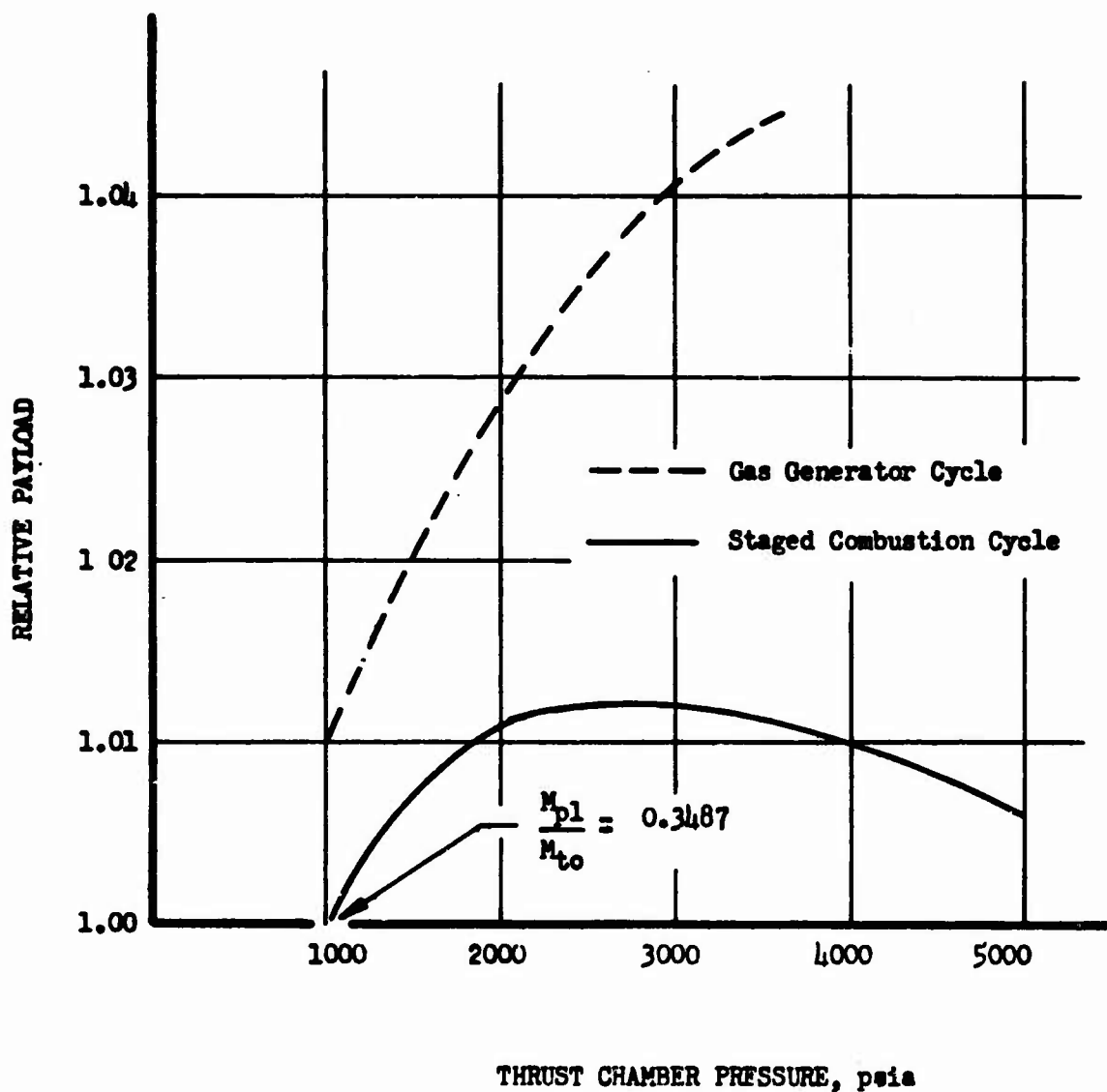
CONFIDENTIAL

Book Two

NOTE:

PROPELLANTS • $N_2O_4/A-50$

$F_T = 2M \text{ lbs}$



Relative Payload vs Thrust Chamber Pressure, Upper-Stage
Vehicle-- $F_1 = 10,000 \text{ ft/sec (u)}$

Figure X-A-11

CONFIDENTIAL

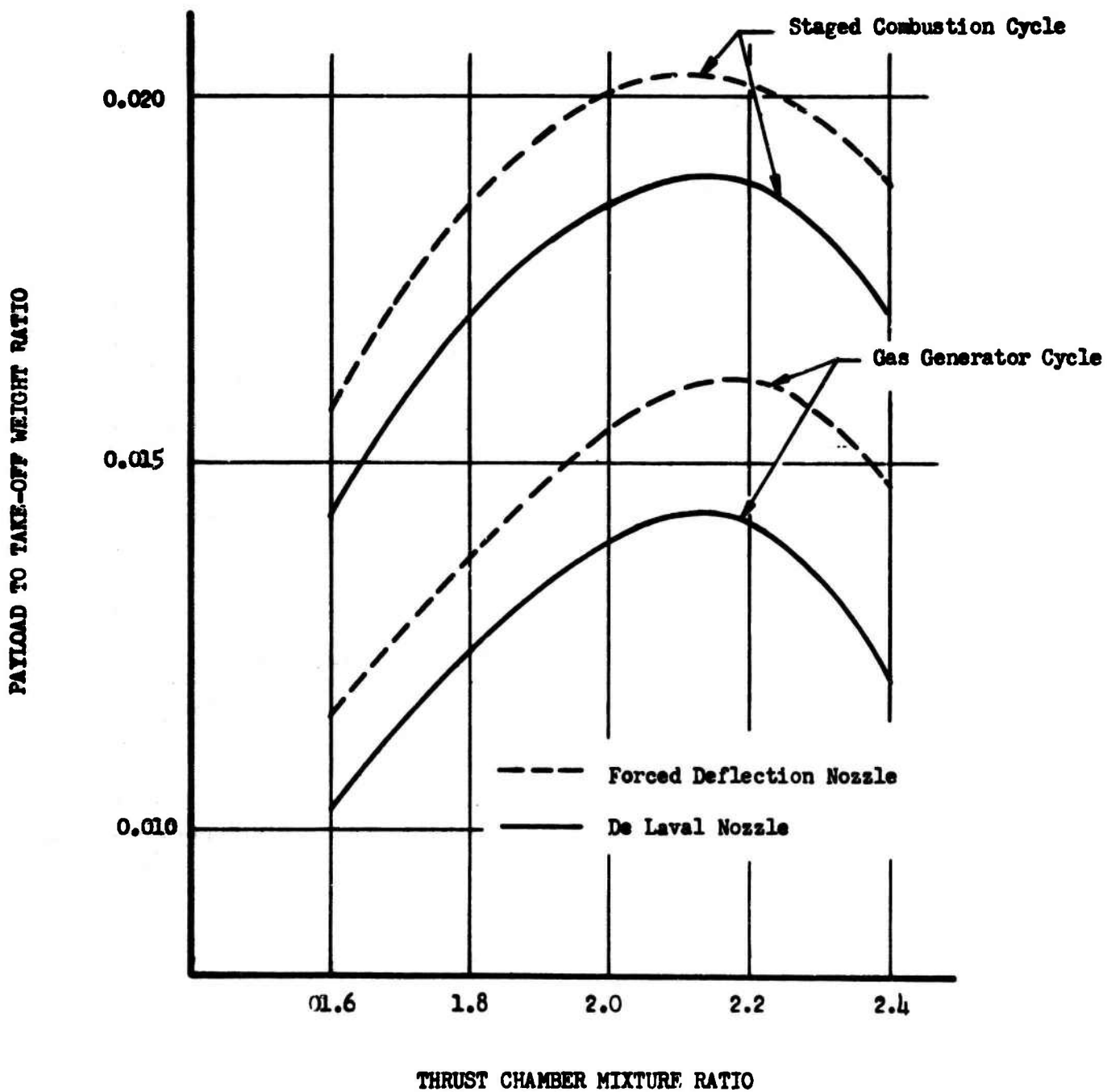
CONFIDENTIAL

Book Two

NOTE:

PROPELLANTS - $\text{H}_2\text{O}_2/\text{A-50}$

SINGLE STAGE TO 300 NM ORBIT



Payload to Takeoff Weight Ratio vs Thrust Chamber Mixture Ratio (u)

Figure X-A-12

CONFIDENTIAL

CONFIDENTIAL

Book Two

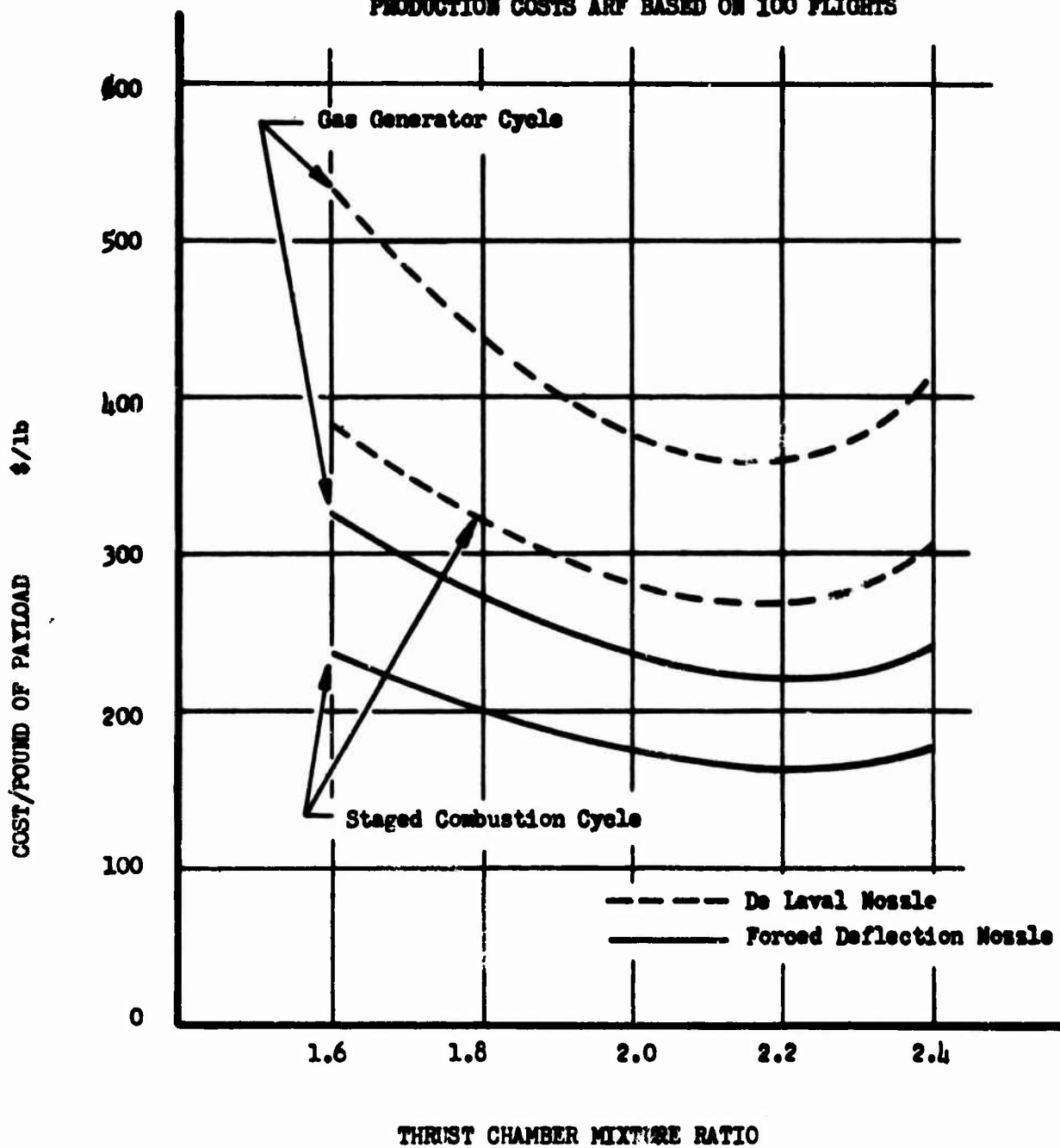
NOTE:

PROPELLANTS $N_2O_4/A-50$

SINGLE STAGE TO 300 NM ORBIT

$P_{s.l.} = 4.5 \times 10^6$ lb

PRODUCTION COSTS ARE BASED ON 100 FLIGHTS



Vehicle Cost per Pound of Payload vs Thrust Chamber Mixture Ratio (u)

Figure X-A-13

CONFIDENTIAL

CONFIDENTIAL

Book Two

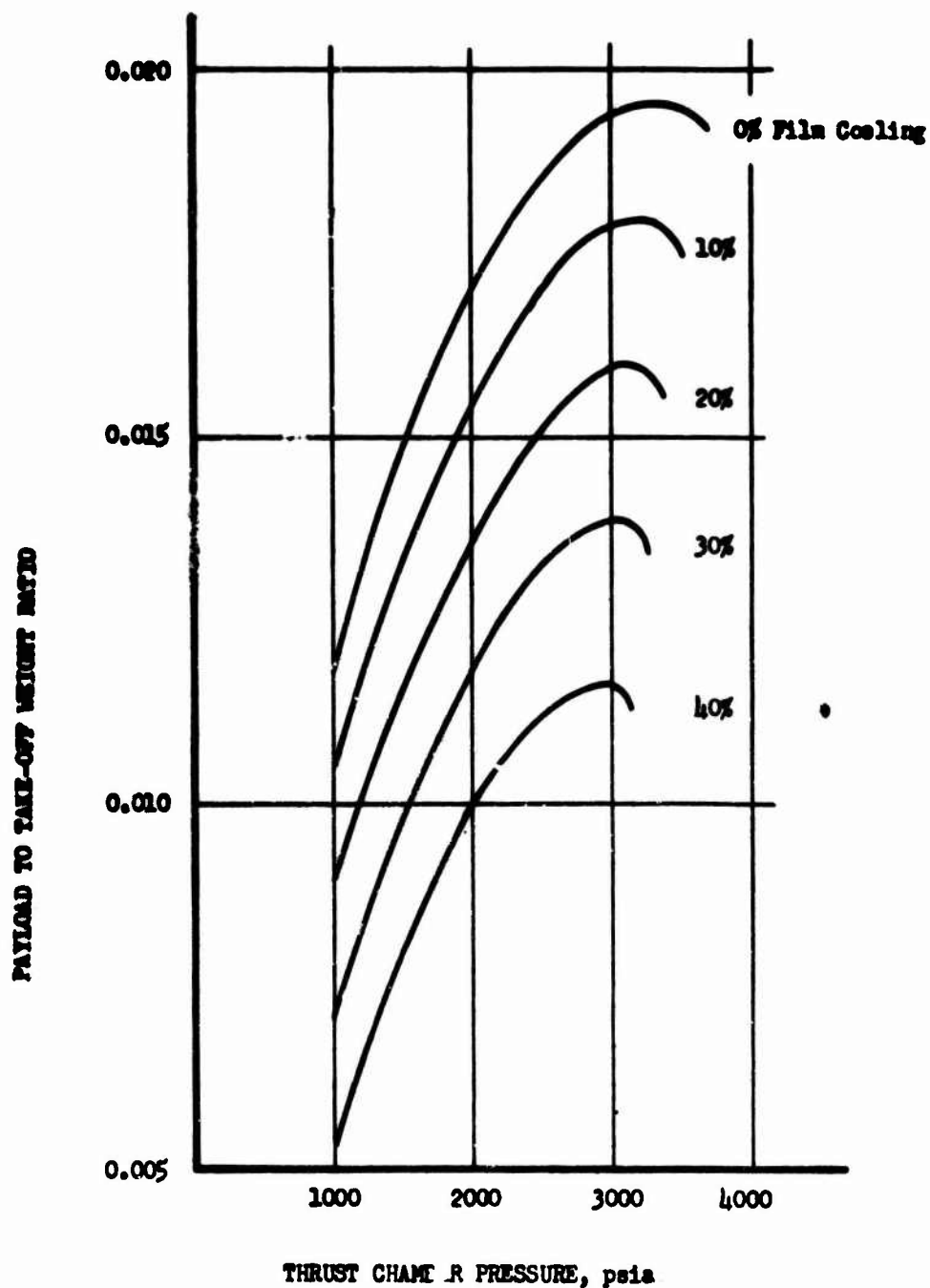
NOTE:

PROPELLANTS - H_2O_2/H_2

SINGLE STAGE TO 300 NM ORBIT

INTERVAL = 1212

MRing = 2.1



Effect of Film Cooling on Delivered Payload, Staged Combustion Cycle (u)

Figure X-A-14

CONFIDENTIAL

CONFIDENTIAL

Book Two

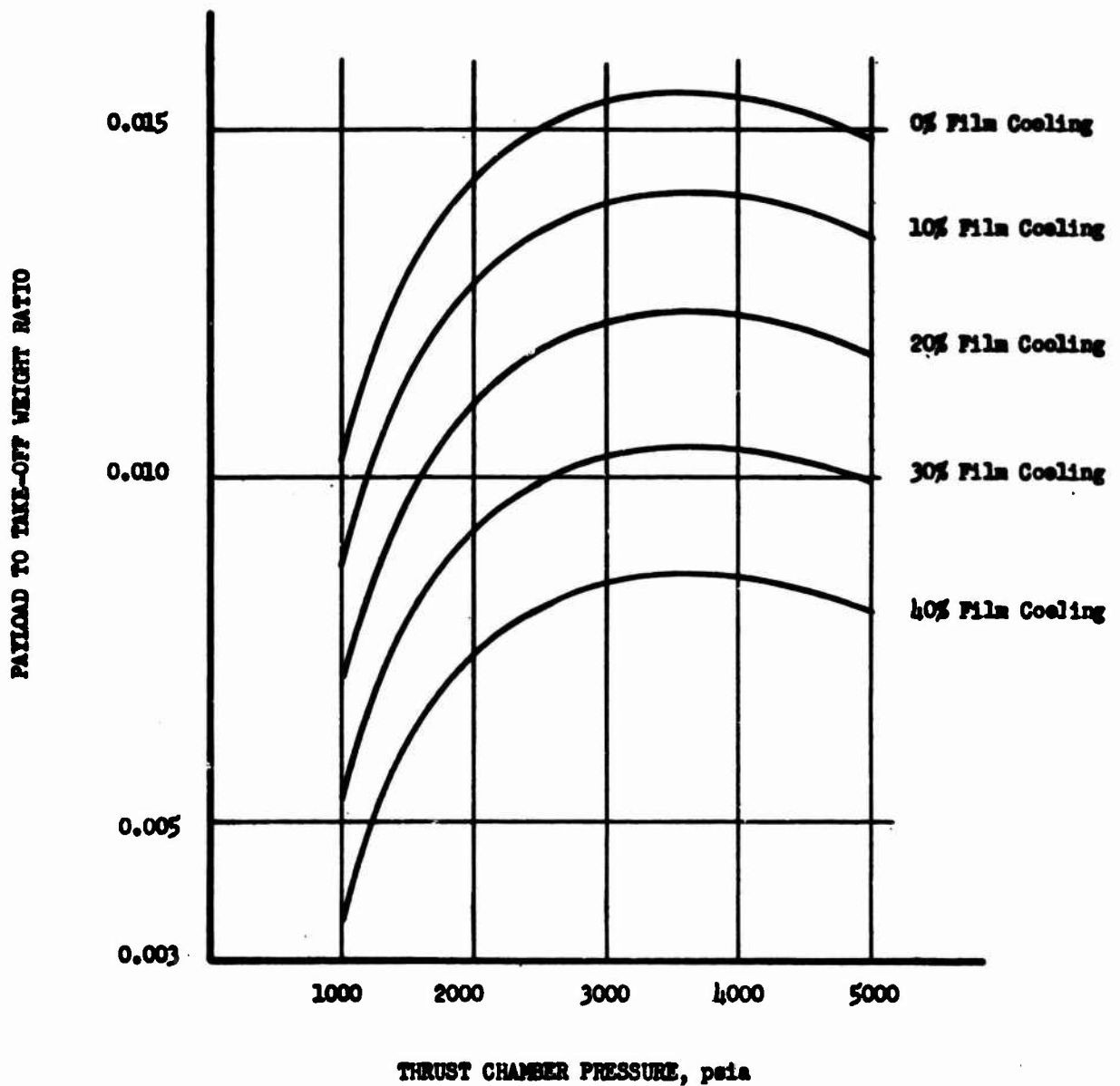
NOTE:

PROPELLANTS - $H_2O_2/A-50$

SINGLE STAGE TO 300 NM ORBIT

DE LAVAL NOZZLE

$MR_{inj} = 2.1$



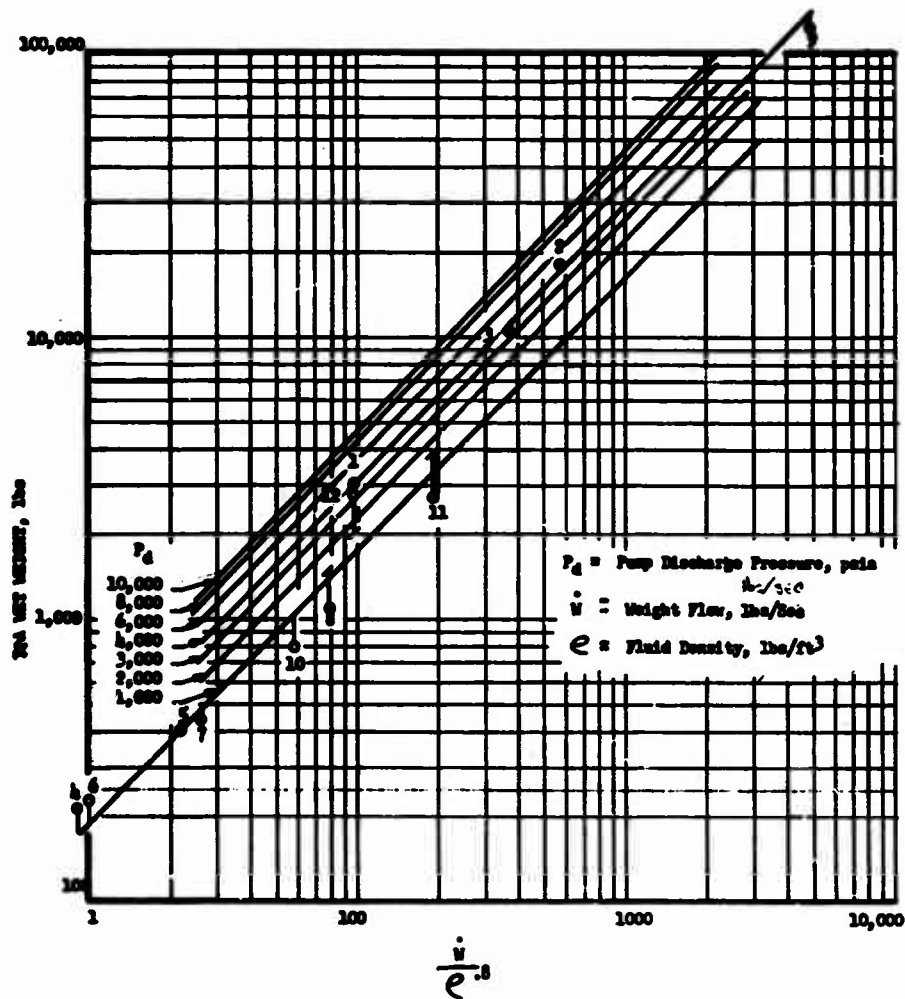
Effect of Film Cooling on Delivered Payload, Gas Generator Cycle (u)

Figure X-A-15

CONFIDENTIAL

CONFIDENTIAL

Book Two



No.	Engine	Propellant	Pump Discharge Pressure-psia	TWA Weight-lb
1	800 K 1b F	H ₂ O ₂ /A-50	4000	3000
2	4.5 N 1b F	H ₂ O ₂ /A-50	4000	17,500
3	2 N 1b F	LO ₂ /LN ₂	4000	10,600
4	Titan I 2nd Stage	LO ₂ /RP-1	1000	24
5	Titan I 1st Stage	LO ₂ /RP-1	1000	402
6	Titan II 2nd Stage	H ₂ O ₂ /A-50	1000	238
7	Titan II 1st Stage	H ₂ O ₂ /A-50	1000	470
8	800 K 1b F	LO ₂	1300	11000
9	24 N 1b F	LO ₂ /LN ₂	4000	126,000
10	Double Booster 400 K 1b F	LO ₂ /RP-1	1200	800
11	N-1	LO ₂	1500	22000
12	N-1	LN ₂	1500	2900

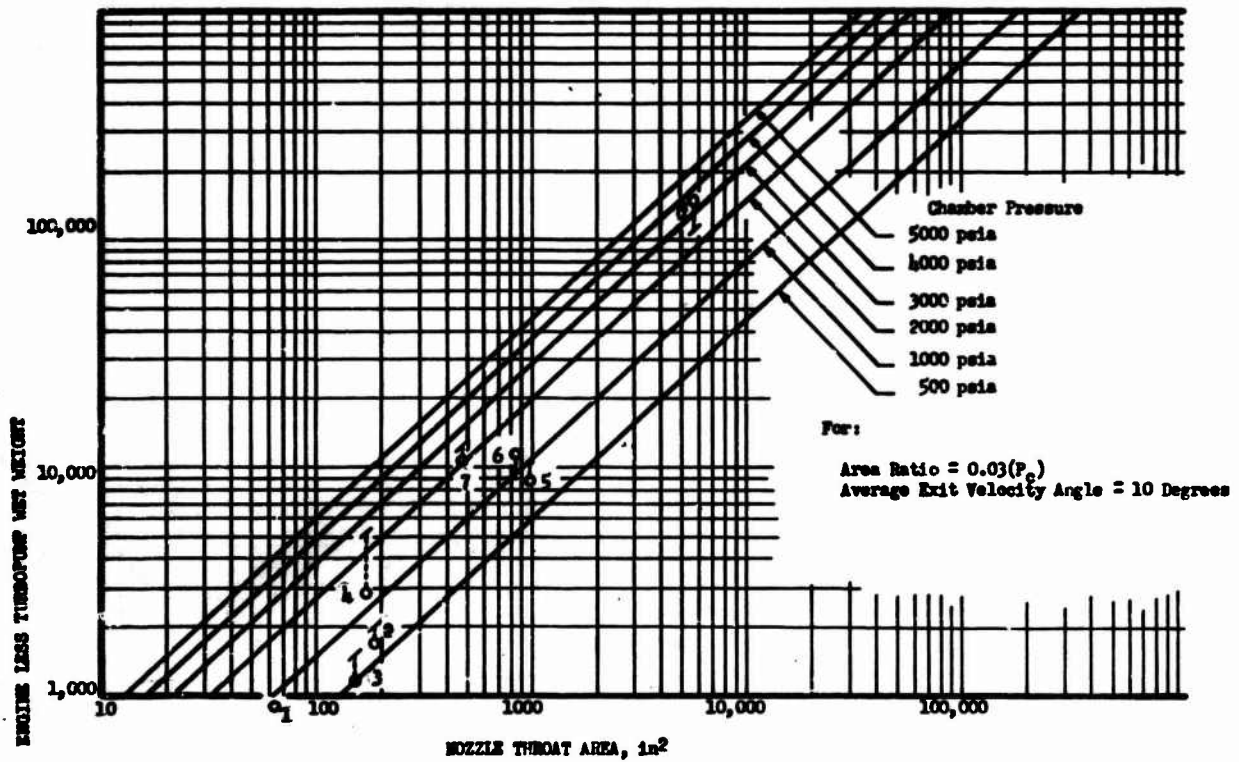
Turbopump Weights (u)

Figure X-B-1

CONFIDENTIAL

CONFIDENTIAL

Book Two



Engines used to Correlate the Analytical Weight Studies

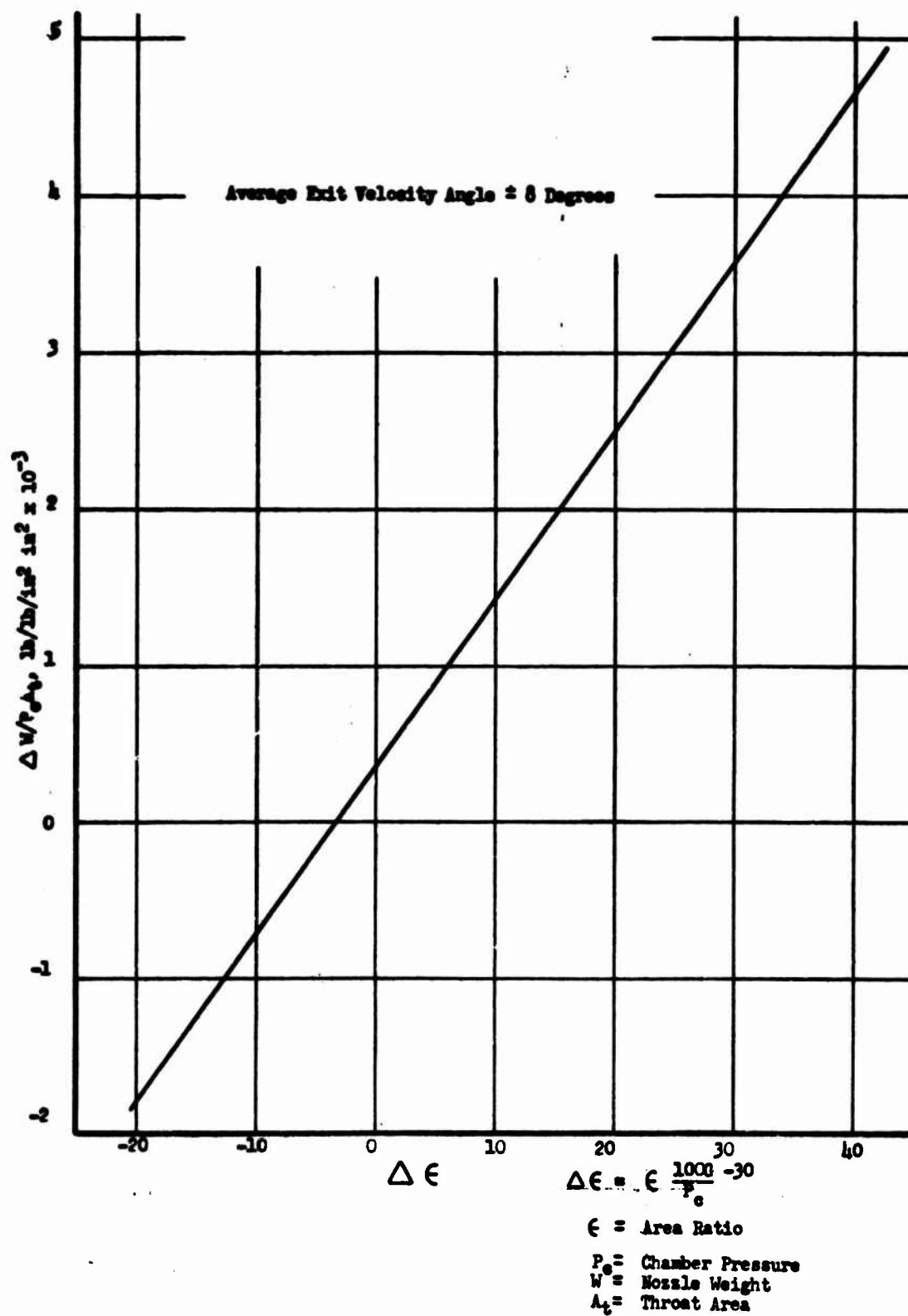
Key	Production Engines	P_c , psia
1	LR91-AJ-5 (Titan II 2nd Stage)	819
2	LR87-AJ-5 (Titan II 1st Stage)	766
3	Engine Weight Studies	
3	200K (O_2/H_2)	
4	800K ($H_2O_2/A-50$)	
5	HS -10 (1.5M $O_2/PP-1$)	
6	M-1 (1M O_2/H_2)	
7	2M	
8	24M	

Engine Less TPA Weights (u)

Figure X-B-2

CONFIDENTIAL

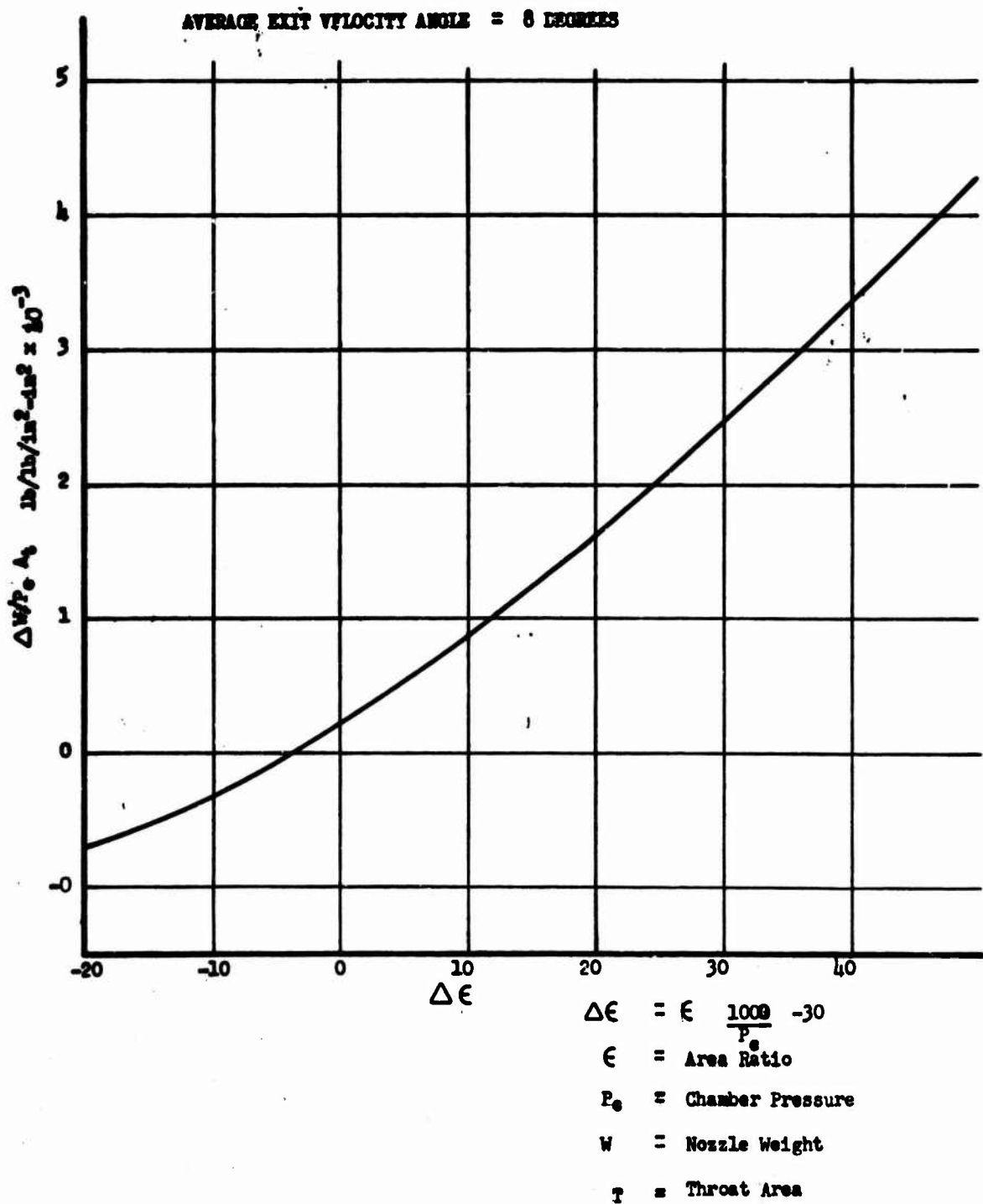
Book Two



DeLaval Nozzle Weight Variations

Figure X-B-3

Book Two



Forced-Deflection Nozzle Weight Variation

Figure X-B-4

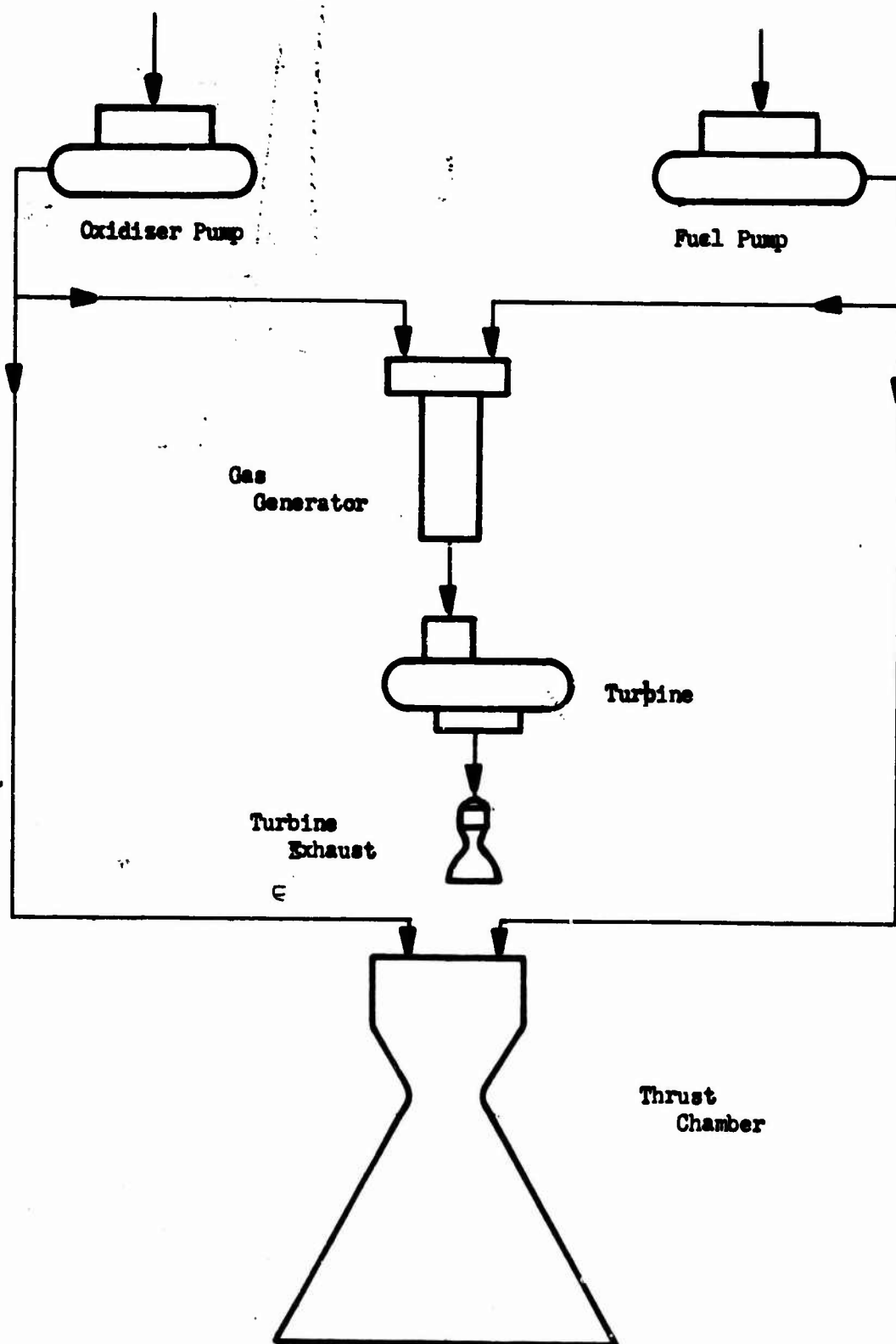
CONFIDENTIAL

<u>Symbol</u>	<u>Definition</u>
A_2	Exit area of nozzle, sq in.
A_t	Nozzle throat area, sq in.
C_T	Thrust coefficient
C_p	Specific heat at constant pressure, Btu/lb-°R
c^*	Characteristic velocity, ft/sec
g	Gravity constant, ft/sec ²
Δh	Enthalpy drop across nozzle, ft-lb/lb
$d(\Delta h)$	Increase in enthalpy resulting from pump work, ft-lb/lb
H	Pump head rise, ft
I_{sE}	Overall engine specific impulse, sec
$d I_{sPW}$	Specific impulse resulting from pump work, sec
I_{sTMC}	Thrust-chamber specific impulse obtained from thermochemical data, sec
I_{sTC}	Effective thrust chamber specific impulse, $I_{sTMC} + d I_{sPW}$, sec
I_{sD}	Specific-impulse degradation, sec
I_{sTE}	Specific impulse of the turbine exhaust products, sec
J	778 ft-lb/Btu
K	Ratio of specific heats
K_1, K_2, K_3, K_{ind}	Constants
MR_E	Overall engine mixture ratio
MR_{GG}	Gas-generator mixture ratio
MR_{TC}	Thrust-chamber mixture ratio
η_f	Fuel pump efficiency
η_o	Oxidizer pump efficiency
η_t	Turbine efficiency
P_c	Combustion pressure, psia
P_D	Pump discharge pressure, psia
P_1	Turbine exit pressure, psia
P_2	Nozzle exit pressure, psia
P_3	Ambient pressure, psia
R	Gas constant $\frac{ft \cdot lb}{lb \cdot mole \cdot ^\circ R}$
ΔT	Temperature drop across the turbine, °R
V_e	Effective exhaust velocity, ft/sec
\dot{w}_{fGG}	Gas-generator fuel flow rate, lb/sec
\dot{w}_{oGG}	Gas-generator oxidizer flow rate, lb/sec
\dot{w}_{fTC}	Thrust-chamber fuel flow rate, lb/sec
\dot{w}_{GG}	Total gas-generator flow rate ($\dot{w}_{oGG} + \dot{w}_{fGG}$), lb/sec
\dot{w}_{TC}	Total thrust-chamber flow rate ($\dot{w}_{oTC} + \dot{w}_{fTC}$), lb/sec
λ	Divergence coefficient

Symbols for Cycle Analysis (u)

Figure X-C-1

CONFIDENTIAL



Gas Generator Cycle Schematic Diagram

Figure X-C-2

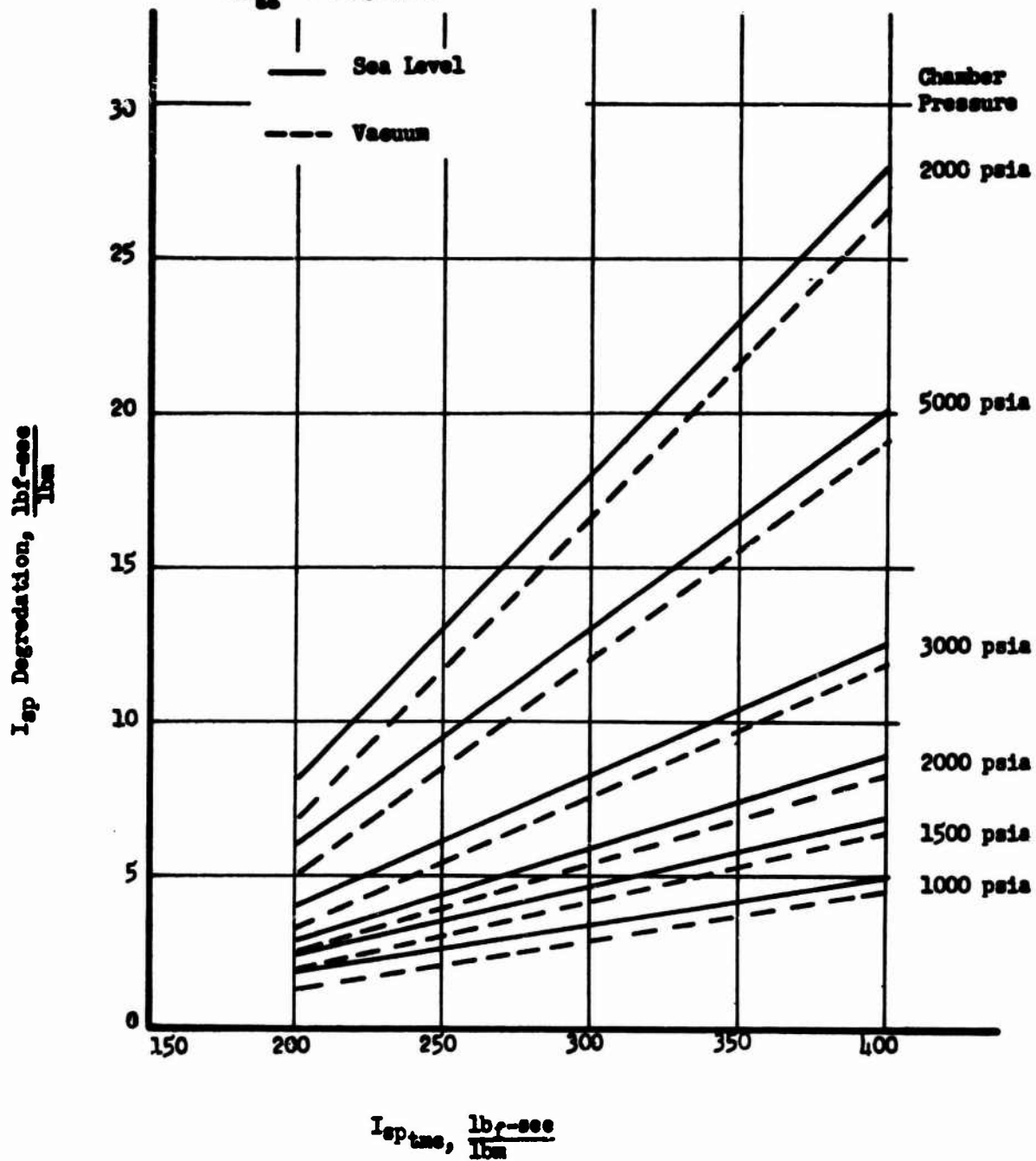
Book Two

NOTE:

Propellants, $H_2O_2/A-50$

$NR_{to} = 2.0:1.0$

$NR_{gg} = .0850:1.0$



I_{sp} Degradation, Gas Generator Cycle

Figure X-C-3

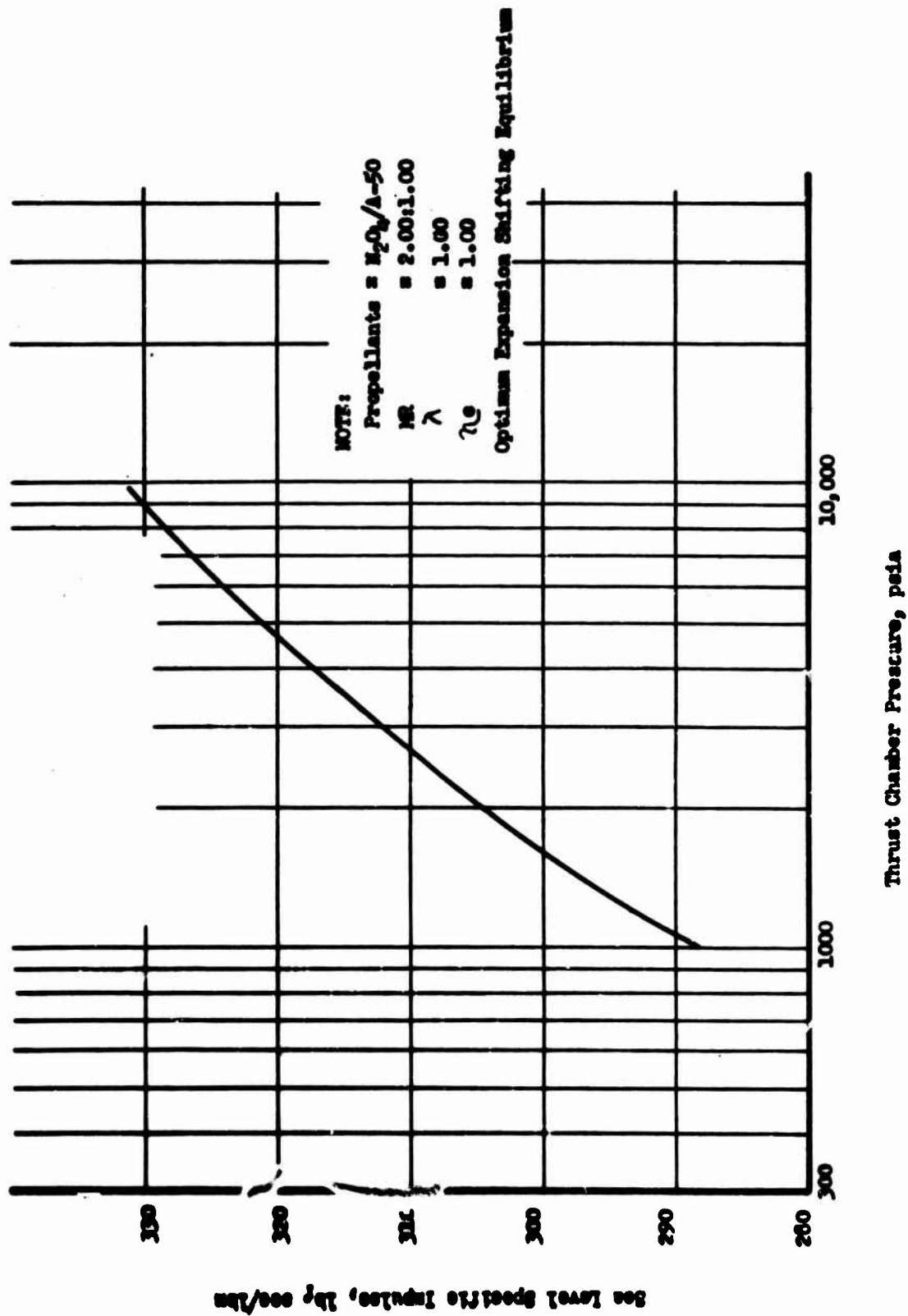
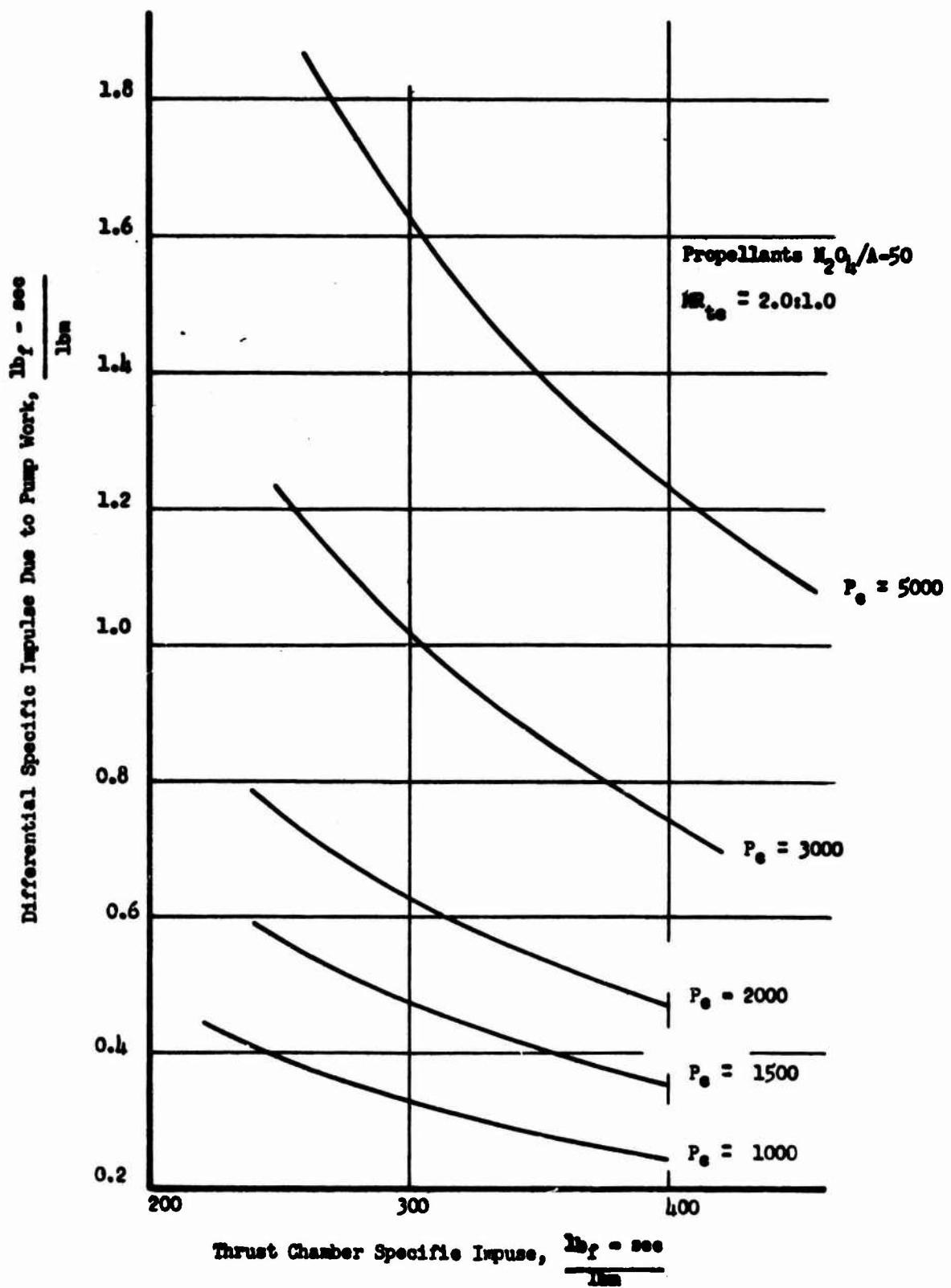


Figure X-C-4

Specific Impulse vs Chamber Pressure

Book Two



ΔI_s Due to Pump Work

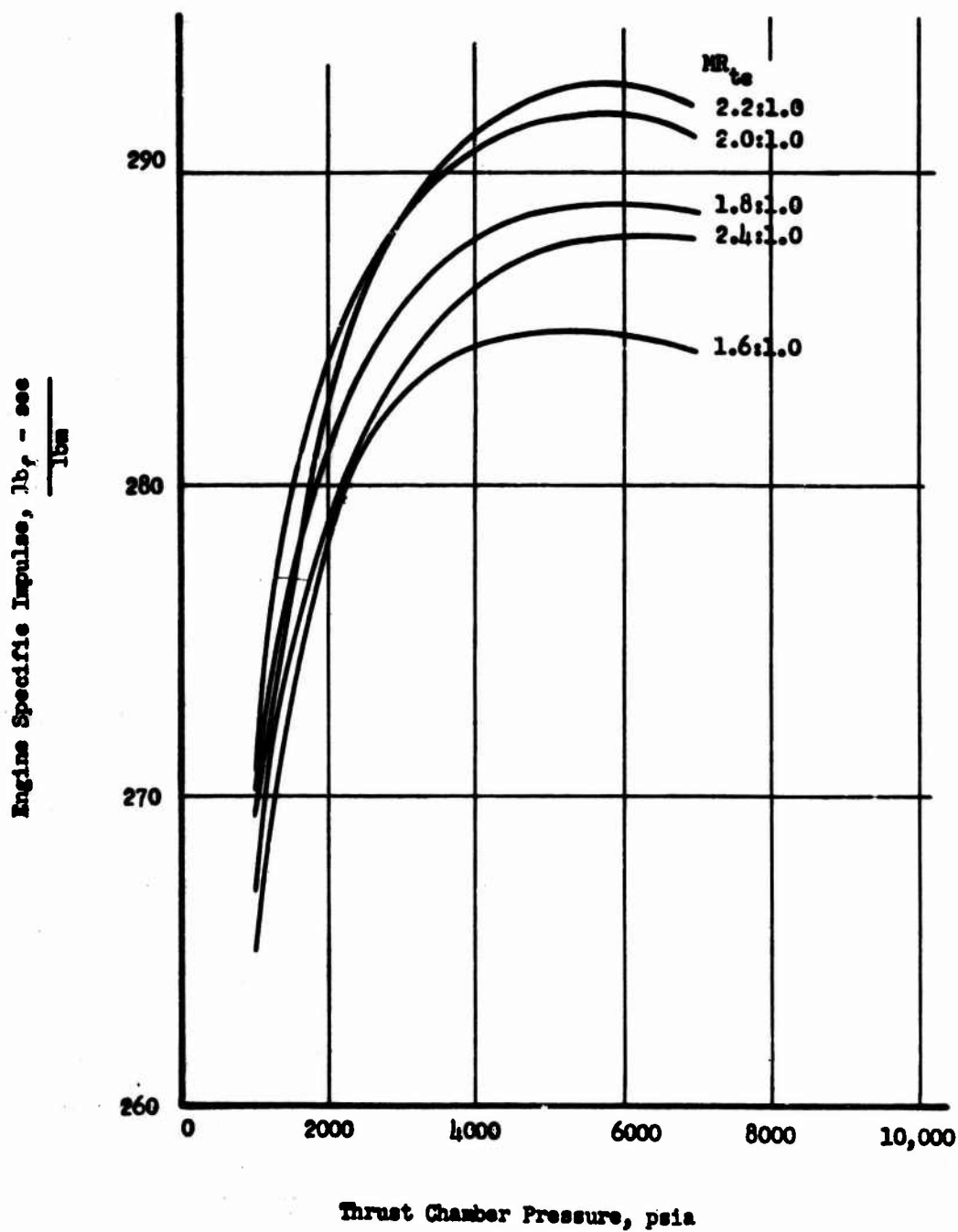
Figure X-C-5

Book Two

NOTE:

Propellants: $\text{N}_2\text{O}_4/\text{A-50}$

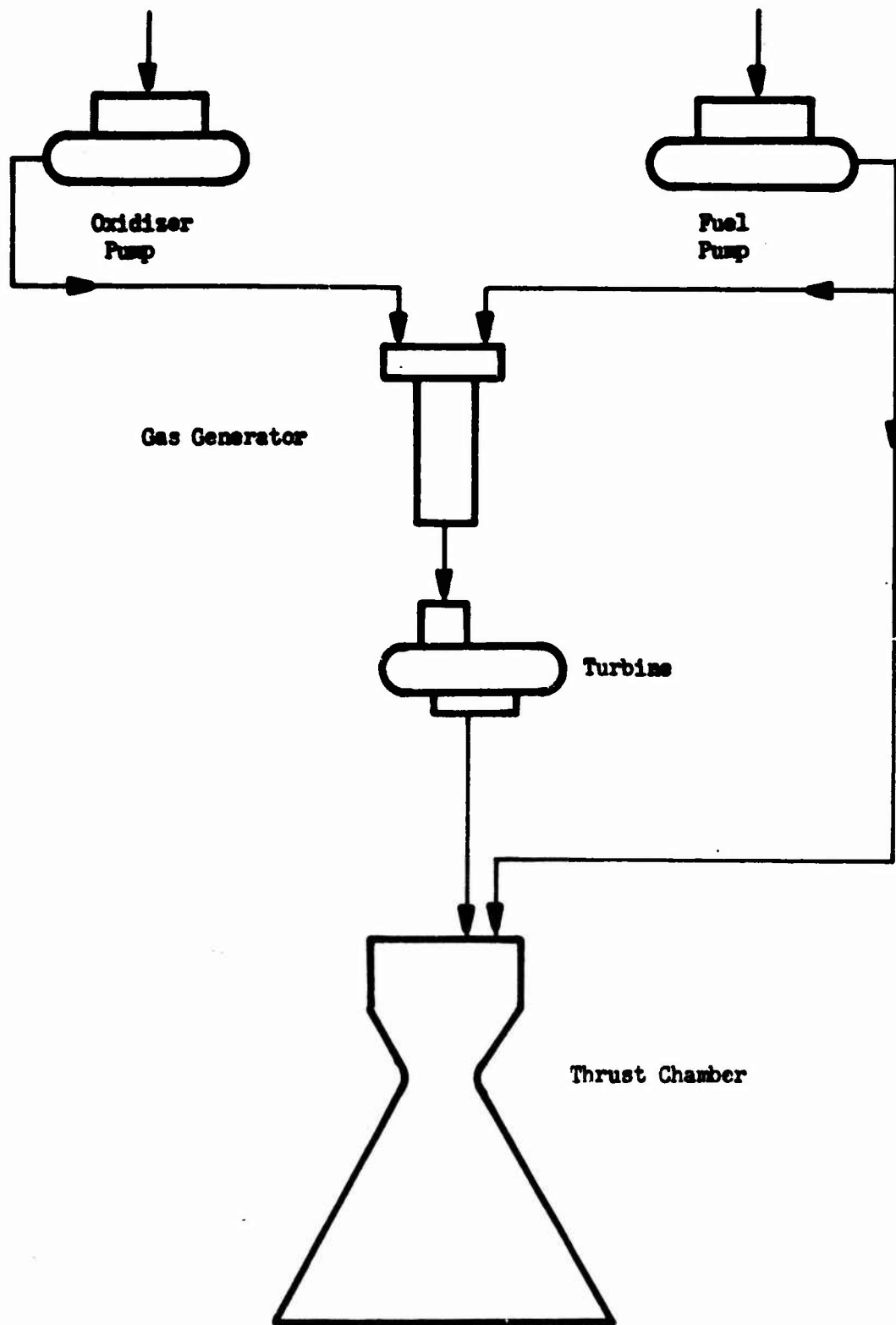
$\text{MR}_{\text{gg}} = .085:1.0$



Specific Impulse vs Chamber Pressure, Gas Generator Cycle

Figure X-C-6

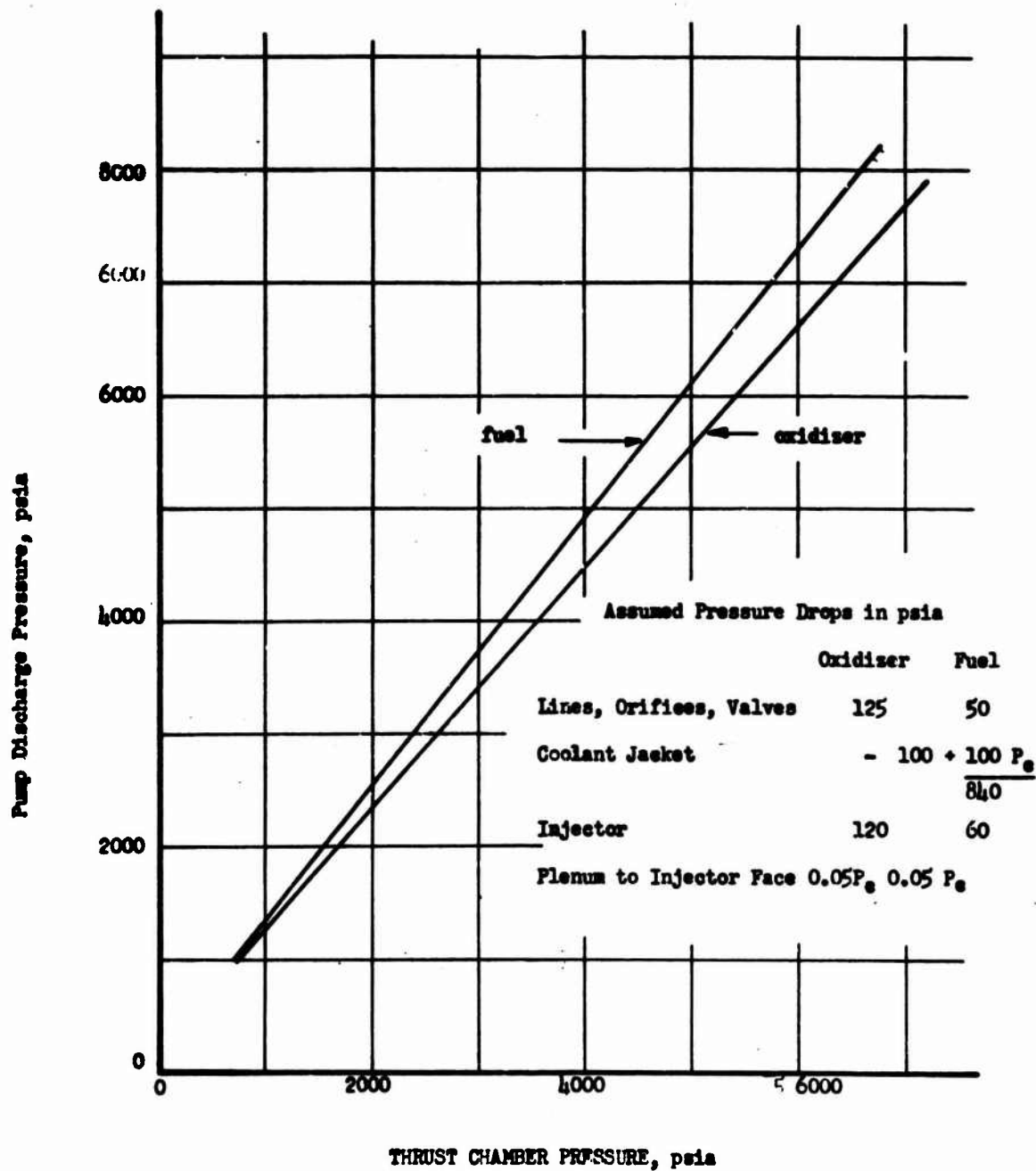
Book Two



Staged Combustion Cycle Schematic

Figure X-C-7

Book Two



Pump Discharge Pressure vs Chamber Pressure, Gas Generator Cycle

Figure X-C-8

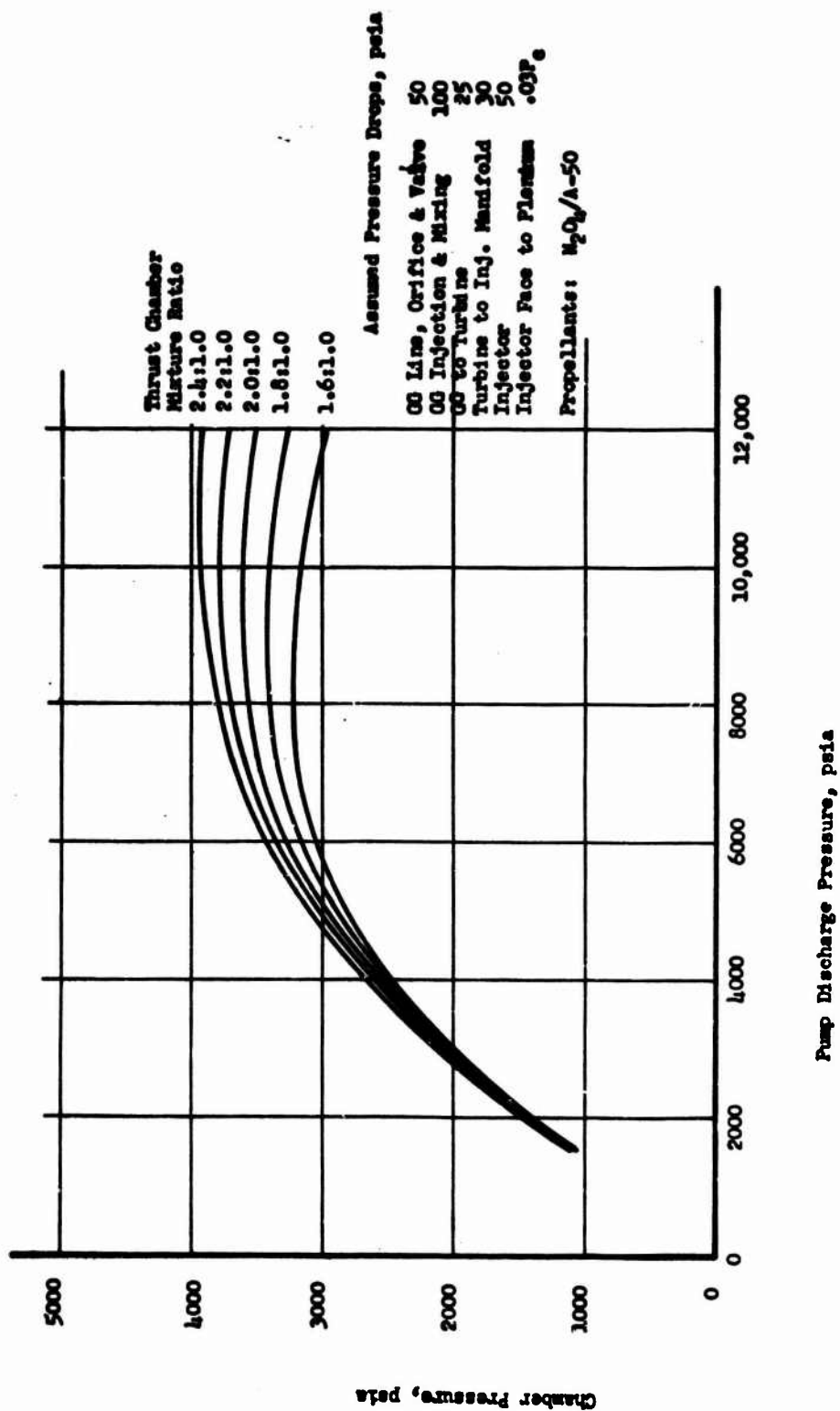
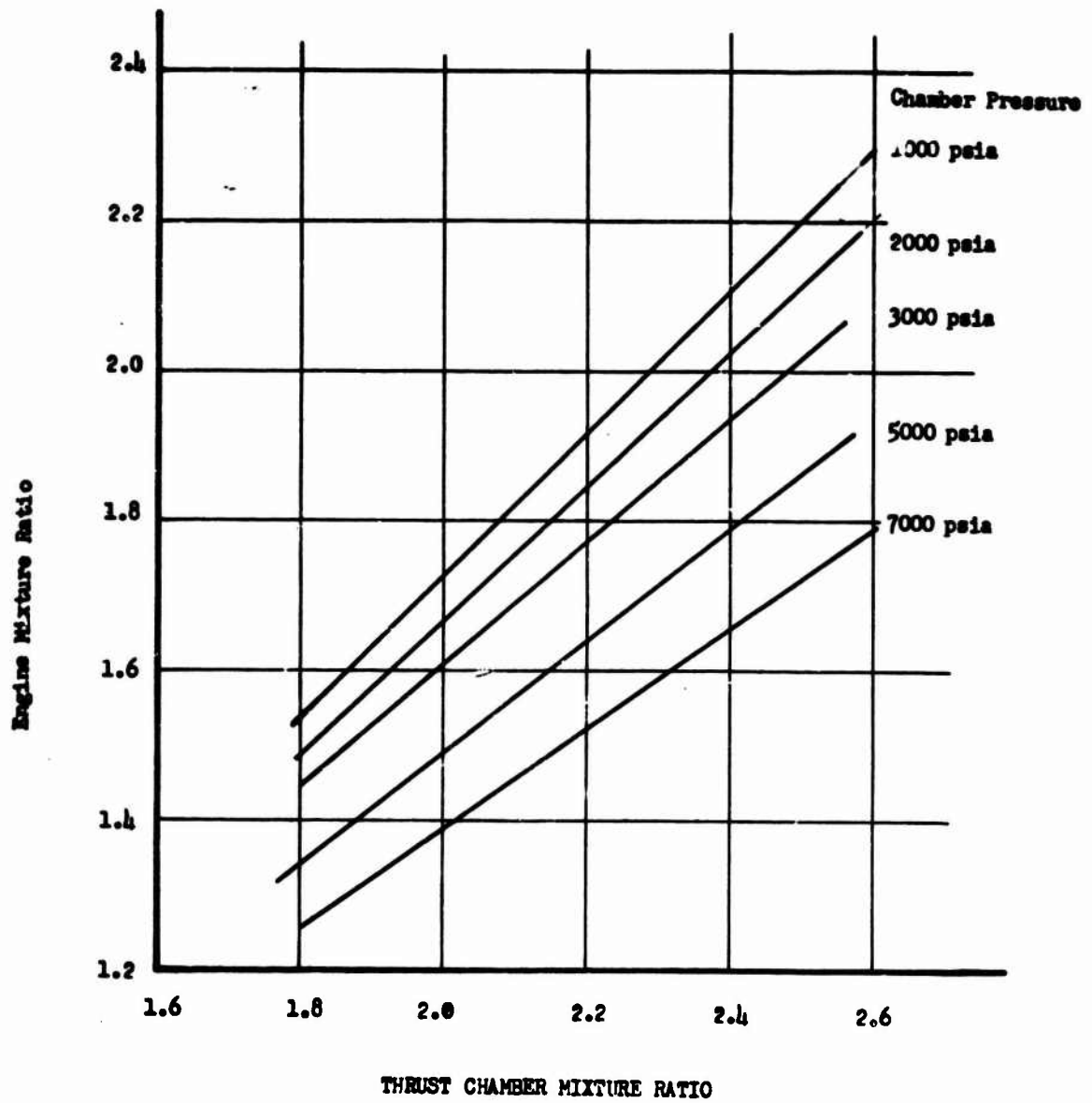


Figure X-C-9

Chamber Pressure Pump Discharge Pressure, Staged Combustion Cycle

Book Two

Propellants $H_2O_2/A-50$
 $MR_{gg} = .005:1.0$



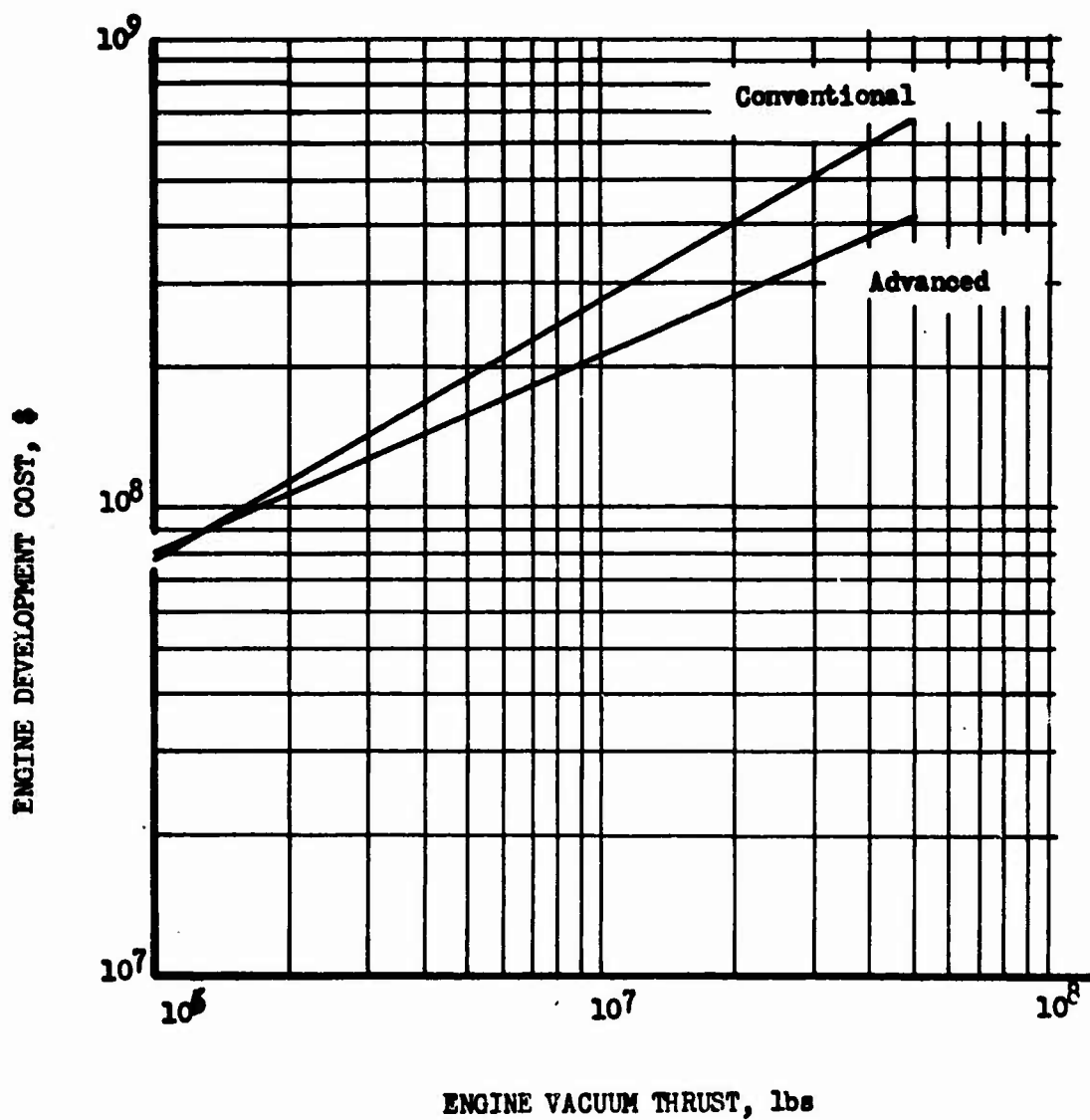
Engine Mixture Ratio vs Thrust Chamber Mixture Ratio

Figure X-C-10

Book Two

Propellants - $N_2O_4/A-50$

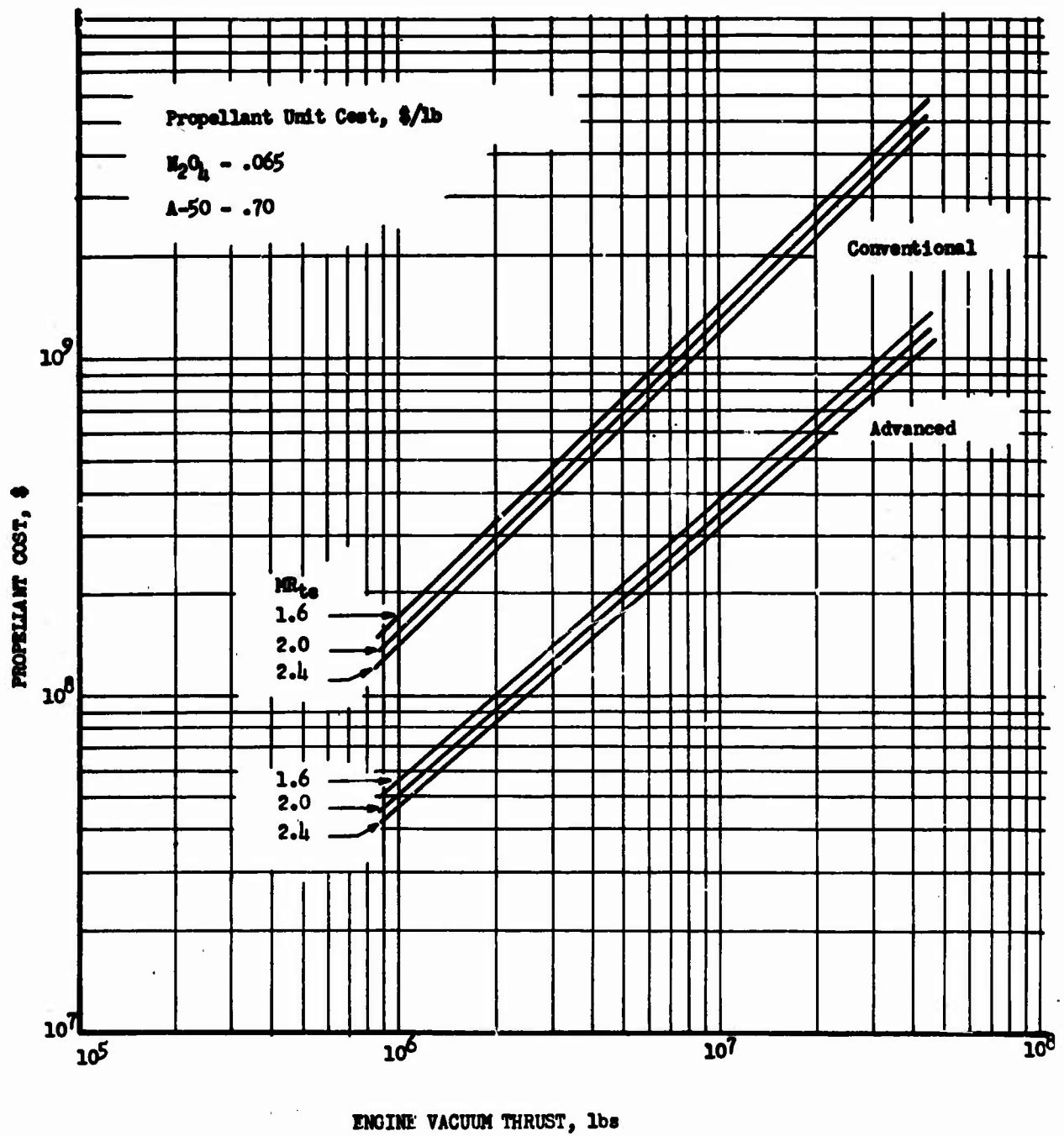
Cost includes engineering, test fabrication
and R&D tooling



Engine Development Cost

Figure X-D-1

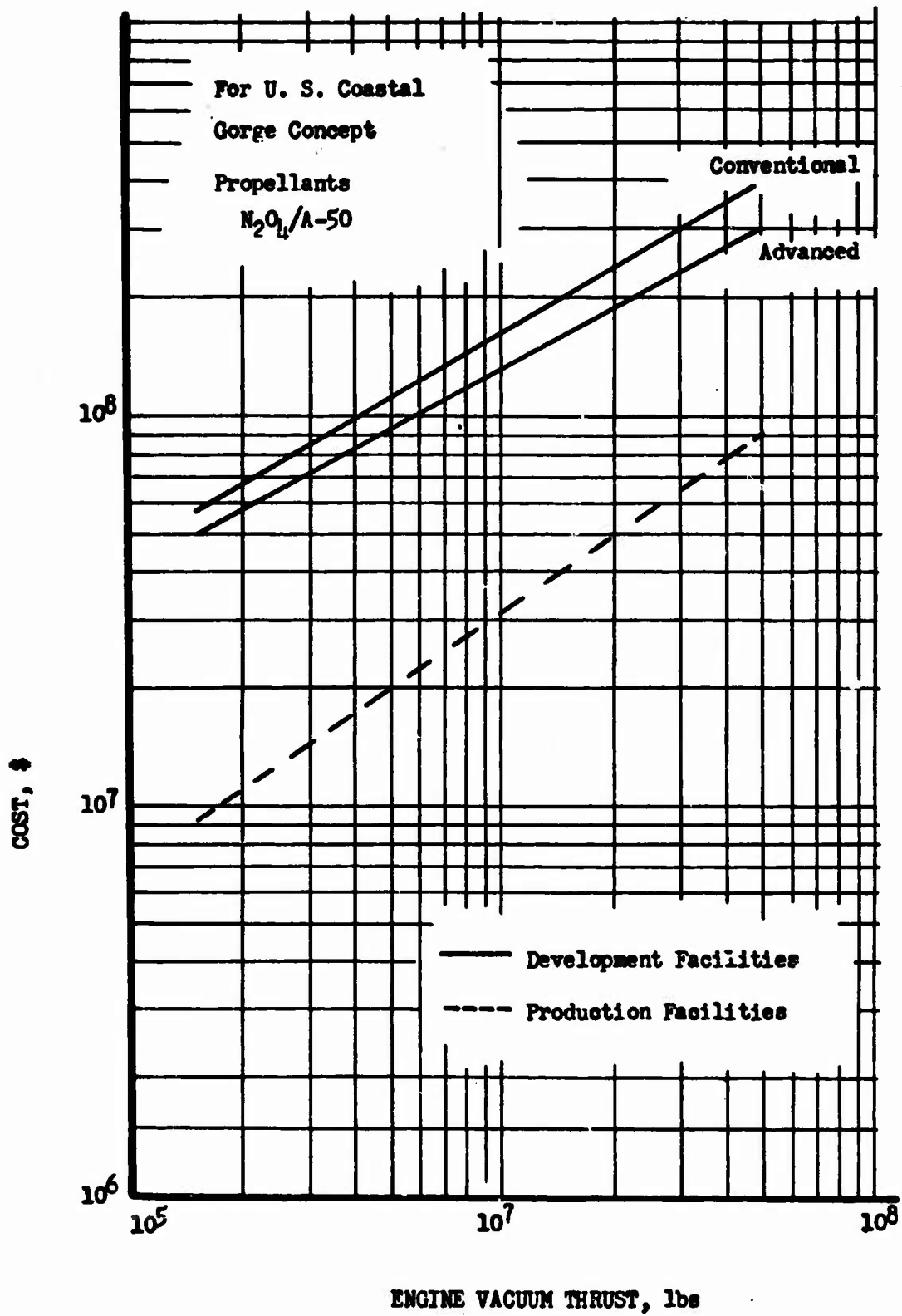
Book Two



Propellant Costs for Engine Development

Figure X-D-2

Book Two



Facility Costs

Figure X-D-3

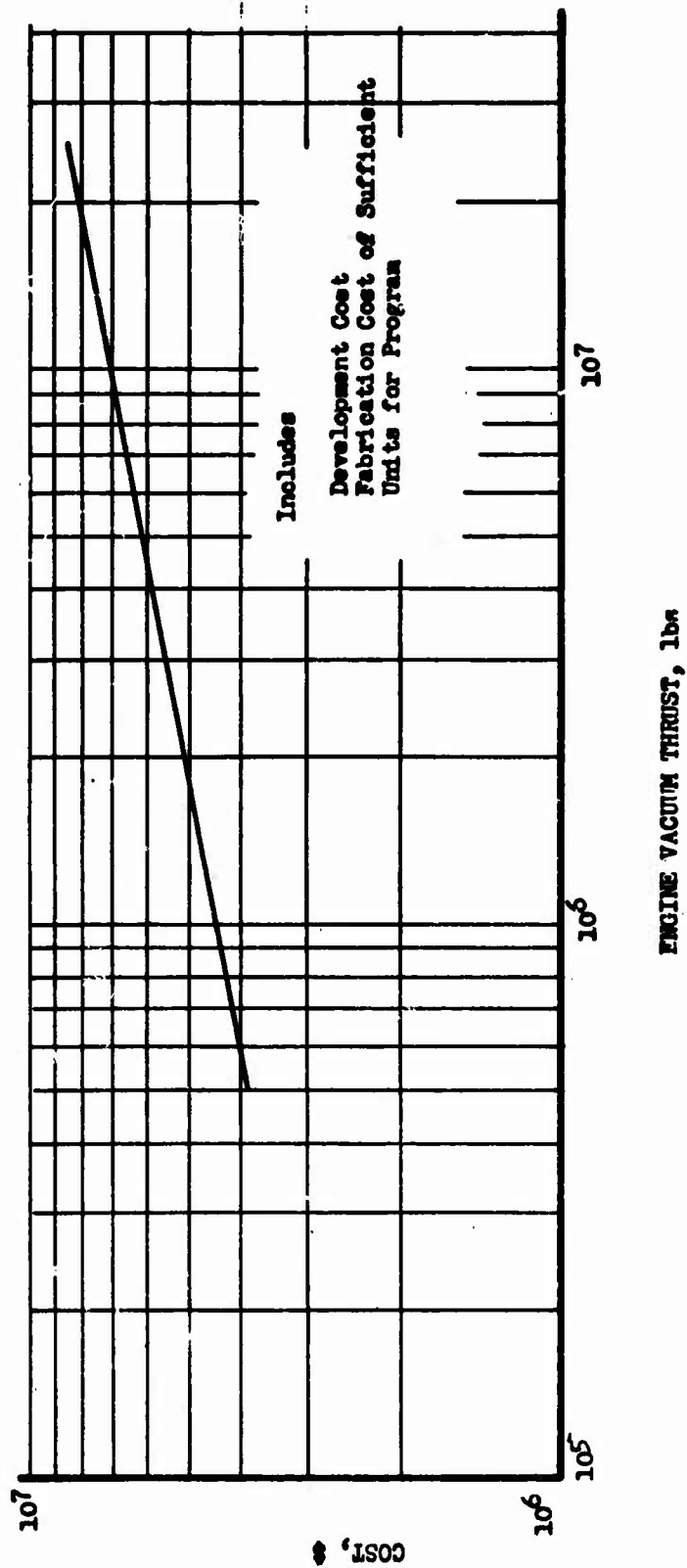


Figure X-D-4

GSE Costs

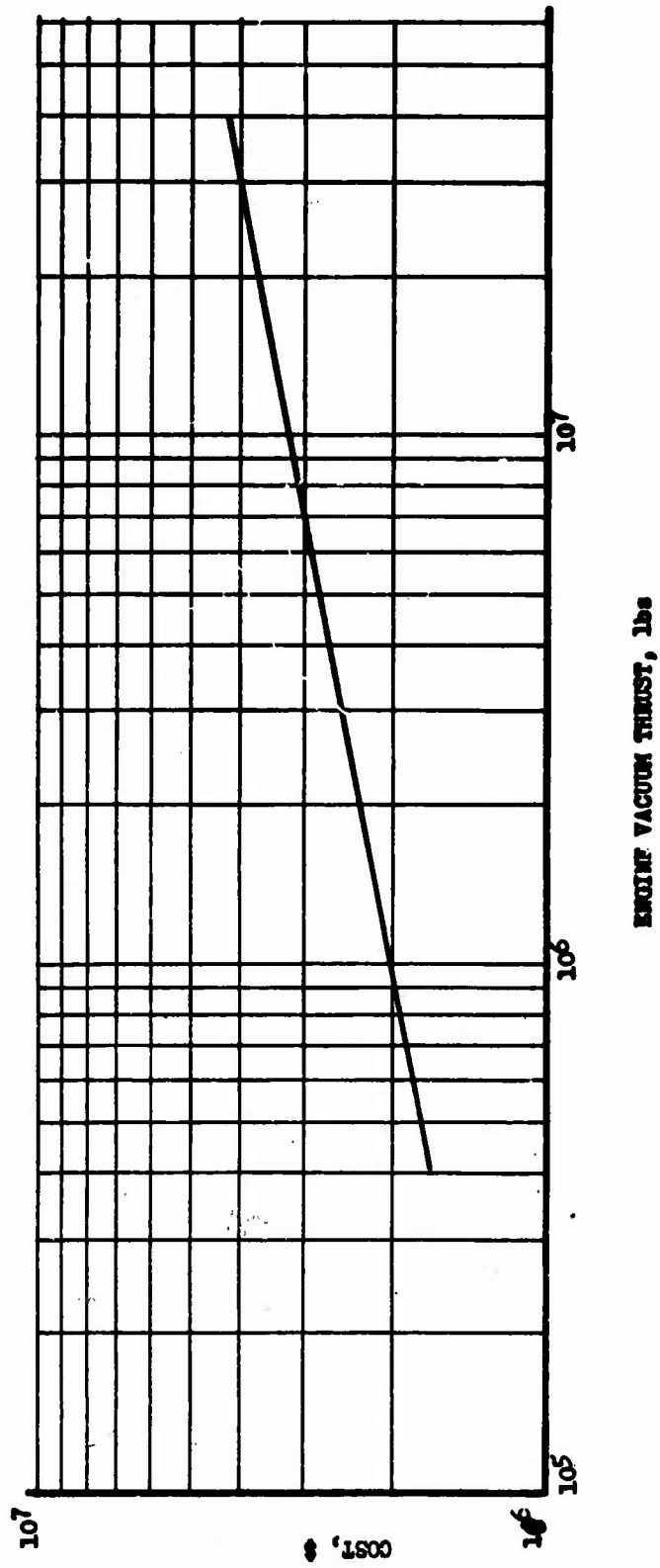
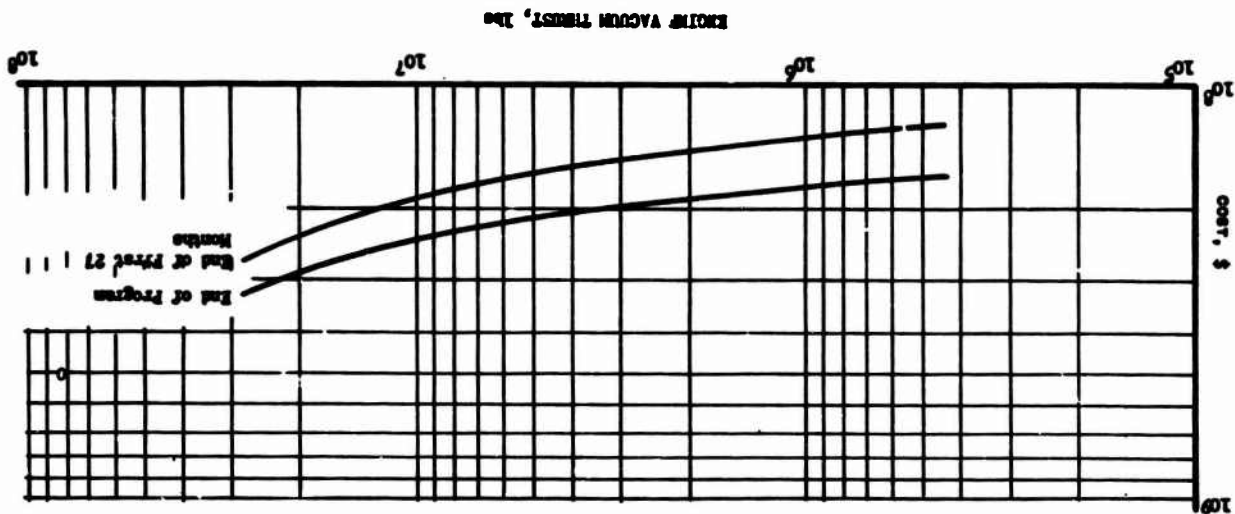


Figure X-D-5

Engine Production Tooling Costs



STAGE DEVELOPMENT PROGRAM
COST SUMMARY
(INCLUDES ONE DELIVERED STAGE)

	TITAN STAGE 1	STANDARD VEHICLE STAGE 1	ON 18 THRUST BOOSTER (0.2/1.2)
FIRST 27 MONTHS (THROUGH DELIVERY OF FIRST UNIT) ENGINEERING & PROJECT CONTROL	42.1	42.1	42.1
TOOLING (LARGE) (CAPITAL EQUIPMENT)	7.7	7.7	7.7
MANUFACTURE DEVELOPMENT (8 UNITS) (FABRICATION & MATERIAL ONLY)*	7.5	16	21
GROUND EQUIPMENT DEVELOPMENT	1/0	7.2	12.8
TEST STANDS (2 POSITIONS) (INCLUDING PROPELLANT STORAGE)	60	60	60
TEST STAND OPERATION PROPELLANT (60 FULL DURATION RUNS)	4.8	7.3	8.2
BATTLESHIP STAGE (FABRICATION & MATERIAL ONLY)*	.4	2.8	8.4
FIRST DELIVERED STAGE (FABRICATION & MATERIAL, INSTRUMENTATION & 8005, PRODUCTION TEST) ENGINE	.3	1.2	2.2
	.8	2.2	4.0
	.6	2.4	4.3
	.4	1.1	2.0
TOTAL FOR FIRST 27 MONTHS	128.6	149.0	173.8
POST DELIVERY DEVELOPMENT AND PROJECT CONTROL EXCLUSIVE OF HARDWARE (6 YEARS)	41.2	41.2	41.2
TOTAL FOR ENTIRE PROGRAM (7 YEARS, 3 MONTHS)	167.8	190.2	215.0

Stage Development Cost

* ASSUMED TO BE 1/2 OF TOTAL STAGE FABRICATION COST

Figure X-D-6

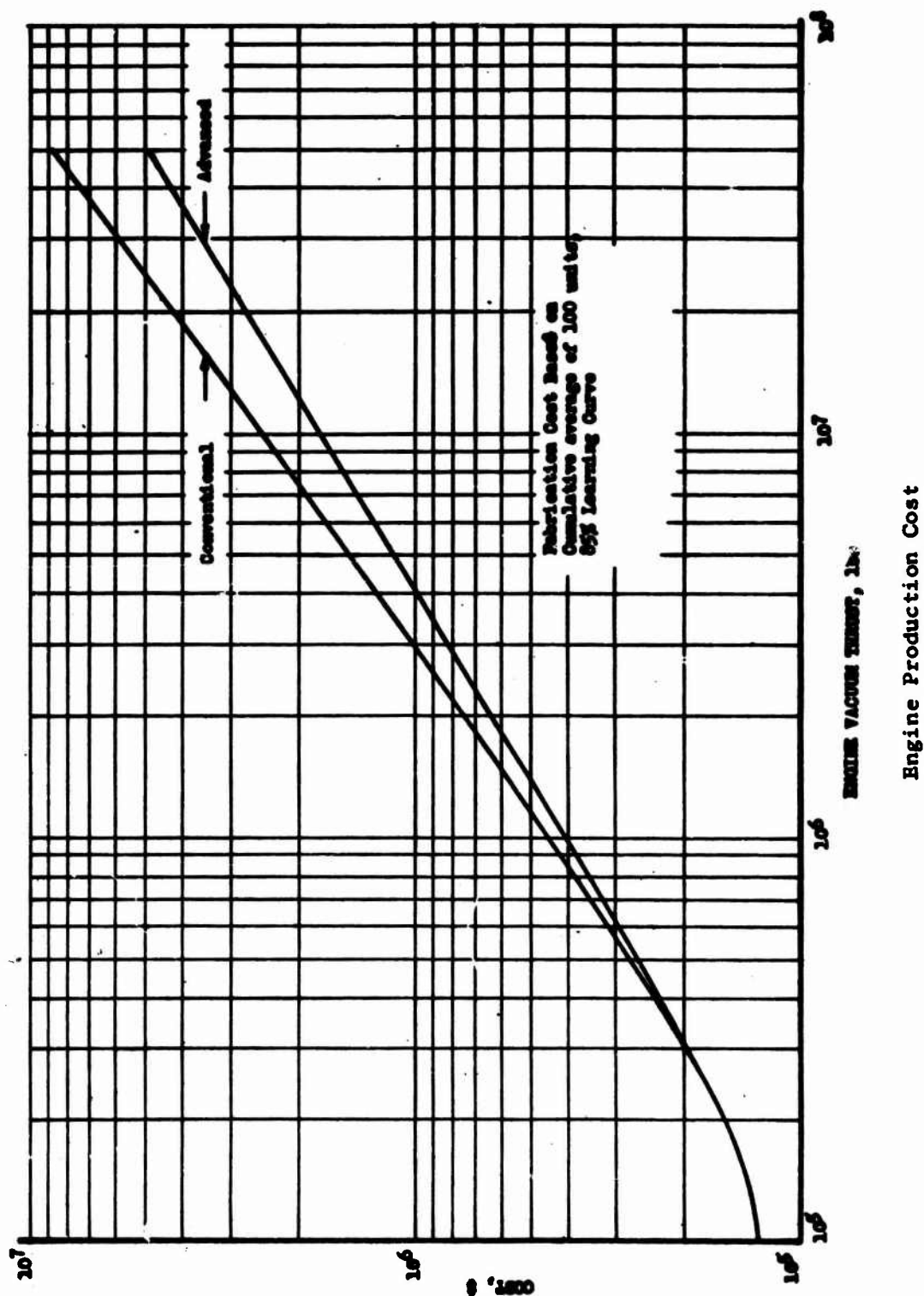


Figure X-D-7

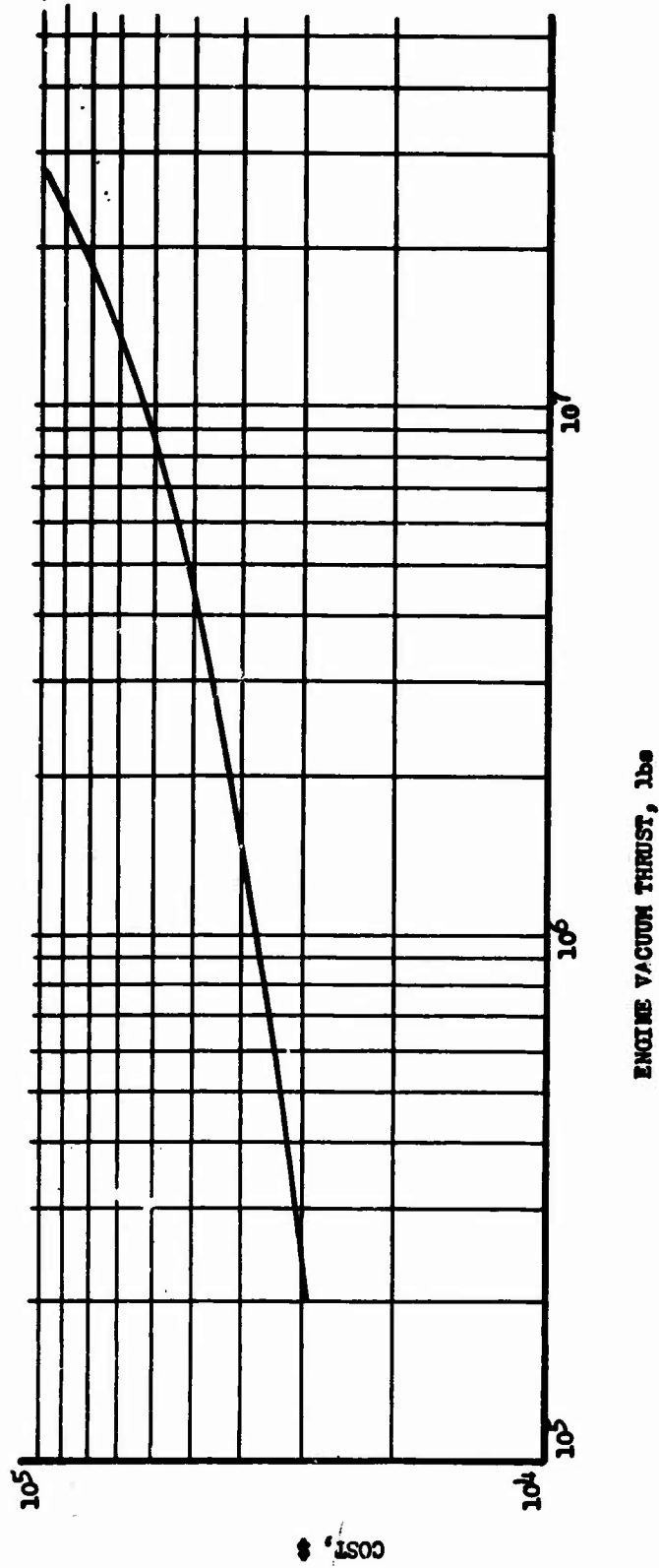
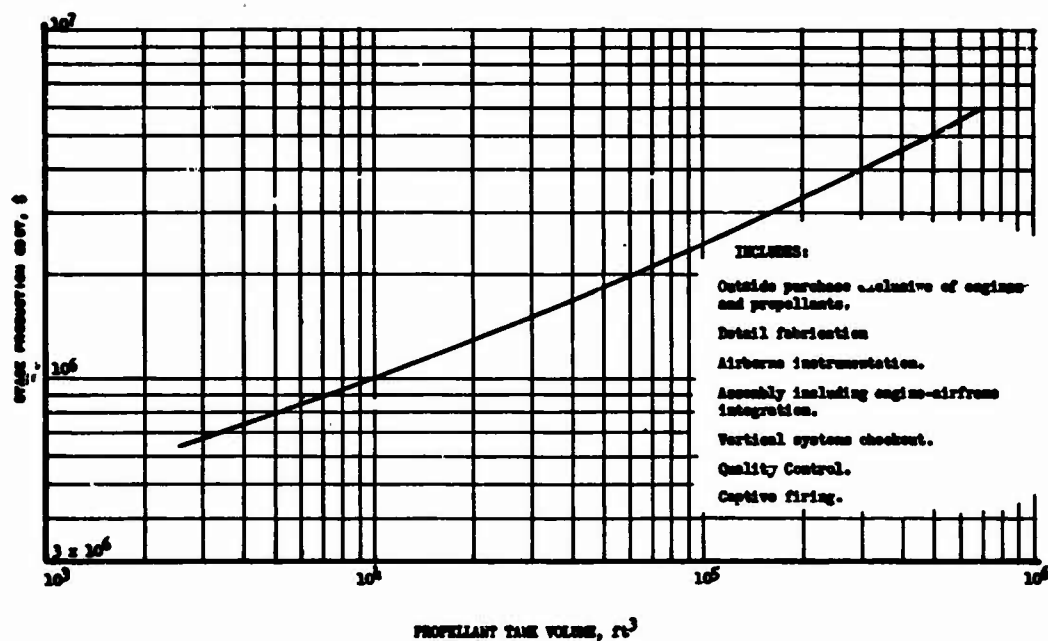


Figure X-D-8

Engine Acceptance Testing Cost

Book Two



PRODUCTION COSTS I STAGE OUR AVE 500 UNITS 85% LEARNING CURVE

	TOTAL	STANDARD	SM
I. OUTSIDE PURCHASE DETAIL FABRICATION	304,000	1,470,000	2,543,000
II. AIRFRAME INSTRUMENTATION	19,000	19,000	19,000
III. ASSEMBLY PRODUCTION TESTING VERTICAL SYSTEM C/O G.C.	198,000	198,000	198,000
TOTAL AIRFRAME PRODUCTION	521,000	1,687,000	2,760,000
IV. ERECTION IN TEST STAND CAPTIVE FIRING	129,000	193,000	240,000
TOTAL COST AT AF MFG PLANT	650,000	1,880,000	3,000,000
PROPELLANT TANK VOLUME	2,800	51,300	154,000

Stage Production Cost

Figure X-D-9

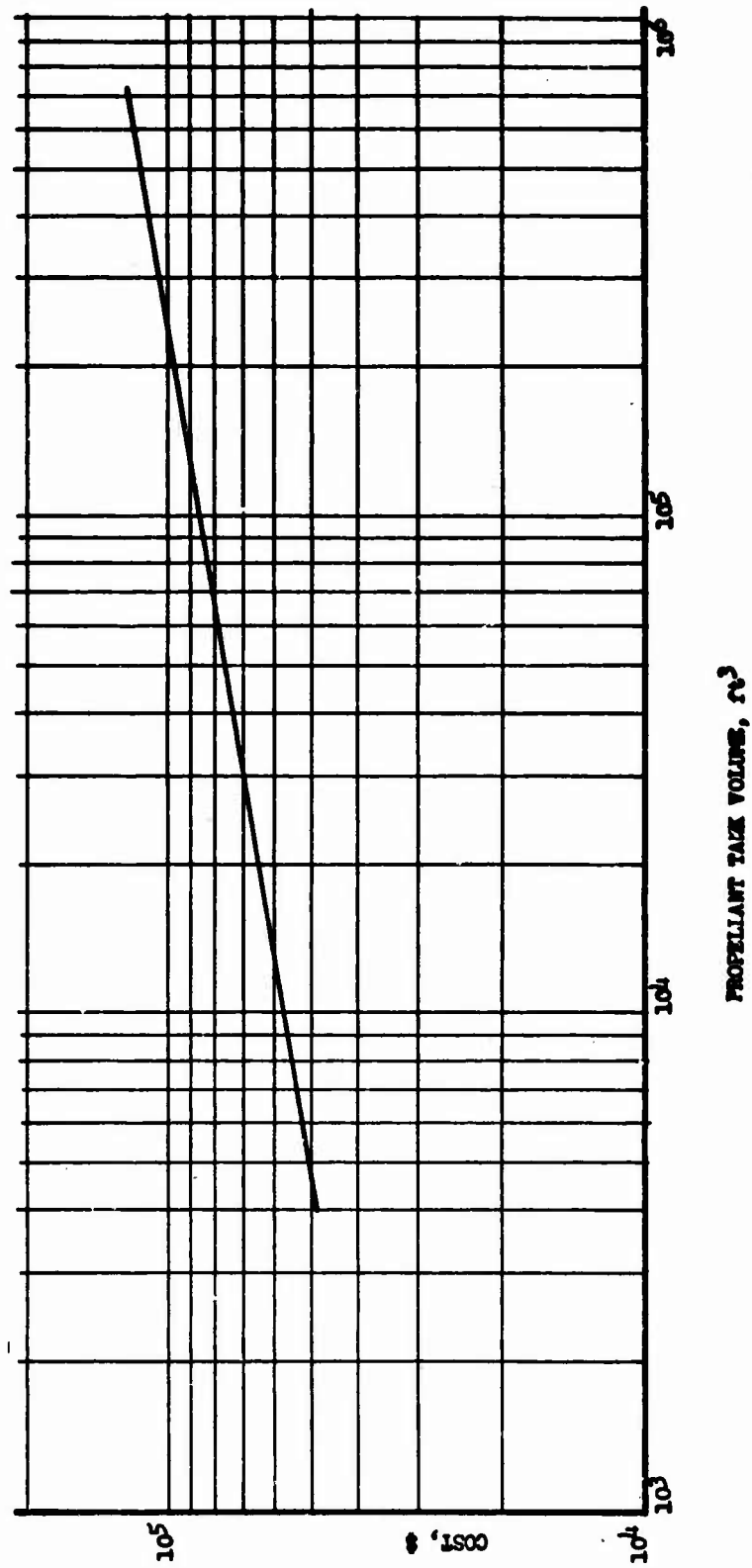
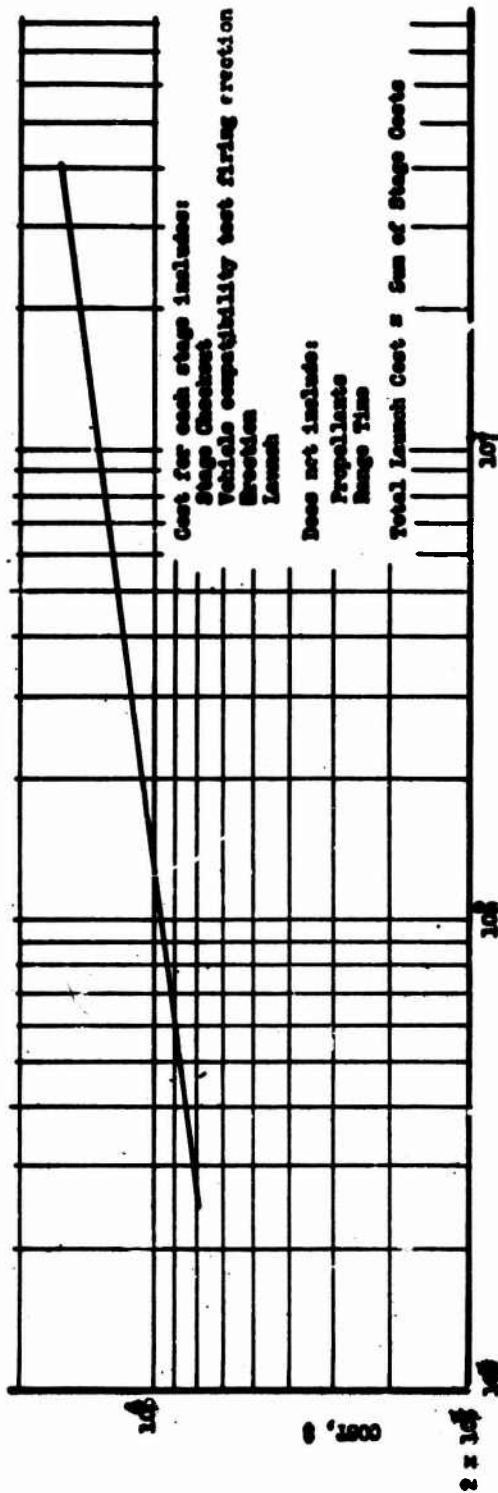


Figure X-D-10

Stage Transportation Cost



ENGINE VACUUM THRUST, lbs.

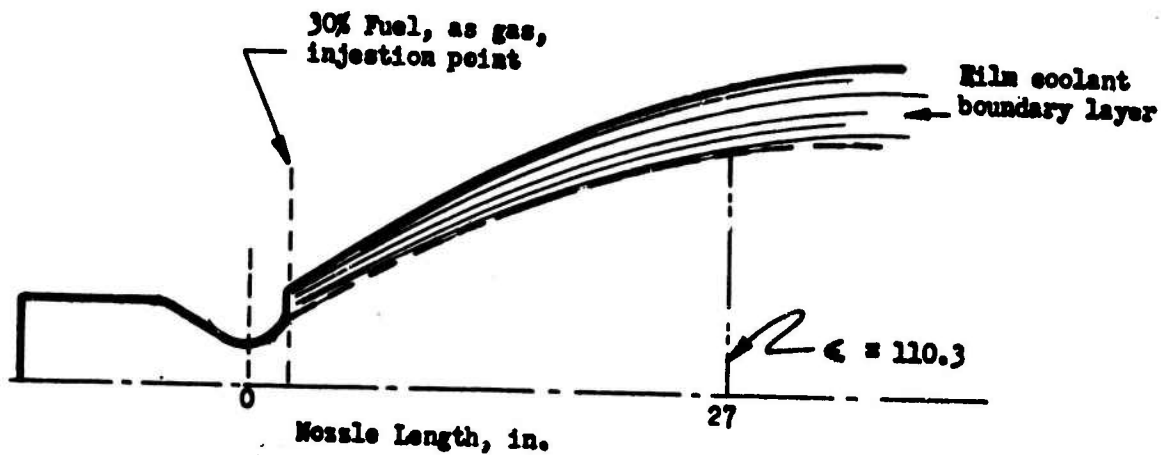
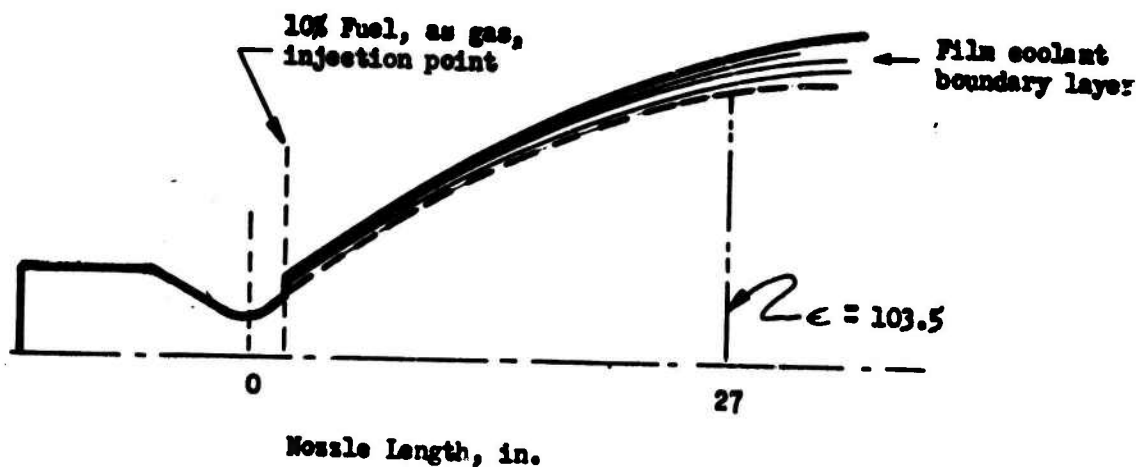
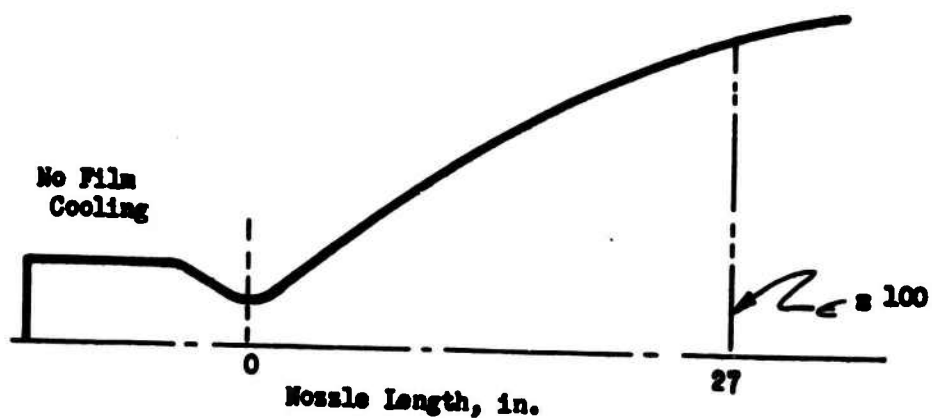
Stage Launch Operation Cost

Figure X-D-11



Figure X-D-12

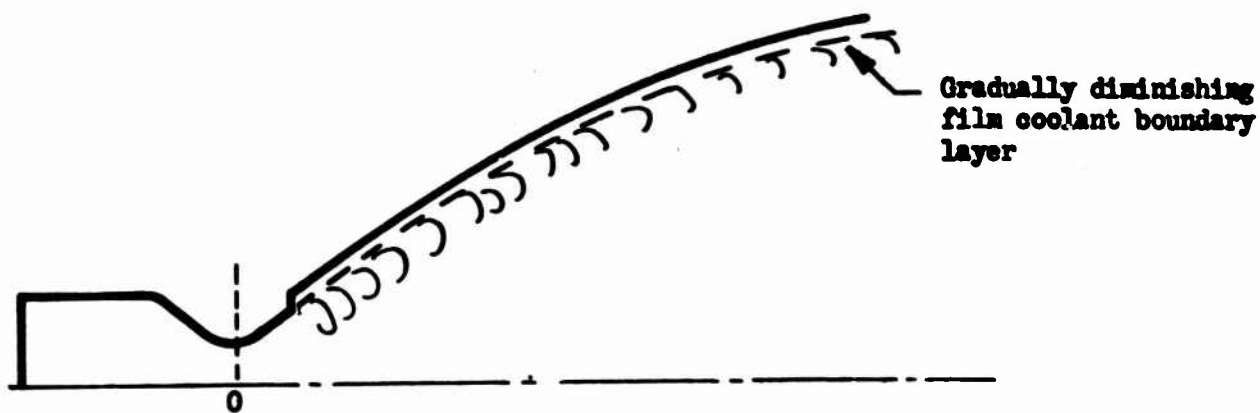
Book Two



Film-Cooling Model, No Mixing

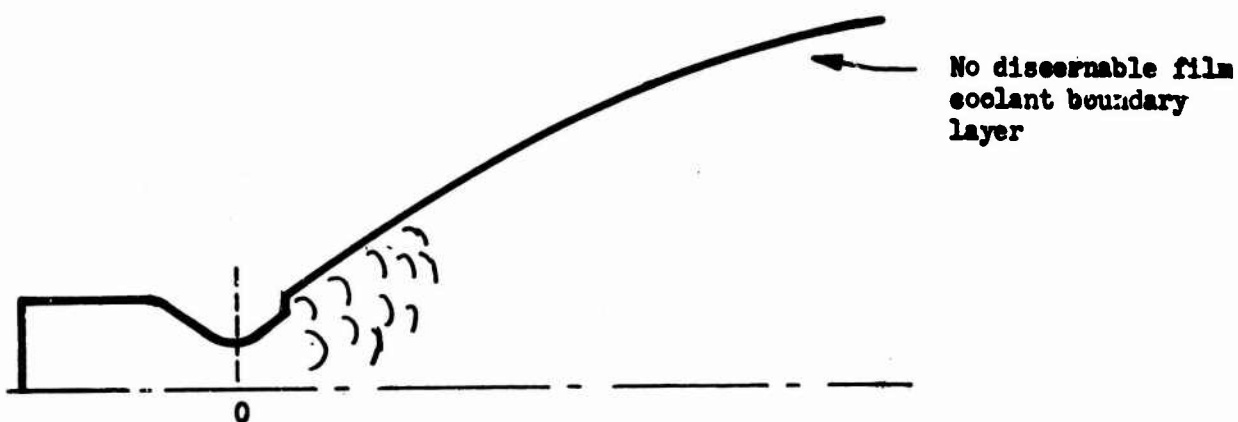
Figure X-E-1

Book Two



Nozzle Length

Partial mixing assumes uniform film coolant mixing with combustion products.



Nozzle Length

Complete mixing assumes all film coolant is mixed with combustion products at the fuel decomposition point.

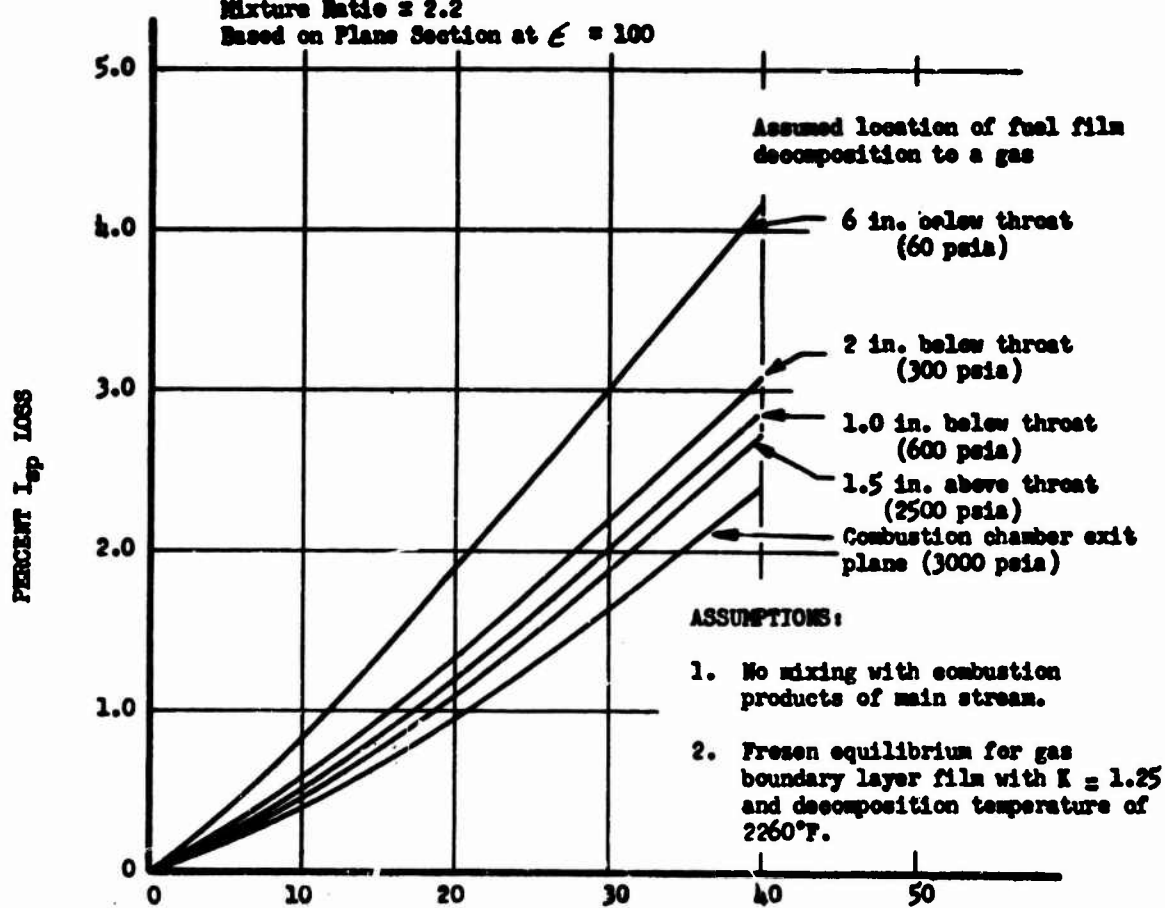
Film-Cooling Models, Partial and Complete Mixing

Figure X-E-2

Book Two

NOTE:

Coolant: A-50 gas
 Propellants: H_2O_2 /A-50
 Chamber Pressure = 3000 psia
 Mixture Ratio = 2.2
 Based on Plane Section at $\epsilon = 100$



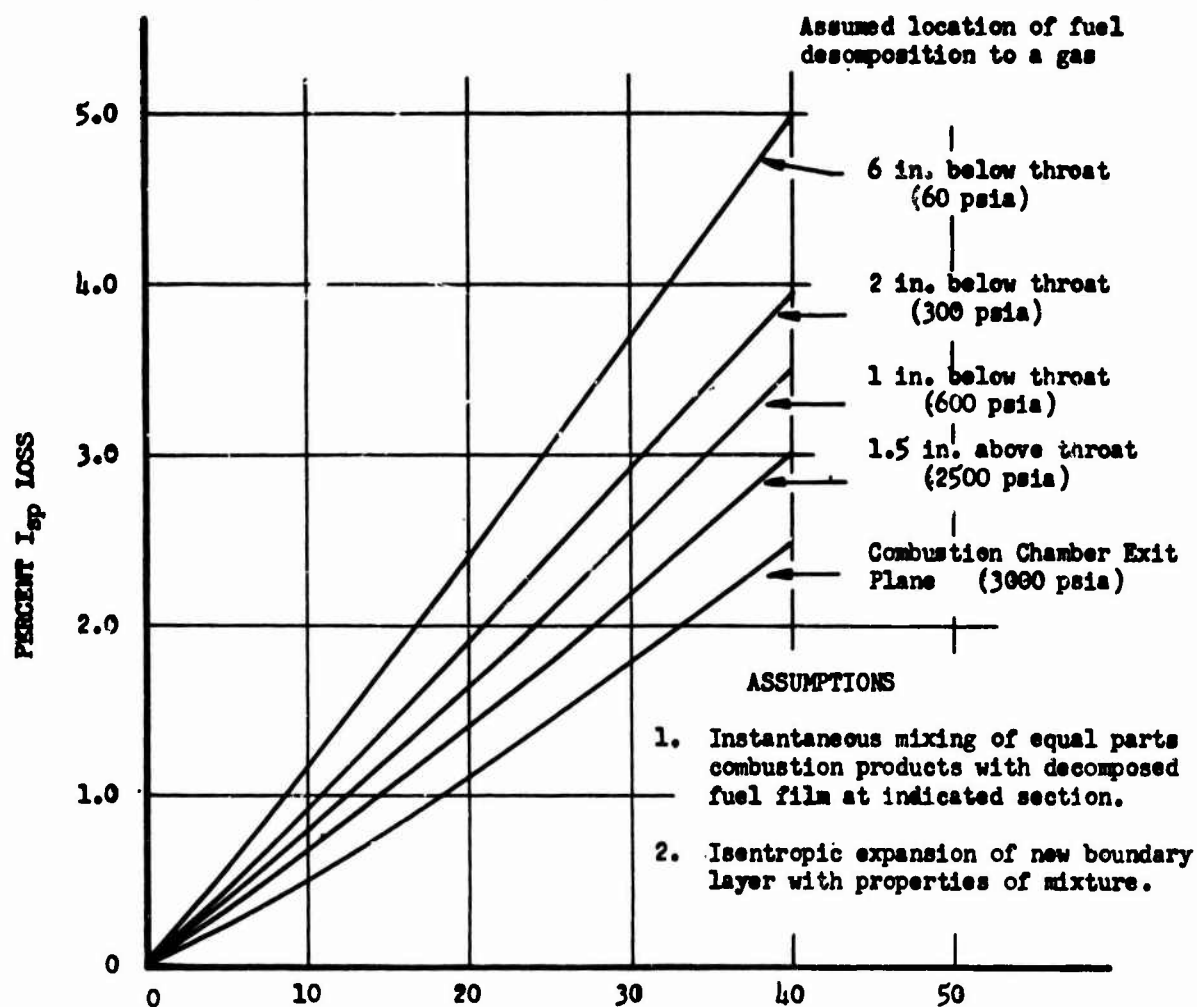
Specific Impulse Loss Due to Film Cooling, No Mixing

Figure X-E-3

Book Two

NOTE:

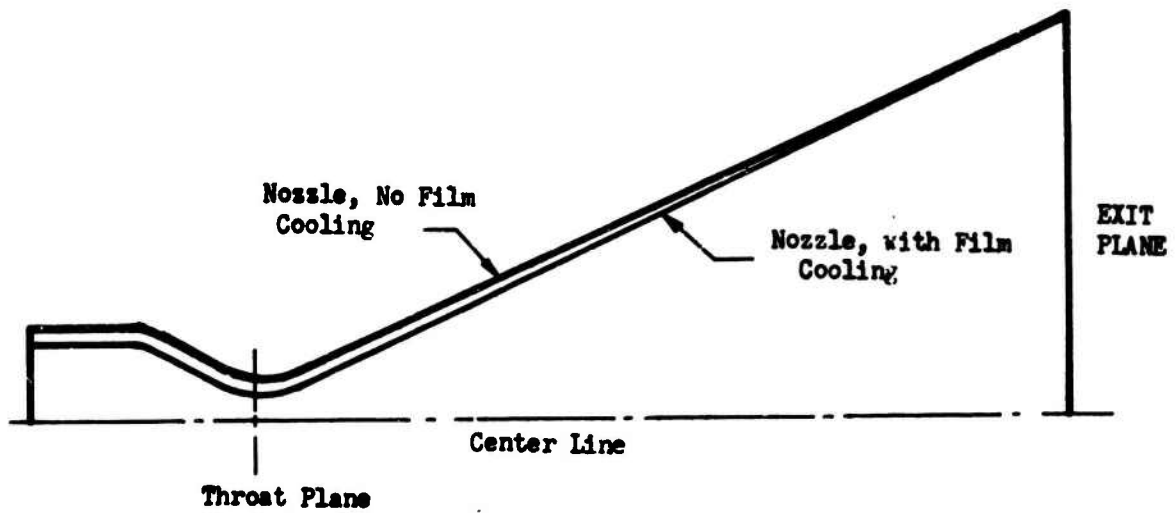
1. Coolant - A-50
2. Propellants - $\text{H}_2\text{O}_2/\text{A-50}$
3. Chamber Pressure = 3000 psia
4. Mixture Ratio = 2.2
5. Based on plane section at $\epsilon = 100$



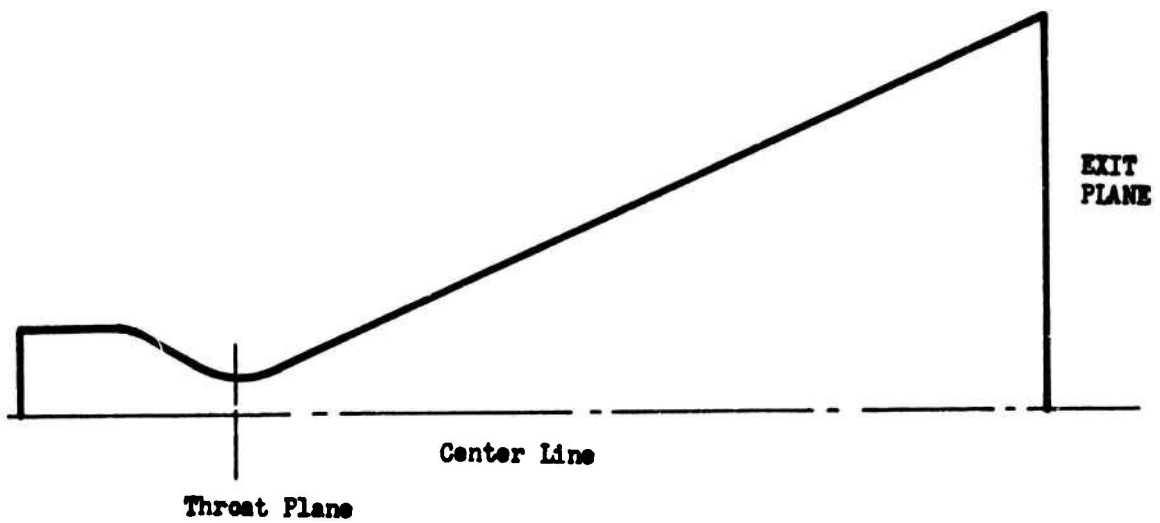
Specific Impulse Loss Due to Film Cooling, Partial Mixing

Figure X-E-4

Book Two



Complete mixing assumes film coolant is entirely mixed with the combustion product at the fuel decomposition point.



Assuming uniform amount of film coolant mixing with combustion products.

Film-Cooling Models, Complete Mixing

Figure X-E-5

Book Two

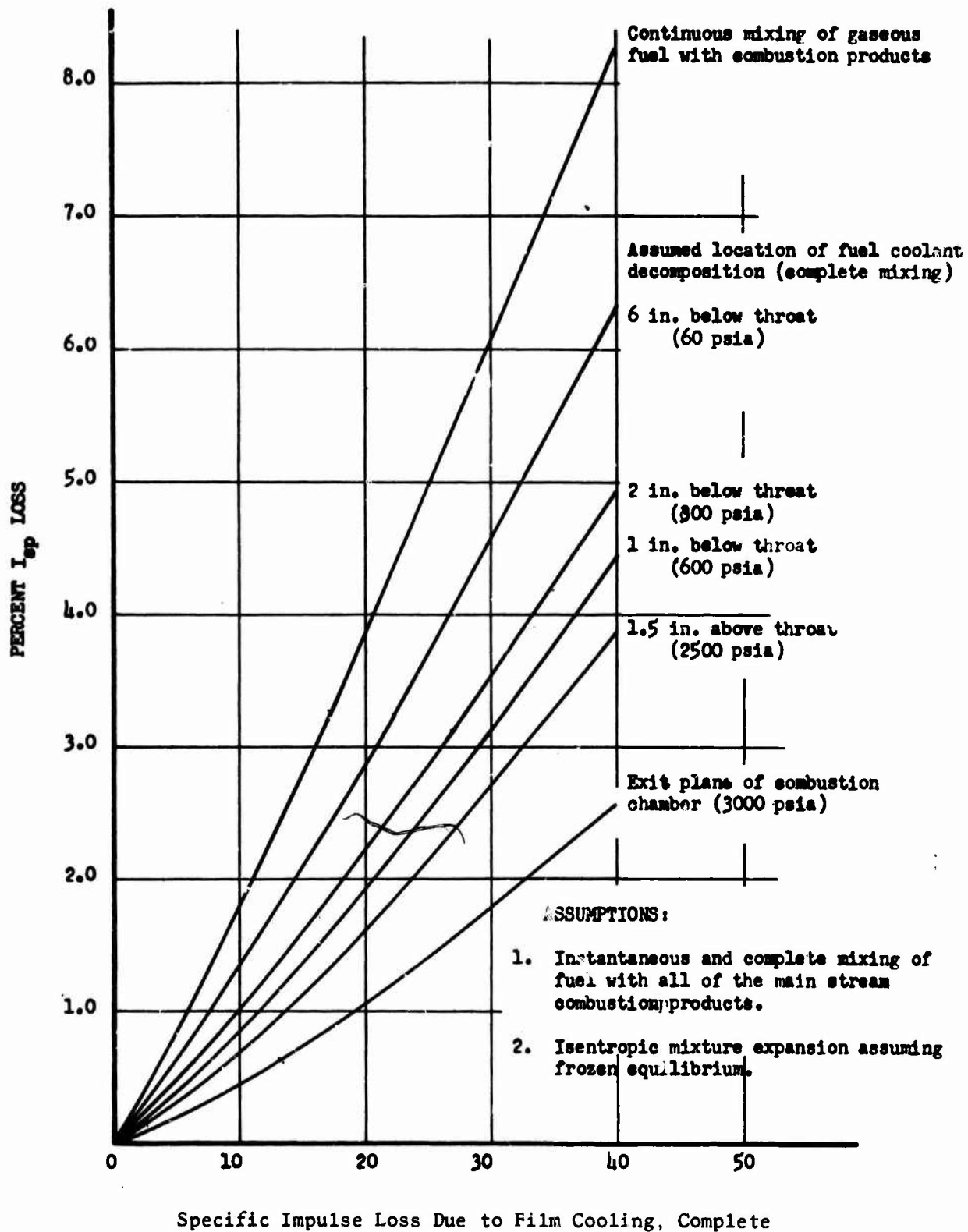


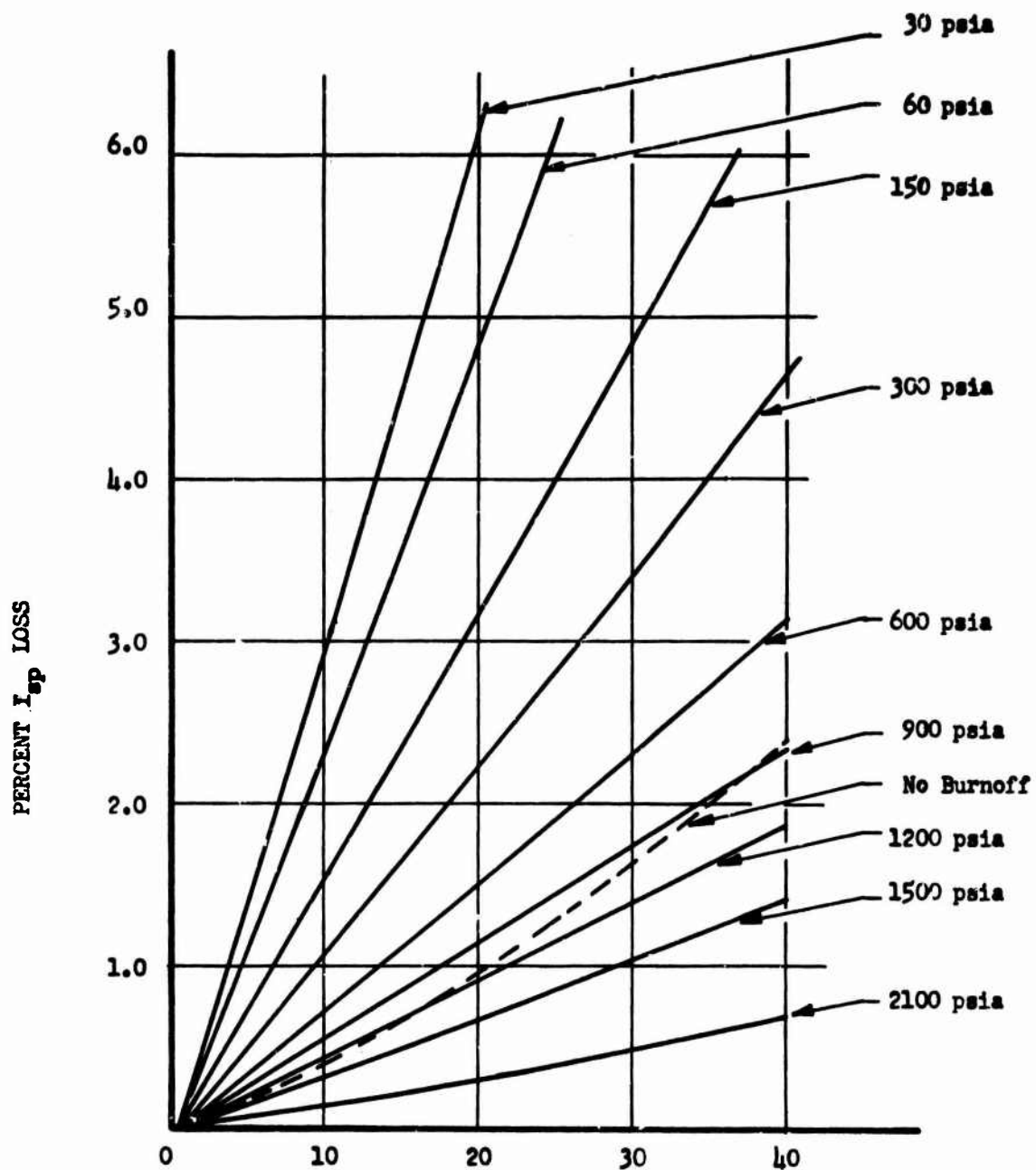
Figure X-E-6

Book Two

NOTE:

1. Coolant - A-50
2. Propellant $\text{N}_2\text{O}_4/\text{A-50}$
3. Chamber pressure = 300 psia
4. Mixture Ratio = 2.2
5. Assuming Frozen Equilibrium

Pressure at oxidizer
injection point.



Specific Impulse Loss Due to Film Cooling with Burnoff

Figure X-E-7

CONFIDENTIAL

Book Two

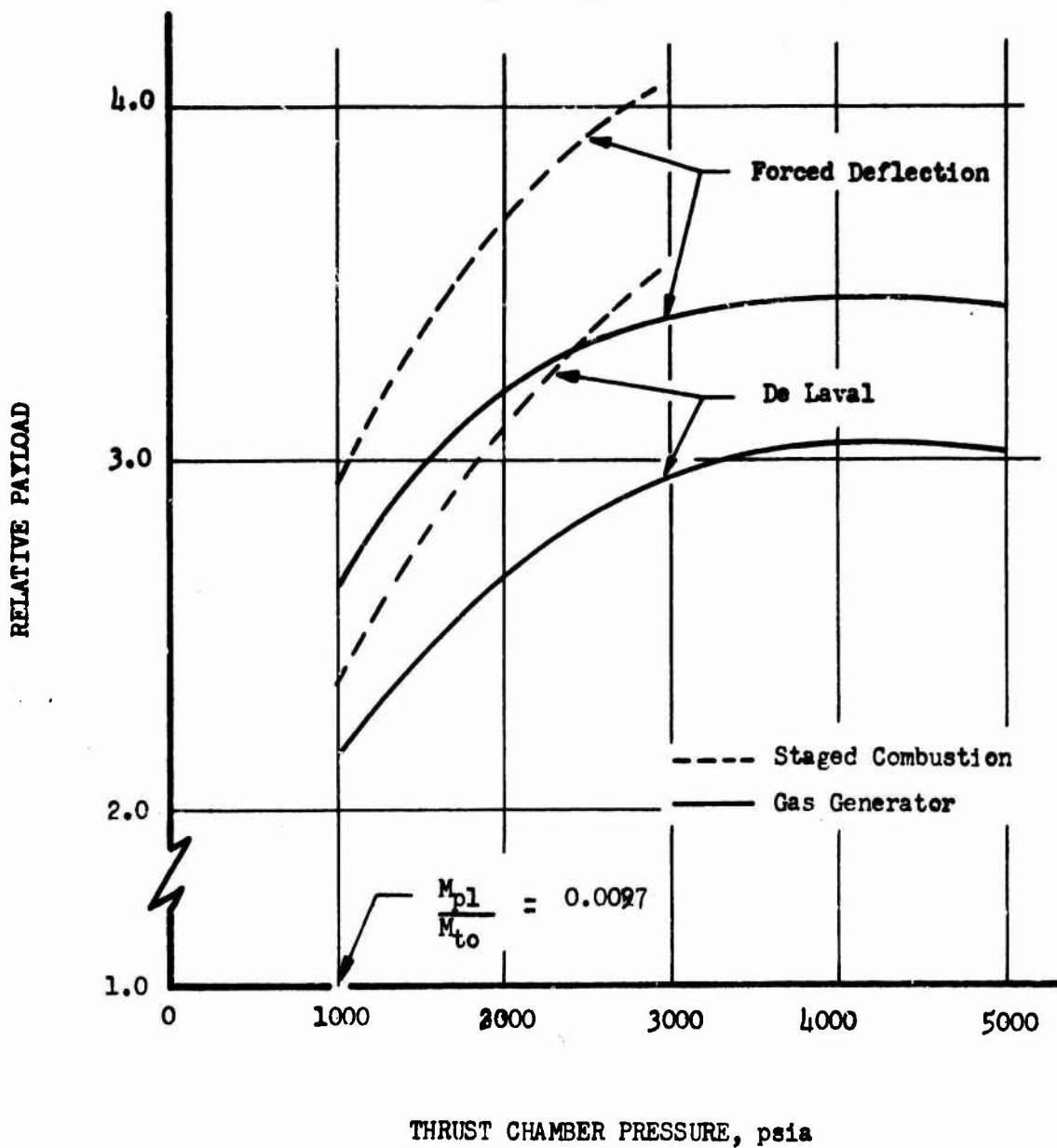
NOTE:

Propellants $N_2O_4/N_2H_4 + Al$

Optimum Mixture Ratio

Optimum Percent Al

300 N.M. Single Stage to Orbit Vehicle



Relative Payload vs Chamber Pressure, $N_2O_4/N_2H_4 + Al$ (u)

Figure X-F-1

CONFIDENTIAL

CONFIDENTIAL

Book Two

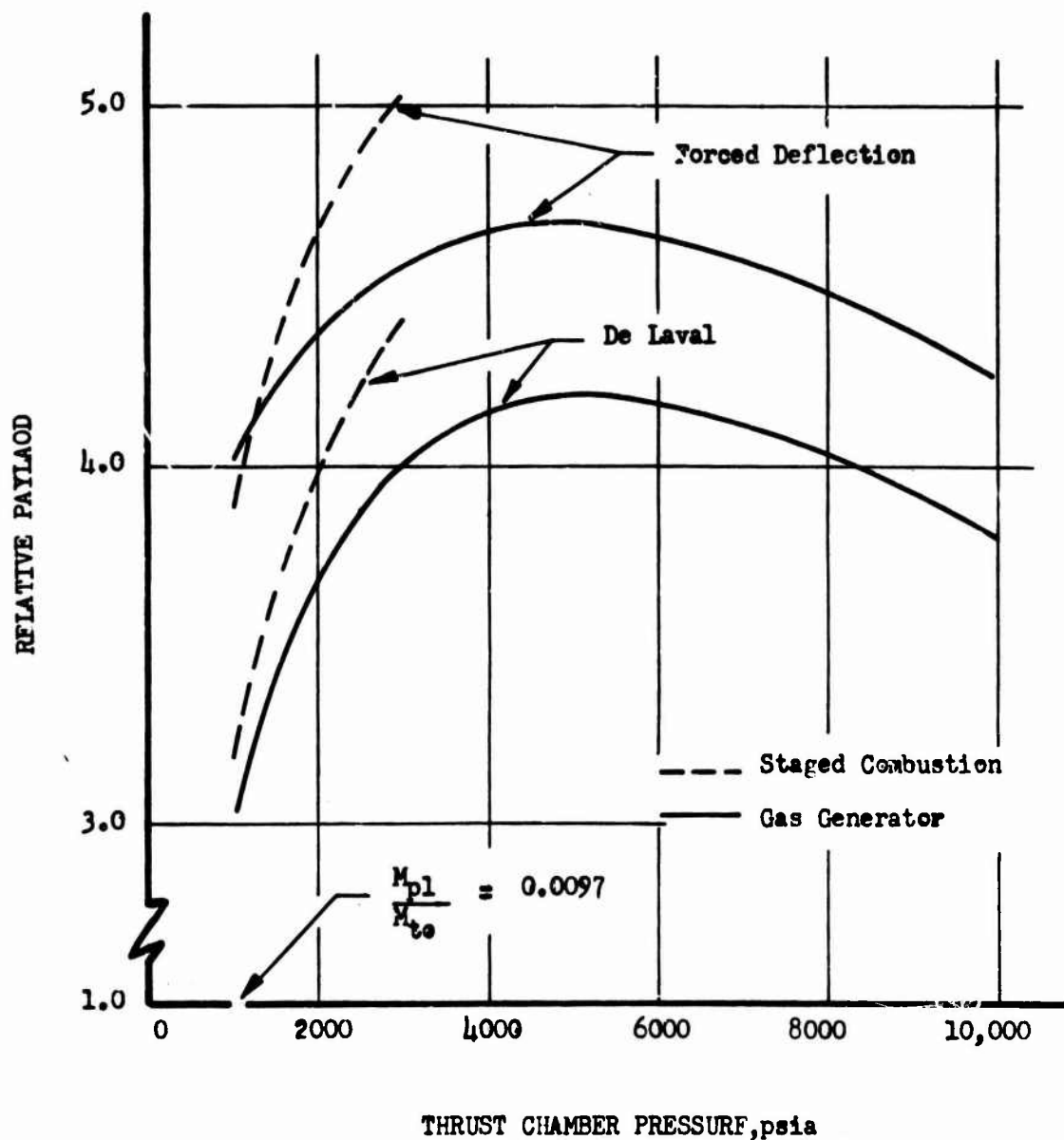
NOTE:

Propellants - $N_2O_4/N_2H_4 + AlH_3$

Optimum Mixture Ratio

Optimum Percent AlH_3

300 N.M. Single Stage to Orbit Vehicle



Relative Payload vs Chamber Pressure, $N_2O_4/N_2H_4 + AlH_3$ (u)

Figure X-F-2

CONFIDENTIAL

CONFIDENTIAL

Book Two

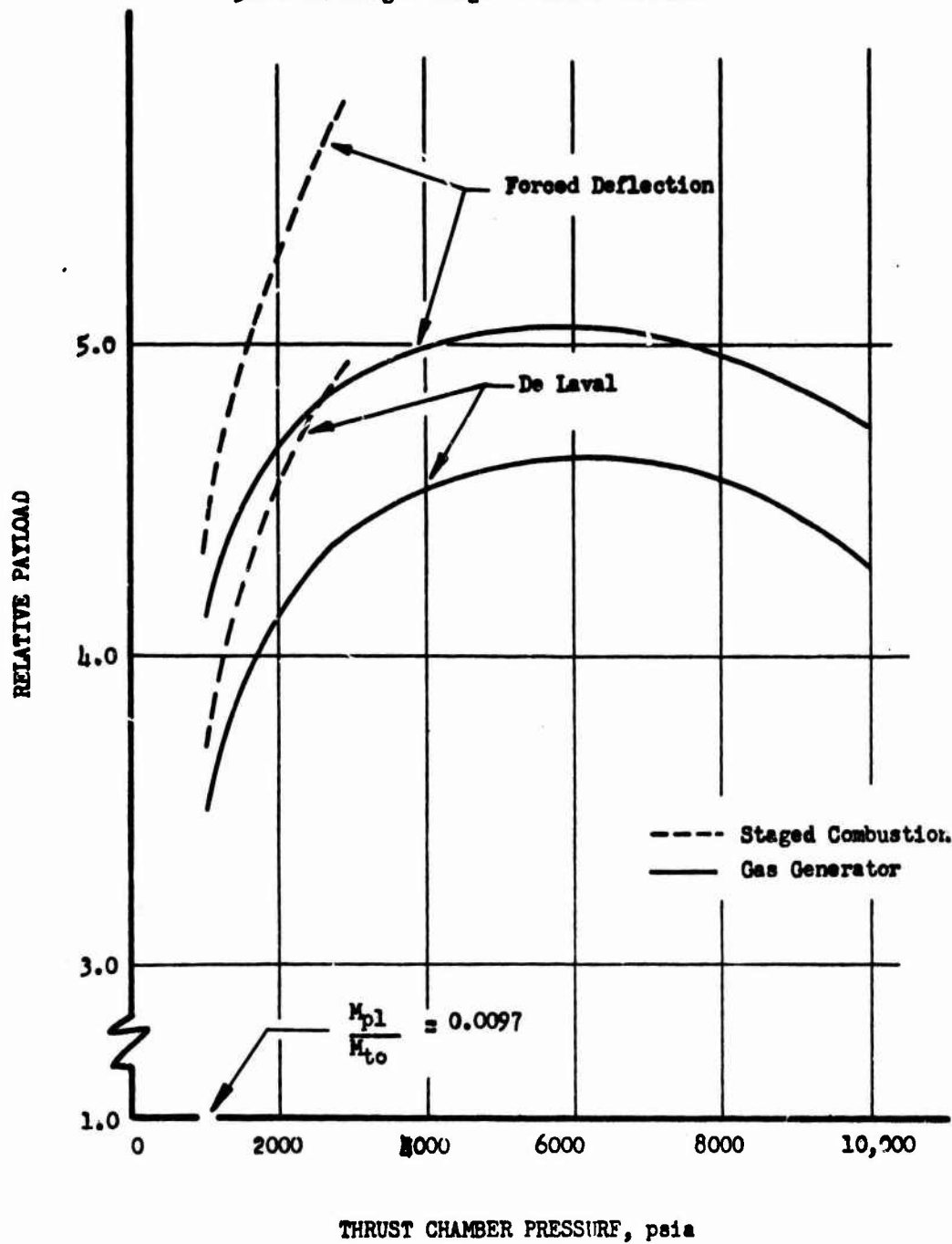
NOTE:

Propellants $N_2O_4/N_2H_4 + Be$

Optimum Mixture Ratio

Optimum Percent Be

300 N.M. Single Stage to Orbit Vehicle



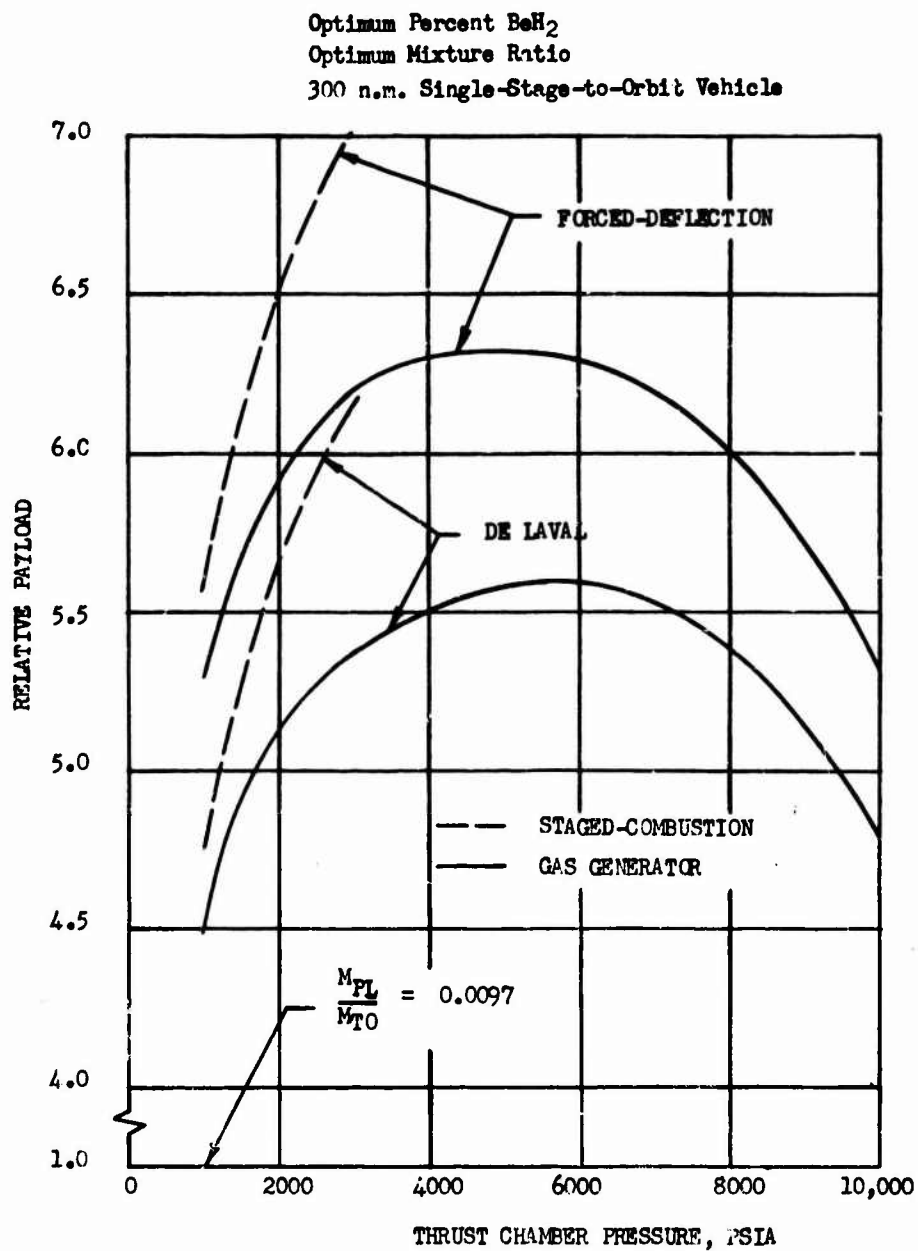
Relative Payload vs Chamber Pressure, $N_2O_4/N_2H_4 + Be$ (u)

Figure X-F-3

CONFIDENTIAL

CONFIDENTIAL

Book Two



Relative Payload vs Chamber Pressure, $N_2O_4/N_2H_4 + BeH_2$ (u)

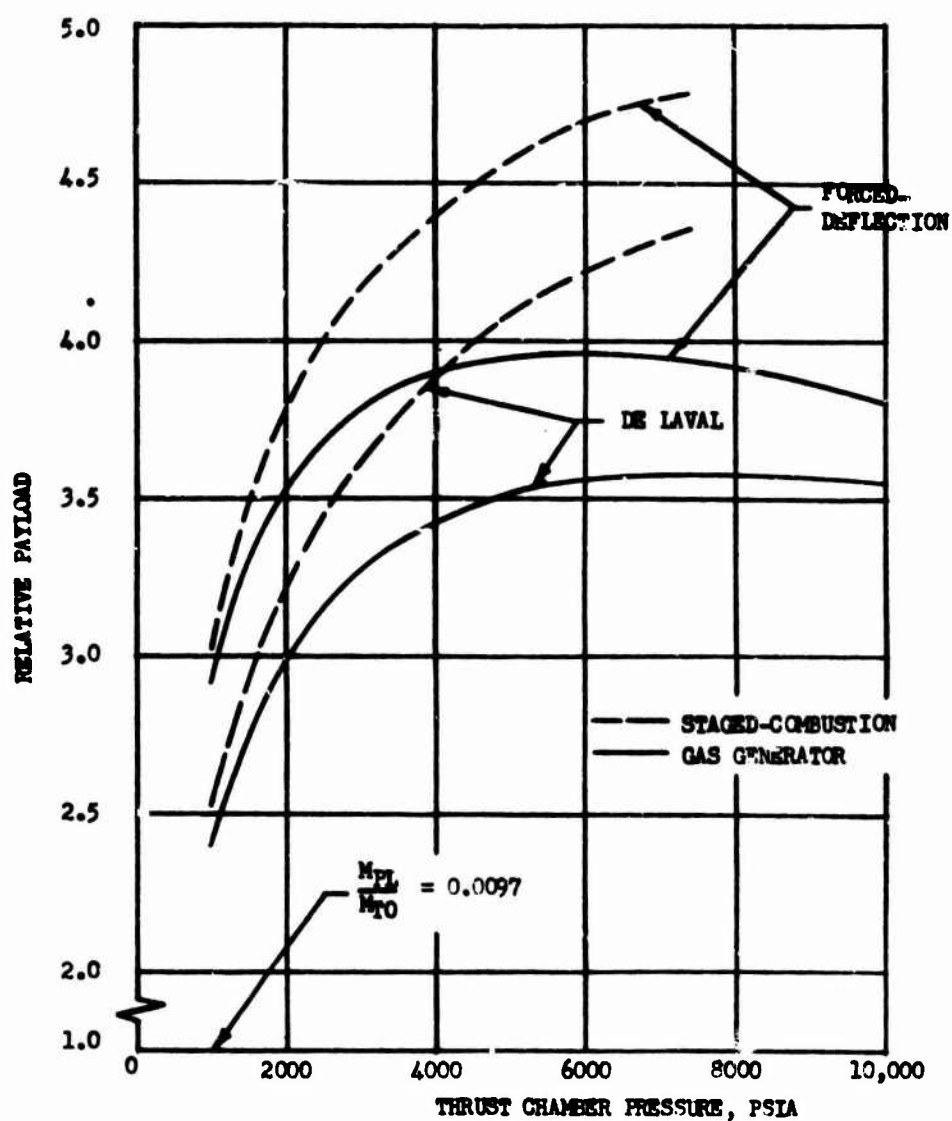
Figure X-F-4

CONFIDENTIAL

CONFIDENTIAL

Book Two

Optimum Percent Al
Optimum Mixture Ratio
300 n.m. Single-Stage-to-Orbit Vehicle



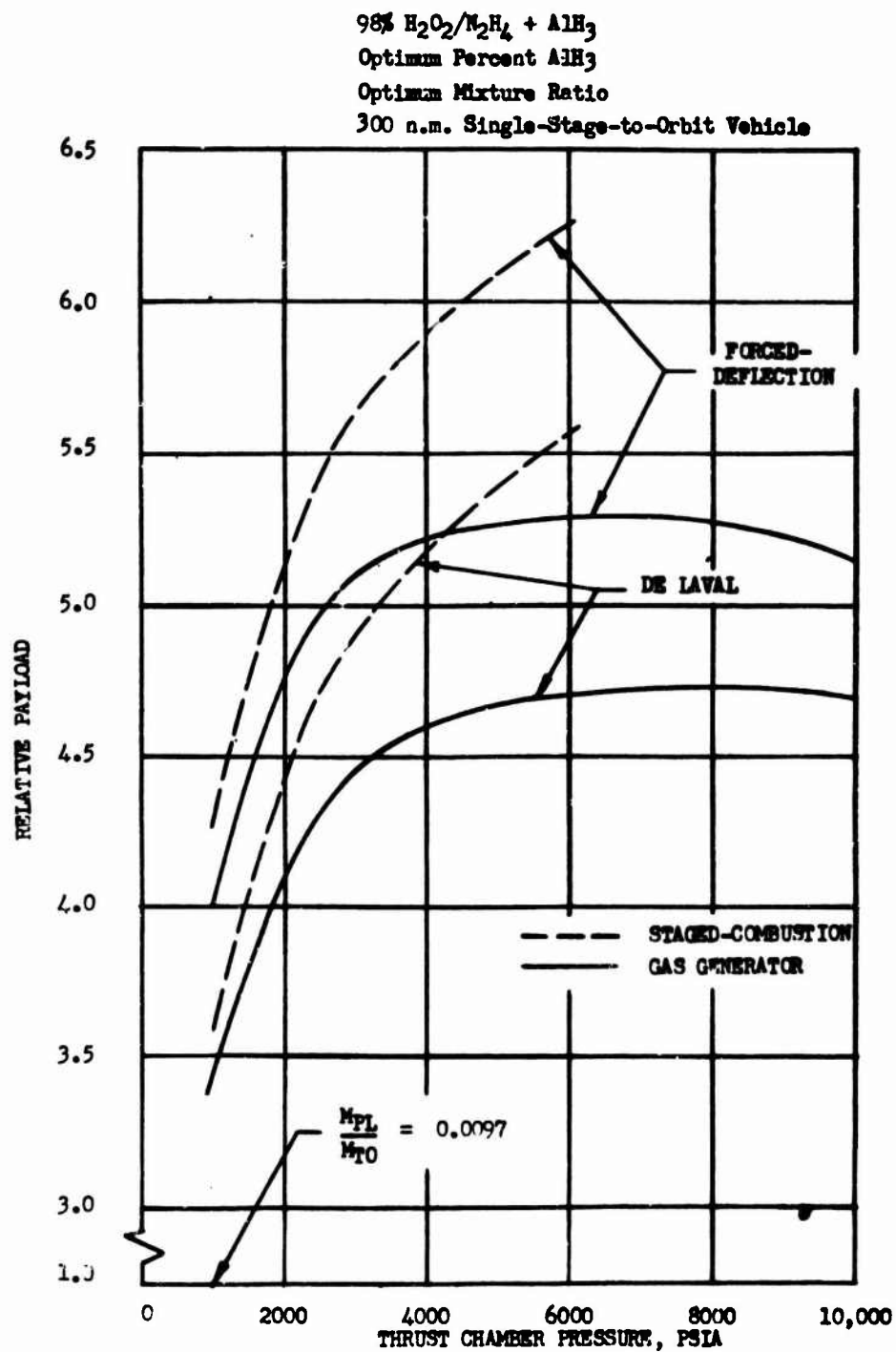
Relative Payload vs Chamber Pressure $H_2O_2/N_2H_4 + Al$ (u)

Figure X-F-5

CONFIDENTIAL

CONFIDENTIAL

Book Two



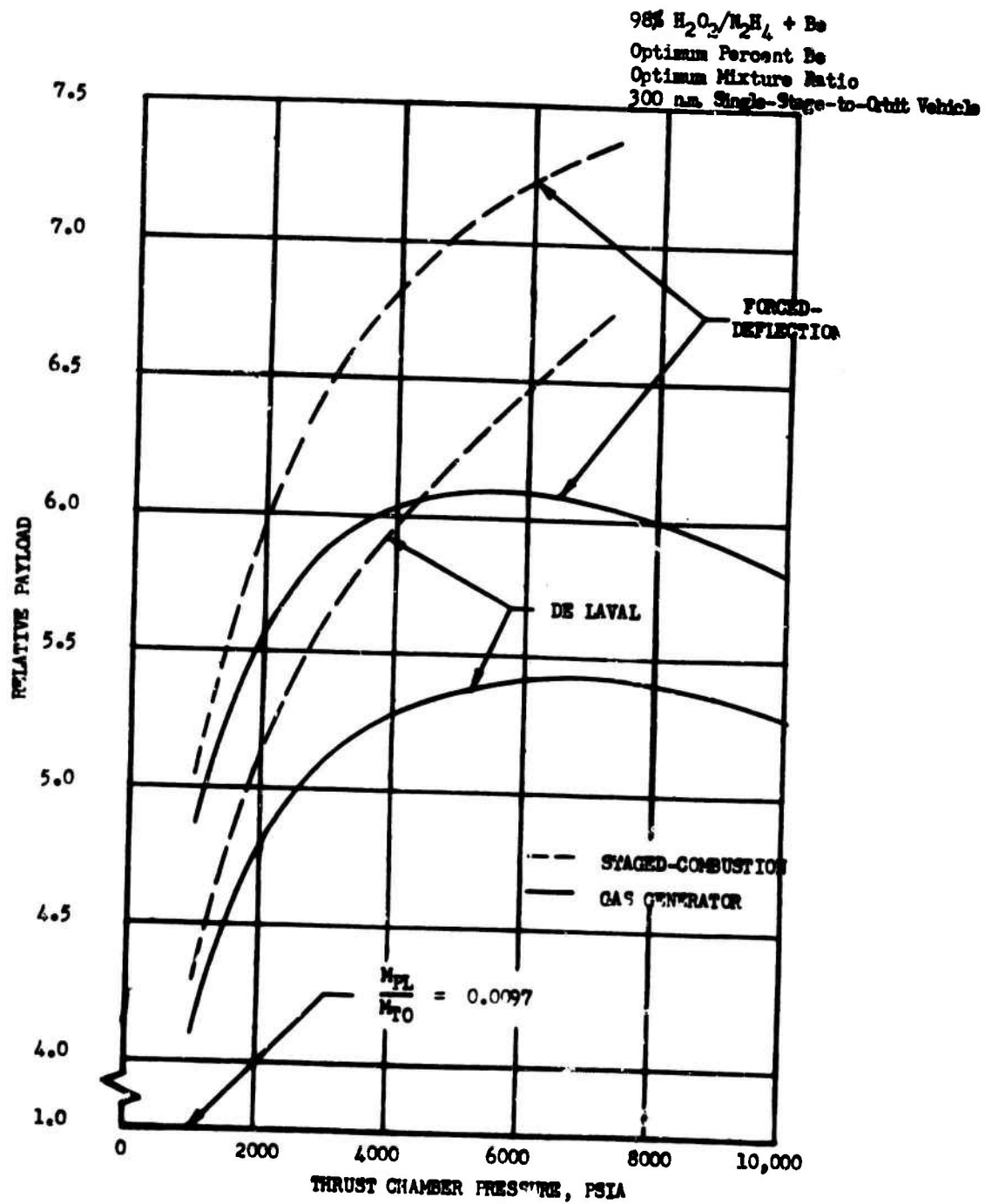
Relative Payload vs Chamber Pressure, $\text{H}_2\text{O}_2/\text{N}_2\text{H}_4 + \text{AlH}_3$ (u)

Figure X-F-6

CONFIDENTIAL

CONFIDENTIAL

Book Two



Relative Payload vs Chamber Pressure, $H_2O_2/N_2H_4 + Be$ (u)

Figure X-F-7

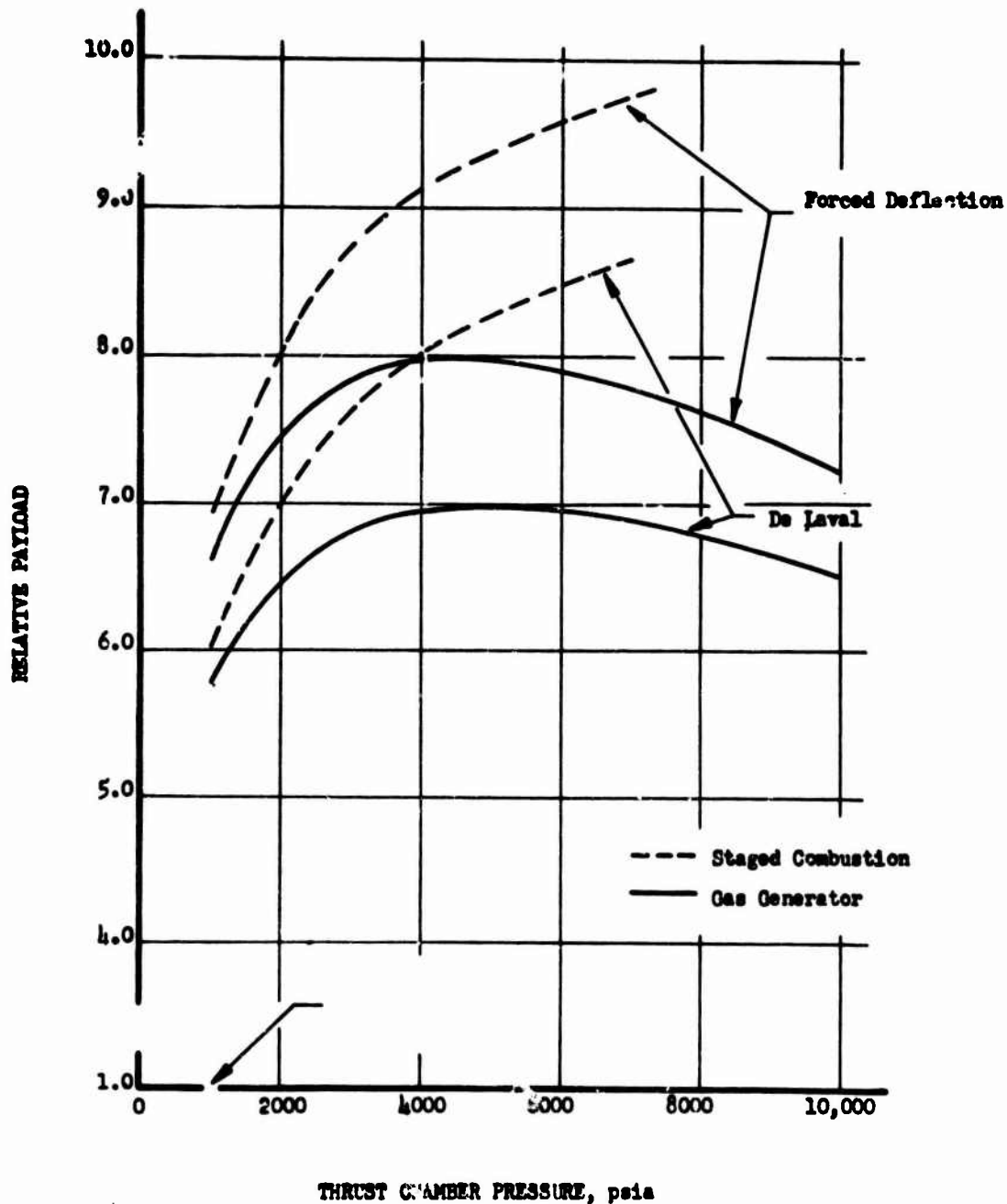
CONFIDENTIAL

CONFIDENTIAL

Book Two

NOTE:

98% $\text{H}_2\text{O}_2/\text{N}_2\text{H}_4 + \text{BeH}_2$
Optimum Percent BeH_2
Optimum Mixture Ratio
300 N.M. Single Stage to Orbit Vehicle



Relative Payload vs Chamber Pressure, $\text{H}_2\text{O}_2/\text{N}_2\text{H}_4 + \text{BeH}_2$ (u)

Figure X-F-8

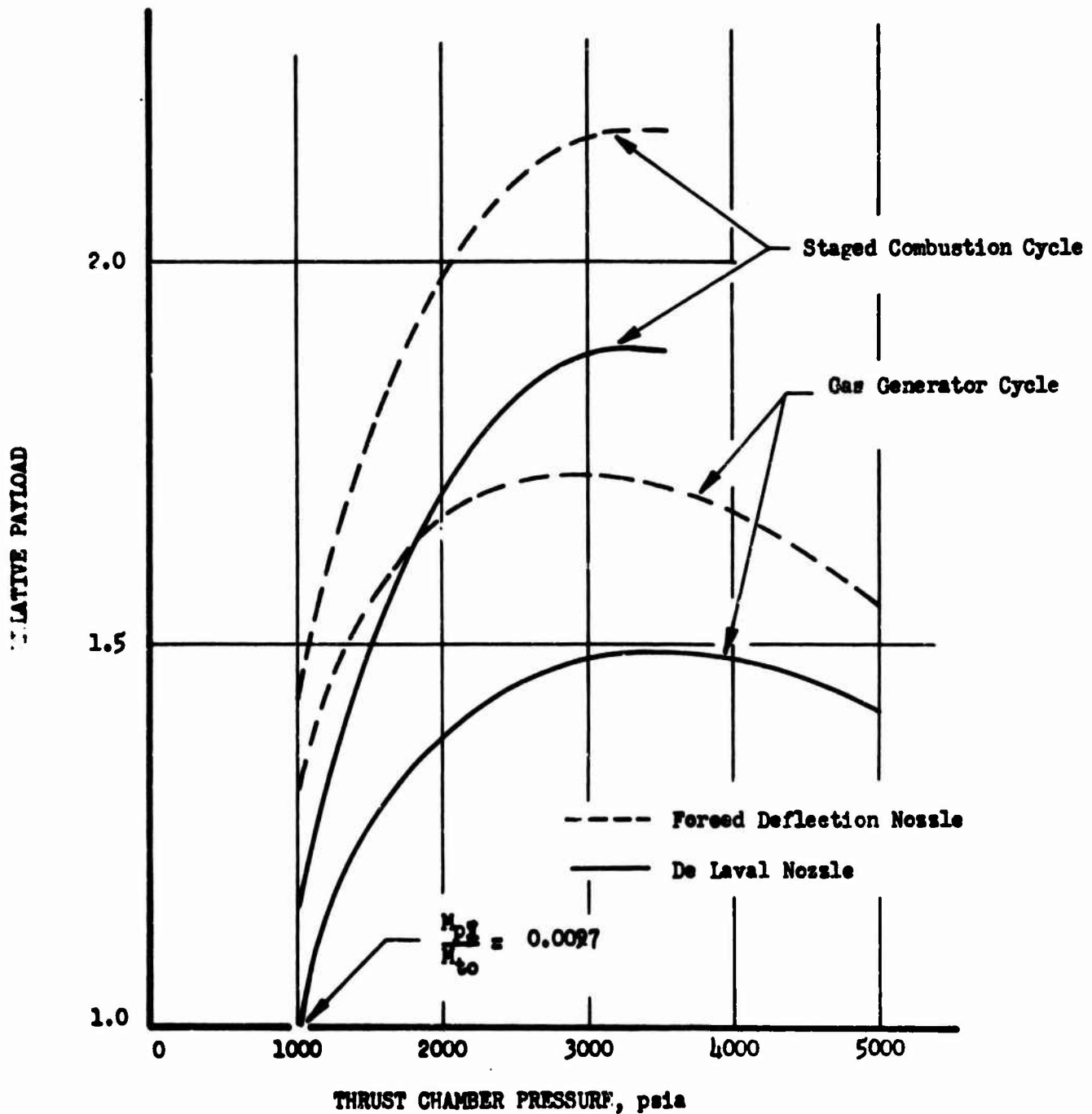
CONFIDENTIAL

CONFIDENTIAL

Book Two

$N_2O_4/A-50$

SINGLE STAGE TO 300 N.M. ORBIT



Relative Payload vs Chamber Pressure, $N_2O_4/A-50$ (u)

Figure X-F-9

CONFIDENTIAL

CONFIDENTIAL

Book Two

XI. FINAL SYSTEMS STUDY

A. INTRODUCTION AND SUMMARY

The objective of the Final System Study was to establish the benefits resulting from incorporating the advanced features of high chamber pressure, staged-combustion engine cycle, and altitude compensating nozzles in future liquid rocket engines. While the Preliminary Systems Study had the same objective, the Final Systems Study was accomplished at the end of the program and could therefore include results from this and other recent programs.

The analysis was conducted using parametric weight data based on design experience and theoretical specific impulse data corrected for known real effects. Much of this analysis was identical to that in the Preliminary System Studies except that the latest data were used. Two additional effects were included as a result of data that were available only recently: (1) a film-cooling model reflecting the effect of film cooling on specific impulse as a function of chamber pressure and (2) nonideal compensation in forced deflection nozzles.

The results presented in Figures XI-F-7 through -9 clearly show the benefit of using high chamber pressure for staged-combustion cycle engines. These curves are relatively flat between 2500 and 5000 psia, with some variation in optimum pressure depending on the stage application. Payload variations within the range are probably within the accuracy of the analysis. Therefore, selection of chamber pressure within this range should be influenced by other practical factors that were not included in this analysis. Use of existing facilities and experience would dictate selection of a chamber pressure of 3000 psia or below. Similar conclusions were reached in the Preliminary Systems Study. However, unlike the results of the Preliminary Systems Studies, the altitude compensating nozzles show no benefit. This was partially due to the nonideal compensation effects used that were not used in the Preliminary Systems Studies and partially due to the choice of 20 modules for the engine system studied. This required use of a large base area, which results in higher performance losses attributable to

CONFIDENTIAL

Book Two

XI, A, Introduction and Summary (cont.)

the nozzles. Use of eight modules might still show significant benefit for the forced-deflection nozzle. Therefore, the conclusion regarding altitude compensating nozzles is that the best nozzle to use will depend on the specific application. The optimum chamber pressure for a gas-generator cycle engine is slightly less than 2000 psia.

A detailed investigation of the effects of cost considerations on the selection of the optimum chamber pressure was performed as part of the Preliminary System Studies (see Section X,D). The conclusion was that the costs attributable to change in chamber pressure were relatively minor, and that optimum chamber pressure should be based upon maximum payload conditions. This cost study was reviewed as part of the Final System Studies; it was determined that the information and philosophy presented in that study is still current and that no new information exists which would alter the results. Therefore, it is concluded that cost is not a major consideration in the selection of optimum chamber pressure; the selection should be based upon performance advantages.

B. ENGINE AND STAGE CONFIGURATIONS

This analysis was restricted to N_2O_4 /AeroZINE 50 propellants, but otherwise includes all the other previously studied parameters: chamber pressure, expansion ratio, stage application, DeLaval and forced-deflection nozzles and staged-combustion and gas-generator cycles.

The basic engine configuration utilized for booster and single-stage applications was the 20-module 2,000,000-lb total thrust system recently intensively studied at Aerojet (using Aerojet's Advanced Storable Engine concept). This engine was chosen in order to benefit from study, and has been investigated with both DeLaval and forced-deflection nozzles. Twenty-module forced-deflection and DeLaval engine installations are shown in Figures XI-B-1 and XI-B-2, respectively.

The upper-stage engine contains four 100,000-lb-thrust modules with DeLaval nozzles.

CONFIDENTIAL

Book Two

XI, Final Systems Study (cont.)

C. MODULE AND ENGINE PERFORMANCE

1. Module Performance

No performance penalty is associated with the staged cycle; the gas-generator cycle, however, has such a penalty, which was evaluated from data presented in Section X,C,4 for a turbine inlet temperature of 1670°F. Figure X-C-5 gives the pump work as a function of thermochemical specific impulse and chamber pressure, and Figure X-C-3 gives the cycle specific impulse degradation as a function of thermochemical plus pump work specific impulses. As summarized in Figure XI-C-2, the net specific impulse before combustion and expansion is thermochemical alone, I_{TMC} , for the staged cycle, and thermochemical plus pump work less cycle degradation, I , for the gas-generator cycle.

A 98% combustion efficiency was used throughout this study. The percent specific impulse loss due to film cooling was computed as 40 times the ratio of film cooling flow rate (from Figure VIII-E-4) to total module flow rate. Film cooling efficiencies η_{FC} , are shown in Figure XI-C-1.

2. Nozzle Performance

DeLaval nozzle efficiency includes the effects of geometry, friction and real gas losses. A constant value of 96.2% was used in this study; a constant value is reasonable since the sum of geometry and friction losses remains nearly constant as area ratio increases. A 12° nozzle exit angle was also assumed; while an extensive tradeoff study between nozzle weight and performance as a function of exit angle was not performed, the 12° angle is near optimum.

CONFIDENTIAL

Book Two

XI, C, Module and Engine Performance (cont.)

Forced-deflection nozzle designs were accomplished within the following constraints:

- a. Twenty modules of constant TPA housing size with 1-in. clearance between adjacent housings.
- b. Module throat area varying inversely with chamber pressure.
- c. Internal expansion section exits touching.
- d. Forced-deflection skirt exit angle of 12.5° .

Geometric performance losses were derived from data in Ref 1 and friction losses from Ref 2. Real gas losses were those discussed in Section VIII, A.

As with the DeLaval nozzles, the exit angle has not been optimized for maximum payload.

Delivered specific impulse for the staged cycle forced-deflection nozzles as a function of ambient pressure is shown in Figures XI-C-2 through 4.

c. Net Performance

Net specific impulse efficiencies, η_{IS} , and delivered vacuum specific impulses, I_{del} , are presented in Figure XI-C-1. Also presented are the injector mixture ratio, MR_{inj} , which corresponds to maximum specific impulse, along with the engine mixture ratio, MR_E , and bulk density, ρ_{B_E} , which include the additional oxidizer for film cooling.

CONFIDENTIAL

Book Two

XI, Final Systems Study (cont.)

D. TRAJECTORY SIMULATION

The mission considered was a 300-NM orbit with polar launch (nonrotating earth). This trajectory was simulated by means of Aerojet Computer Program 293 utilizing a Titan drag coefficient and the 1962 ARDC model atmosphere. Significant trajectory shaping parameters are:

- Vertical rise to 280 fps
- Instantaneous "kick" in missile attitude
- Constant attitude until angle of attack returns to zero
- Gravity turn trajectory to staging point
- Constant pitch rate until orbital velocity is reached at 50 NM
- Hohmann transfer to 300 NM (impulsive burning)

The size of the orbital payload for this engine indicates that a manned mission is likely; therefore, the single-stage system is throttled to reduce maximum accelerations to a tolerable level; this also permits lightweight airframe design. The resultant similarity in thrust-to-weight vs time histories between single- and two-stage vehicles permits, with judicious selection of ground rules, use of data from a single trajectory simulation for both vehicles.

The ground rules selected are:

- Constant booster or single-stage liftoff weight: 1,450,000 lb.
- Constant booster or single-stage initial phase propellant flow rate: 7273.2 lb/sec.
- Constant booster or single-stage initial phase propellant wt: 1,105,000 lb.
- Constant vehicle diameter: 18 ft.

The single-stage engine flow rate is reduced to 25% of the initial value, corresponding to shutting down 15 out of 20 modules. The second-stage

CONFIDENTIAL

Book Two

XI, D, Trajectory Simulation (cont.)

engine incorporates four modules, which operate at constant flow rate. In conjunction with the value selected for the propellant weight for the high-thrust phase, the second-stage liftoff thrust-to-weight ratio is nearly equal to that for the single-stage immediately after throttling because both thrust and liftoff weight are lower. While shutdown of 16 modules would be more desirable for either single-stage nozzle type, the conclusions of this study would not be appreciably different.

The constant flow rate assumption leads to considerable analytic simplification as compared to a constant liftoff-thrust condition. Since the sea-level specific impulse varies from engine to engine, the study incorporates a variable liftoff thrust-to-weight ratio with the resulting variation in gravity losses. The effect of changing assumptions is discussed in Section XI,F.

Figures XI-D-1 and 2 show the total velocity increments found for staged-cycle, single-stage vehicles with DeLaval and forced-deflection nozzles, respectively. The correlation between velocity increment and the ratio of sea level to vacuum specific impulse and the sea level specific impulse itself is well supported by the data. This correlation was used to determine the total velocity increment for the gas-generator-cycle vehicles.

Single-stage engine parameters are identical in both high-and low-thrust phases since no loss in vacuum performance has been found for forced-deflection nozzles for throttling down to as low as 50%.

Booster stages are topped by a standard second stage with fixed engine configuration; the liftoff weight is variable according to first-stage jettison weight and propellant weight as necessary to supply a velocity increment equal to that of the single-stage throttled phase. Standard second-stage performance was that of staged-cycle, 2800-psia engines at an area ratio of 83:1.

CONFIDENTIAL

Book Two

XI, D, Trajectory Simulation (cont.)

with jettison weight equal to 7980 lb plus 3.025% of propellant weight. Parametric second stages are sized to provide a velocity increment of 15,500 ft/sec at a constant liftoff weight of 300,000 lb.

CONFIDENTIAL

Book Two

XI, Final Systems Study (cont.)

E. WEIGHT SUMMARY

1. Modules

The constant flow-rate base permits evaluation of module weight as a function of pump discharge pressure only. Pump discharge pressures used for the gas-generator cycle are slightly more conservative than the values shown in Figure X-C-8. Pump discharge pressures for both cycles at a turbine inlet temperature of 1670°F are summarized in the following table. The turbine gases are oxidizer-rich in the staged cycle and fuel-rich in the gas-generator cycle. The cycle analysis is based on efficiencies of 77% for the turbine, 73% for the oxidizer pump, and 71 and 60% for first- and second-stage fuel pumps, respectively.

The module weights, up to a nozzle expansion ratio of 14:1, are found from Figure X-B-3 and summarized below.

Chamber Pressure, psi	Pump Discharge Pressure, psi		Module Weight, lb	
	Staged Cycle	Gas-Generator Cycle	Staged Cycle	Gas-Generator Cycle
1000	2800	1400	310	237
2000	4100	2700	375	305
2800	5400	3800	416	360
4000	7300	5350	470	410
5000	10000	6700	538	462

2. Nozzles

Regenerative DeLaval nozzle weights were calculated by the method presented in Section XI,G.

The skirt weight of the forced-deflection nozzle was computed by evaluating the contours generated for this study at the 0.0777 lb/in.² burnout weight computed for the contour shown in Figure XI-B-1.

CONFIDENTIAL

Book Two

XI, E, Weight Summary (cont.)

The skirt consists of a 1-in. honeycomb structure together with varying thicknesses of asbestos phenolic backup and carbon or silica cloth facing as required. Approximately 600 lb ablation for the illustrated contour was neglected in evaluating the payload capability of this type nozzle.

Skirt weights at burnout are shown in Figure XI-E-1.

3. Engines

The engine components other than modules and nozzles are summarized in Figure XI-E-2. The rack and rail gimbal concept, shown in Figure XI-E-3 is used for pitch and yaw control of the forced-deflection engine; roll control is provided by four small engines fed from the booster pumps. The DeLaval nozzles are gimballed and provide inherent roll control. Weight variation of thrust vector control with study parameters is neglected.

4. Airframes

Airframe weights, summarized in Figure XI-E-4, were evaluated for aluminum skin and stringer construction by means of scaling relationships based on the Titan II and independent engineering estimates. A bulk ullage of 4.74% for propellants loaded at 75°F was calculated to provide tank pressure variation of 20 to 50 psia for propellant temperature variation of 40 to 90°F. Pressurization residuals at 0.212 lb/ft³ were utilized, corresponding to oxidizer vapor pressure at 70°F and fuel tank pressurized to 50 psia by products of combustion at 150°F and molecular weight of 20. A propellant residual equal to 0.5% of useful propellant weight is included to provide for high probability mismatch between engine and loaded mixture ratios.

Interstage weights were computed at 11.1 lb/in. of length based on constant first-stage thrust-to-weight ratios and constant second-stage liftoff

CONFIDENTIAL

Book Two

XI, E, Weight Summary (cont.)

weights. Interstage lengths were computed based on a 0.7/1 elliptic first-stage forward head and a 45° conical second-stage tank bottom. Four second-stage modules with DeLaval nozzles are located such that the envelope of the four nozzle exits is 36 in. less than the interstage diameter (18 ft). The interstage is split 18 in. forward of the second-stage nozzle exit plane, resulting in a constant first-stage portion and a second-stage length, L_2 , equal to the sum of engine length and nozzle exit radius.

Estimated auxiliary system weights are included in the stage jettison weight. The payloads presented in this study are therefore net, or useful weights. Stage mass fractions for area-ratio-optimized, staged-cycle 2800 psi engines with DeLaval nozzles are 0.964, 0.960, and 0.938 for single, booster, and upper stages, respectively.

CONFIDENTIAL

Book Two

XI, Final Systems Study (cont.)

F. RESULTS

As previously discussed, all payloads were computed on the basis of the mixture ratio for optimum vacuum specific impulse, biased to the oxidizer-rich side by film-cooling requirements. Optimum area ratios were determined first and the corresponding payloads used to determine the optimum chamber pressure for the various cycles, stages, and nozzles.

1. Area Ratio Optimization

The data shown in Figures XI-F-1 through 5 were derived for a preliminary film-cooling model. The change to the final film-cooling model does not affect the area-ratio optimization; therefore, the new model was applied to only optimized area ratios in the chamber-pressure optimization.

As shown in Figures XI-F-1 through 5, the differences in optimum area ratios for staged and gas-generator cycle are relatively subtle. The summary curve of optimum area ratio vs chamber pressure in Figure XI-F-6 is therefore given only for the staged cycle.

a. Single Stage and Booster

The DeLaval nozzle pressure for sea-level flow separation at the 3-sigma probability level was found to range from 5.3 psia at a chamber pressure of 1000 psia to 5.0 psia at 5000. For the contours used in this study, the corresponding area ratios vary linearly with chamber pressure from 26.5 at 1000 psia to 112 at 5000 psia. In all cases, the single-stage and booster optimum area ratios are less than the separation value.

The characteristics of payload and area ratio, shown in Figures XI-F-1 through -4 for both nozzles, represent values computed at constant

CONFIDENTIAL

Book Two

XI, F, Results (cont.)

drag coefficient and weight of thrust vector control system. Since both of these increase with area ratio, the indicated optimum area ratios are somewhat too large.

In addition to the above factors, system cost considerations dictate the choice of an area ratio slightly less than the optimum value. The best choice is therefore probably 5 to 10% less than the values indicated in Figure XI-F-6.

b. Upper Stage

The area-ratio limitation of the DeLaval (forced-deflection not applicable) nozzle imposed by the previously discussed engine envelope diameter of 180 in., with the modules in the neutral position, is a linear variation with chamber pressure from 43 at 1000 psia to 205 at 5000 psia. This limitation, as shown in Figure XI-F-5, affects only the 1000 psia to 2800 psia engines.

The extremely large optimum area ratio found for regenerative nozzle construction suggests that radiation-cooled nozzle extensions may be advantageous. While the lighter nozzle construction, if applicable, would give an increase in both optimum area ratio and payload, the diameter limitation discussed above indicates that the conclusions of this study would differ only slightly.

The effects of thrust-vector-control weight and system cost considerations, in addition to the neglected effect of increasing interstage bending moments, again dictate the choice of an area ratio somewhat smaller than the computed optimum.

2. Chamber Pressure, Cycle and Nozzle Comparisons

Figures XI-F-7 through 9 show the variation of normalized and area-ratio-optimized payload with chamber pressure for the three stages considered.

CONFIDENTIAL

Book Two

XI, F, Results (cont.)

Single-stage and booster payloads for the DeLaval nozzle are shown for two different drag losses. The 100% drag curve represents data generated for the same drag coefficient and reference area as the forced-deflection nozzles. However, the DeLaval nozzle is subject to considerably greater base drag. The blocked base area of the forced-deflection nozzle represents a significant portion of the stage cross section that is not subject to drag. In addition, the pressure on the rearward facing tank bottom is considerably higher for the forced deflection nozzle because of the blocked base. A rough estimate of the difference between the two nozzles led to a 50% greater drag for the DeLaval nozzle. The payloads corresponding to the addition of 140 ft/sec drag-velocity increment are indicated on Figures XI-F-7 and 8.

As previously discussed, all single-stage and booster payloads were computed for the same liftoff weight and engine flow rate. Since sea-level specific impulse varies from engine to engine, the liftoff thrust to weight ratio and the total mission velocity increment also vary. Since the most realistic comparison is on the basis of constant liftoff thrust-to-weight ratio, a point check was made of the correction to the computed data. The DeLaval staged-cycle engine at 2800 psia has 4.3-sec greater sea-level specific impulse than the corresponding forced-deflection engine. Reducing the DeLaval engine flow rate to give the same liftoff thrust-to-weight ratio as the forced-deflection engine gave a single-stage payload loss of 290 lb. This is typical of the correction required at any chamber pressure for either cycle and can be neglected in comparing nozzles, particularly in view of the probable error in the drag correction.

The flow rate correction has a greater significance in determining the optimum chamber pressure for the single stage and booster from the uncorrected data shown in Figures XI-F-7 and -8. Since the optimized sea level specific impulse increases with chamber pressure for either nozzle, and since the correction to constant thrust-to-weight ratio increases with increasing specific impulse, the optimum chamber pressures are slightly lower than indicated on the figures.

CONFIDENTIAL

Book Two

XI, F, Results (cont.)

It should be noted in comparing payload variation with chamber pressure for the three stage applications with either engine cycle or nozzle that the high pressure payloads are markedly better for the booster stage. This is due to the consideration that the increased engine weight at high pressure is traded off for payload at approximately 4.5:1 lb for the booster and 1:1 lb for single or upper stages.

In view of the previously discussed flow rate correction, it is apparent that for the staged cycle a chamber pressure in the vicinity of 3000 psia is optimum over the range of stage applications. This optimum pressure is slightly lower than that found in the preliminary study (Section X) because of film-cooling characteristics omitted in the preliminary study, as partially offset by the higher turbine temperature (1670°F vs 1200°F) in the final study.

Optimum chamber pressure over the range of stage applications for the gas-generator cycle is somewhat less than 2000 psia. This value is lower than that of the preliminary study because of film-cooling effects.

The forced-deflection nozzle makes a better showing in the booster application because of the previously mentioned tradeoff comparison of jettison weight and payload weight. In considering both booster and single-stage applications, neither nozzle shows a significant advantage. It is apparent that the increased weight for the ablative skirt and the greater performance losses approximately cancel out the forced-deflection advantage in altitude compensation and reduced base drag, at least in this particular design.

CONFIDENTIAL

Book Two

XI, Final Systems Study (cont.)

G. REGENERATIVE DeLAVAL NOZZLE WEIGHT

The detailed study in which the regeneratively cooled DeLaval nozzle weights were derived is given in this section. The incorporation of these weights into the study is discussed in Section XI,E.

1. Tubes and Oxidizer

Since the data on module weight shown in Figure X-B-3 is used as representing the complete engine up to an area ratio of 14:1, this section is concerned only with wet nozzle weight beyond that point. High fluid velocities are not required for adequate heat transfer in this area, and tube design is affected only by geometric, weight, and pressure-drop criteria.

The assumptions used in the following analysis are:

- (1) Fluid velocity: $V = 40$ ft/sec
- (2) Double pass construction
- (3) Module oxidizer flow rate: $\dot{w}_0 = 250$ lb/sec
- (4) Average oxidizer density: $\rho_0 = 80.5$ lb/ft³
- (5) Density of Inconel 718 tubes: $\rho_T = 0.296$ lb/in.³
- (6) Working stress: $S = 60,000$ psi
- (7) Variable tube wall thickness: 0.010 in. minimum

The general tube cross section is a hemispherically ended rectangle where x is the hemisphere inside diameter in inches, y is the flat length in inches and t is the wall thickness in inches. The diameter of the gas stream, D , is used as the mean diameter of the oxidizer annulus. The total number of tubes is N , and the oxidizer pressure is p , in psi.

CONFIDENTIAL

Book Two

XI, G, Regenerative DeLaval Nozzle Weight (cont.)

The basic relationships are derived as follows:

$$\pi D = N(x + 2t)$$

$$S = \frac{px}{2t}$$

$$2\omega_o = N(.785x^2 + xy) \frac{V}{144} p_o$$

$$Nx = (.785x + y) = \frac{(2)(250)(144)}{(80.5)(40)} = 22.4$$

$$\text{Tube weight/in. } W_T = .296 Nt \left[\pi(x + t) + 2y \right]$$

$$\text{Oxidizer weight/in. } W_o = \frac{2\omega_o}{12V} = \frac{(2)(250)}{(12)(40)} = 1.04$$

Stress-Designed Tubes

$$t = \frac{px}{2S} = \frac{px}{120,000}$$

$$\pi D = N \left[x + \frac{px}{60,000} \right] = Nx \left[\frac{60,000 + p}{60,000} \right]$$

$$x = \frac{\pi D}{N} \frac{60,000}{60,000 + p}$$

$$y = \frac{22.4}{Nx} - .785x$$

$$= \frac{22.4(60,000 + p)}{60,000 \pi D} - \frac{.785(60,000) \pi D}{N(60,000 + p)}$$

$$= \frac{60,000 + p}{8420 D} - \frac{148,000 D}{N(60,000 + p)}$$

The above equation indicates that for constant pressure and number of tubes, the flat height decreases with increasing diameter. The limiting diameter is found as follows:

CONFIDENTIAL

Book Two

XI, G, Regenerative DeLaval Nozzle Weight (cont.)

$$y = c_s D_{max} = \frac{60,000 + p}{35,300} \sqrt{N}$$

The stress-designed tube weight is found for any section as follows:

$$s^W_T = \frac{.465 p D}{(60,000 + p)^2} \left[\frac{D}{N} (299,000 + 4.95p) + \frac{(60,000 + p)^2}{4210 D} \right]$$

This relationship is valid only thickness equal to or greater than 0.010 in.

$$t = \frac{px}{120,000} = \frac{p}{120,000} \frac{60,000\pi D}{N(60,000 + p)} = \frac{\pi}{2} \frac{pD}{N(60,000 + p)}$$

$$D_{min} = .00637N \frac{60,000 + p}{p}$$

0.010 in. tubes

$$\pi D = N(x + .020)$$

$$x = \frac{\pi D}{N} - .020$$

$$y = \frac{22.4}{Nx} - .785x = \frac{22.4}{\pi D - .020N} - .785 \left(\frac{\pi D}{N} - .020 \right)$$

The limiting diameter (circular tubes) is similarly

$$F^D_{max} = 1.7 \sqrt{N} + .00637N$$

The fabrication minimum tube weight is

$$F^W_T = .00296N \left[1.57 \left(\frac{\pi D}{N} - .020 \right) + .031 + \frac{44.8}{N \left(\frac{\pi D}{N} - .020 \right)} \right]$$

CONFIDENTIAL

Book Two

XI, G, Regenerative DeLaval Nozzle Weight (cont.)

The tube design regimes are shown in Figure XI-G-1 and the tube weight vs diameter characteristics in Figure XI-G-2. These curves were used to generate typical designs such as the one shown in Figure XI-G-3 for 10,000 psi. The particular saw toothed curve shown was initiated for 100 tubes at the throat. Since it is likely that a different member of initial tubes would be chosen for every nozzle expansion, the purpose of this study is best suited by utilizing the average curves shown in Figure XI-G-3.

In addition to tube weight, the previously calculated constant oxidizer weight of 1.04 lb/in. was used together with an additional 0.26 lb/in. for brazing, longitudinal stiffening, tube splits, and manifolds. The sum of these components is plotted in Figure XI-G-4 as a function of area ratio.

2. Stiffeners

The circumferential stiffener weights shown in Figure XI-G-5 were computed for the sea-level start-transient loading. As the chamber pressure builds up, the separation plane moves down the nozzle until the nozzle flows full. The separation is expected to be asymmetric because of slight contour irregularities and becomes even more asymmetric because of elastic deformation of the nozzle. While ambient pressure exists uniformly around the outside of the nozzle, the gas side pressures are ambient immediately downstream of the separation point and approximately 4.7 psia in the region just upstream of the separation point. Every nozzle cross section, at a particular chamber pressure, is subject to a collapsing pressure differential of 10 psia around part of its circumference.

The circumferential extent of the collapsing pressure is a function of the elasticity of the nozzle and was not computed. Section bending moments, however, were computed for circumferential arcs of 60°, 90°, and 120°. The maximum moment was found for an angle of 90° and used throughout the analysis.

CONFIDENTIAL

Book Two

XI, G, Regenerative DeLaval Nozzle Weight (cont.)

Tube stiffness was neglected and a V-band stiffener computed at a 38-in. nozzle exit diameter for Inconel 718 at a working stress of 100 ksi. This same cross section was used at all other stations, leading to a somewhat conservative analysis, since the bending moment varies with diameter squared and maximum exit diameters for sea-level operation are near 38 in. over the range of chamber pressures.

In conjunction with the assumption of linear variation of stress, the above analysis leads to stiffener weights per inch of nozzle length which vary linearly with diameter from 0.185 at 10 in. to 0.695 at 38 in.

The stiffeners calculated above would be more than adequate for the symmetrical collapsing load at sea level with the engine at full chamber pressure and for the external aerodynamic loading at maximum flight dynamic pressure.

Altitude engines are not subject to the start transient separation loading or the external aerodynamic loading. Stiffener weights equal to 30% of the values indicated by the analyses above are used to cover handling requirements and flutter.

CONFIDENTIAL

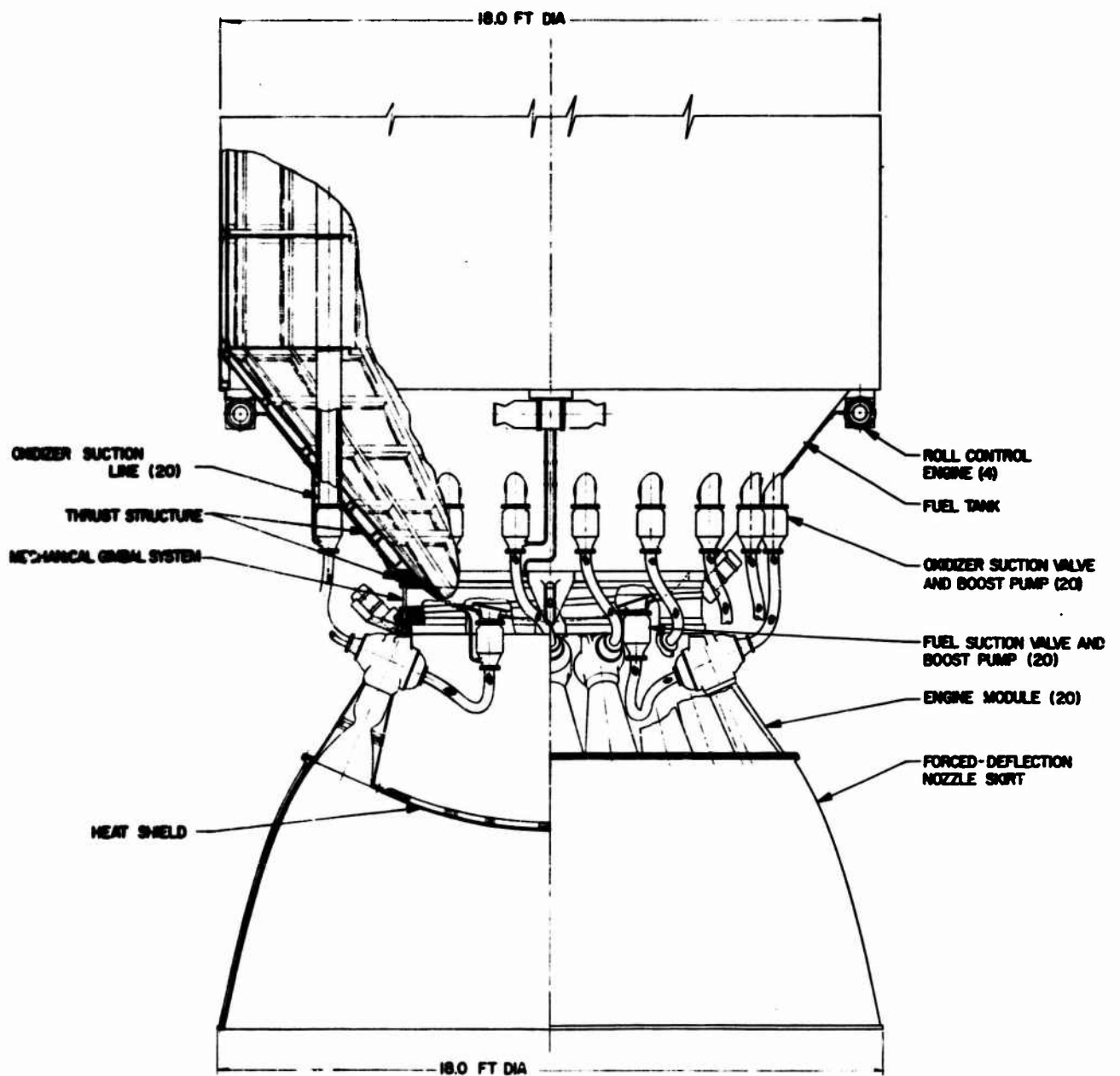
Book Two

REFERENCES

1. The Design and Analysis of Altitude-Compensating Nozzles, Contract AF 04(611)-8548, Report SRL, Aerojet-General Corporation, December 1964.
2. Study of High Effective Area Ratio Nozzles for Spacecraft Engines, Report NAS 7-136F, Aerojet-General Corporation, June 1964.

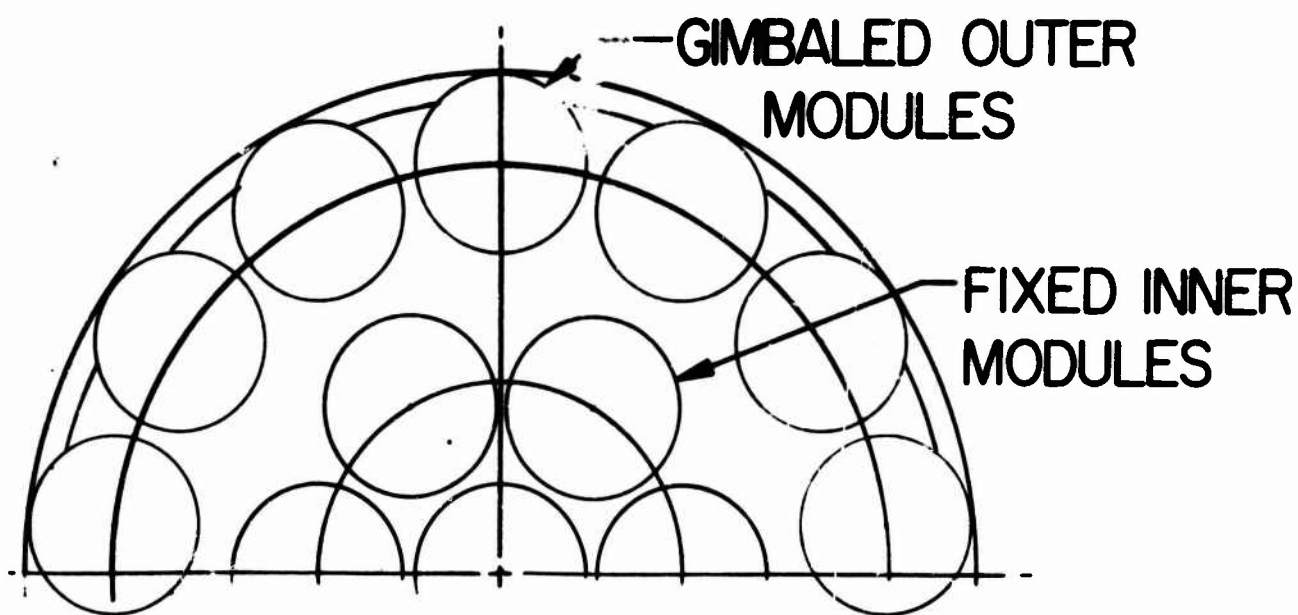
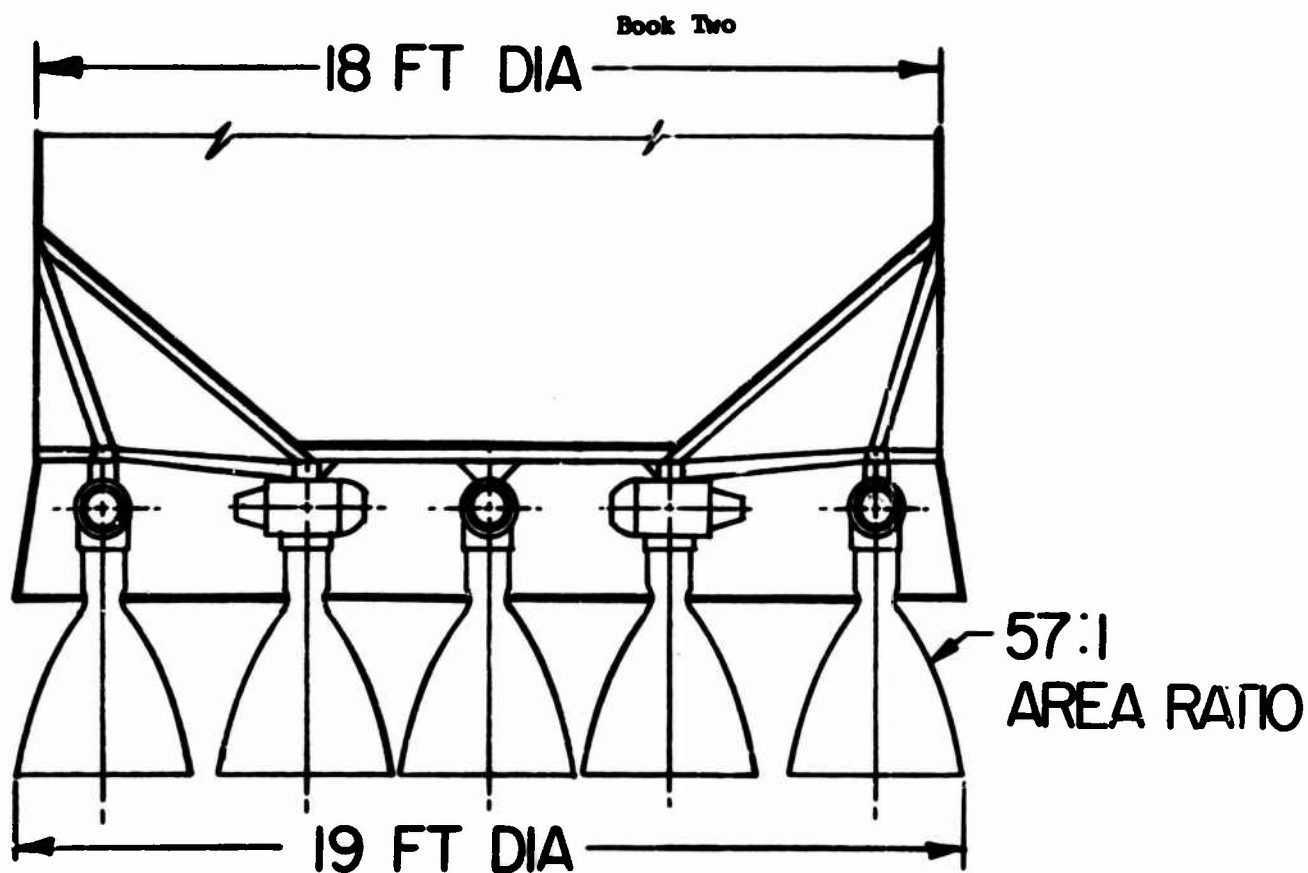
CONFIDENTIAL

Book Two



Forced-Deflection Engine Installation, 20-Module Design

Figure XI-B-1



DeLaval Engine Installation, 20-Module Design

Figure XI-B-2

CONFIDENTIAL

Book Two

P_c (psia)	Area Ratio	I_{TWC} (sec)	MR_{ini}	$\frac{\omega_{Tc}}{\eta_{Tc}}$ (lb/sec)	MR_E	ρ_{Eg} (lb/ft ³)	I (sec)	Delay			Forced Deflection		
								η_{Ts}	I_{del} (sec)	Gas Gen I_{del} (sec)	η_{Ts}	I_{del} (sec)	Gas Gen I_{del} (sec)
1000	7	305.4		0	1.93	74.39	302.7	0.9428	287.9	285.4			
	10	314.1		1.00	1.97	74.56	311.3		296.1	293.5			
	20	328.8			2.07	74.97	325.7		310.0	307.1			
	30	336.4			2.10	75.09	333.2				0.9320	313.5	310.5
	40	341.1			2.12	75.17	337.8				0.9330	318.2	315.2
2000	60	347.2			2.13	75.21	343.8		321.6	318.5	0.9349	324.6	321.4
	20	330.0	2.05		2.101	75.09	324.4	0.9365	309.0	303.8			
	35	339.9	2.08		2.132	75.21	333.9		318.3	312.7			
	40	342.0	2.08		2.132	75.21	335.9		320.3	314.6			
	50	345.3	2.09		2.142	75.25	339.2		323.4	317.7			
2800	30	337.6	2.12		2.22	75.54	329.7	0.9312	314.4	307.0			
	40	342.3	2.13		2.33	75.58	334.2		318.7	311.2			
	50	345.6	2.13		2.23	75.58	337.4		321.8	314.2	0.9222	321.0	313.3
	60	348.1	2.14		2.24	75.61	339.7				0.9248	325.4	317.6
	70	350.2	2.14		2.24	75.61	343.4		326.1	318.3	0.9254	328.3	320.4
4000	80	351.9	2.15		2.25	75.65	346.2				0.9262	330.7	322.7
	100	354.8	2.15		2.25	75.65	348.4						
	120	357.1	2.15		2.272	75.73	326.9	0.0252	312.5	302.4			
	30	337.8	2.12		2.283	75.77	334.4		319.9	309.4			
	50	345.8	2.13		2.293	75.81	336.8		322.2	311.6			
5000	60	348.3	2.14		2.293	75.81	338.8		324.2	313.5			
	70	350.4	2.14		2.294	75.81	343.1		328.4	317.4			
	100	355.0	2.15		2.306	75.85	324.6	0.9215	311.5	299.1			
	30	338.0	2.12		2.328	75.92	332.0		318.8	305.9	0.9087	320.0	307.0
	50	346.0	2.14		2.338	75.96	336.3		323.1	309.9	0.9092	322.9	309.7
80	70	350.6	2.15		2.338	75.96	337.8		327.3	313.9	0.9097	325.4	311.8
	80	352.2	2.15										
	100	355.2	2.15										
120	357.7	2.15			2.338	75.96	342.8						

Vacuum Performance Summary (u)

Figure XI-C-1

CONFIDENTIAL

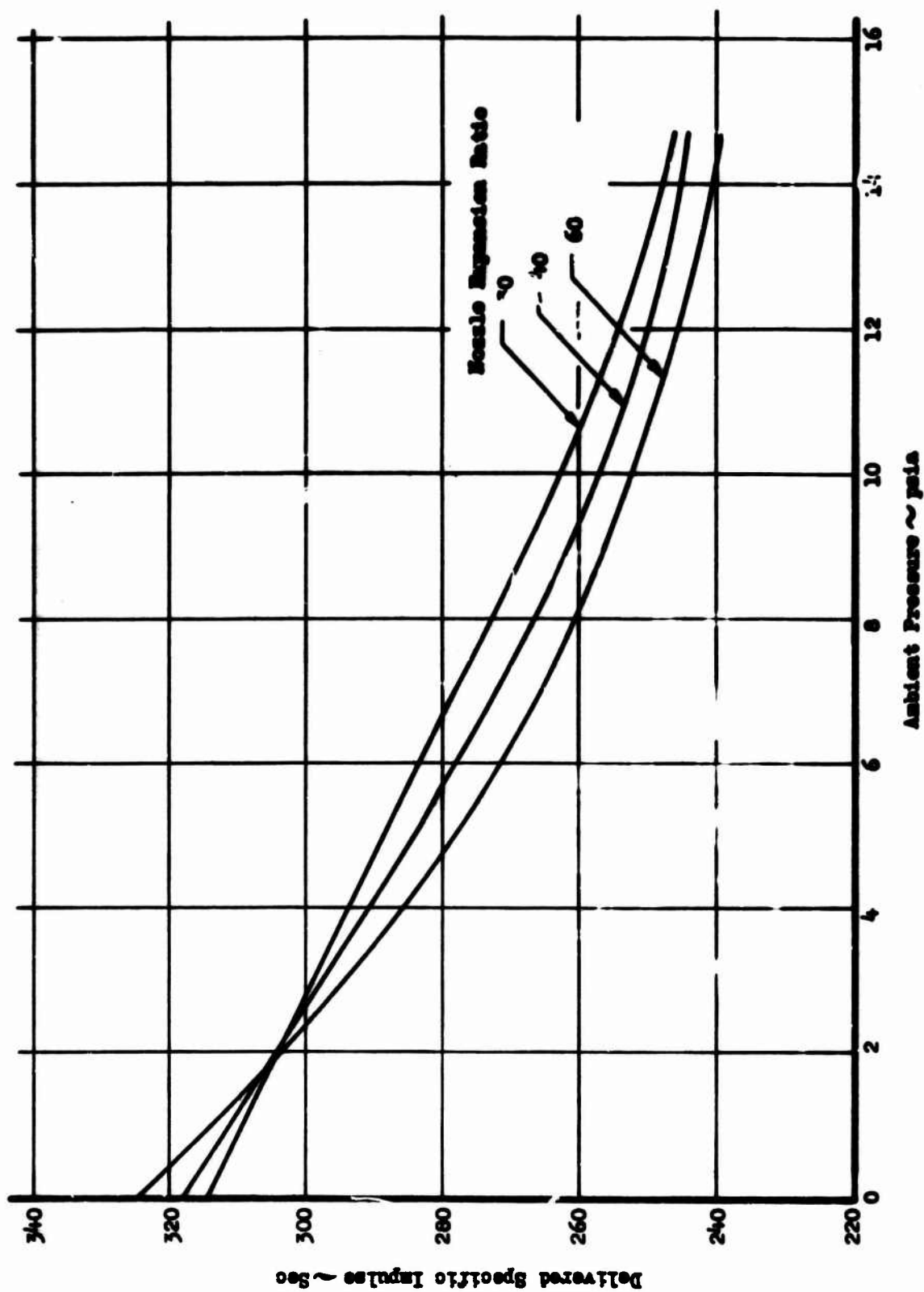
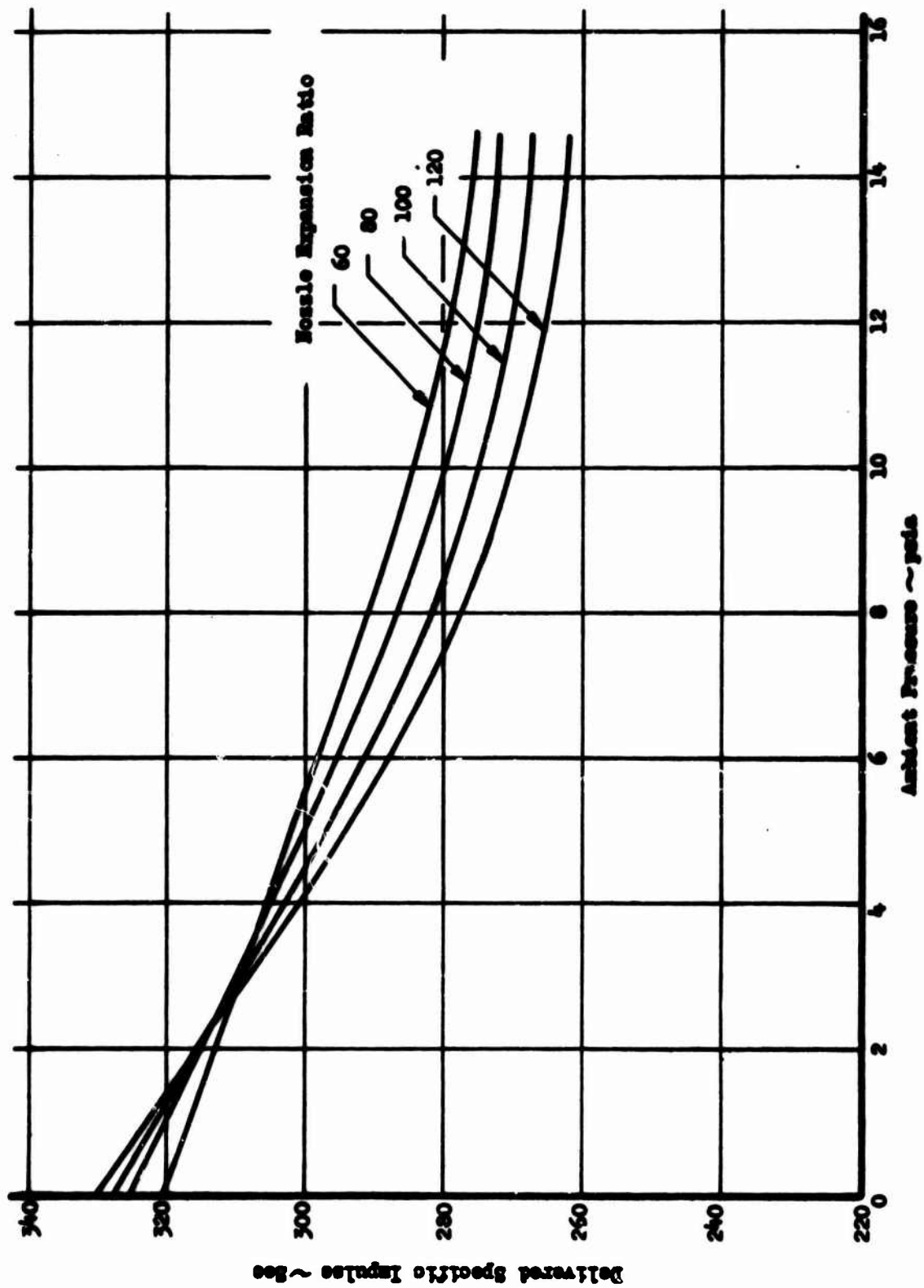


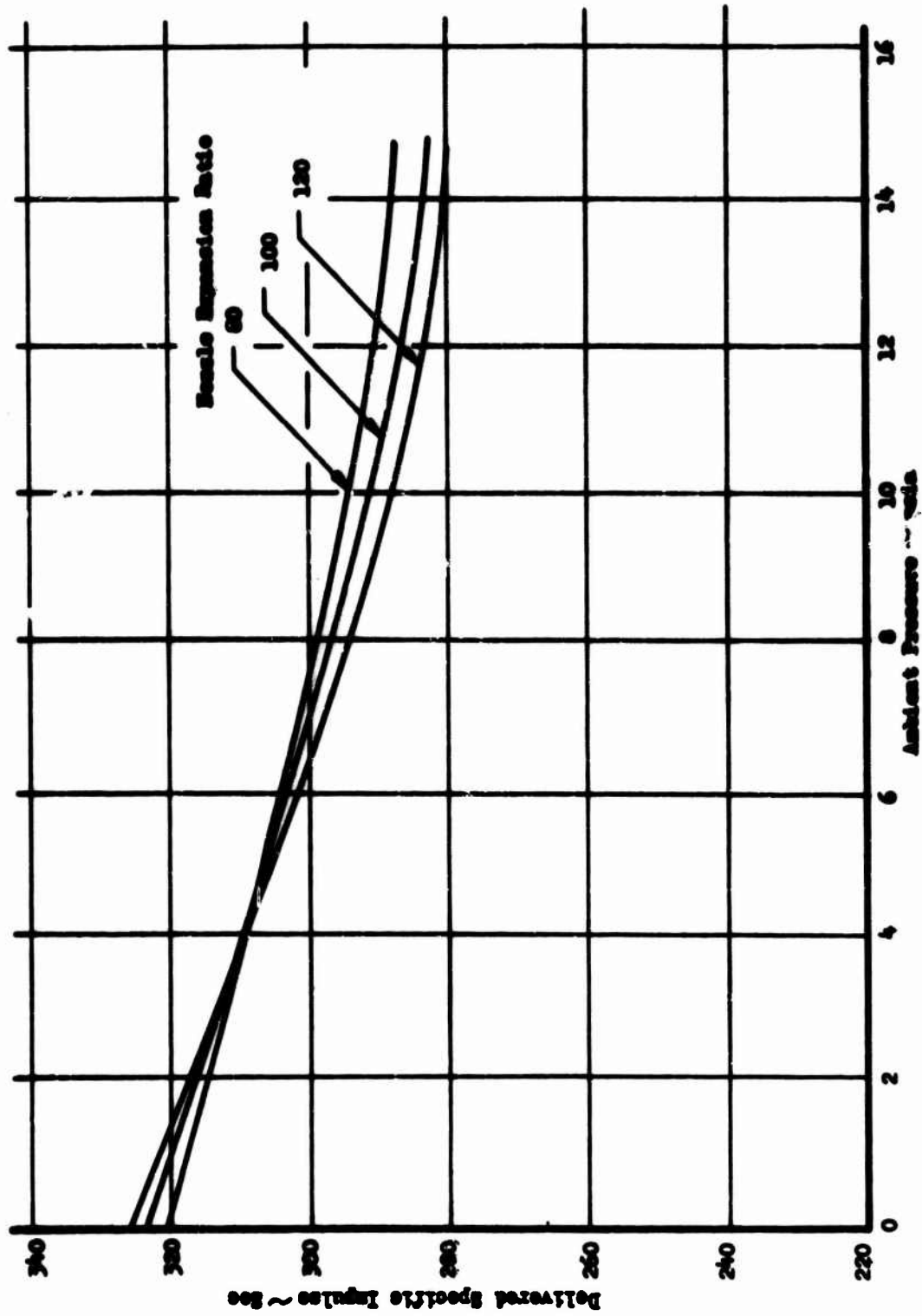
Figure X1-C-2

Forced-Deflection Engine Altitude Compensation, 1000-psi Chamber Pressure



Forced-Deflection Engine Altitude Compensation, 2000-psi Chamber Pressure

Figure XI-C-3

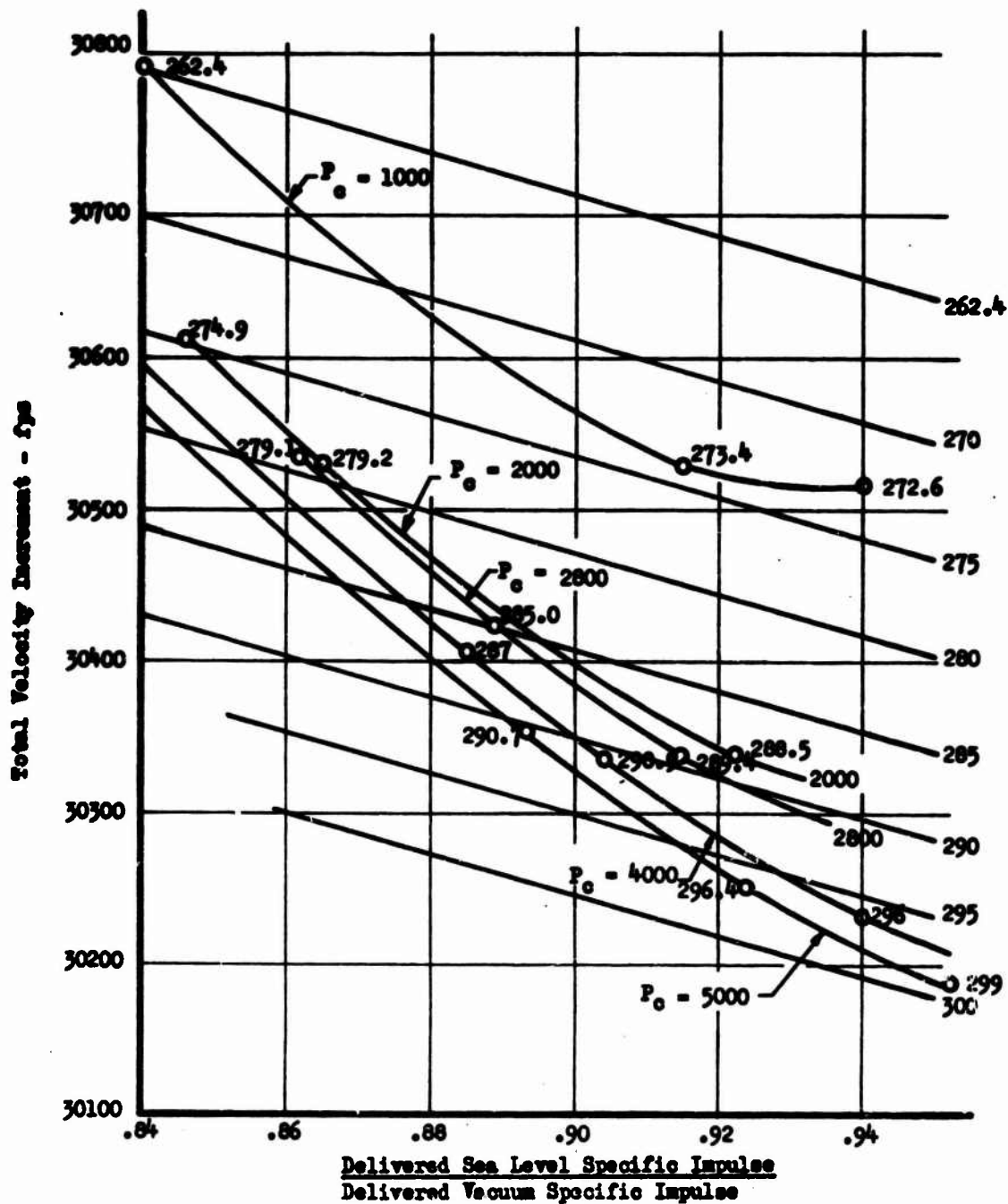


Forced-Deflection Engine Altitude Compensation, 5000-psi Chamber Pressure

Figure XI-C-4

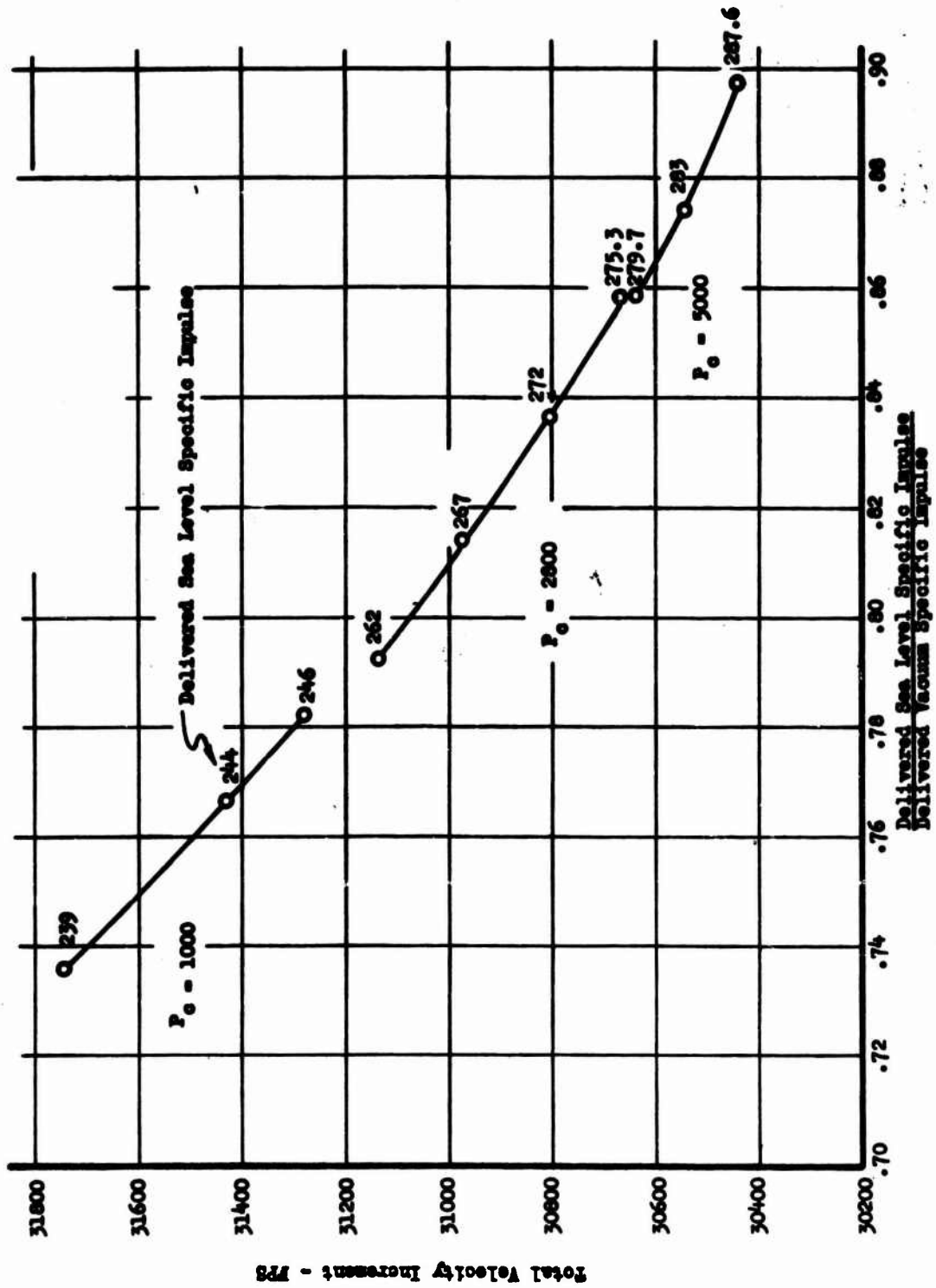
Book Two

Values Given Below are Delivered Sea Level
Specific Impulse



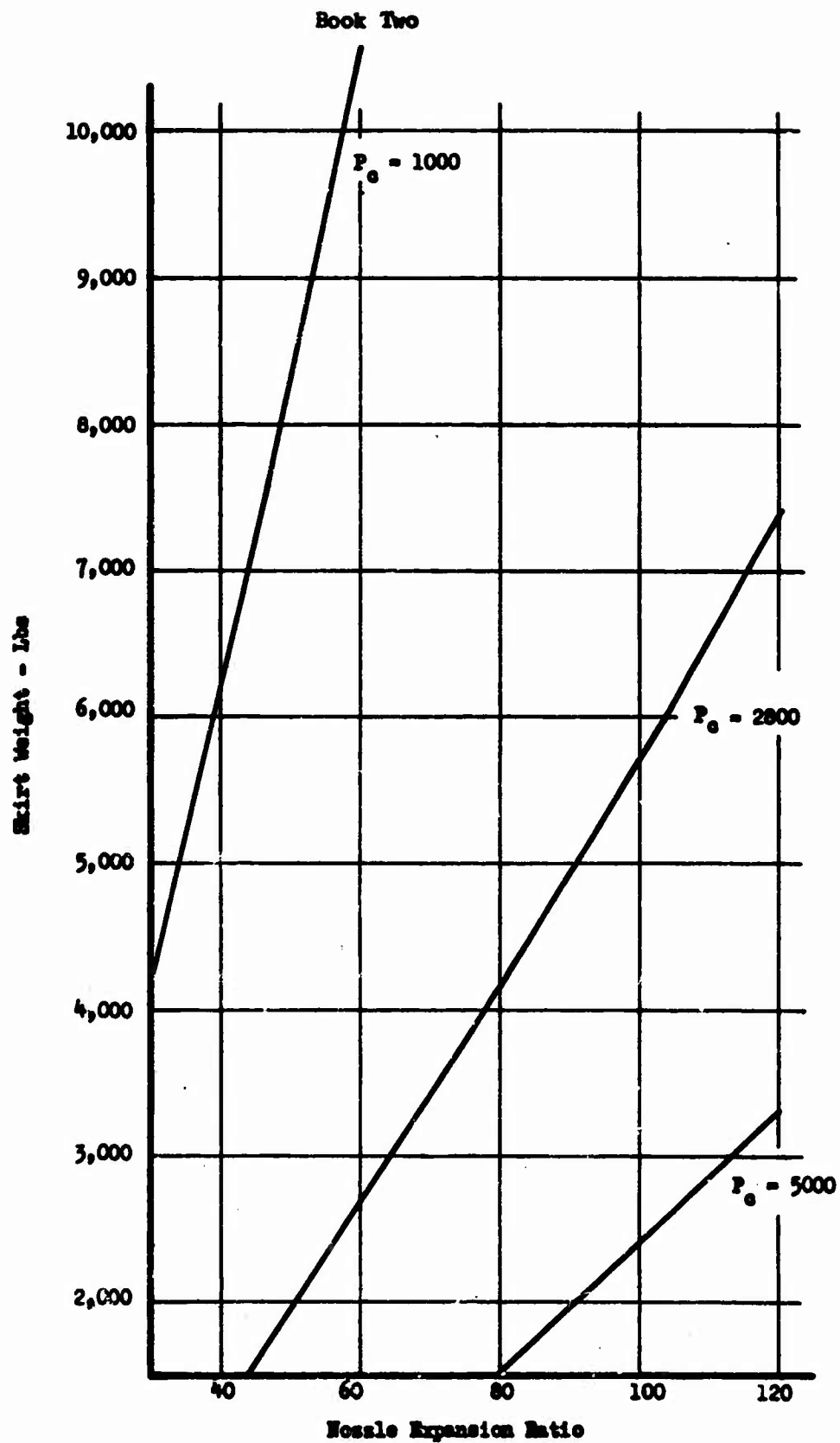
Total Velocity Increments, DeLaval Nozzles

Figure XI-D-1



Total Velocity Increments, Forced Deflection Nozzles

Figure XI-D-2



Forced Deflection Skirt Weight

Figure XI-E-1

Book Two

20-Module Forced-Deflection (Booster or Single-Stage)

	<u>Constant</u>	<u>Thrust Sensitive</u>
Modules (20) Expansion Ratio 14		
Internal Expansion Section (20)		
Module Thrust Structure (20)		220
Conical Supports (20)		600
Suction Line (40)	400	
Pack and Rail Gimbal Including Actuators		800
Roll Control Engine and Lines (4)	200	
Heat Shield	600	
Ablative Skirt		
Total	<u>1200</u>	<u>1620</u>
$\frac{F_{vac}}{1000}$		2370
Thrust Sensitive Weight Factor		0.684

20-Module DeLaval Engine (Booster or Single-Stage)

	<u>Constant</u>	<u>Thrust Sensitive</u>
Modules (20) Expansion Ratio 14		
Nozzle Skirts (20)		
Suction Line (40)	400	
Gimbals (13)		325
Actuators (26)	520	
Base Heating Insulation	<u>1000</u>	
Total	<u>1920</u>	<u>325</u>
$\frac{F_{vac}}{1000}$		2400
Thrust Sensitive Weight Factor		0.135

4-Module Second-Stage Engine

	<u>Constant</u>	<u>Thrust Sensitive</u>
Modules (4) Expansion Ratio 14		
Nozzle Skirts (4)		
Suction Line (8)	80	
Gimbals (4)		80
Actuators (4)	60	
Base Heating Insulation	<u>800</u>	
Total	<u>940</u>	<u>80</u>
$\frac{F_{vac}}{1000}$		480
Thrust Sensitive Weight Factor		0.167

Engine Weight Summary

Figure XI-E-2

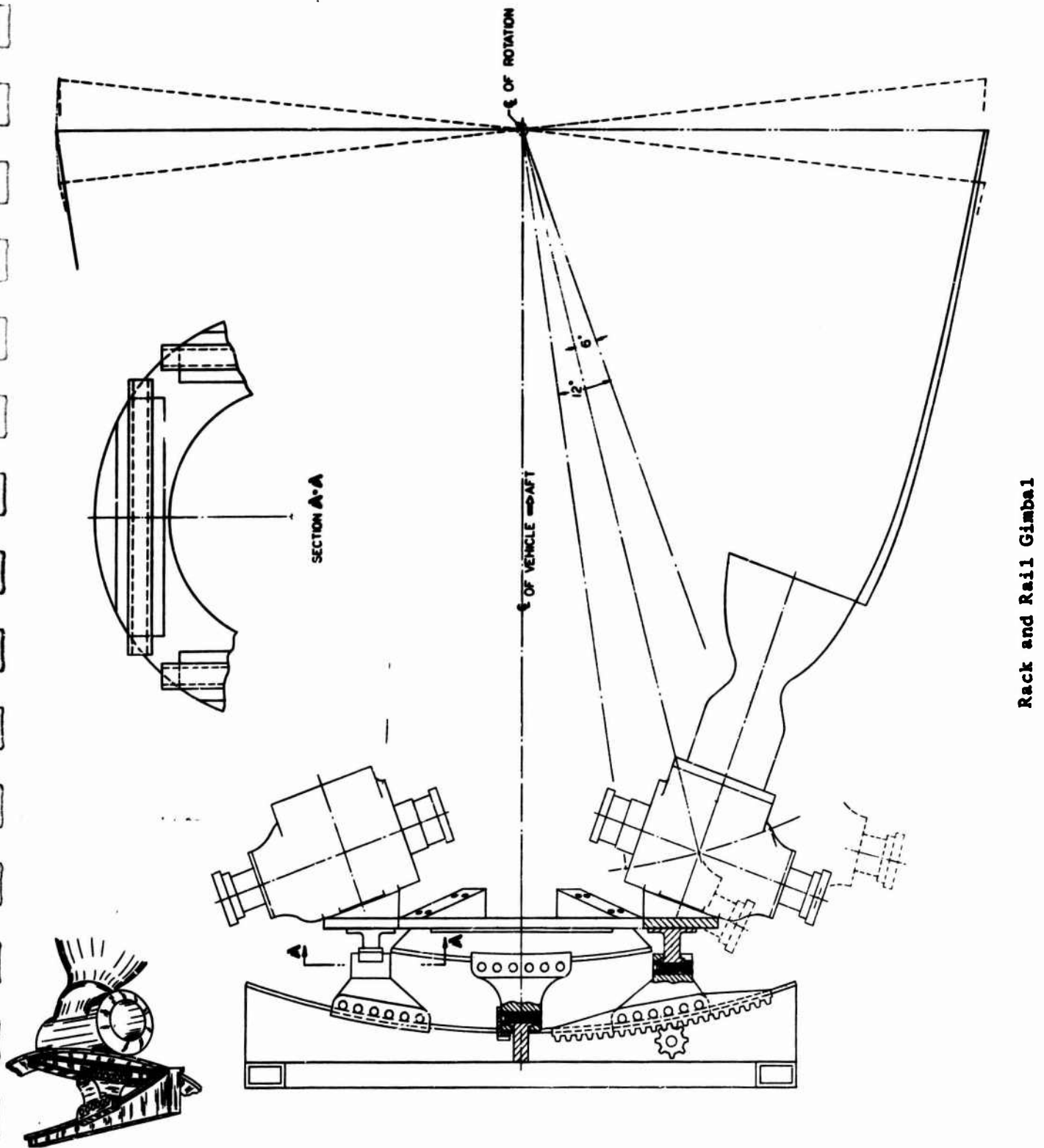


Figure XI-E-3

Book Two

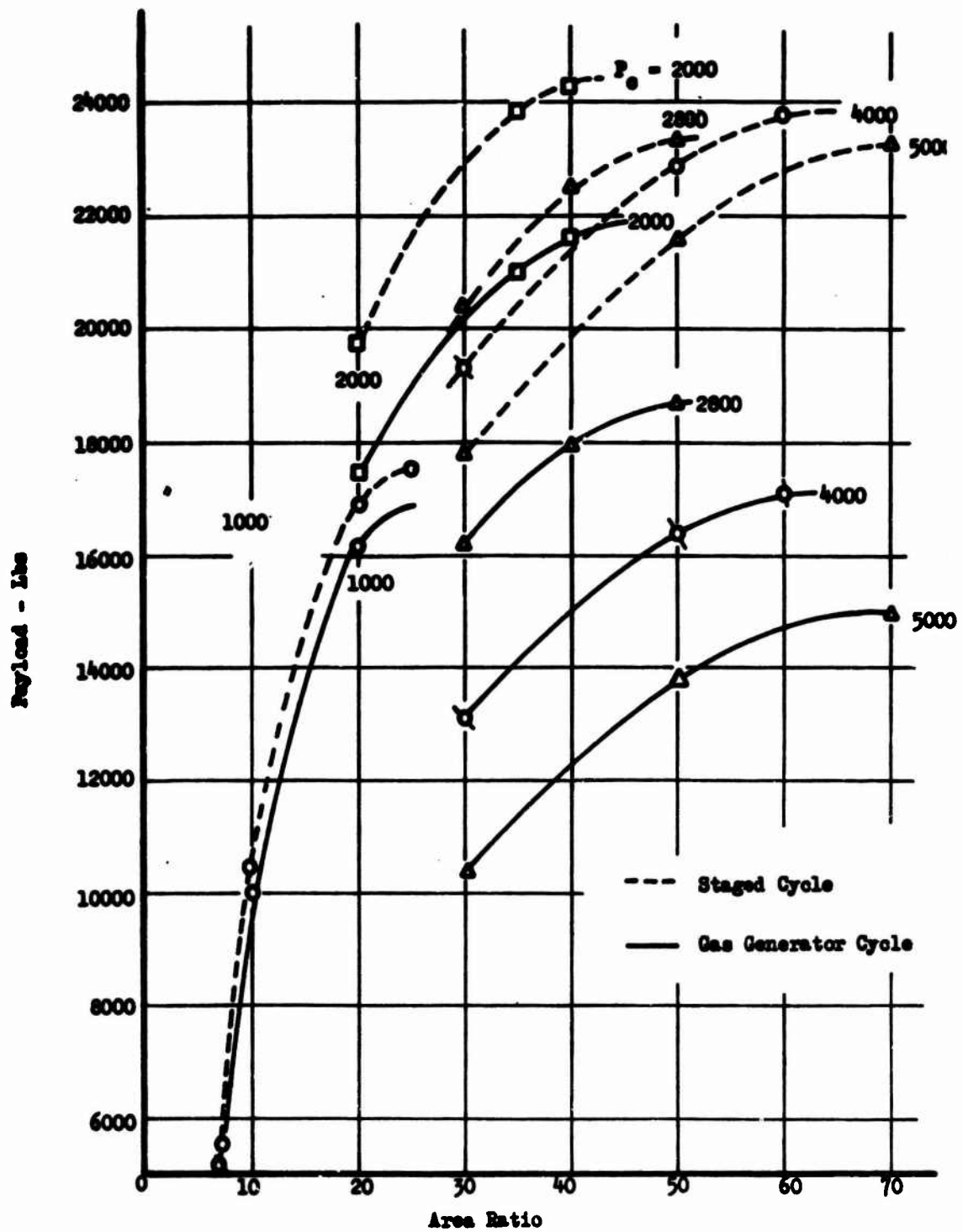
	<u>Single Stage</u>	<u>Booster</u>	<u>Upper Stage</u>
Tankage	$1.123 \frac{W_p}{\rho_B}$	$1.153 \frac{W_p}{\rho_B}$	$1.688 \frac{W_p}{\rho_B}$
Pressurization Residuals	$0.222 \frac{W_p}{\rho_B}$	$0.222 \frac{W_p}{\rho_B}$	$0.222 \frac{W_p}{\rho_B}$
Residual Propellant	$0.005 W_p$	$0.005 W_p$	$0.005 W_p$
Engine Thrust Ring	$0.653 \frac{F_{vac}}{1000}$	$0.653 \frac{F_{vac}}{1000}$	$0.653 \frac{F_{vac}}{1000}$
Aft Skirt	1282	1282	$11.1 L_2$
Forward Skirt	700	1110	1000
Thrust Structure	$0.832 \frac{F_{vac}}{1000}$	$0.832 \frac{F_{vac}}{1000}$	$0.832 \frac{F_{vac}}{1000}$
Misc. (Guidance, Electrical, Velocity Vernier, Retro, Power Supply)	2500	2090	2060

Where	W_p	Usable Propellant Weight	- lb
	ρ_B	Bulk Density	- lb/ft ³
	F_{vac}	Vacuum Thrust	- lb
	L_2	Length of Second-stage interstage section	- in.

Airframe Weight Summary

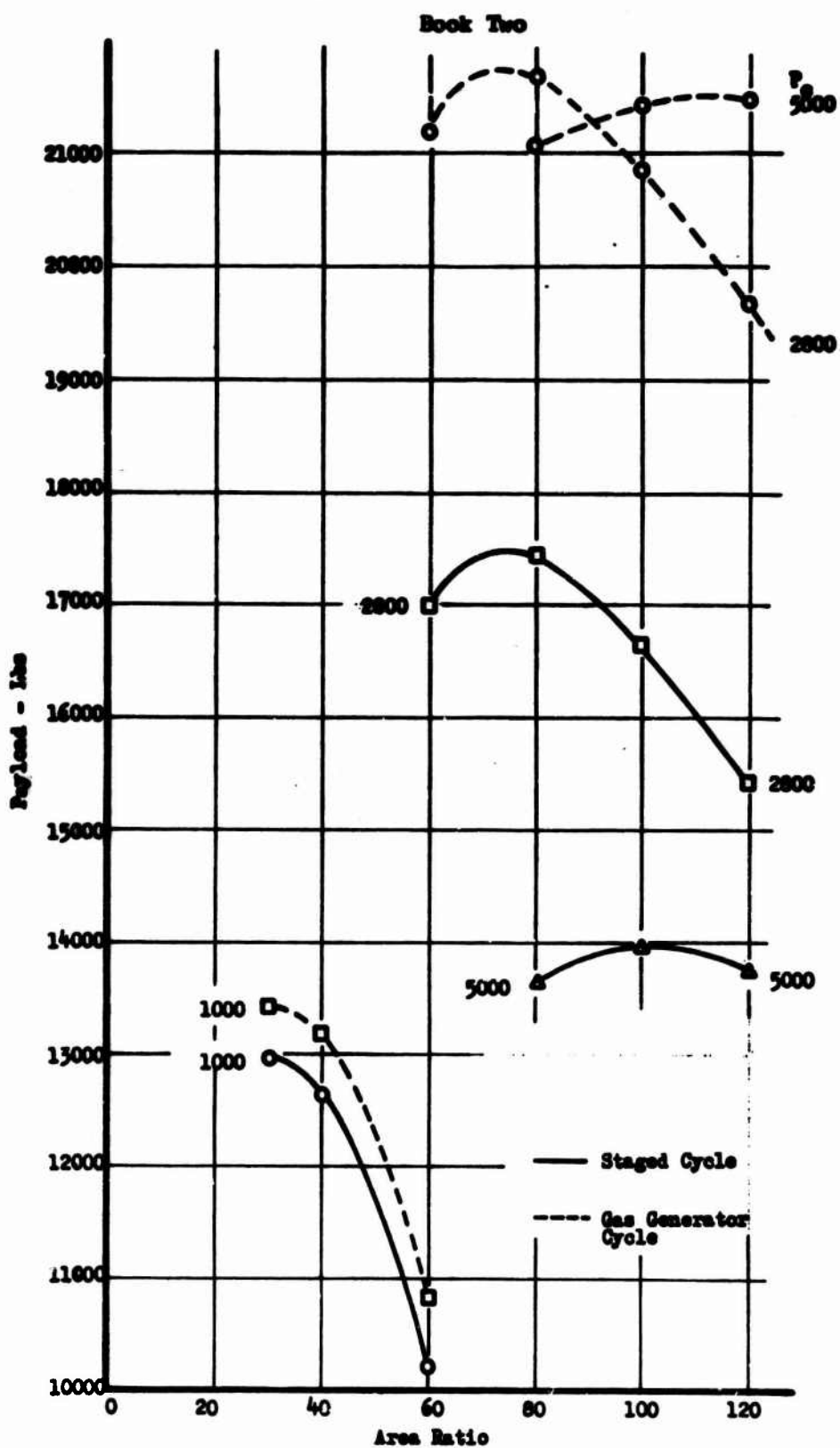
Figure XI-E-4

Book Two



Area Ratio Optimization, Single-Stage DeLaval Nozzle

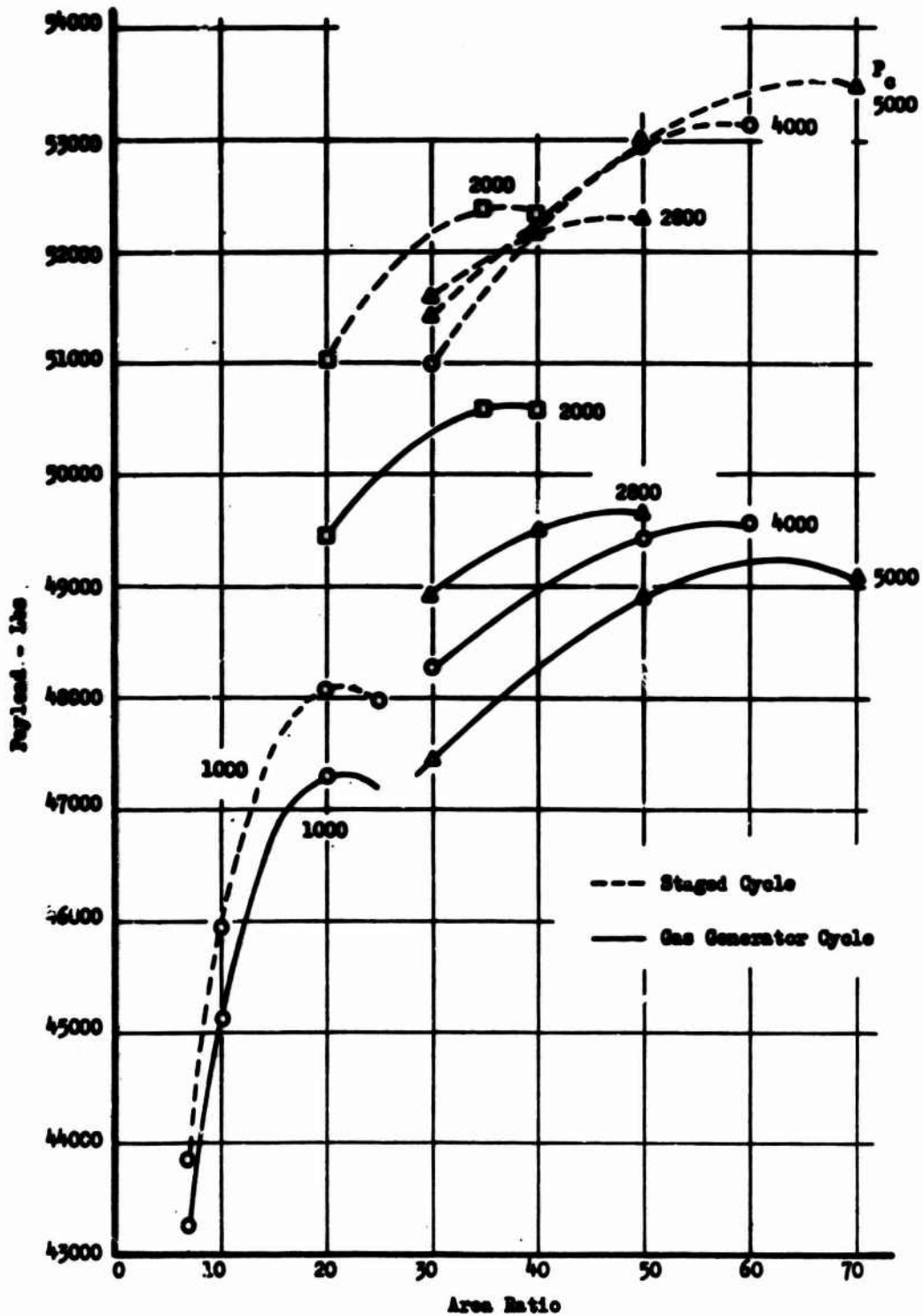
Figure XI-F-1



Area Ratio Optimization, Forced-Deflection Nozzle

Figure XI-F-2

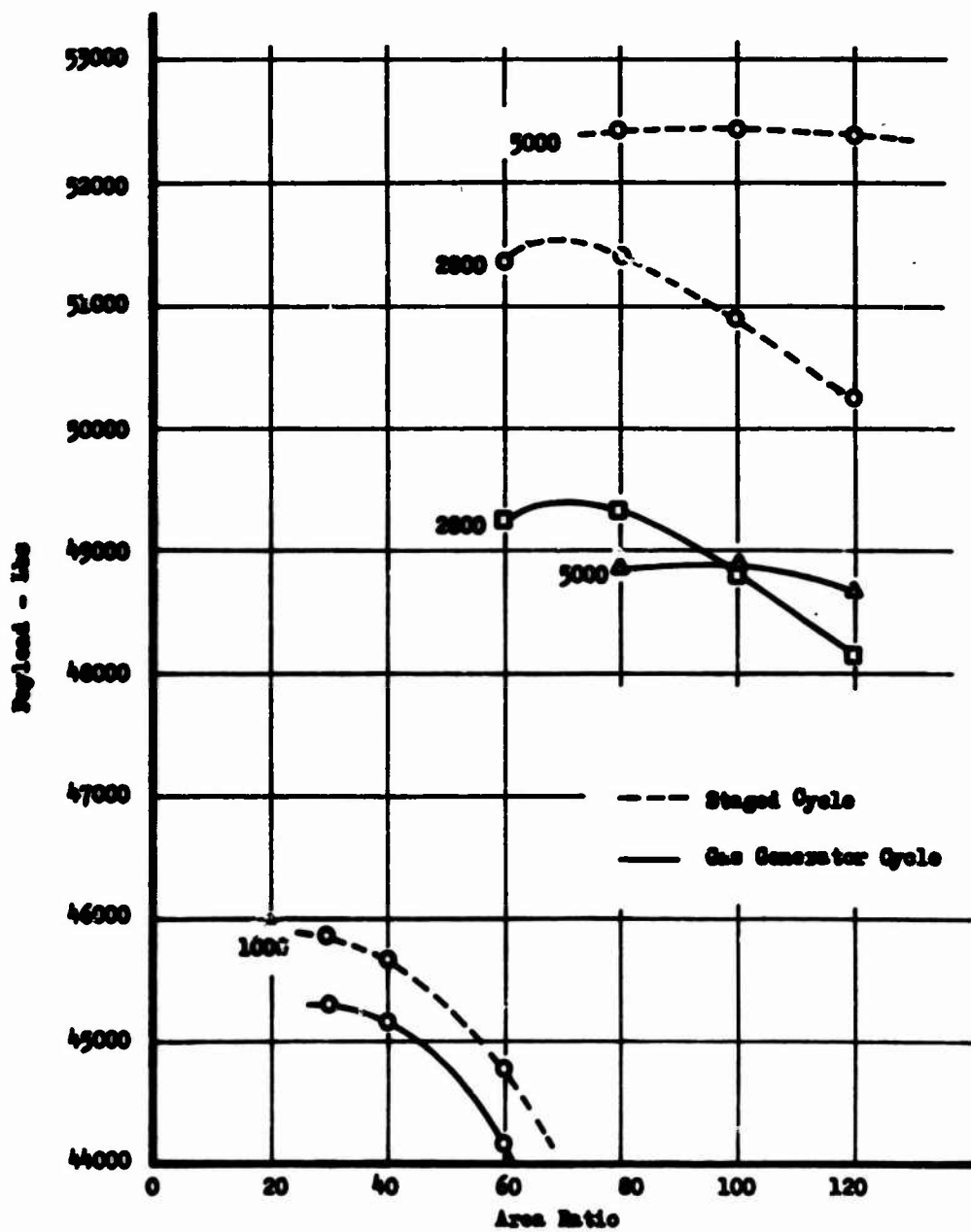
Book Two



Area Ratio Optimization, Booster DeLaval Nozzle

Figure XI-F-3

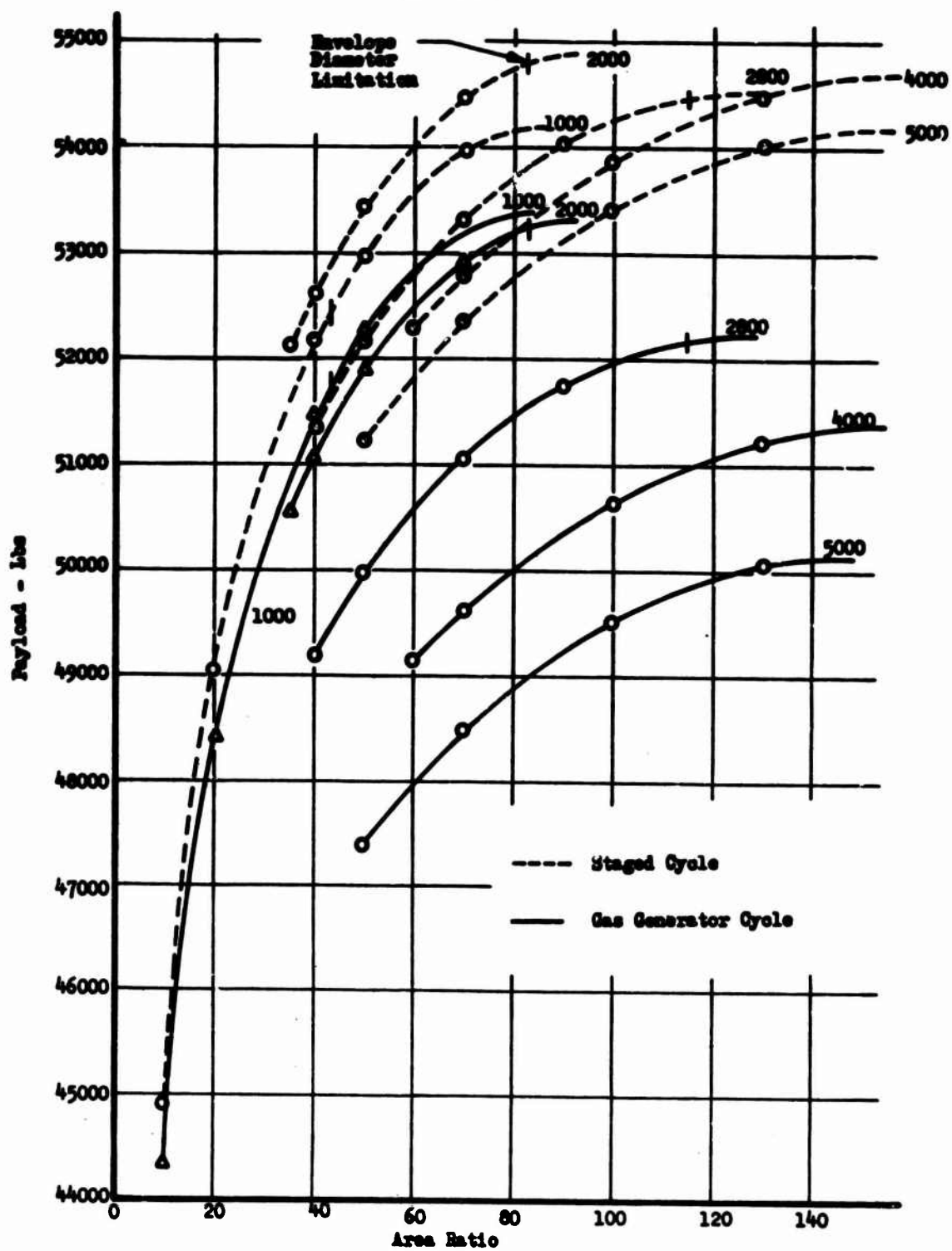
Book Two



Area Ratio Optimization, Forced-Deflection Nozzle

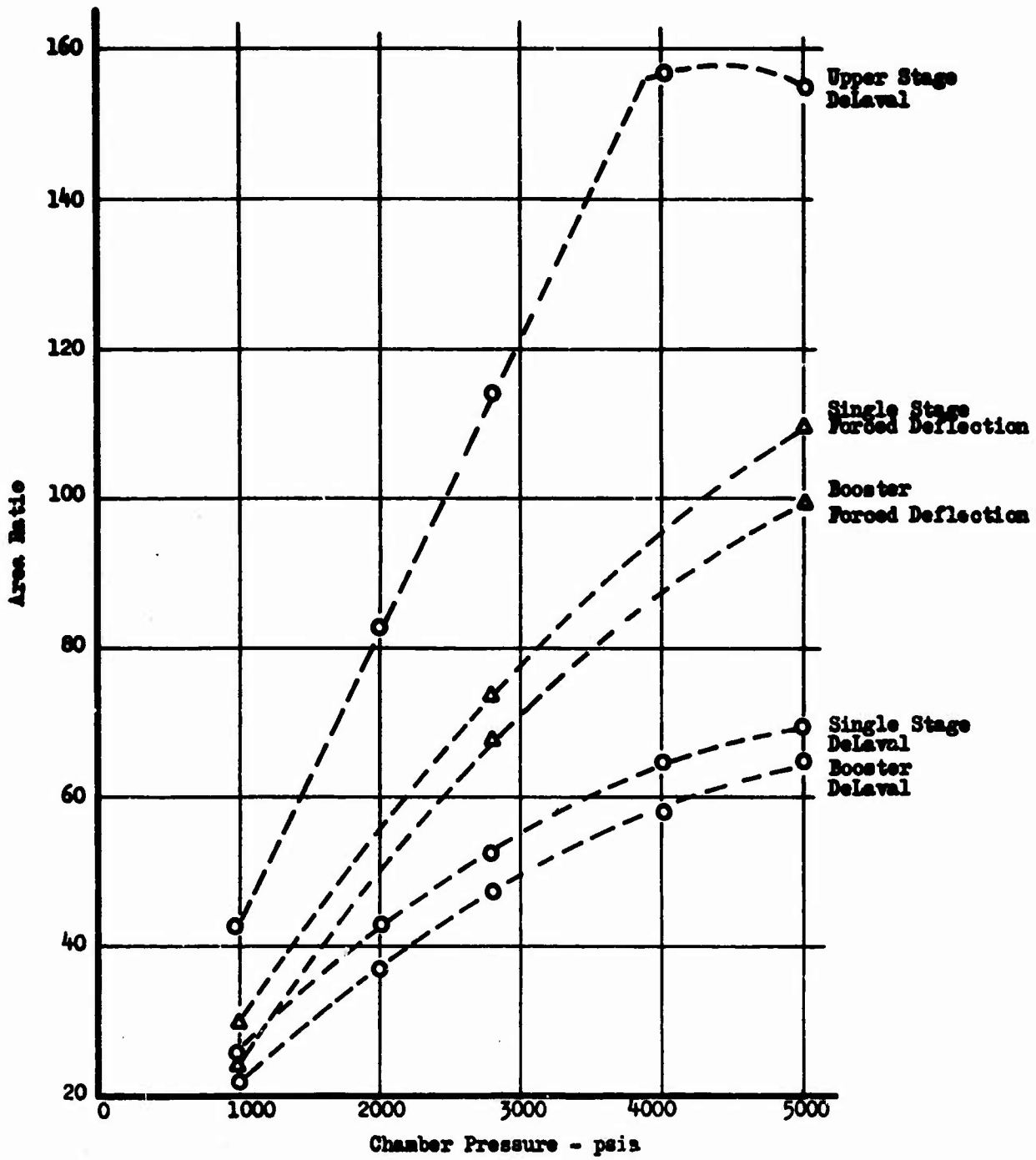
Figure XI-F-4

Book Two



Area Ratio Optimization, Upper-Stage DeLaval Nozzle

Figure XI-F-5

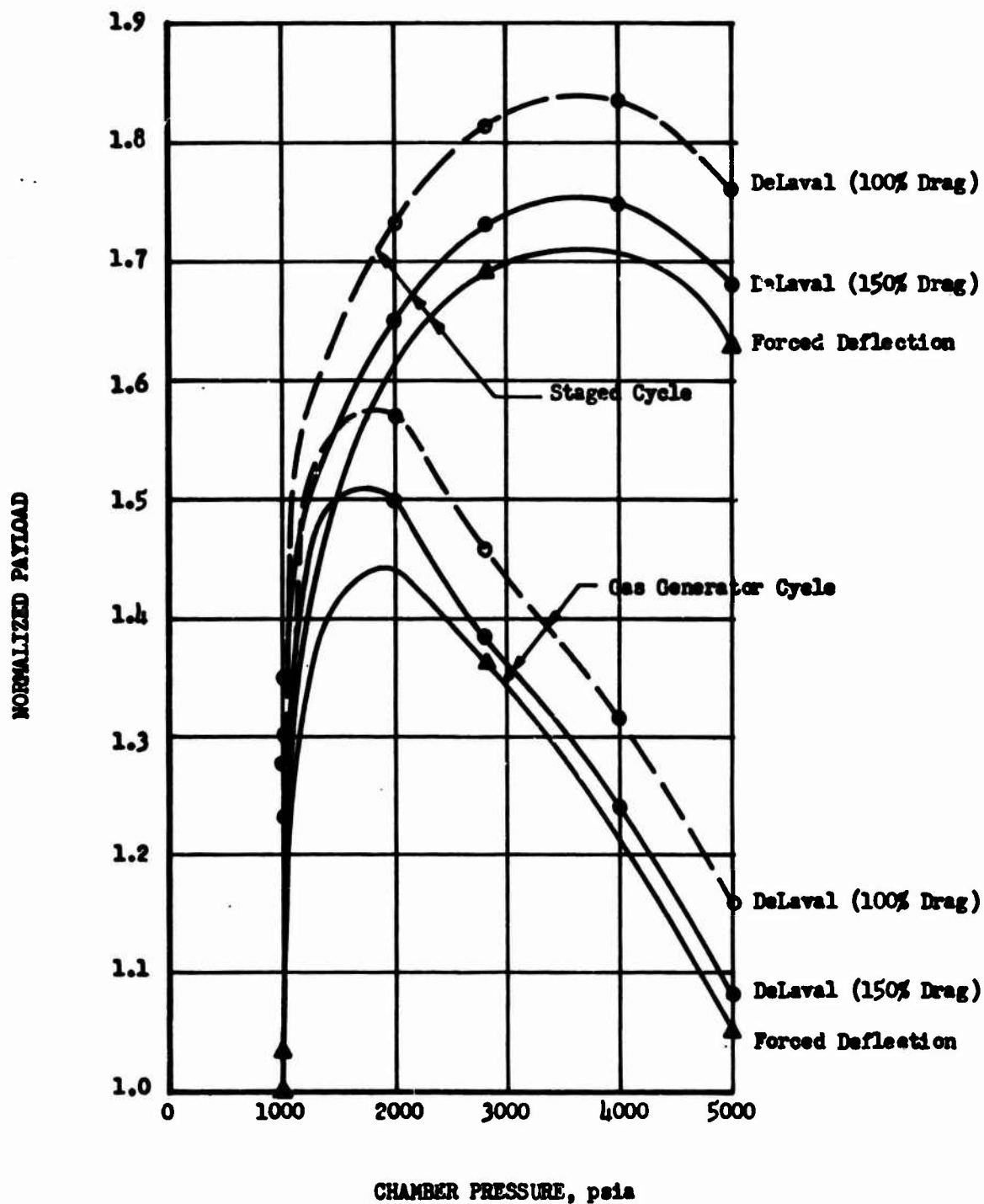


Optimum Area Ratio vs Chamber Pressure, Stage Cycle

Figure XI-F-6

Book Two

Single Stage to 300 N.M. Orbit With a Reference
Payload = 12,970 lbs.

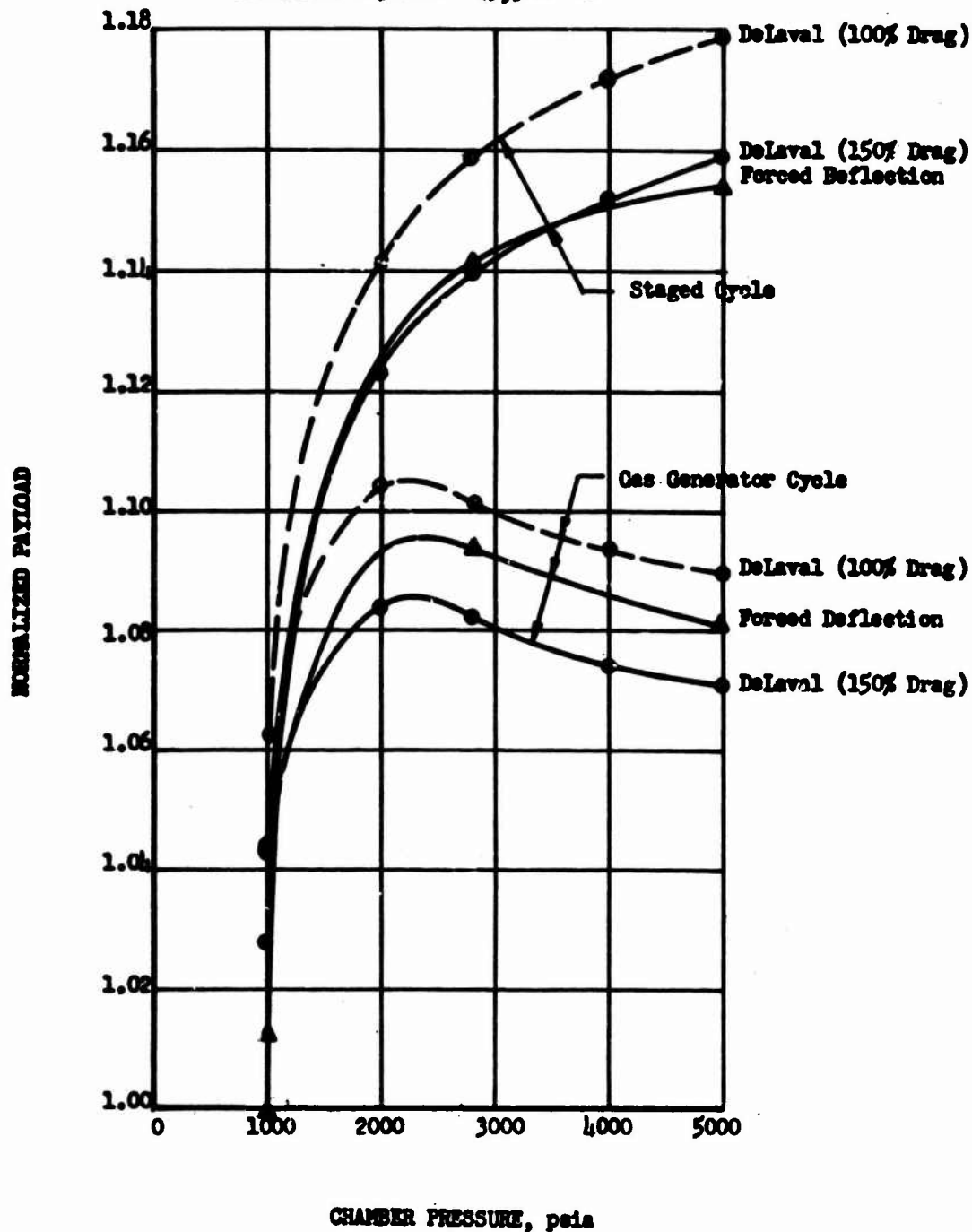


Chamber Pressure Optimization, Single Stage

Figure XI-F-7

NOTES:

Booster Stage
Standard Upper Stage Added to Complete Mission to
300 M.M. Orbit
Reference Payload = 45,300 lbs



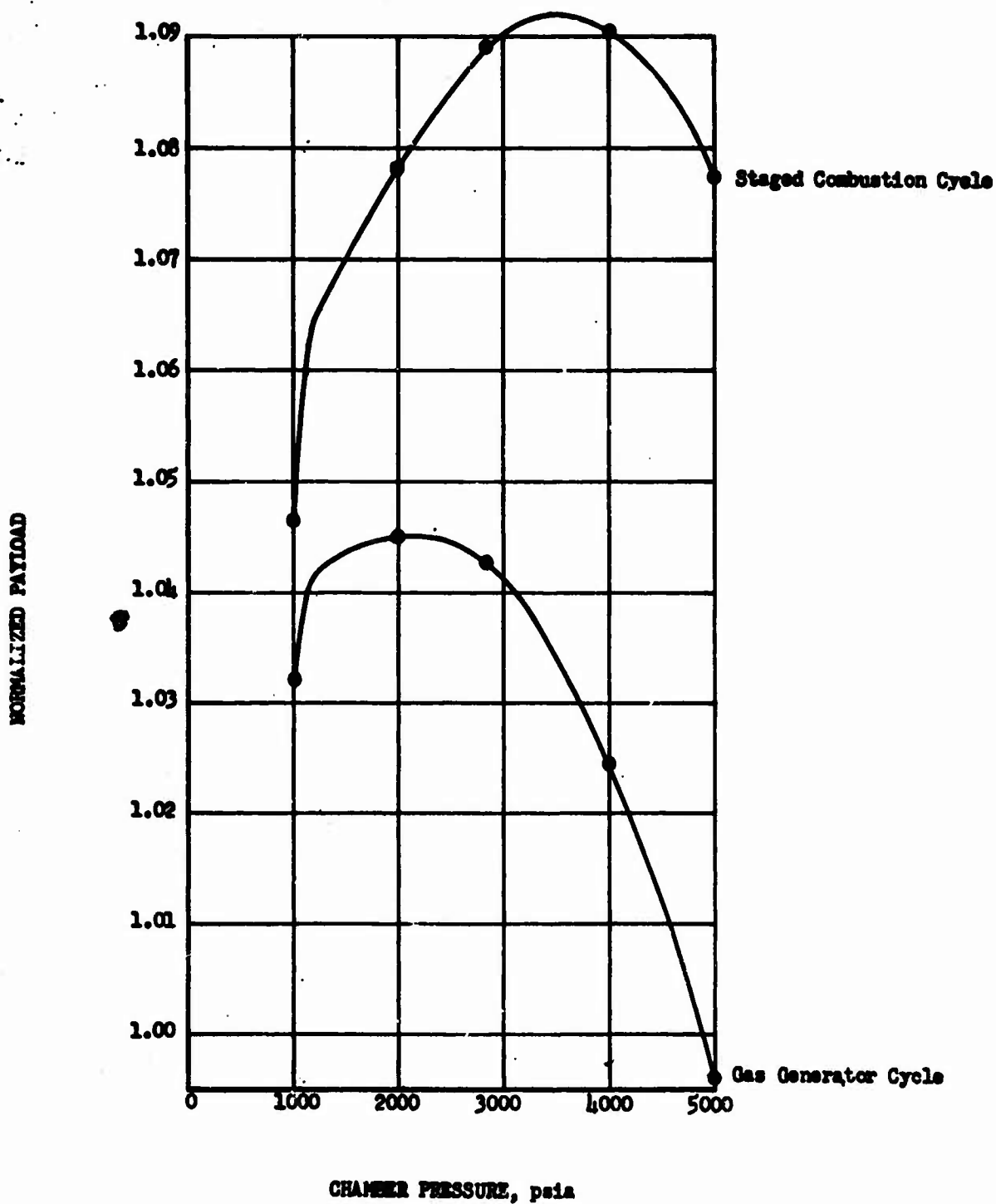
Chamber Pressure Optimization, Booster

Figure XI-F-8

Book Two

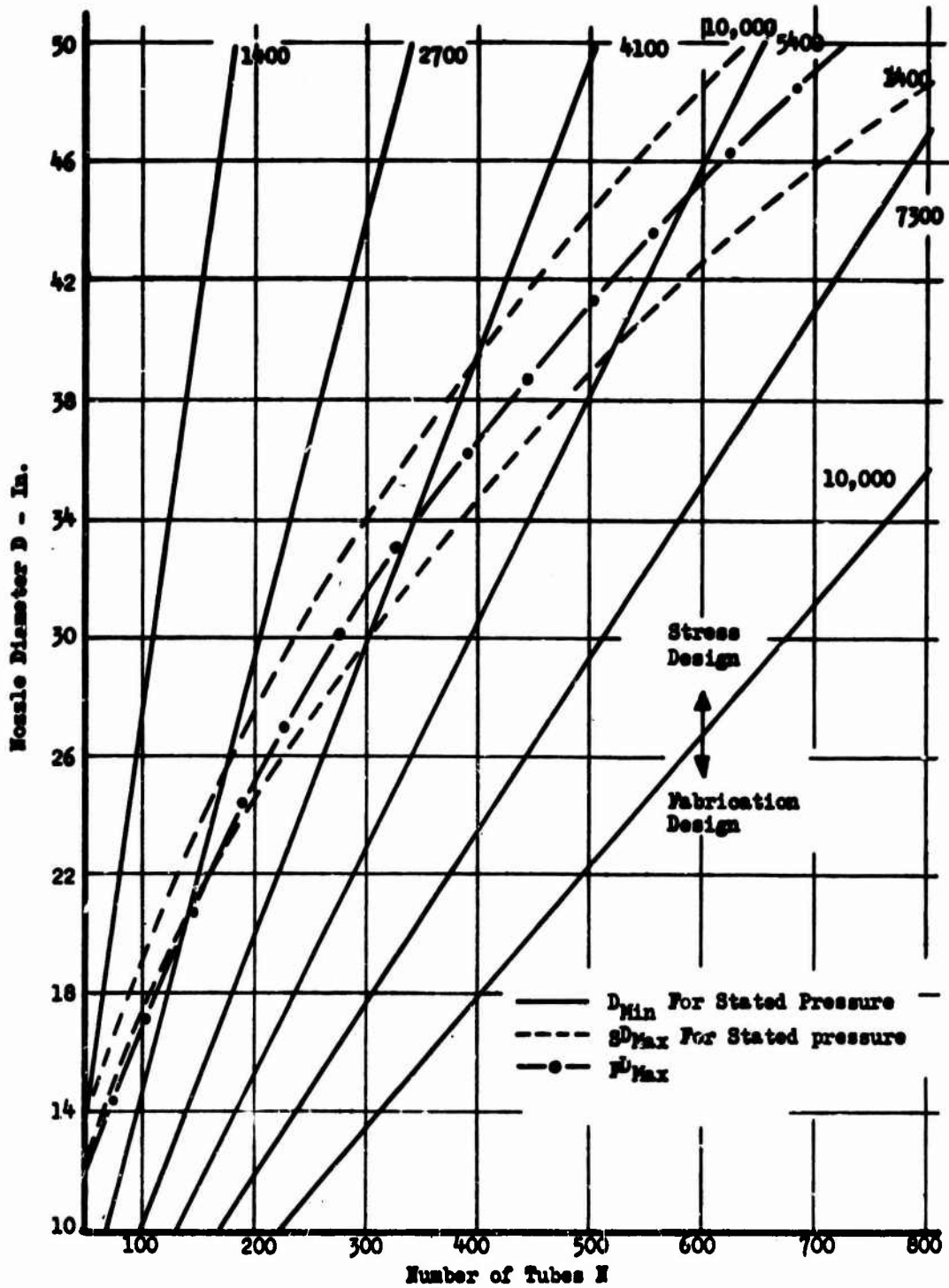
NOTE:

Upper Stage DeLaval Nozzles
 Velocity Increment = 155,000 f.p.s.
 Lift Off Weight = 300,000 lbs.
 Reference Payload = 50,130 lbs.



Chamber Pressure Optimization, Upper Stage

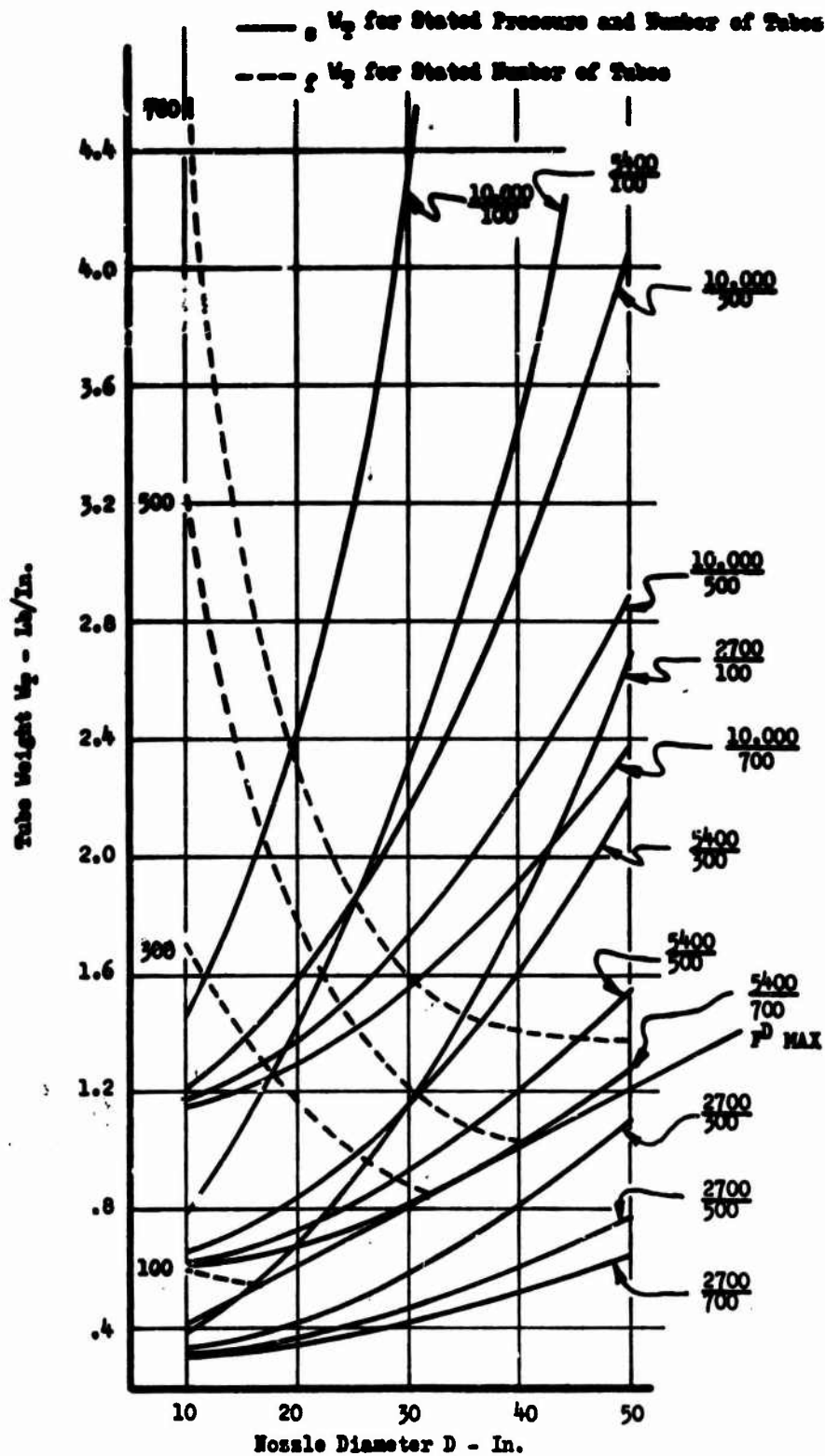
Figure XI-F-9



Tube Design Regimes

Figure XI-G-1

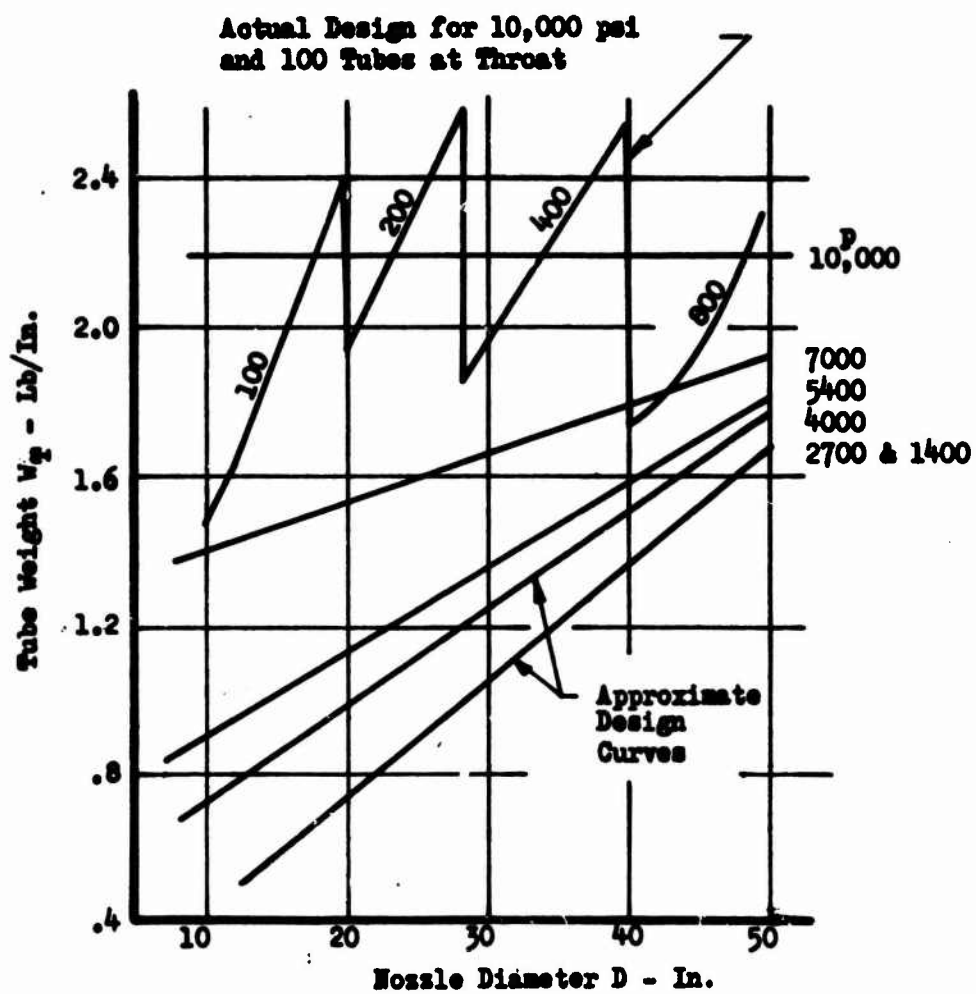
Book Two



Tube Weight vs Diameter Design Curves

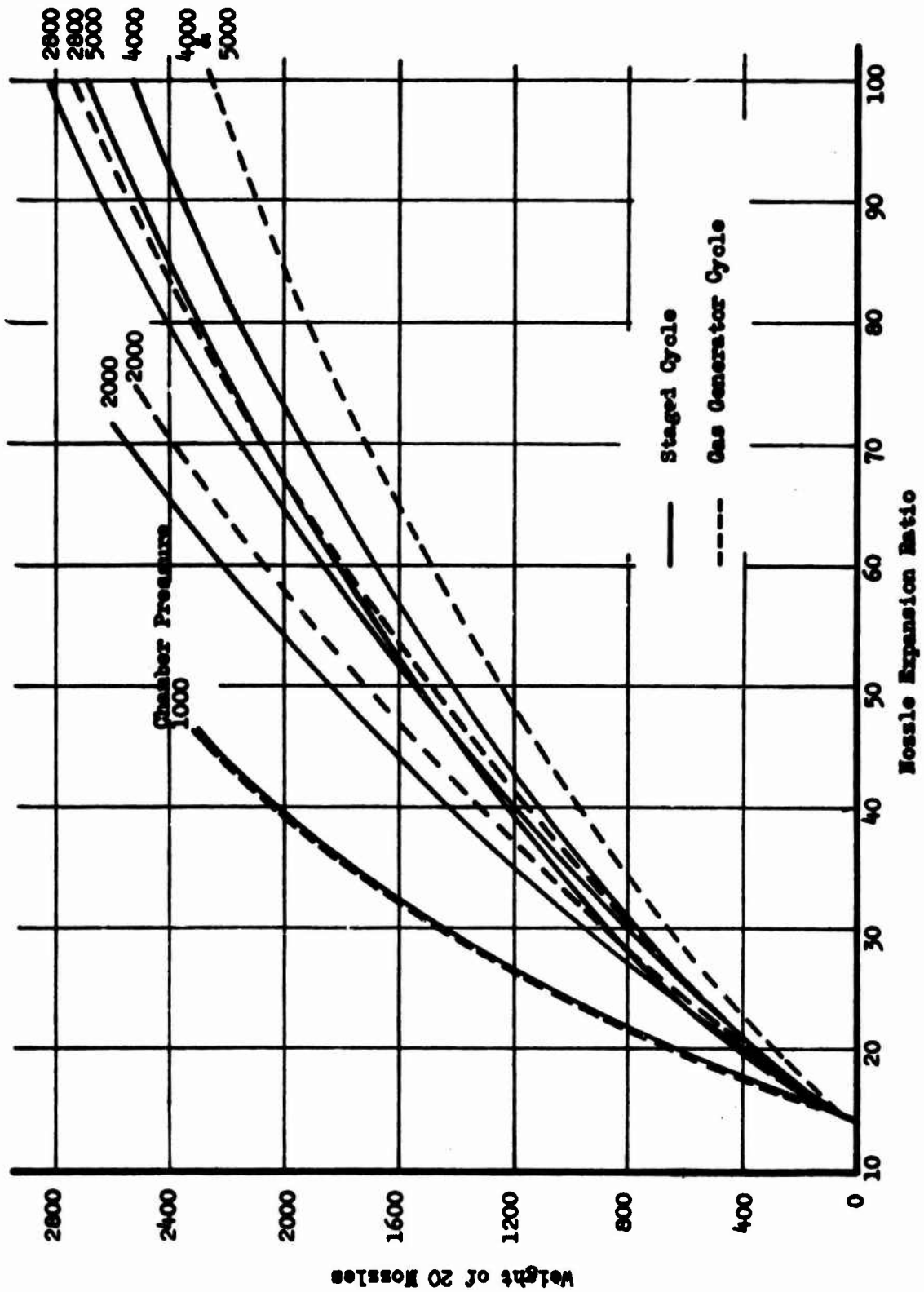
Figure XI-G-2

Book Two



Tube Weight vs Diameter

Figure XI-G-3



DeLaval Nozzle Weight

Figure XI-G-4

Weights are For 20 Sea Level Start Nozzles

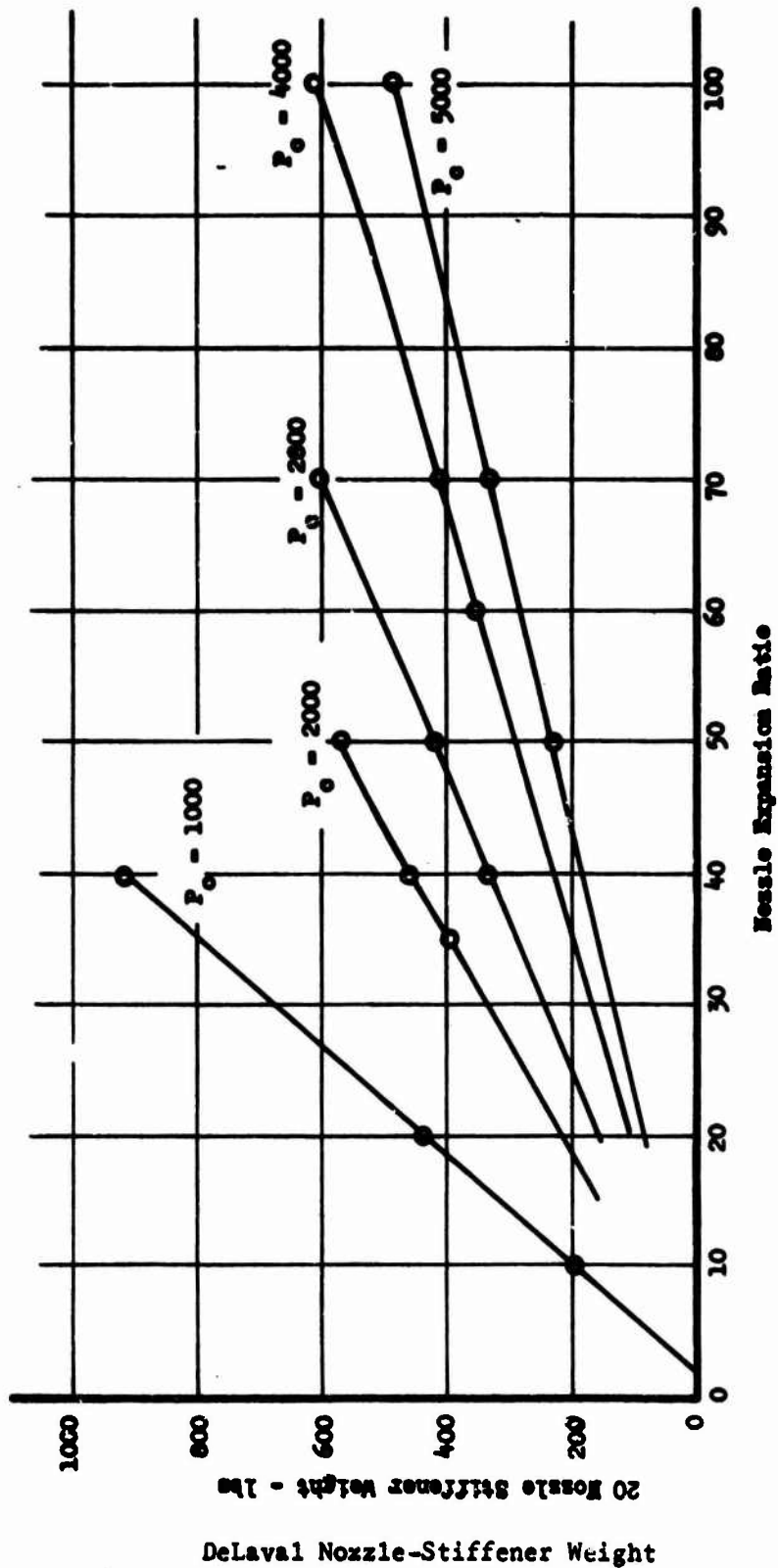


Figure XI-G-5

Book Two

XII. TEST STAND OPERATION

All high-pressure thrust chamber and turbopump development testing conducted during this program was performed on Aerojet's Test Stand H-3. The testing system used was a "breadboard" high-pressure turbopump engine having built-in flexibility features to allow operation over the required range of pressure and flow-rate conditions of the program. The expected availability of a developed high-pressure turbopump design from the Integrated Components Program, (Contract AF 04(611)-8017) was the basis for the selection of a pump-fed engine system, rather than a high-pressure tank-fed system. In addition to a lower initial cost, this system provided the additional knowledge of high-pressure turbopump operation.

A detailed description of the engine testing system, together with its associated equipment, instrumentation, and controls, is given in Section XII,A, below. The analytical steady-state and transient computer programs, used throughout the program for engine balance and data evaluation, are discussed briefly in Section XII,B. The turbopumps were considered a part of the test facilities in this program; however, extensive development effort was performed during this contract in modifying the design of the original turbopumps of Contract AF 04(611)-8017 to a configuration suitable for conducting the tests in this program. Because of the extensive effort involved, a separate section, XII,C, below, is included to discuss the turbopump development effort. A summary of the turbopump development test data, together with the test results from the initial test stand activation checkout tests performed with the pumping system, is also included.

A. ENGINE TESTING SYSTEM

The engine testing system, as defined for this discussion, is comprised of the test engine with its associated mechanical facility equipment, the engine instrumentation, and the engine control system. Each of these is discussed in the paragraphs below.

Book Two

XII, A, Engine Testing System (cont.)

1. Test Engine

In the engine configuration a single $\text{LO}_2/\text{RP-1}$ gas generator was used to drive separate high-pressure oxidizer and fuel turbopumps. The high-pressure propellants were then directed to the thrust chamber through two high-pressure ball valves. The engine is shown schematically in Figure XII-A-1. Principal mechanical components include the storable propellant tanks, $\text{LO}_2/\text{RP-1}$ propellant tanks, gas generator valve, gas generator, hot-gas manifold, oxidizer and fuel turbopumps, discharge and recirculation lines, thrust chamber valves, and the thrust chamber. By referring to the schematic and to five photographs shown in Figures XII-A-2 through -6, the relationship of the components to one another can be seen. Discussions for each major component follow; any development work or modifications required on the components during the program are also reported.

a. Storable Propellant Run Tanks and Main Propellant Supply Lines

The AeroZINE 50 and nitrogen tetroxide propellant run tanks supply the main propellants to the turbopumps; both are 2100-gal pressure vessels capable of withstanding a pressure of 1000 psig. Each tank has a 6-in.-dia discharge line and a 4-in.-dia recirculation line leading to the test stands. A pressure regulator is plumbed to each tank and a safety valve is installed on each line. This one set of propellant tanks services Test Stands H-1, H-2, and H-3. Valves located within these lines are opened or closed as required to supply propellant to any of the three test stands. Prior to conducting tests, each tank is pressurized with gaseous nitrogen to a predetermined pressure. This pressure setting is instrumental in determining proper engine balance.

b. Liquid Oxygen and RP-1 Propellant Run Tanks

The liquid oxygen and RP-1 propellant run tanks are used to supply propellant to the gas generator; both are 250-gal vessels capable of withstanding 1200-psig pressure. Each tank has a 2-in.-dia supply line connecting to

Book Two

XII, A, Engine Testing System (cont.)

Test Stands H-1, H-2, H-3, and a pressure regulator and safety valve are installed in each line. Similarly to the main propellant tanks, these tanks are pressurized with gaseous nitrogen to a predetermined pressure prior to each test. This pressure setting is also instrumental in determining proper engine balance.

c. Gas Generator Valve

The gas generator valve is a rocker-arm and pintle-type valve. The motion of an actuator operates a rocker arm, which causes the oxidizer and fuel pintles to move in a fixed relation to one another. Propellant flows axially through the valve body and annularly around the valve pintle. The controlling flow area is then the annular area between the contoured pintle and the valve seat.

This gas generator valve was initially designed for Titan I first-stage engines, and was intended to be used with a bootstrap-engine starting sequence. Initial pressure-fed engine tests (performed under Contract AF 04(611)-8017) indicated an excessive gas generator pressure rise rate occurred with a normal 1.0-sec valve opening time. It was decided that the pintle contours of both the oxidizer and fuel valves should be changed.

A short computer program was set up to determine pintle contours such that a linear rise rate of generator chamber pressure would occur with increased valve opening. Fuel and oxidizer pintles were fabricated on the basis of the results of the computer program. The gas generator rise-rate resulting from the use of these pintles was not perfectly linear with valve opening position, but the rise rate appeared to be suitable for starting the engine. Figure XII-A-7 illustrates a typical plot of gas generator chamber pressure versus time resulting from the use of the modified gas generator valve. The gas generator system was tested twice to verify the operation and repeatability of the hardware. Turbine nozzle simulators were used to provide a sonic nozzle in each branch of the Y-shaped turbine feed manifold. No difficulty was experienced with either test, and the results indicated proper valve operation and repeatability.

Book Two

XII, A, Engine Testing System (cont.)

Subsequent thrust chamber operation using this modified gas generator valve demonstrated that the generator pressure rise rate during the steep portion of the pressure-versus-time curve caused a corresponding steep increase in turbine speed, pump discharge pressure, and thrust chamber pressure. A stepped opening of the gas-generator valve corrected this situation. The modified control system used two orificed pilot valves instead of one valve to feed actuation fluid to the generator valve actuator. One of the valves is closed during actuation of the generator valve to provide two opening rates. Figure XII-A-8 illustrates percent valve open position and the resultant gas generator chamber pressure versus time. Improvement in the secondary rise rate is apparent over the previous rise rate shown in Figure XII-A-7. The gas generator valve was opened in this manner for the remainder of the test program.

d. Gas Generator and Y-Manifold

The gas generator, originally designed on the Titan program, is a 5-in.-dia cylinder with an injector having five rows of like-on-like doublets and an outer row of single fuel orifices. The gas generator has a valve interface on the injector end and a flanged outlet on the outlet end. This generator is ignited with 28-v, 400-cycle current; the igniter system worked flawlessly during the entire test program.

An integral part of the gas generator system is the Y-shaped hot-gas manifold which delivers hot gases from the generator to the turbine inlet manifold of each turbopump. Each lag of the manifold contains commercial bellows and restrainers to allow for thermal expansion without loading the turbine manifold. Excessive distortion of the bellows is prevented by a closely fitted sleeve, visible in Figure XII-A-3. An orifice holder is spaced between the Y-manifold and turbine inlet flanges. An orifice in this location reduces turbine total inlet pressure and permits a power balance required for any particular test.

Book Two

XII, A, Engine Testing System (cont.)

e. Turbopumps

The turbopumps used to deliver high-pressure storable propellants were originally designed for Contract AF 04(611)-8017, "Integrated Components Program, Phase I." Each turbopump assembly consists of a Titan II first-stage turbine, a bearing housing, and a single-stage centrifugal pump, all on a common shaft. The fuel and oxidizer turbopumps are identical except for minor differences in the impellers and shrouds. During development, it was found necessary to partially redesign these turbopumps to carry the loads and create the head rise required by the test program. The required redesign and development work was accomplished jointly by Contracts AF 04(611)-8548, "Integrated Components Program, Phase II," and AF 04(611)-8191, "High Chamber Pressure Rocketry Program." A discussion of the pump development program is included in Section XII,C.

f. Propellant Lines and Orifices

Major propellant lines include the suction lines, discharge lines, and recirculation lines. Orifices were installed in each of these lines; their locations are shown in Figure XII-A-1.

The suction lines are part of the basic test facility and serve Test Stands H-1, H-2, and H-3. Because of the single set of remotely located propellant tanks serving these three stands, the length of the suction line is approximately 80 pipeline feet. Orifices were installed in the suction lines near the test engine to reduce the amplitude oscillations in the suction system (present on any short-duration test, but complicated by the long lines).

High-pressure discharge lines connected the turbopumps to the thrust chamber assembly. Orifices were installed in these lines to measure propellant flow rates, supplementing the flowmeter data.

Book Two

XII, A, Engine Testing System (cont.)

Recirculation lines were part of the engine system and connected the pump discharge propellant circuits back to the propellant tanks. These lines were used to return all pump discharge flow to the storage tanks during pump testing, and to return to the storage tank that portion of the propellant discharged by the pump but not required by the thrust chamber being tested. (The turbopumps were designed to be used with the 100,000-lb-thrust ICP engine system. Since the engine of Contract AF 04(611)-8191 produces 50,000-lb thrust at approximately the same head rise, it was necessary to operate the pumps at approximately the 100,000-lb-thrust flow rates, and then recirculate the excess flow back to the propellant tanks.) Orifices in the recirculation lines were used to control the recirculation flow and to drop the line pressure to below 1000 psig prior to the propellant entering the propellant tank.

g. Thrust-measuring System

The entire pumping system and thrust chamber with its valves are mounted on a movable thrust frame. A load cell and hydraulic cylinder are used together with a standard load cell to calibrate the load cell so that its thrust readings may be corrected as required. The load cell was used during pump testing to determine the quantity and direction of any unbalanced thrust from pump operation. The entire thrust frame was inclined downward at an angle of 15°.

h. Thrust Chamber Valves

Consolidated Controls Corporation supplied the thrust chamber valves. They are water-actuated ball valves that employ a fail-safe feature of spring closure should actuation pressure be lost. The ball-type valve is nearly hydraulically balanced. This feature is desirable for high-pressure application, since it does not alter its operating characteristics under pressure. Unfortunately, a ball valve permits only limited control over flow rate during the opening and closing operations. This is a result of the rapid change of resistance with advancing valve position. The primary control of thrust chamber pressure during the engine transients is obtained with the gas generator valve.

Book Two

XII, A, Engine Testing System (cont.)

The valves are seen in Figure XII-A-5. The oxidizer valve has a $2\frac{1}{2}$ -in.-dia flow passage, and the fuel valve has a 2-in.-dia flow passage. The inlet and discharge flanges of both valve bodies are machined with Conoseal surfaces, all being the same size to facilitate interchangeability.

2. Data Acquisition and Instrumentation

a. Data Acquisition

The prime item of data-sampling equipment available in Test Area H is an Aerojet-General-built digital system featuring the following capabilities: two channels sampled 250 times/sec, 25 channels sampled 50 times/sec, 92 channels sampled 16.7 times/sec, and four digital flow channels sampled 50 times/sec. The data are accumulated in four-digit samples and transmitted to a central data processing center where they are recorded on magnetic tape. An IBM 7040 digital computer is programmed to convert the digital samples into engineering units and print out the results. As a convenient addition to data processing, the conversion has been supplemented with a data-averaging program. Using this program, data for a specified interval may be averaged and the maximum deviation within that interval specified along with its direction from the average (i.e., plus or minus).

The area also has one 50-channel Consolidated Electrodynamics Corp. oscillograph and three 18-channel units. These are used to continuously record those functions deemed most essential to engine operation so that their relationships with one another may be observed and evaluated.

Very high frequency data are recorded on a four-channel Ampex FM tape recorder. In addition, the area has a six-channel on-line Miller cathode-ray oscillograph for direct recording of high-frequency data. The Ampex tape recording is played back at a fraction of its recording speed for good resolution of amplitude and frequency. This input is fed to another oscillograph for data reduction. The Miller recorder produces its record directly.

Book Two

XII, A, Engine Testing System (cont.)

The equipment discussed above constitutes the main sources of acquiring data for this program; however, the control room also has 22 Brown strip-chart recorders and two 4-channel Sanborn recorders. These are used for engine firing setup purposes and for quick-look data.

A great deal of qualitative as well as quantitative information was obtained through the use of two high-speed cameras and one low-speed camera. The value of these films cannot be over-emphasized when attempting to analyze hardware failures. At high frame rates (1000 to 2000 frames/sec), it is possible to pinpoint the beginning of metal erosion, the ejection of throat or other parts, or other occurrences.

b. Instrumentation

Measurement of pressures, temperatures, flow rates, and thrust were a normal part of every test firing. Pressures were measured with Taber, Standard Controls, and Dynisco strain-gage-type transducers in the total range 0 to 6000 psig. Potter turbine-type flowmeters were used to measure all flows. They were supplemented by orifice pressure-drop calculations of flow rates. Temperatures were obtained from chromel-alumel thermocouples, shielded, unshielded, and high-response types. Some selected temperatures were obtained using Narmac tungsten-tungsten 26% rhenium thermocouples, copper-constantan thermocouples, and resistance thermometers. High-frequency pressure oscillations were measured with Kistler piezoelectric transducers.

The accuracy of each of the recorded functions was not measured for this particular engine testing system. However, the following is a list of the functional accuracies for the Titan system as reported in Technical Memorandum 125, Revision D, Contract AF 04(647)-521:

Pressure	0.140%
Thrust	0.145%

Book Two

XII, A, Engine Testing System (cont.)

Flow rate	0.192%
Temperatures	0.118°F (resistance thermometer)
	0.50% (copper-constantan)
	0.75% (chromel-alumel)

It is not likely that the percent of error reported for the flow rate is applicable to this program because of the short duration of the majority of the tests.

3. Controls

It is necessary to start up and shut down a rocket engine in a specified sequence to prevent hardware damage. The controls portion of test area services provide the devices and circuitry required to obtain control of the specified sequence and the supporting system. In addition, it is desirable to provide engine firing controls to protect the test hardware from as many system malfunctions as possible without unduly complicating the sequence.

a. Sequence

Section XII,B,2, discusses the evaluation of an engine start and shutdown sequence through the use of the transient engine simulation program. For the High Pc engine, the opening order and opening rates of the two thrust chamber valves and the gas generator valve were established using data obtained from that program. In general, the transient program predicted satisfactory start and shutdown transients very accurately; however, the assumptions involved in the program are not able to account for combustion efficiencies at partial chamber pressure or two-phase flow, present during gaseous nitrogen injector purge operations. Therefore, some empirical calculations were required to supplement the program as written.

The engine testing conducted during this program produced much experience in the area of the correct sequencing on transient operation of high chamber pressure engines. Specific recommendations include the following:

- (1) increase thrust chamber pressure rapidly at startup to about one-half to one-third

Book Two

XII, A, Engine Testing System (cont.)

of final chamber pressure, (2) shut off gaseous injector purges at such a time that the injector manifold pressure reaches zero just before the liquid enters, (3) purge out one propellant at a time on shutdown to prevent prolonged chamber pressure oscillations resulting from the presence of a compressible fluid in the injector manifolds, and (4) purge out AeroZINE 50 fuel regenerative cooling tubes with water to prevent spontaneous decomposition of the fuel caused by heat soak-back.

b. Malfunctions

The malfunction circuits used to provide engine safety are described in this section. The engine schematic (Figure XII-A-1) shows all of the components controlled by malfunction systems.

If the thrust chamber valves fail to open, the pump discharge pressure will rise rapidly, ultimately bursting the pump. Therefore, a timer is used (calibrated to time-out just after a first-motion microswitch makes contact in each thrust chamber valve); failure of either switch to make contact before the timer runs out signals a malfunction shutdown. If either thrust chamber valve or recirculation valve closes during the firing, that pump discharge line will be overpressurized. Final-motion microswitches were installed in each of these valves to signal a malfunction shutdown if the switch opened prior to FS_2 .

Pump overspeed trips were used in conjunction with both turbopumps to provide against closure of the stand select valve (pump suction) or a large drop in downstream resistance. The units were set about 4000 rpm above expected operating speed.

If the gas generator valve failed to open, opened too slowly, or had an excessive opening delay, or if the gas generator igniters failed to cause ignition, the pressure rise in the gas generator would be zero, or less than expected. Any of the mentioned cases was considered a malfunction. To sense this condition

Book Two

XII, A, Engine Testing System (cont.)

and protect against it, a timer was used in conjunction with a pressure switch. The pressure switch had to make contact before the timer timed-out or a malfunction was signalled.

The thrust chamber itself was protected from overpressure by a new device created for this program and now used on the NERVA, M-1, and Apollo Programs--the high transient pressure shutdown device, or HTPSD unit. The HTPSD unit is a type of electrical pressure switch. When the signal from a calibrated transducer reaches a preset level, a relay is tripped and a malfunction shutdown results. It is a high-response circuit which can react in 1.5 millisecon, a period short enough to shutdown the engine when a large-size particle passes through the throat.

B. ENGINE ANALYTICAL COMPUTER PROGRAMS

The operation of the test engine system was greatly aided in this program by the extensive use of two of Aerojet's analytical computer programs: the Steady-state Program 102 and the Engine Transient Program 109. These programs were used throughout the program to determine the engine balance points and the start and shutdown sequences. In addition, the programs were used for test data evaluation, determination of allowable test parameter tolerances, and as an aid for component design. Each of the two basic programs are discussed briefly in the following paragraphs.

1. Steady-State Program

The steady-state engine program is a hydraulic simulation of an entire turbopump-fed engine system, including all required tankage. It contains the equations necessary for the simulation of almost any liquid rocket engine. In addition to the liquid system resistances, it contains program storage for component performance characteristics so that the torque and fluid horsepower required by the

Book Two

XII, B, Engine Analytical Computer Programs (cont.)

propellant pumps can be obtained from the generating system and drive turbines. Propellant performance characteristics, as a function of chamber pressure, mixture ratio, and area ratio are also included.

The steady-state program found its greatest use in determining the engine balance point for each test firing and in evaluating the test data. The program is designed to automatically evaluate the data from one test firing and then rebalance the engine for the next test. It contains a number of bias factors which can be evaluated from the data so that the input program curves yield actual engine performance. These bias factors remain in the program for the rebalance computation. A tabulation was made of these bias factors for each data evaluation so that any change could be noted and investigated. In the same way, records were kept of values of balance orifice Kw and certain line resistances to check for system changes or to flag possible errors in weight flows.

The same program is used in reverse order to evaluate the engine sensitivity to a set of specified tank pressures, a different thrust chamber combustion efficiency, a different mixture ratio in either gas generator or chamber, a changed resistance, or any of a large number of possibilities, singly or in combination. Thus with this program it can be determined how closely the parameter must be controlled in order to confine a test firing within the specified limits.

Another use for this program is to aid in designing engine testing system components. By adding, subtracting, or altering the operating characteristics of any component, the program can be made to evaluate the effect of this change on the entire engine system. Hardware is not designed or altered if the result would prove inadequate or would tax the testing system beyond its limitations. The steady-state program was used in the redesign of the gas-generator valve pintles for the High Pc test engine.

XII, B, Engine Analytical Computer Programs (cont.)

2. Transient Program

The transient analysis program assists in the analysis of liquid-rocket engine transients by means of a high-speed digital computer. Both steady-state and transient programs are similar in that each must obtain a balanced engine system before proceeding to the next computation. A balanced engine system is one in which all parameters at component interfaces are equal (e.g., flow rate through the pump is equal to flow rate through the pump discharge line; chamber pressure is equal to the injector downstream pressure; flows through the injector are the same as the flows used to calculate chamber pressure; turbine exhaust pressure used to calculate speed is the same as the exhaust pressure calculated in the exhaust duct).

In the steady-state program, the derivatives of pressure, speed, and flow rate are zero with respect to time; in the transient program, the derivatives are not necessarily zero. For instance, if the torque delivered by the turbine is greater than the torque required by the pump, the remaining energy results in a change in speed. The new speed is used in the next time-interval computation. In a similar manner, the transient program accounts for fluid inertia in the lines and volume capacitance in the thrust chamber.

The engine is divided into separate components (lines, valves, tanks, pumps, turbines, injectors, cooling tubes, thrust chamber, and exhaust ducts). Each component is represented by a program subroutine. The subroutines are groups of equations that consider the effects of fluid inertia, rotating mass inertia, volume capacitance, fluid resistance, and combustion phenomena. Computations proceed at finite time intervals (usually 0.001 to 0.01 sec). The differential equations are replaced by numerical difference equations. Integrated solution is obtained by using a modified Newton-Raphson Integration Method and a fixed integration increment (time interval) throughout each case.

Book Two

XII, B, Engine Analytical Computer Programs (cont.)

The basic subroutines of the main program are linked together by a referencing system to form a mathematical model of any liquid rocket engine that can be represented by the programmed subroutines. The referencing establishes the location of the components in the engine system. The referencing also establishes the location of the various parameters within the program data region that are needed by each subroutine. The input data for each subroutine includes referencing initial conditions, transient conditions (starter energy, valve sequencing), and component empirical data.

Typical start and shutdown transients used in High Pc Program testing, as calculated by the transient computer program, are shown in Figures XII-B-1 and XII-B-2, respectively. The plots, as shown, are plotted automatically as part of the computer operation.

C. TURBOPUMP DEVELOPMENT PROGRAM

1. Introduction

The fuel and oxidizer turbopumps used on this program were originally designed for the "Integrated Components Program (ICP)," Contract AF 04(611)-8017. Each is composed of a single-stage centrifugal pump, connected directly to a Titan II first-stage turbine. The connecting shaft is supported by bearings retained in a separate housing located between the pump and turbine. The turbopump design is shown in Figure XII-C-1.

During the ICP Program, several satisfactory engine tests were performed in which the turbopumps were used, and no difficulties were anticipated for the High Pc Program. Four turbopump tests were performed as part of the High Pc Program to verify proper operation of the pumping system. During these tests orifices were used to simulate the downstream resistances offered by the thrust

Book Two

XII, C, Turbopump Development Program (cont.)

chamber; the propellants were recirculated back to the propellant tanks. No abnormalities were evident in the data generated by tests; these data are summarized in Figures XII-C-2 through -5. Following these tests, the pumping system was considered ready for the first TCA test.

During the subsequent High Pc Test Program, three failures of the oxidizer turbopump occurred. Each of these occurrences, together with the action taken as a result of the failures, is discussed in Paragraphs XII,C,2 through 4 below.

2. Turbopump Failure--Test 1.2-01-YAM-001

The first TCA test, 1.2-01-YAM-001, was performed on 31 May 1963. During this test considerable erosion of the thrust-chamber injector was experienced, which produced severe chamber pressure perturbations. At approximately 2 sec after FSI, the oxidizer turbopump exploded, terminating the test. The turbopump failure was attributed to impeller-to-shroud rubbing as a result of these large perturbations, and not to turbopump design inadequacies. Therefore, the test engine was rebuilt using another oxidizer turbopump of the same original configuration.

3. Turbopump Failure--Test 1.2-01-YAP-005

Prior to resuming the thrust chamber testing, a pumping system checkout test was performed on 8 August 1963. This test, 1.2-01-YAP-005, resulted in the failure of the oxidizer turbopump assembly, which was nearly identical in nature to the first failure. The data for this test are presented in Figure XII-C-6.

A thorough failure analysis of this turbopump was performed. It was concluded that a pump impeller rub caused the pump to explode, similar to the previous failure. It was further concluded that the thrust bearing failed, allowing the impeller to rub on the shroud. A detailed analysis of the entire bearing housing assembly was made, which disclosed the design was marginal for the axial thrust calculated to be present in the test firings. Therefore, a redesign of the turbopump was required prior to resuming the High Pc Test Program.

Book Two

XII, C, Turbopump Development Program (cont.)

The redesigned turbopump is shown in Figure XII-C-7. The following changes were incorporated in this design as compared to the original design:

a. The original single thrust bearing was replaced with a set of two tandem matchground ball bearings to provide increased axial thrust load capacity. The type of ball cage was modified from inner-race-riding to outer-race-riding. This change provided better bearing lubrication and cooling. It allows the oil, which is injected into the area near the inner race, free entry into the bearing. The oil then circulates by centrifugal force through the rotating balls and works its way toward the outer race.

b. The bearings, housings, and shafts were modified to accept the tandem thrust bearings.

c. The number and size of jets in the internal lubrication system were modified to ensure that the velocities were sufficient to penetrate the bearing windage barrier and to provide sufficient flow to cool the bearing. An oil-jet velocity of 57 ft/sec is used to inject the oil into the bearings against the windage barrier generated by the rotation of the bearing at 20,000 rpm.

d. The test stand lubrication system was modified to provide 30% more flow and greater pressure, necessary for the modified jet system described above, and to provide increased scavenge capacity to remove the oil (scavenge flow capacity was three times the supply). In addition, the oil system did not reuse oil, but pumped oil from a supply tank to a scavenge tank to avoid bearing contamination.

e. Axial thrust measuring sleeves were designed and installed in the bearing housing of each turbopump assembly.

f. The fuel and oxidizer pumps were operated with four return-to-suction thrust balance lines to reduce thrust balance cavity pressure and the accompanying axial thrust.

Book Two

XII, C, Turbopump Development Program (cont.)

As a result of these design changes, the performance of the pumps in the modified configuration was highly satisfactory and consistent. The fuel pump used to test hardware on this contract was on the test stand continuously for 16 months, without disassembly or internal inspection. During this period it was started 39 times, and ran full-duration 30 times. Subsequent disassembly and inspection of this pump showed no abnormalities, and it was capable of further tests. Because of the troubles previously encountered with the oxidizer pump, it was disassembled and inspected several times to verify that it was in good condition.

4. Turbopump Failure--Test 1.2-02-YAM-021

Using the new turbopump configuration, analyses were performed to determine the pump operating point and corresponding axial thrust for each thrust chamber configuration and chamber pressure planned for evaluation in the test program. It was determined that the axial thrust was within allowable limits for most of the hardware to be evaluated, but that under the flow and head-rise conditions required for certain cooled TCA configurations, the thrust would be too high in the oxidizer turbopump. It was decided to design a new impeller and diffuser for these specific tests in which extended back vanes were used to reduce the high axial load attendant with the standard impeller. This new configuration was subsequently fabricated and evaluated by component testing in which an electric motor was used to drive the impeller. Test results indicated the configuration would perform satisfactorily under the turbopump operating conditions.

The first test with the oxidizer turbopump which incorporated an extended backvane impeller was performed on 9 January 1965. This test, 1.2-02-YAM-021, was an evaluation of the cooled throat and exit cone at 3000 psia chamber pressure. The oxidizer pump discharge pressure required for this test was substantially higher than required for previous TCA testing (4444 psig compared to 3400 psig). This test concluded with the destruction of the oxidizer turbopump. The failure analysis performed and the decisions reached for future testing are related in the following paragraphs.

Book Two

XII, C, Turbopump Development Program (cont.)

Turbopump components were checked for cumulative deflections as this could result in a reduction in clearances. This analysis indicated a possible clearance reduction of from 0.0307 to 0.0462 in. Build-up clearance was 0.035 in.; therefore, interference was possible.

An analysis of inducer-blade loading showed that on the basis of one pressure-loading profile of an assembled blade, the bending stress could have been as high as 83,500 psi, which is in excess of the 65,000-psi ultimate strength of T652 forging.

Start-transient data show a rough thrust chamber start, which reflected back to the turbopump as large pressure oscillations.

Comparisons with previous failures show a unique area of failure in the rupturing of the suction housing.

No abnormalities were uncovered during reviewing of the assembly and test stand installation.

The possibility of fatigue failure was investigated; it was calculated that operation at the resonant frequency for approximately 55 sec is possible before failure will occur.

On the basis of the results of the investigations performed, it was concluded that the failure was caused by the impeller rubbing the mating shroud as a result of either component deflections or by an impeller-inducer-vane failure.

On the basis of the analyses performed, together with program cost and time considerations, the following recommendations were made for future high-pressure oxidizer turbopump operation:

Book Two

XII, C, Turbopump Development Program (cont.)

(1) Use the original OTPA configuration (without extended backvane impeller) for all future testing. This TPA configuration has characteristically high values of shaft axial thrust; however, no difficulties have been experienced in its present configuration.

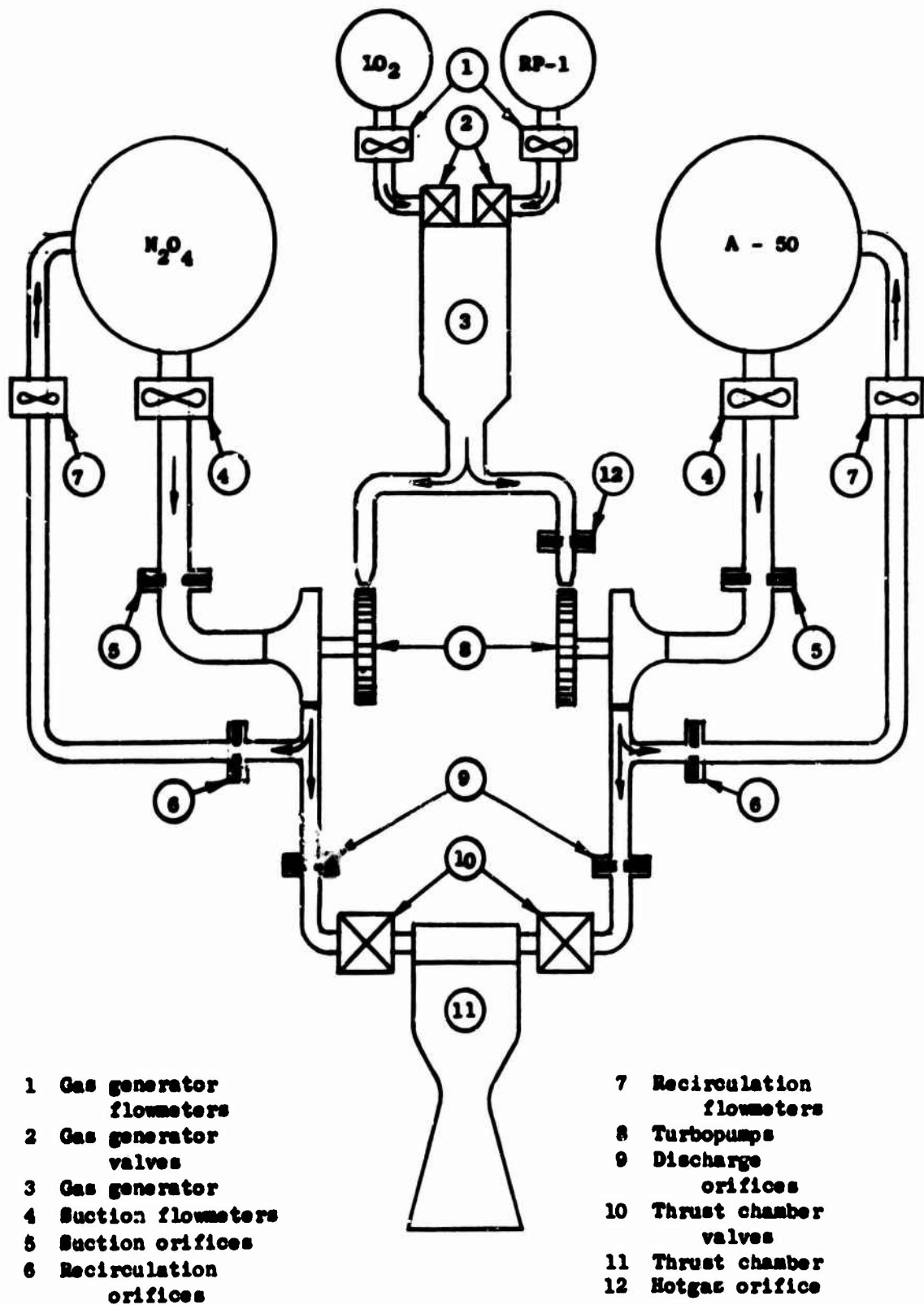
(2) Limit discharge pressure to 3,650 psig (which keeps the axial thrust below the maximum allowable).

(3) Limit suction pressure to 500 psia, with a recirculation line installed to minimize pressure oscillations.

(4) Operate at a minimum $Q/N = 0.050$ and maximum $Q/N = 0.066$.

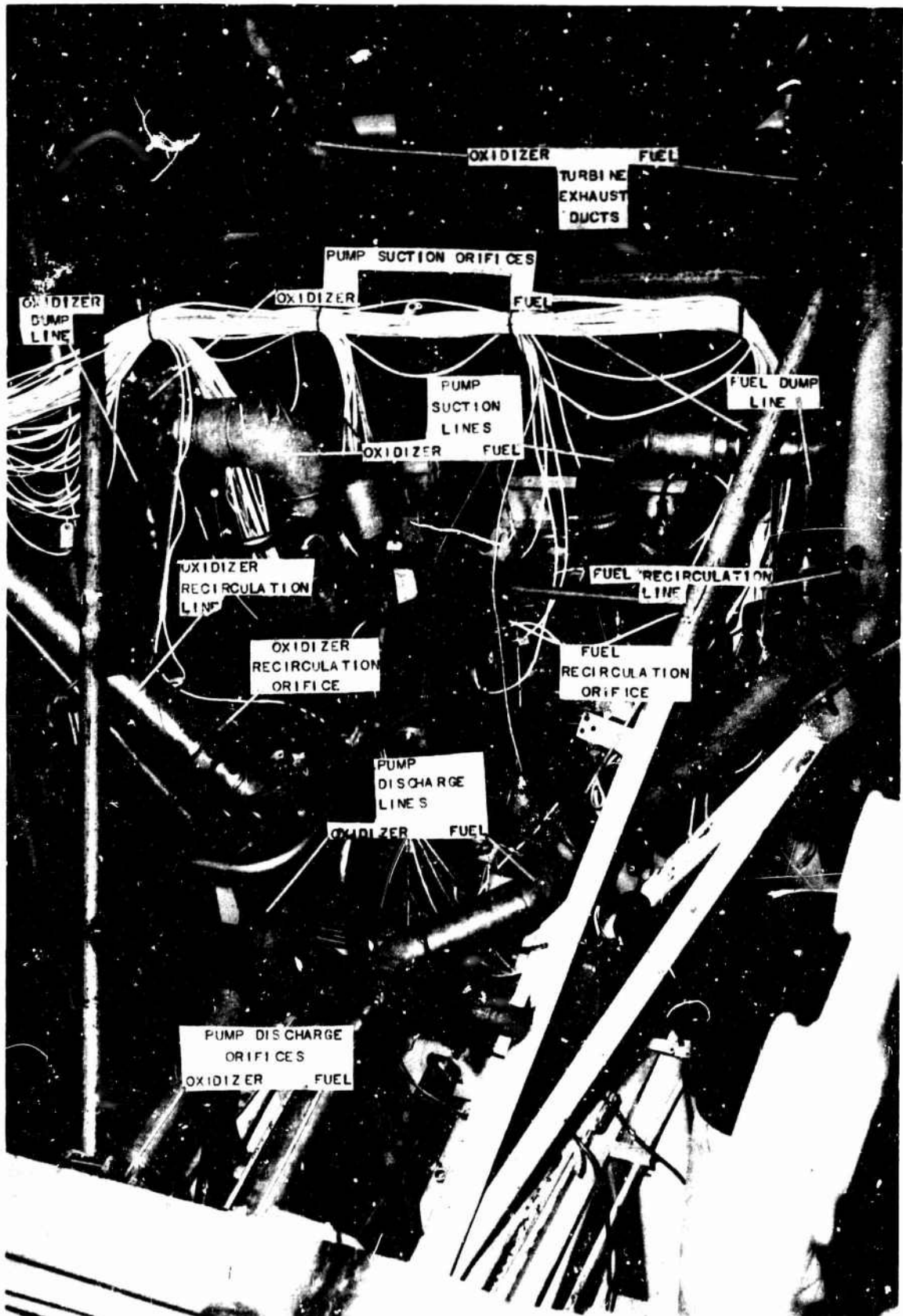
These recommendations were followed for the remainder of the Contract AF 04(611)-8191 test program. No additional failures were encountered; the turbopump operated satisfactorily during all tests.

Book Two



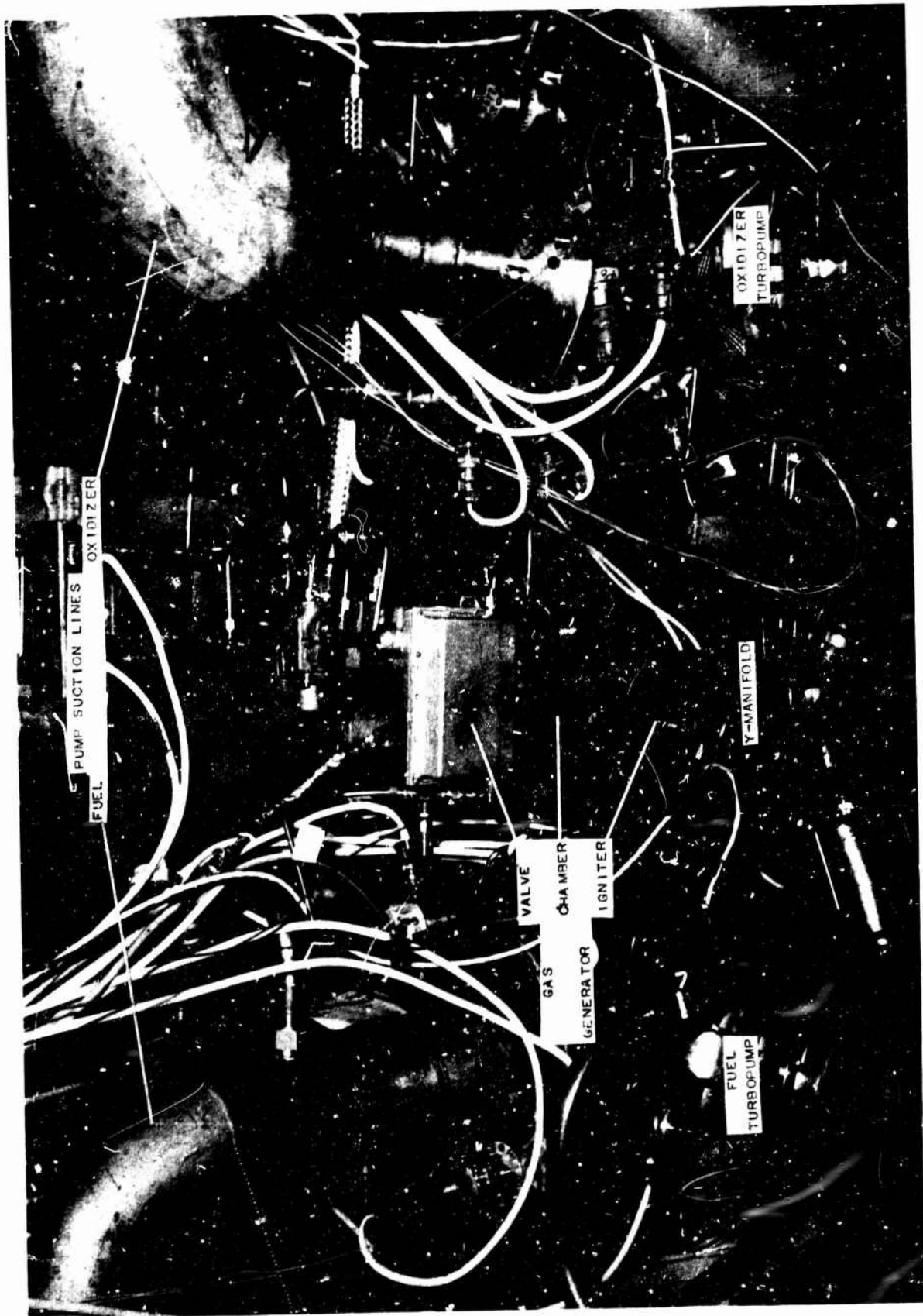
Test Engine Schematic Diagram

Figure XII-A-1



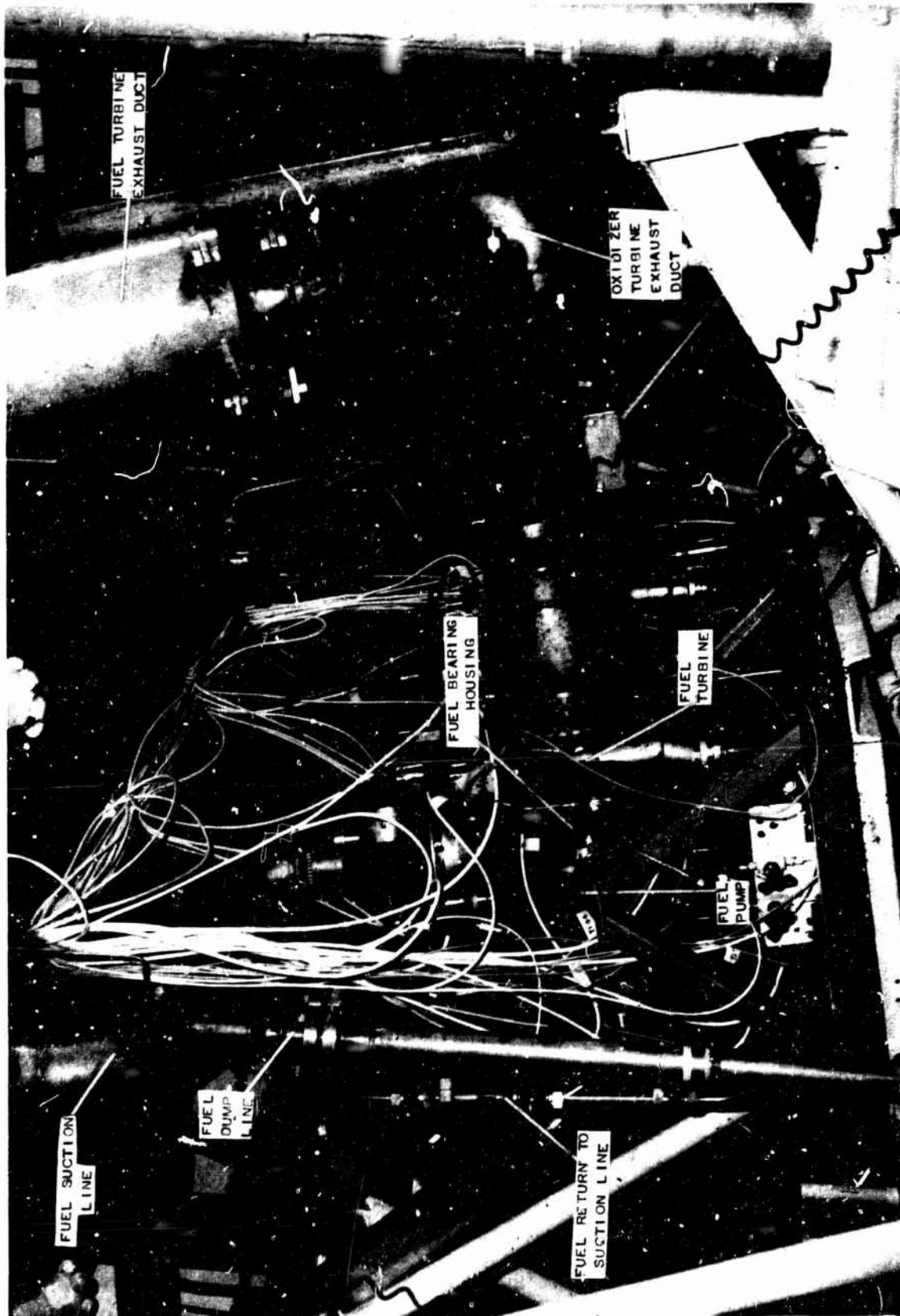
Pump System Installation, Test Stand H-3

Figure XII-A-2



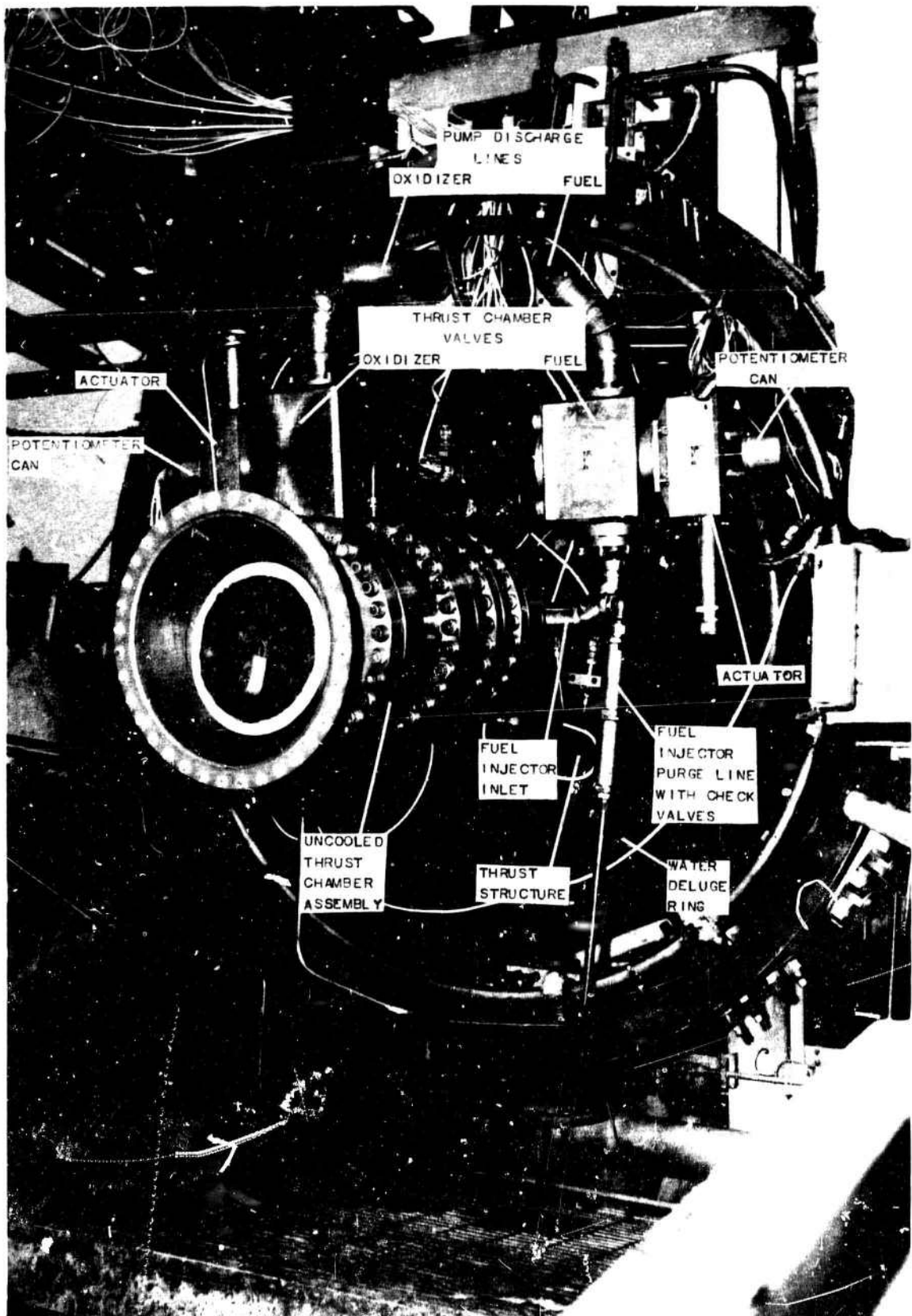
Gas Generator and Y-Manifold Installed on Test Stand H-3

Figure XII-A-3

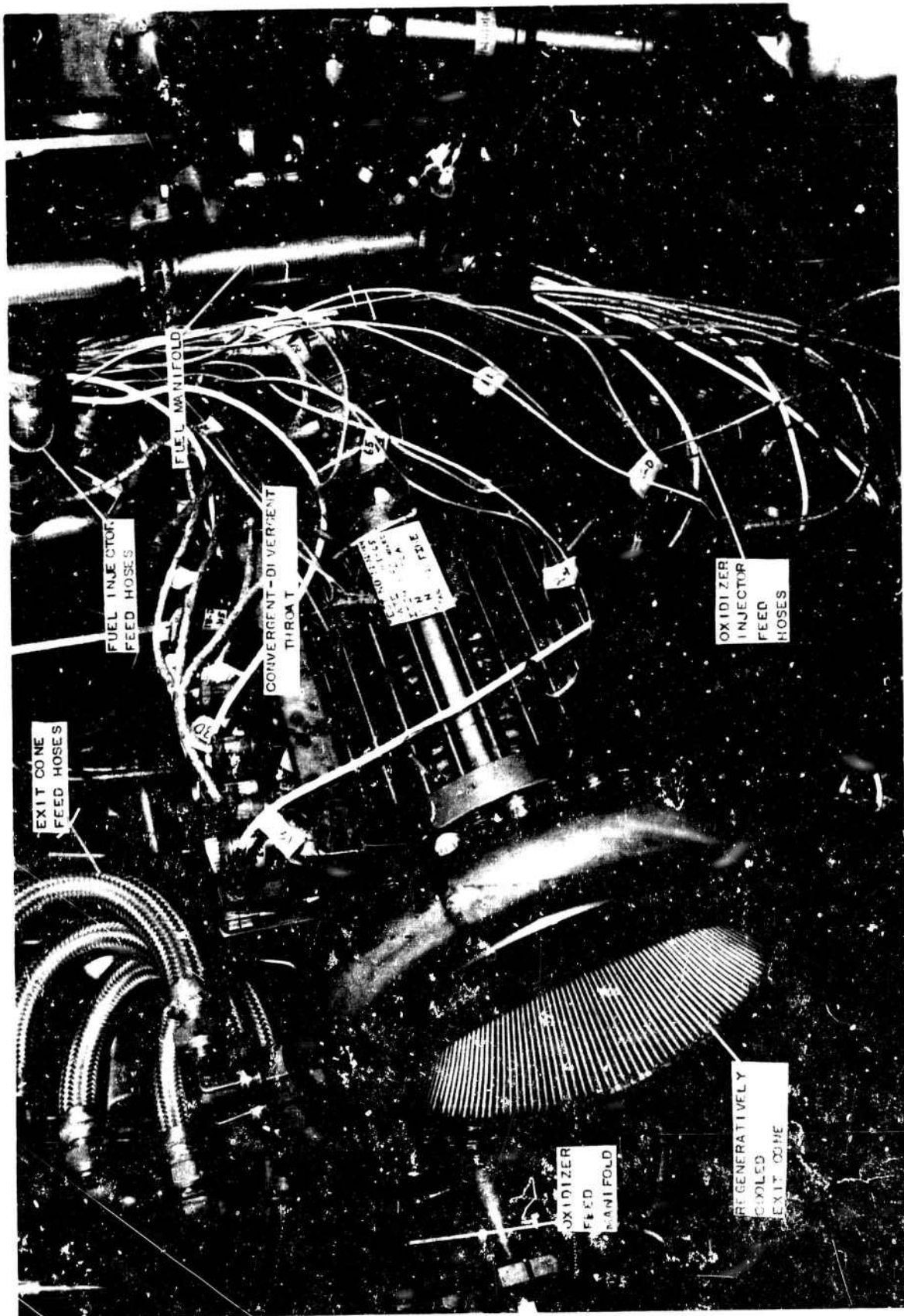


Fuel Turbopump Installation, Test Stand H-3

Figure XII-A-4

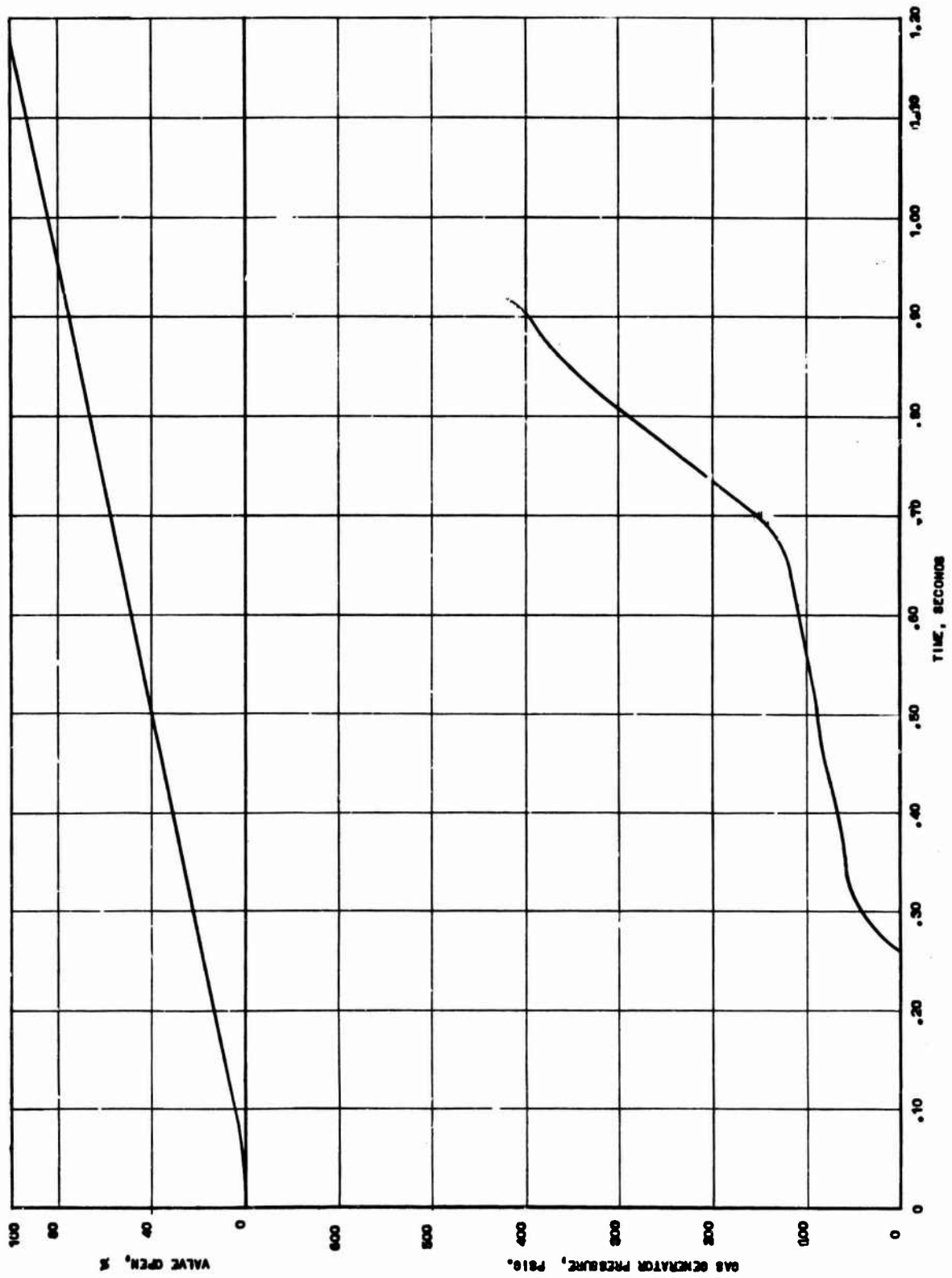


Uncooled Thrust Chamber Assembly Installed on Test Stand H-3



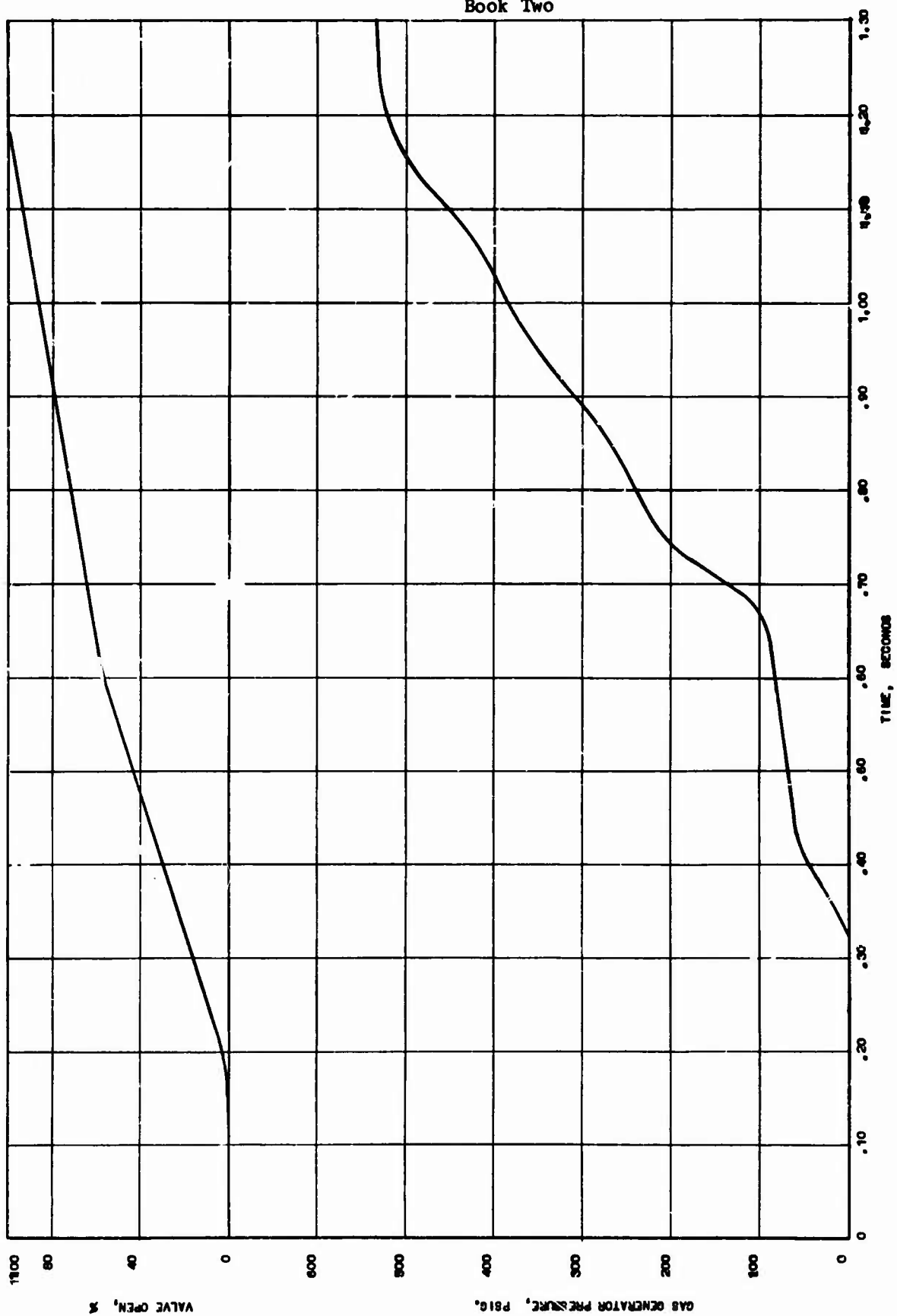
Cooled Throat and Exit Cone Installed on Test Stand H-3

Figure XII-A-6



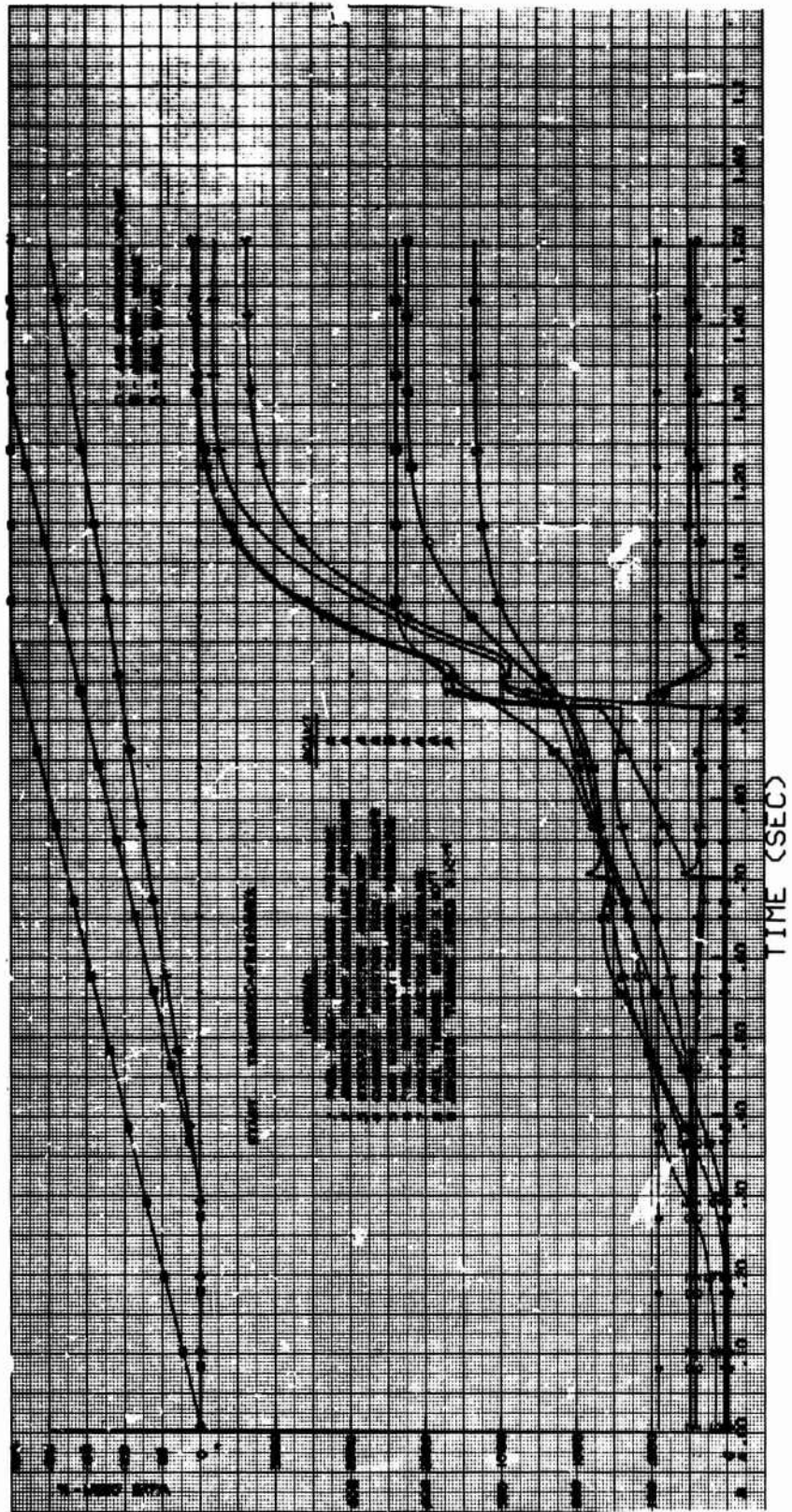
Original Gas Generator Valve Sequence

Figure XII-A-7

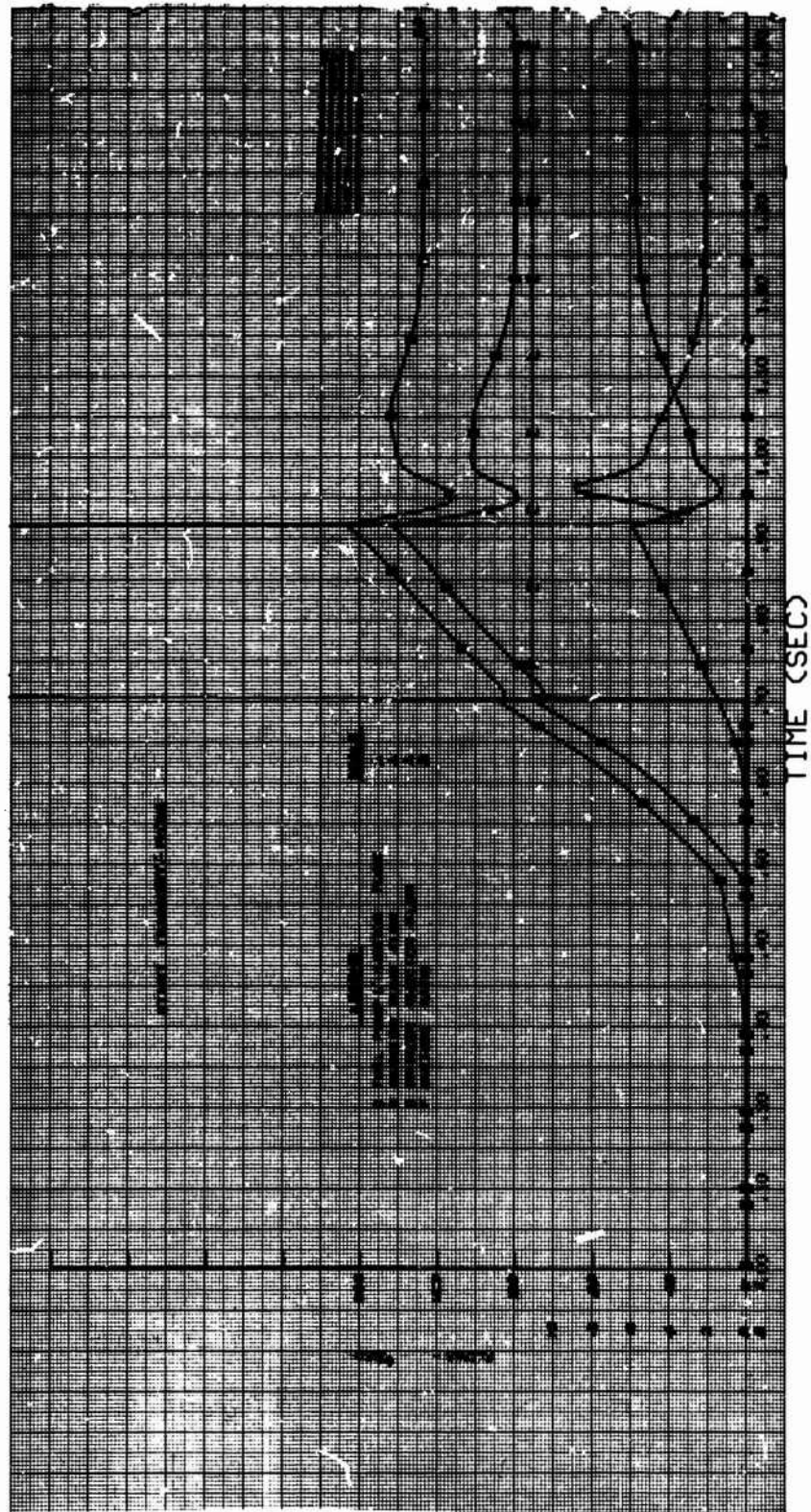


Final Gas Generator Valve Sequence

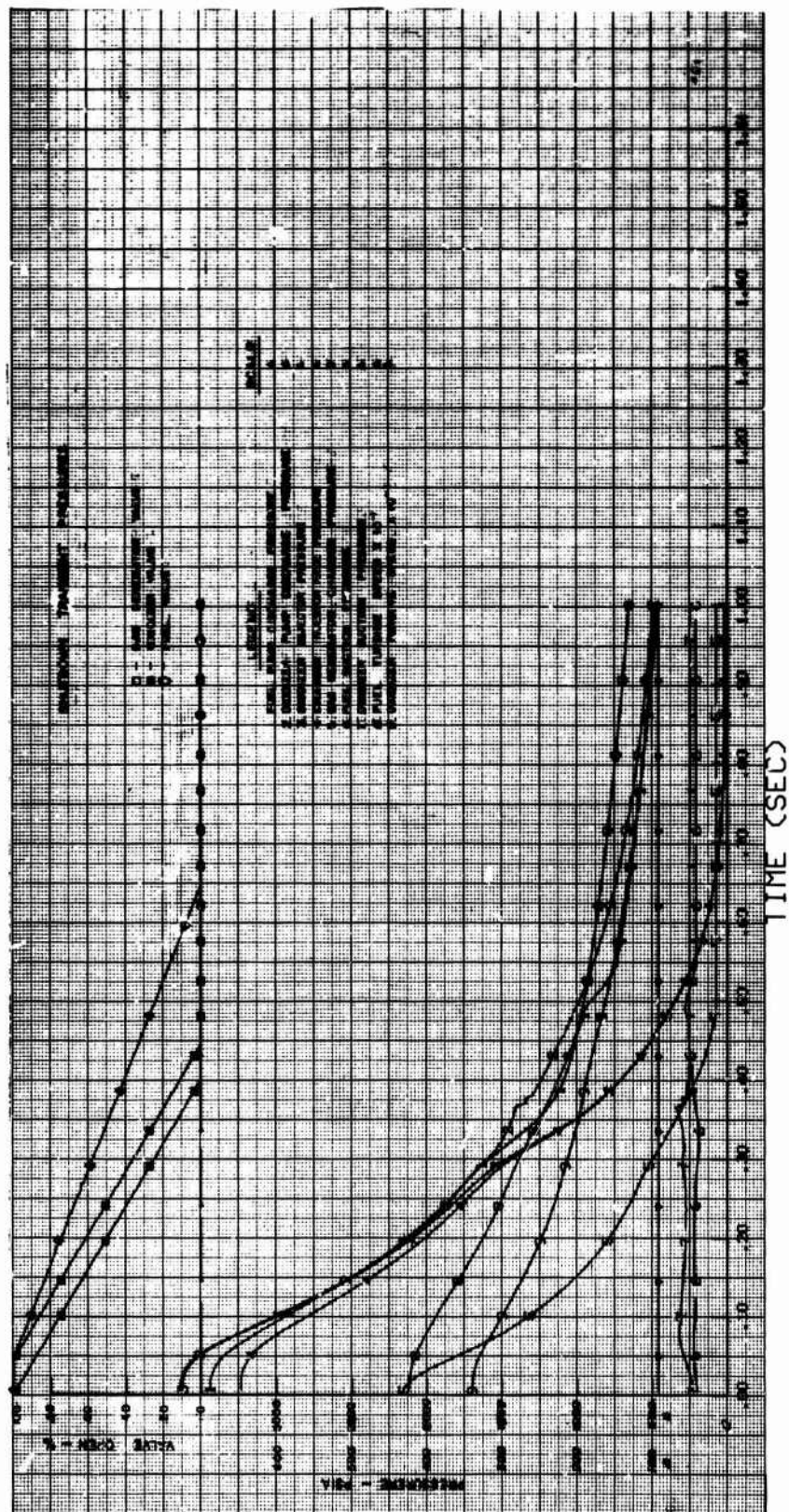
Figure XII-A-8



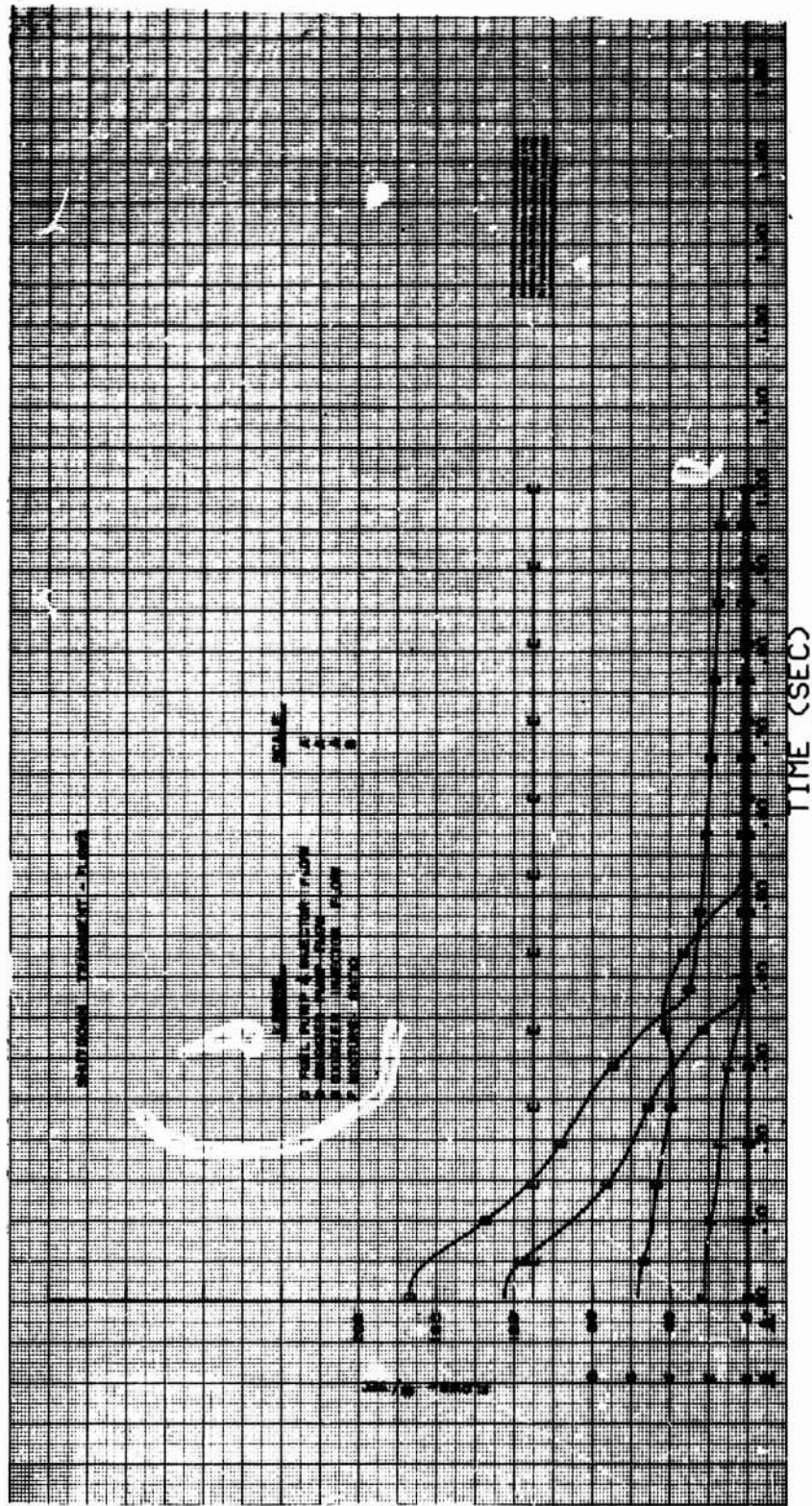
Typical Uncooled TCA Start Transient



Typical Uncooled TCA Start Transient



Typical Uncooled TCA Shutdown Transient

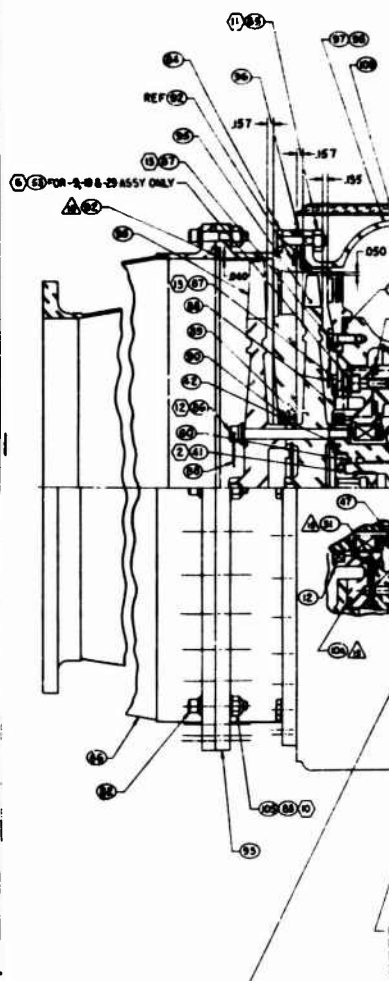


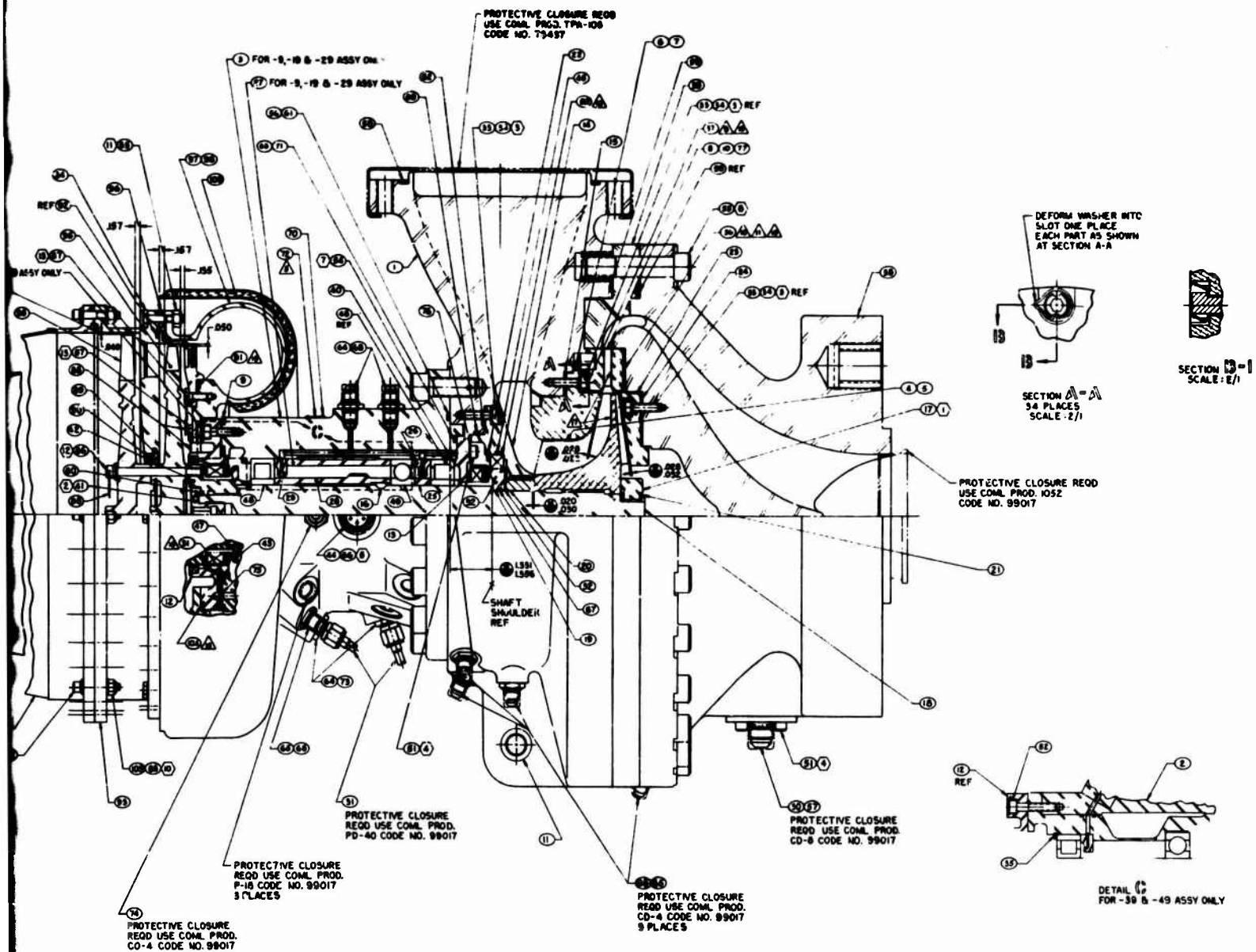
Typical Uncooled TCA Shutdown Transient

RING-BACKUP	80
REDUCER	79
PIPE ADAPTOR	78
O-RING	77
SEAL CODE NO. 83259	76
SEAL CODE NO. 08199	75
FITTING	74
UNION	73
O-RING	72
REDUCER	71
PLUG	70
O-RING	69
UNION	68
O-RING	67
O-RING	66
NATORQ SEAL	65
O-RING	64
O-RING (TEFLON)	63
O-RING	62
O-RING	61
O-RING CODE NO. 78943	60
O-RING 13.501X-038 DIA (ROSS SECT. (TEFLON))	59
GASKET CODE NO. 72433	58
GASKET CODE NO. 72433	57
	56
BOLT	55
BOLT	54
SCREW-CAP	53
NATORQ SEAL	52
SCREW-CAP	51
SEAL CODE NO. 71840	50
BEARING-BALL (MATCH SET)	49
BEARING-ROLLER	48
GASKET	47
	46
O-RING	45
PROBE SPEED PICKUP	44
FACE-SEAL	43
COUPLING-SHAFT	42
RETAINER-COUPLING	41
MATERIAL	ITEM NO

NATORQ SEAL	119
UNION	118
NATORQ SEAL	117
REDUCER	116
SHAFT-PUMP-REWORK	115
	114
SPACER-SLEEVE-INNER	113
RING-JET-OIL	112
RING-LUBE (MATCH SET)	111
SPACER-SLEEVE	110
O-RING	109
HOUSING-BEARING-INSTRUMENT	108
HOUSING-BEARING	107
ADAPTER-PROBE-SPEED PICKUP	106
WASHER	105
GASKET-SPIRAL WOUND	104
O-RING	103
UNION	102
SNAP RING	101
INSULATION ASSY MANIFOLD CODE NO. 72741	100
SHIM (TEFLON)	99
NATORQ SEAL	98
MANIFOLD TURBINE INLET	97
NOZZLE-FIRST STAGE	96
ROTOR TURBINE-SECOND STAGE	95
ROTOR TURBINE-FIRST STAGE	94
NOZZLE-SECOND STAGE	93
GASKET-SPIRAL WOUND	92
GASKET-SPIRAL WOUND	91
SEAL-LABYRINTH	90
SNAPRING CODE NO. 70136	89
WIRE-LOCK	88
BOLT CODE NO. 82831	87
BOLT CODE NO. 56873	86
NUT CODE NO. 85639	85
BOLT CODE NO. 82831	84
NUT CODE IDENT NO. 82831	83
BOLT MACHINE	82
RING BACKUP	81
MATERIAL	ITEM NO

SHIM	40
	39
	38
SHIM	37
SHIM	36
	35
WASHER-CUP	34
SCREW-CAP	33
SHIM	32
GASKET	31
FITTING-BLEED	30
RING-LUBE	29
HOUSING-DISCHARGE	28
HOUSING-DISCHARGE	27
FILTER, BENDIX	26
	25
SHIM	24
PLATE-BACKVANE	23
SPIROLOX RETAINING RING CODE NO. 80724	22
TAB-LOCKING	21
SPACER	20
RING-WEARING	19
	18
NUT	17
	16
SHIM	15
HOUSING-SEAL	14
SEAL ASSY-PUMP	13
SEAL ASSY-TURBINE	12
BUSHING	11
DIFFUSER	10
RING	9
	8
SHROUD-IMPELLER	7
SHROUD-IMPELLER	6
IMPELLER	5
IMPELLER	4
	3
	2
HOUSING INLET	1
	0





2

Original Turbopump Assembly Design

Figure XII-C-1

Book Two

1.	OTPA	PN 282910-9	SN 003
2.	FTPA	PN 282910-19	SN 004
3.	GGA	PN 223780	SN 0-13

Test Duration: 5.889 sec

<u>OTPA Data</u>		<u>FTPA Data</u>		<u>GGA and Turbine Data</u>	
P _{os}	220 psig	P _{fs}	230 psig	P _{cgg}	390 psig
P _{od}	3290 psig	P _{fd}	3157 psig	P _{oti}	352 psig
P _o	1.45	P _f	0.89	T _{oti}	1275°F
Q _o	706 gpm	Q _f	417 gpm	P _{fti}	300 psig
N _{to}	16,112 rpm	N _{tf}	20,890 rpm	T _{fti}	1160°F
Q/N*	0.0438	Q/N*	0.0199	W _{ot} *	12.5 lb/sec
ΔH/N ² *	1.87 x 10 ⁺⁵	ΔH/N ² *	1.71 x 10 ⁺⁵	W _{ft} *	10.7 lb/sec
P _{id}	2209 psig	P _{id}	2339 psig	W _{og}	6.3 lb/sec
P _{drd}	3257 psig	P _{drd}	3155 psig	W _{fg}	16.9 lb/sec
				MR _{gg}	0.373

Comments: ρ = Specific Gravity

P_{id} = Impeller Discharge Pressure

P_{drd} = Diffuser Ring Discharge Pressure

* = Calculated Data

Pumping System Data, Test 1.2-02-YAP-001

Figure XII-C-2

Book Two

1.	OTPA	PN 282910-9	SN 003
2.	FTPA	PN 282910-19	SN 004
3.	GGA	PN 223780	SN 0-13

Test Duration: 7.226 sec

<u>OTPA Data</u>		<u>FTPA Data</u>		<u>GGA and Turbine Data</u>	
P _{os}	216 psig	P _{fs}	222 psig	P _{cgg}	453 psig
P _{od}	3440 psig	P _{fd}	4140 psig	P _{oti}	420 psig
P _o	1.41	P _f	0.89	T _{oti}	1280°F
Q _o	816 gpm	Q _f	479 gpm	P _{fti}	295 psig
N _{to}	16,500 rpm	N _{tf}	22,450 rpm	T _{fti}	1210°F
Q/N*	0.0495	Q/N*	0.0213	W _{ot} *	16.1 lb/sec
ΔH/N ² *	1.89 x 10 ⁺⁵	ΔH/N ² *	1.99 x 10 ⁺⁵	W _{ft} *	11.2 lb/sec
P _{id}	2320 psig	P _{id}	3100 psig	W _{og}	7.46 lb/sec
P _{drd}	3400 psig	P _{drd}	4180 psig	W _{fg}	19.8 lb/sec
				MR _{gg} *	0.377

Comments: P = Specific Gravity

P_{id} = Impeller Discharge Pressure

P_{drd} = Diffuser Ring Discharge Pressure

* = Calculated Data

Pumping System Data, Test 1.2-02-YAP-002

Figure XII-C-3

Book Two

1.	OTPA	PN 282910-9	SN 003
2.	FTPA	PN 282910-19	SN 004
3.	GGA	PN 223780	SN 0-13

Test Duration: 5.16 sec

<u>OTPA Data</u>		<u>FTPA Data</u>		<u>GGA and Turbine Data</u>	
P _{os}	209 psig	P _{fs}	218 psig	P _{c_{gg}}	500 psig
P _{od}	3897 psig	P _{fd}	3685 psig	P _{oti}	470 psig
P _o	1.40	P _f	0.89	T _{oti}	1350°F
Q _o	886 gpm	Q _f	450 gpm	P _{f_{ti}}	240 psig
N _{to}	17,400 rpm	N _{tf}	20,970 rpm	T _{f_{ti}}	1240°F
Q/N*	0.051	Q/N*	0.0215	W _{ot} *	17.4 lb/sec
ΔH/N ² *	1.93 x 10 ⁺⁵	ΔH/N ² *	2.03 x 10 ⁺⁵	W _{it} *	8.89 lb/sec
P _{id}	3460 psig	P _{id}	2710 psig	W _{og}	7.5 lb/sec
P _{d_{rd}}	3850 psig	P _{d_{rd}}	3670 psig	W _{fg}	18.8 lb/sec
				MR _{gg}	0.40

Comments: ρ = Specific Gravity
 P_{id} = Impeller Discharge Pressure
 P_{d_{rd}} = Diffuser Ring Discharge Pressure
 * = Calculated Data

Pumping System Data, Test 1.2-02-YAP-003

Figure XII-C-4

Book Two

1.	OTPA	PN 282910-9	SN 003
2.	FTPA	PN 282910-19	SN 004
3.	GGA	PN 223780	SN 0-13

Test Duration: 5.217 sec

<u>OTPA Data</u>		<u>FTPA Data</u>		<u>GGA and Turbine Data</u>	
P _{os}	200 psig	P _{fs}	215 psig	P _{c_{gg}}	468 psig
P _{od}	3591 psig	P _{fd}	3486 psig	P _{oti}	440 psig
P _o	1.42	P _f	0.89	T _{oti}	1330°F
Q _o	848 gpm	Q _f	440 gpm	P _{fti}	225 psig
N _{to}	16,800 rpm	N _{tf}	20,440 rpm	T _{fti}	1200°F
Q/N*	0.0	Q/N*	0.0215	W _{ot} *	16.2 lb/sec
ΔH/N ² *	1.925 x 10 ⁻⁵	ΔH/N ² *	2.01 x 10 ⁻⁵	W _{ft} *	8.27 lb/sec
P _{id}	2980 psig	P _{id}	2690 psig	W _{og}	7.16 lb/sec
P _{d_{rd}}	3550 psig	P _{d_{rd}}	3450 psig	W _{fg}	17.3 lb/sec
				MR _{gg}	0.414

Comments: P = Specific Gravity
 P_{id} = Impeller Discharge Pressure
 P_{d_{rd}} = Diffuser Ring Discharge Pressure
 * = Calculated Data

Pumping System Data, Test 1.2-02-YAP-004

Figure XII-C-5

Book Two

1.	OTPA	PN 282910-9	SN 005
2.	FTPA	PN 282910-19	SN 004
3.	GGA	PN 230196-1	SN 0-13

Test Duration: 5.219 sec

<u>OTPA Data</u>		<u>FTPA Data</u>		<u>GGA and Turbine Data</u>	
P _{os}	270 psia	P _{fs}	271 psia	P _{cgg}	428 psia
P _{od}	3105 psia	P _{fd}	3267 psia	P _{oti}	398 psia
P _o	1.40	P _f	0.88	T _{oti}	1238°F
Q _o	878 gpm	Q _f	497 gpm	P _{fti}	290 psia
N _{to}	15,740 rpm	N _{tf}	21,050 rpm	T _{fti}	1080°F
Q/N*	0.0558	Q/N*	0.0236	W _{ot} *	16.11 lb/sec
$\Delta H/N^2$	1.885×10^{-5}	$\Delta H/N^2$ *	1.770×10^{-5}	W _{ft} *	12.33 lb/sec
P _{id}	2355 psia	P _{id}	**	W _{og}	7.80 lb/sec
				W _{fg}	20.65 lb/sec
				MR _{gg}	0.378

Comments: P = Specific Gravity
P_{id} = Impeller Discharge Pressure
P_drd = Diffuser Ring Discharge Pressure
* = Calculated Data
** = Invalid Data

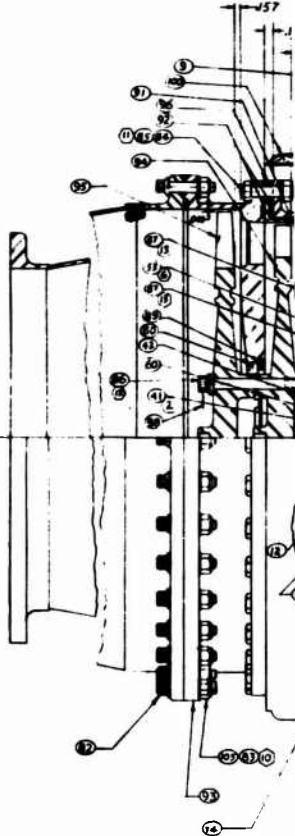
Pumping System Data, Test 1.2-02-YAP-005

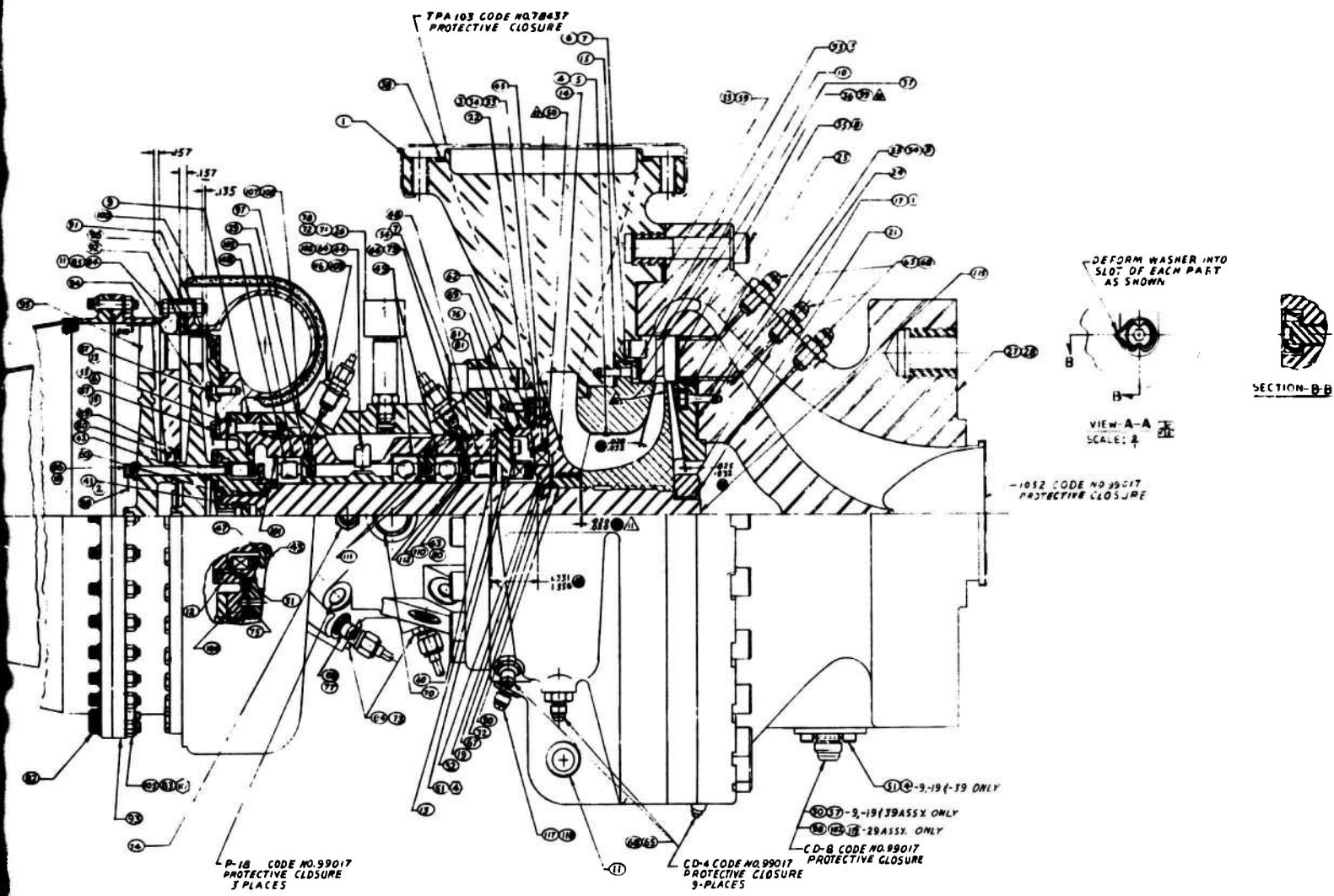
Figure XII-C-6

WASHER			106
GASKET, SPIRAL WOUND			104
			103
			102
			101
INSULATION ASSY MANFOLD			100
			99
MANFOLD TURBINE INLET			98
MANFOLD TURBINE INLET			97
NOZZLE, FIRST STAGE			96
NOZZLE, SECOND STAGE			95
NOZZLE, SECOND STAGE			94
GASKET, SPIRAL WOUND			93
GASKET, SPIRAL WOUND			92
GASKET, SPIRAL WOUND			91
GASKET, SPIRAL WOUND			90
GASKET, SPIRAL WOUND			89
GASKET, SPIRAL WOUND			88
GASKET, SPIRAL WOUND			87
GASKET, SPIRAL WOUND			86
GASKET, SPIRAL WOUND			85
GASKET, SPIRAL WOUND			84
GASKET, SPIRAL WOUND			83
GASKET, SPIRAL WOUND			82
GASKET, SPIRAL WOUND			81

			80
			79
			78
DIFFUSER			77
SEAL			76
SEAL			75
FITTING			74
UNION			73
IDENT PLATE			72
			71
SCREW DRIVE			70
O-RING			69
UNION			68
O-RING			67
O-RING			66
NATORQ SEAL			65
O-RING			64
O-RING			63
O-RING			62
O-RING			61
O-RING			60
GASKET			59
GASKET			58
GASKET			57
RING, BACKUP			56
BOLT			55
3/16-18 1 1/2 SPS UNBRAKE SELF-LOCKING SCREW			54
SCREW, CAP			53
SCREW, CAP			52
SCREW, CAP			51
SEAL			50
BEARING, BALL			49
BEARING, ROLLER			48
GASKET			47
PIPE, EXHAUST			46
O-RING			45
PROBE, SPEED PICKUP			44
FACE SEAL			43
COUPLING, SHAFT			42
RETAINER, COUPLING			41

SHIM			40
FLANGE			39
HOUSING DISCHARGE			38
SHIM			37
SHIM			36
SNAP RING			35
WASHER, CUP			34
SCREW, CAP			33
SHIM			32
GASKET			31
FITTING, BLEED			30
RING LUBE			29
SPACER, INNER			28
SPACER, OUTER			27
RING LUBE			26
SPACER, INNER			25
SHIM			24
PLATE, BACKWAVE			23
SPROCKET RETAINING RING			22
TAB LOCKING			21
SPACER			20
RING WEARING			19
SHAFT			18
NUT			17
KEY			16
SHIM			15
HOUSING, SEAL			14
SEAL ASSY			13
SEAL ASSY			12
BUSHING			11
DIFFUSER			10
RING			9
DIFFUSER			8
SHROUD, IMPELLER			7
SHROUD, IMPELLER			6
IMPELLER			5
IMPELLER			4
HOUSING, BEARING			3
HOUSING, BEARING			2
HOUSING INLET			1





2

Final Turbopump Assembly Design

Figure XII-C-7